Universidad de Oviedo

Programa de Doctorado en Materiales

Estudio de procesos con quarks top y L1 trigger en el Run 3 del LHC

Study of top quark processes and L1 trigger in the Run 3 of the LHC

Doctorando:

Carlos Vico Villalba

Oviedo, Mayo 2025

Universidad de Oviedo

Programa de Doctorado en Materiales

Estudio de procesos con quarks top y L1 trigger en el Run 3 del LHC

Study of top quark processes and L1 trigger in the Run 3 of the LHC

Doctorando:

Carlos Vico Villalba

Directores:

Dra. Bárbara Alvarez González

Dr. Santiago Folgueras Gómez

Oviedo, Mayo 2025

Universidad de Oviedo

AUTORIZACIÓN PARA LA PRESENTACIÓN DE TESIS DOCTORAL

Año Académico: 2024/2025

1.- Datos personales del autor de la Tesis		
Apellidos: Vico Villalba	Nombre: Carlos	
DNI/Pasaporte/NIE: 71727632Q	Teléfono: 618773971	Correo electrónico: vicocarlos@uniovi.es

2.- Datos académicos	
Programa de Doctorado cursado: Materiales	
Órgano responsable: Centro Internacional de Postgrado	
Título definitivo de la Tesis	
Español/Otro Idioma: Estudio de procesos con quarks top y L1 trigger en el Run 3 del LHC.	Inglés: Study of top quark processes and L1 trigger in the Run 3 of the LHC.
Rama de conocimiento: CIENCIAS	

3.- Autorización del Director/es y Tutor de la tesis	
D/Dª: Bárbara Alvarez González	DNI/Pasaporte/NIE: 48935068S
Departamento/Instituto: Departamento de Física	
D/Dª: Santiago Folgueras Gómez	DNI/Pasaporte/NIE: 71668032D
Departamento/Instituto/Institución: Departamento de Física	
Autorización del Tutor de la tesis	
D/Dª: Francisco Javier Cuevas Maestro	DNI/Pasaporte/NIE: 13735601R
Departamento/Instituto: Departamento de Física	

Autoriza la presentación de la tesis doctoral en cumplimiento de lo establecido en el Art. 32 del Reglamento de los Estudios de Doctorado, aprobado por el Consejo de Gobierno, en su sesión del día 20 de julio de 2018 (BOPA del 9 de agosto de 2018)

En Oviedo a 12 de mayo de 2025

Director/es de la Tesis — Tutor de la Tesis

Fdo.: — Fdo.:

SR. PRESIDENTE DE LA COMISIÓN ACADÉMICA DEL PROGRAMA DE DOCTORADO EN MATERIALES

FOR-MAT-VOA-009 (Reg.2018)

Universidad de Oviedo

RESOLUCIÓN DE PRESENTACIÓN DE TESIS DOCTORAL

Año Académico: 2024/2025

1.- Datos personales del autor de la Tesis		
Apellidos: Vico Villalba	Nombre: Carlos	
DNI: 71727632Q	Teléfono: 618773971	Correo electrónico: vicocarlos@uniovi.es

2.- Datos académicos	
Programa de Doctorado cursado: Materiales	
Órgano responsable: Centro Internacional de Postgrado	
Departamento/Instituto en el que presenta la Tesis Doctoral: Departamento de Física	
Título definitivo de la Tesis	
Español: Estudio de procesos con quarks top y L1 trigger en el Run 3 del LHC.	Inglés: Study of top quark processes and L1 trigger in the Run 3 of the LHC.
Rama de conocimiento: ☐ Arte y Humanidades X Ciencias ☐ Ciencias de la Salud ☐ Ciencias Sociales y Jurídicas ☐ Ingeniería y Arquitectura	
Señale si procede: X Mención Internacional ☐ Mención Industrial X Idioma de presentación de la Tesis distinto al español ☐ Presentación como compendio de publicaciones	

3.- Autorización del Presidente de la Comisión Académica	
D: Jaime A. Viña Olay	DNI: 10828913F
Departamento/Instituto: Departamento de Ciencia de los Materiales e Ingeniería Metalúrgica	

Resolución: La Comisión Académica del Programa de Doctorado en Materiales en su reunión de fecha 22/05/2025, acordó la presentación de la tesis doctoral a la Comisión de Doctorado, previa comprobación de que la tesis presentada y la documentación que la acompaña cumplen con la normativa vigente, según lo establecido en el Art.32.8 del Reglamento de los Estudios de Doctorado, aprobado por el Consejo de Gobierno, en su sesión del día 20 de julio de 2018 (BOPA del 9 de agosto de 2018)
Además, informa:

	Favorable	Desfavorable
• Mención Internacional	X	☐
• Mención Industrial	☐	☐
• Idioma	X	☐
• Presentación como compendio de publicaciones	☐	☐

FOR-MAT-VOA-012 (Reg. 2018)

Universidad de Oviedo

Justificación

La tesis *titulada "Estudio de procesos con quarks top y L1 trigger en el Run 3 del LHC"* y la documentación presentada por el doctorando Carlos Vico Villalba y sus directores de tesis los Dres. Bárbara Alvarez González y Santiago Folgueras Gómez (ambos del Departamento de Física), cumple con los requisitos para ser presentada a la Comisión de Doctorado y para optar al Doctorado Internacional.

Gijón, 22 de mayo de 2025
Presidente de la Comisión Académica del Programa de Doctorado

Fdo.: Jaime A. Viña Olay

Contra la presente Resolución, podrá interponer recurso de alzada ante el Rectorado, en el plazo de un mes, a partir del día siguiente al de la presente notificación, de conformidad con el art. 122 de la Ley 39/2015, de 1 de octubre, de Procedimiento Administrativo Común de las Administraciones Públicas

SR. DIRECTOR DEL CENTRO INTERNACIONAL DE POSTGRADO

Universidad de Oviedo

RESUMEN DEL CONTENIDO DE TESIS DOCTORAL

1.- Título de la Tesis	
Español: Estudio de procesos con quarks top y L1 trigger en el Run 3 del LHC.	Inglés: Study of top quark processes and L1 trigger in the Run 3 of the LHC.

2.- Autor	
Nombre: Carlos Vico Villalba	DNI: 71727632q
Programa de Doctorado: Materiales	
Órgano responsable: Centro Internacional de Postgrado	

FOR-MAT-VOA-010 (Reg.2018)

RESUMEN en español (máximo 4000 caracteres)

Esta tesis doctoral se enmarca en el área de la física experimental de altas energías y ha sido desarrollada en el laboratorio europeo CERN (European Organization for Nuclear Research). En particular, se basa en el análisis de datos obtenidos por el experimento CMS, uno de los cuatro principales experimentos del Gran Colisionador de Hadrones (LHC). A lo largo de las distintas publicaciones que componen la tesis, se han estudiado diversos mecanismos de producción de partículas en colisiones protón-protón.

En primer lugar, se presentan medidas de la producción asociada de pares de quarks top y antiquarks top junto con bosones W (ttW), utilizando estados finales con al menos dos leptones. Este proceso constituye un fondo relevante en el estudio de la producción de pares de quarks top en asociación con bosones de Higgs. Las mediciones se han realizado con datos recogidos por el experimento CMS durante los años 2016, 2017 y 2018, correspondientes a colisiones protón-protón a una energía en el centro de masas de 13 TeV. En particular, se ha determinado la sección eficaz inclusiva del proceso, empleando el conjunto de datos más extenso jamás registrado en física de aceleradores. Este resultado representa, hasta la fecha, la medición más precisa disponible para esta cantidad dentro del Modelo Estándar. Asimismo, se han obtenido secciones eficaces diferenciales —a nivel de partícula y corrigiendo los efectos del detector— para algunos de los observables más relevantes del proceso ttW, utilizando el mismo conjunto de datos.

Adicionalmente, se han realizado mediciones en el contexto del sector electrodébil del Modelo Estándar, mediante la determinación directa de la sección eficaz de producción simultánea de un bosón W y un bosón Z (WZ). A diferencia del proceso ttW, este canal no incluye quarks top en el estado final, lo que permite maximizar la pureza y la precisión de la medida en un entorno con baja multiplicidad hadrónica. El estado final se caracteriza por la presencia de al menos tres leptones cargados y energía transversa faltante, asociada a la producción de neutrinos en las desintegraciones de los bosones W. Esta medición representa, además, la primera realizada con un nuevo conjunto de datos recogido por el LHC a partir de 2022, nunca antes analizado. La sección eficaz de producción se presenta con una precisión relativa del 3.5 %, lo que constituye el resultado más preciso disponible actualmente para esta cantidad. Esta medida completa, además, una trayectoria de más de 15 años de estudios sobre las propiedades del proceso WZ en el LHC.

La tesis incluye también una contribución al mantenimiento de los sistemas de tubos de deriva y al desarrollo del sistema de *trigger* del experimento CMS en el marco de la Fase 2, que contempla una serie de actualizaciones necesarias para operar en las condiciones de alta luminosidad previstas en el High Luminosity LHC (HL-LHC). En particular, se presentan estudios destinados a caracterizar los posibles efectos de envejecimiento de los detectores debido a su operación continua en un entorno de alta radiación, concluyéndose que, a pesar de estas condiciones, la eficiencia de detección y reconstrucción de muones no se verá comprometida de forma significativa por el

Universidad de Oviedo

deterioro de los tubos de deriva. Asimismo, se propone un nuevo algoritmo capaz de identificar eventos en los que un muón de alto momento transverso pierde una fracción relevante de energía por radiación de frenado, un tipo de señal que hasta ahora no podía seleccionarse en tiempo real durante la toma de datos. Este algoritmo ha sido diseñado para su implementación en la electrónica del sistema de detección, lo que permitirá acceder a este tipo de eventos durante la operación del HL-LHC.

RESUMEN en Inglés

This doctoral thesis is framed within the field of experimental high-energy physics and has been carried out at the European laboratory CERN (European Organization for Nuclear Research). Specifically, it is based on the analysis of data collected by the CMS experiment, one of the four main experiments at the Large Hadron Collider (LHC). Throughout the various publications that are included in the thesis, different mechanisms of particle production in proton-proton collisions have been studied.

First, measurements of the associated production of top quark -- antiquark pairs together with W bosons (ttW) are presented, using final states with at least two leptons. This process, it constitutes a relevant background in the study of top quark pair production in association with Higgs bosons. The measurements were performed using data collected by the CMS experiment during the years 2016, 2017, and 2018, corresponding to proton-proton collisions at a center-of-mass energy of 13 TeV. In particular, the inclusive cross section of the process has been determined using the largest dataset ever recorded in particle accelerators. This result currently represents the most precise measurement available for this quantity within the Standard Model (SM). In addition, differential cross sections — at particle level and corrected for detector effects — have been measured for some of the most relevant observables of the ttW process, using the same dataset.

Additionally, measurements have been performed in the context of the electroweak sector of the SM through the direct determination of the production cross section of a W and a Z boson produced simultaneously (WZ). Unlike the ttW process, this channel does not include top quarks in the final state, which allows for enhanced purity and precision in a low-hadronic-multiplicity environment. The final state is characterized by the presence of at least three charged leptons and missing transverse energy, associated with neutrinos from W boson decays. This measurement also represents the first performed with a new dataset collected by the LHC starting in 2022, which had not been analyzed before. The production cross section is reported with a relative precision of 3.5%, representing the most precise result currently available for this quantity. Furthermore, this measurement completes over 15 years of studies of the WZ production process at the LHC.

The thesis also includes a contribution to the maintenance of the drift tube system and to the development of the CMS experiment's trigger system in preparation for Phase 2, which includes a series of upgrades needed to operate under the high-luminosity conditions expected at the High Luminosity LHC (HL-LHC). In particular, studies are presented that aim to characterize potential aging effects in the detectors due to prolonged operation in a high-radiation environment. It is concluded that, despite these conditions, the muon detection and reconstruction efficiency will not be significantly degraded by the deterioration of the drift tubes. Moreover, a new algorithm is proposed to identify events in which a high-transverse-momentum muon loses a significant fraction of its energy through bremsstrahlung radiation — a class of signal that, until now, could not be selected in real time during data-taking. This algorithm has been designed for implementation in the experiment's detector electronics, enabling access to such events already at the time of data taking.

SR. PRESIDENTE DE LA COMISIÓN ACADÉMICA DEL PROGRAMA DE DOCTORADO EN MATERIALES.

Universidad de Oviedo

INFORME DE EVALUACIÓN PARA LA PRESENTACIÓN Y DEFENSA DE TESIS DOCTORAL
ASSESSMENT REPORT FOR THE PRESENTATION AND DEFENSE OF A PhD THESIS

Nombre y apellidos del doctorando/a. / *Name and surname of the PhD Student*: Carlos Vico Villalba
Título de la tesis / *Title of the thesis*: Study of top quark processes and L1 trigger in the Run 3 of the LHC
Nombre y apellidos del evaluador/a / *Name and surname of the reviewer*: Carlos Francisco Erice Cid
Institución de afiliación del evaluador / Reviewer's institution of affiliation: Boston University
DNI o Pasaporte / *ID Card or Passport No.*: 71683340 E

VALORACIÓN SOBRE LA MEMORIA / *ASSESSSMENT OF THE SUBMITTED REPORT*

Por favor, indique la valoración que le merece la memoria de tesis, marcando en una escala de 1 a 5, donde 1 significa muy malo y 5 significa muy bueno /
Please, indicate your assessment by ticking a number between 1 and 5, where 1 means very poor and 5 means very good:

- La tesis cumple con los estándares de calidad establecidos en su campo / *The thesis meets the quality standards established in its field:*
  ☐ 1 ☐ 2 ☐ 3 ☐ 4 ☒ 5
- La tesis representa una contribución significativa y novedosa al conocimiento en su campo / *The thesis represents a significant and novel contribution to knowledge in its field*:
  ☐ 1 ☐ 2 ☐ 3 ☐ 4 ☒ 5
- La metodología utilizada es apropiada para la investigación realizada / *The methodology used is appropriate for the research conducted*:
  ☐ 1 ☐ 2 ☐ 3 ☐ 4 ☒ 5
- La estructura y estilo de la memoria (organización, redacción, etc.) son adecuados / *The structure and style of the document (organization, writing, etc.) are appropriate*:
  ☐ 1 ☐ 2 ☐ 3 ☐ 4 ☒ 5

RECOMENDACIÓN PRELIMINAR / *PRELIMINARY RECOMMENDATION*

Elegir una de las siguientes opciones / Choose one of the following options:

☒ Recomienda se proceda a la defensa pública / *Proceeding with public defense is recommended*.

FOR-MAT-VOA-2024-050_

☐Recomienda se proceda a la defensa pública, una vez que el doctorando/a haya realizado los cambios necesarios para responder a las cuestiones que se plantean en la sección posterior / *Proceeding with public defense is recommended once the PhD student has made the necessary changes to address the issues raised in the subsequent section*.

☐No recomienda que se proceda a la defensa pública, puesto que el trabajo requiere de una modificación sustancial, de acuerdo con las indicaciones dadas en la sección posterior / *Proceeding with public defense is not recommended, since the thesis requires a substantial modification, in accordance with the indications given in the subsequent section*.

PROPUESTA DE MODIFICACIONES MENORES O SUSTANCIALES / *PROPOSAL FOR MINOR OR SUBSTANTIAL MODIFICATIONS*

(Rellenar solo si se ha elegido una de las dos últimas opciones en la sección anterior. Utilice el espacio que sea necesario / *Fill out only if one of the last two options has been chosen in the previous section. Use as much space as necessary*)

Fecha / *Date*: 8 de Mayo de 2025 **Firma / *Signature*:**

Universidad de Oviedo

INFORME DE EVALUACIÓN PARA LA PRESENTACIÓN Y DEFENSA DE TESIS DOCTORAL
ASSESSMENT REPORT FOR THE PRESENTATION AND DEFENSE OF A PhD THESIS

Nombre y apellidos del doctorando/a. / *Name and surname of the PhD Student*:
Carlos Vico Villalba
Título de la tesis / *Title of the thesis*:
Study of top quark processes and L1 trigger in the Run 3 of the LHC
Nombre y apellidos del evaluador/a / *Name and surname of the reviewer*:
Alexander Grohsjean
Institución de afiliación del evaluador / Reviewer's institution of affiliation:
University of Hamburg
DNI o Pasaporte / *ID Card or Passport No.*:
C1TGPCR24

VALORACIÓN SOBRE LA MEMORIA / *ASSESSSMENT OF THE SUBMITTED REPORT*

Por favor, indique la valoración que le merece la memoria de tesis, marcando en una escala de 1 a 5, donde 1 significa muy malo y 5 significa muy bueno /
Please, indicate your assessment by ticking a number between 1 and 5, where 1 means very poor and 5 means very good:

- La tesis cumple con los estándares de calidad establecidos en su campo / *The thesis meets the quality standards established in its field:*
  ☐ 1 ☐ 2 ☐ 3 ☐ 4 ☒ 5
- La tesis representa una contribución significativa y novedosa al conocimiento en su campo / *The thesis represents a significant and novel contribution to knowledge in its field*:
  ☐ 1 ☐ 2 ☐ 3 ☒ 4 ☐ 5
- La metodología utilizada es apropiada para la investigación realizada / *The methodology used is appropriate for the research conducted*:
  ☐ 1 ☐ 2 ☐ 3 ☐ 4 ☒ 5
- La estructura y estilo de la memoria (organización, redacción, etc.) son adecuados / *The structure and style of the document (organization, writing, etc.) are appropriate*:
  ☐ 1 ☐ 2 ☐ 3 ☐ 4 ☒ 5

RECOMENDACIÓN PRELIMINAR / *PRELIMINARY RECOMMENDATION*

Elegir una de las siguientes opciones / Choose one of the following options:

☒ Recomienda se proceda a la defensa pública / *Proceeding with public defense is recommended*.

☐Recomienda se proceda a la defensa pública, una vez que el doctorando/a haya realizado los cambios necesarios para responder a las cuestiones que se plantean en la sección posterior / *Proceeding with public defense is recommended once the PhD student has made the necessary changes to address the issues raised in the subsequent section*.

☐No recomienda que se proceda a la defensa pública, puesto que el trabajo requiere de una modificación sustancial, de acuerdo con las indicaciones dadas en la sección posterior / *Proceeding with public defense is not recommended, since the thesis requires a substantial modification, in accordance with the indications given in the subsequent section*.

PROPUESTA DE MODIFICACIONES MENORES O SUSTANCIALES / *PROPOSAL FOR MINOR OR SUBSTANTIAL MODIFICATIONS*

(Rellenar solo si se ha elegido una de las dos últimas opciones en la sección anterior. Utilice el espacio que sea necesario / *Fill out only if one of the last two options has been chosen in the previous section. Use as much space as necessary*)

Fecha / *Date*: 21/5/2025

Firma / *Signature*:

A mi madre y a mi padre,
hoy soy doctor por ellos.

Agradecimientos

Es para mí un gran orgullo poder decir que, durante los últimos nueve años dedicados a la física —cuatro de grado, uno de máster y cuatro de doctorado—, he tenido la increíble oportunidad de trabajar como investigador en uno de los laboratorios más prestigiosos del mundo: el CERN, particularmente en el experimento CMS. Nada de esto podría haber sido posible si no fuera por toda la gente que ha seguido mi carrera durante todos estos años, y es por ello que me gustaría dedicar unas palabras de agradecimiento; pues es por el apoyo que he tenido que hoy termino mi etapa predoctoral.

Como investigador, formo parte del Grupo de Física de Altas Energías de la Universidad de Oviedo. En primer lugar, quiero expresar mi agradecimiento a mis directores de tesis, Bárbara y Santiago, investigadores de prestigio y auténticos modelos a seguir, por su paciencia y consejo. Me han seguido desde mis comienzos en el grado, y es a dia de hoy que gran parte de mis logros lo atribuyo a lo que he aprendido de ellos. También a Javi, Isidro y Kike, quienes, durante la carrera, me convencieron —consciente o inconscientemente— de dedicarme a la Física de Partículas. Gracias en particular a Kike, por enseñarme a ser riguroso y conciso a la hora de explicarme (aunque a dia de hoy me sigue costando). Finalmente, agradezco a Javier Cuevas, quien considero un ejemplo absoluto de lo que un implica ser un científico. Debo también dar las gracias a aquellos miembros que, aunque hoy no forman parte directa del grupo, siempre han sido considerados como tales (pues *once Uniovi, always Uniovi*). En particular, a Pietro, Carlos y Sergio, quienes considero de las personas más inteligentes que he tenido la oportunidad de conocer, y a quienes agradezco por su infinita paciencia a la hora de lidiar con mis multiples preguntas sobre estadística. Siguiendo con grandes mentores, Xuan (¡Xuan!), Víctor (¡Víctor!), Andrea (¡Andreaaa!) y Clara (¡Claraa!) fueron un apoyo esencial, especialmente al inicio de mi doctorado. Solo espero haber podido enseñar a las nuevas generaciones —Pelayo, Prado, Javi, Miguel, Jorge y Dani— una porción de lo mucho que aprendí de ellos. Si bien mi paso por oviedo termina, al menos por un tiempo, sé que queda en buenas manos. Me he propuesto dedicar unas palabras especiales a Miguel, por ser un ejemplo de dedicación y trabajo, que sin duda me ha motivado a intentar mejorar cada día con el objetivo de ser un buen mentor (al igual que otros lo fueron conmigo).

Me gustaría terminar este tramo agradeciéndole infinitamente a mi *bro*, el Dr. Soto (al final me ganaste por un mes). He tenido la gran suerte de trabajar con él desde comienzos de la carrera en física, y además de un gran compañero, ha probado ser un gran amigo (además, claramente le debo mi FPI).

I would like to take a moment to thank all the people from the CMS Collaboration. First and foremost, I want to express my deepest gratitude to Alexander and Si Hyun.

Thank you for teaching me essentially everything I know today about physics modeling, and for trusting me to join the common MC team. I truly believe that the philosophy you bring to this effort represents the reason why people pursue science in the first place, and I am extremely proud to be part of it. Thanks also to Jordan, Geovanny, and all the members of the PPD and GEN groups, who have been essential to the work developed within this collaboration. I would also like to thank all the members of the TOP PAG and TMG groups. I hope that my two years serving as a convener for the subgroup have contributed positively to the development of the TOP physics program. A special thanks goes to my Belgian colleagues from the University of Ghent and Louvain, particularly Tu Thong, Luka, David, and Didar, with whom I had the opportunity to work on the two $\mathrm{t\bar{t}W}$ measurements that are presented in my thesis.

Gracias también al resto de personas con las que he tenido la oportunidad de compartir esta experiencia, en particular a Guillelmo, Andrea Cardini, toda la gente del IFCA, incluyendo a Celia, Pedro y Nicolò; así como a la gente del IFIC y del CIEMAT.

Esta última parte quisiera dedicársela a otra gente que ha sido vital para el desarrollo de mi tesis, más allá del mundo de la investigación. Gracias a todos mis amigos de "Valhalla", Fonsito, Nachete, Rubenín, Mesinen, Rober, Pablo y Juanma; siempre habéis sido una buena via de escape para despejar la cabeza (en parte porque las neuronas desaparecen cuando nos juntamos). Quiero agradecer también a Bustos, Angelillo, Adri, Víctor y Marcos, quienes a pesar de vivir fuera de Asturias, siempre mantengo en la cabeza. Creo que mi mayor apoyo en todos estos años ha sido Sole, a quien también estoy infinitamente agradecido, pues es sin duda quien mejor me conoce, y quien más crisis existenciales me ha aguantado. Solo decir que estoy orgulloso de tener una amiga así (aunque no sepa diferenciar bien cuándo va a llover o no).

Gracias a mis hermanos, Cristina y Fran, quienes me han demostrado lo que significa ser trabajador, buena persona e insistente en la vida. Gracias también a mis cuñados, Jorge y Carolina, que además de buenas personas, son capaces de aguantar esa insistencia que mis hermanos me han enseñado. Gracias a mis sobrinos, a quienes más valoro, Nicolás y Laura, así como Raúl y Jorge; espero haber podido ser un ejemplo para vosotros. Gracias a mis primos (aunque debería decir segundos hermanos), Álvaro, "el ídolo", y a Ana, de quien estoy igualmente sumamente orgulloso y que puedo decir, sin duda, es también "mi ídolo" (gracias también por entrar en un salón a oscuras para recuperar mi PSP cuando eramos pequeños). Gracias a mis tíos, Elia (mi primera profesora) y Jose (y a la —a dia de hoy— pequeña Laia), Horacio (me enorgullece decir que te hice caso, y me acabé juntando con los listos), Juan y Mariló, Mirian y Jesús, Marigeli, Mabel, Diego y Ani. A mis abuelos, Carlos y Olga, Pepita y Vico, y a mis tíos abuelos, Cuqui y José, Hector y Mayín, Javier y Blanqui.

Finalmente, gracias a mis padres, Ana y José, a quienes básicamente les debo todo, y por quienes intento dar siempre el cien por cien de mi trabajo.

Table of Contents

List of Figures

List of Tables

1 Introduction

In the pursuit of a precise understanding of nature, scientists have devoted considerable time and effort to the development of new theories that aim to mathematically describing nature. In particle physics, the Standard Model (SM) stands as the most predictive framework, tracing its origins to the unified electroweak theory proposed by Weinberg and Salam [1,2]. Experimental validation of this new theory came in 1973 with the observation of neutral weak currents at CERN [3], confirming also earlier work by Glashow [4]. Since then, key milestones include the discovery of W and Z bosons by the UA1 and UA2 experiments in 1983 [5–8], the top quark by the CDF and D0 experiments in 1995 [9,10], and, ultimately, the Higgs boson by the CMS and ATLAS experiments in 2012 [11,12], fulfilling the primary goal of the Large Hadron Collider (LHC).

Many fundamental questions in particle physics remain unanswered, and researchers at the LHC continue to explore the energy frontier using data recorded by its experiments. The LHC is the successor to the Large Electron-Positron (LEP) collider, which ceased operations in the year 2000. It is currently the largest and only operational accelerator capable of probing the quantum nature of high-energy proton-proton (pp) collisions. The LHC began producing collision data in 2010 during Run 1 (2010–2013) at a centre-of-mass energy of 7 TeV, which was increased to 8 TeV. After a two-year shutdown, Run 2 commenced in 2015 with an increased centre-of-mass energy of 13 TeV, and resulted in a dataset of 137.2 fb^{-1} by 2018 —approximately ten times the data collected during two decades of Tevatron operations. In 2022, Run 3 began at a centre-of-mass energy of 13.6 TeV, closing the gap to the LHC design energy of 14 TeV.

This thesis contributes to the community of high energy physics (HEP) through publications that explore fundamental aspects of pp physics using data from the CMS experiment during the Run 2 and Run 3 eras of the LHC. Specifically, it focuses on the associated production of top quarks and bosons. A key challenge in measuring the properties of these particles lies in the extremely short lifetimes of the top quark, W boson, and Z boson [13], making direct detection effectively impossible at large experiments. Instead, their properties are inferred from the final state decay products. I have focused my work on exploring final states with at least two charged leptons. These multileptonic signatures are then used as a probe to different phenomenological aspects of the SM.

For instance, the top quark, being the heaviest elementary particle within the SM, yields the strongest coupling to the Higgs boson. Consequently, studying its properties is crucial for testing the Higgs mechanism and probing potential scenarios beyond-the-SM (BSM). Furthermore, as a color-charged particle, the top quark serves as an essential probe for Quantum Chromodynamics (QCD). At the LHC, top quarks are primarily produced through two mechanisms: in top-antiquark top pairs ($\mathrm{t\bar{t}}$), or singly (single top production). The latter, which constitutes the main focus of this thesis, is also the dominant production mode in terms of cross section. At higher orders in QCD, associated production modes of $\mathrm{t\bar{t}}$ with bosons ($\mathrm{t\bar{t}X}$, where X can be a W, Z, H or γ) emerge. These topologies are characterized by a much smaller cross section —about a thousand times smaller than that of the $\mathrm{t\bar{t}}$ process. Nevertheless, the data collected during Run 2 of the LHC have made possible to measure the properties of this kind of processes at the highest precision.

The study of top quark pair production in association with a W boson ($\mathrm{t\bar{t}W}$) constitutes a key component of this work. I have measured the properties of this process at both the inclusive and differential cross-section levels using the Run 2 dataset [14, 15]. This process has several interesting features, starting from the fact that it is one of the main backgrounds in the analysis of $\mathrm{t\bar{t}}$ in association with a Higgs boson ($\mathrm{t\bar{t}H}$), which already by itself is a direct probe for the yukawa coupling of the Higgs boson to the top quark. Furthermore, $\mathrm{t\bar{t}W}$ has been one of the main topics of discussion in the HEP community for years, as its cross section has been consistently shown to be above the SM predictions at the highest accuracies. Several approaches, that I have thoroughly studied during my doctoral period, have been proposed in order to close the gap between theory and prediction.

I have also studied the associated production of two massive bosons at the LHC, the so-called diboson production modes. Diboson production cross sections are interesting physical observables at the LHC, as they are relatively common —often with higher cross sections than those of $\mathrm{t\bar{t}X}$ processes— and are linked to BSM physics through their sensitivity to trilinear gauge couplings (TGCs) [16], that can be studied within the context of effective field theory (EFT) frameworks. In particular, my work has focused on measuring the properties of the WZ process at the inclusive level, exploring final states with at least three charged leptons. In this channel, the WZ process becomes one of the purest channels of diboson production at the LHC, with background contributions as low as 15%, while still maintaining reasonably well statistical representation. This makes it a prime candidate for probing the properties of the electroweak (EW) sector of the SM in a signal dominated environment. I have had the unique opportunity to study this process using the latest dataset recorded by the CMS experiment in 2022, during Run 3 of the LHC [17]. Furthermore, my work represents one of the first published results produced by the CMS collaboration with Run 3 data, serving as a foundation for future measurements with this dataset.

My work would not have been possible without the excellent performance of the CMS experiment in reconstructing the fundamental observables commonly used in HEP data analysis. Throughout my Ph.D, I have contributed to various aspects of detector performance at different levels. My most significant contribution has been dedicated to the Drift Tube (DT) system of CMS, primarily in the context of the detector upgrade for the upcoming High-Luminosity LHC (HL-LHC) era. In particular, I have focused my work on two topics: the characterization of aging effects in muon detection, and new developments of the muon L1 trigger, both of which are contextualized within the DT upgrade plans. In particular, the role of the L1 trigger is crucial in HEP, as it is the first layer of filtering out information produced in the collisions, and therefore it univocally constraints the physics that scientists have access to. It is therefore extremely important to constantly search for new improvements of the system. My contribution has been the development and validation of a new trigger algorithm that triggers events based on the presence of muons with high energy. I have also served multiple times as the DT detector on-call (DOC) expert, a role of responsibility within the DT group. The DOC shift consists on a two-week assignment that involves ensuring that DT operation is smooth during data taking.

As a member of the CMS collaboration, I have contributed to essential work that, while not directly publishable, is crucial for the experiment. My primary focus has been the generation of Monte Carlo (MC) samples to be used in the CMS experiment. For three years, I served as a MC contact person for the TOP group within CMS, and for two years, I held the position of coordinator for the Top Modeling Group (TMG). The latter role, classified as a Level-3 (L3) position[1] within the collaboration, gave the responsibility of coordinating a team of up to five MC contacts, as well as the coordination of all the MC production for the TOP group. This position also required me to engage in all the group activities and approval of results. The CMS collaboration recently recognized my work in MC production with a CMS Award for my "essential contributions to the development of an automated production system for the CMS core background Monte Carlo samples". This award is one of the highest honors granted to members of the collaboration.

This thesis is structured as follows. Chapter 2 provides a brief overview of the theoretical framework underlying the research in particle physics, including essential concepts from quantum field theory and the SM. Chapter 3 describes the experimental setup used to collect the data analyzed in this work, with a focus on the LHC and, in particular, the CMS experiment. Given the significant contributions of this thesis to the improvement of MC event generation within CMS, Chapter 4 discusses the modeling of signal processes and the role of MC simulation in connecting theoretical predictions with experimental observations. In Chapter 5 details about how the simulations must be corrected to match features that are only present in the data are given. The core results of the thesis are presented in Chapters 6 and 7, which detail the measurements of the inclusive and differential $\mathrm{t\bar{t}W}$ cross section at 13 TeV, and the inclusive WZ cross section at 13.6 TeV, respectively. Additional work related to the CMS detector upgrade for the HL-LHC is presented in Chapter 8. Finally, Chapter 9 presents the summary and conclusions of this thesis.

[1] There are three categories of coordination in CMS: L1 coordinate areas of physics, L2 coordinate different groups within an area, and L3 coordinate sub-groups within these groups.

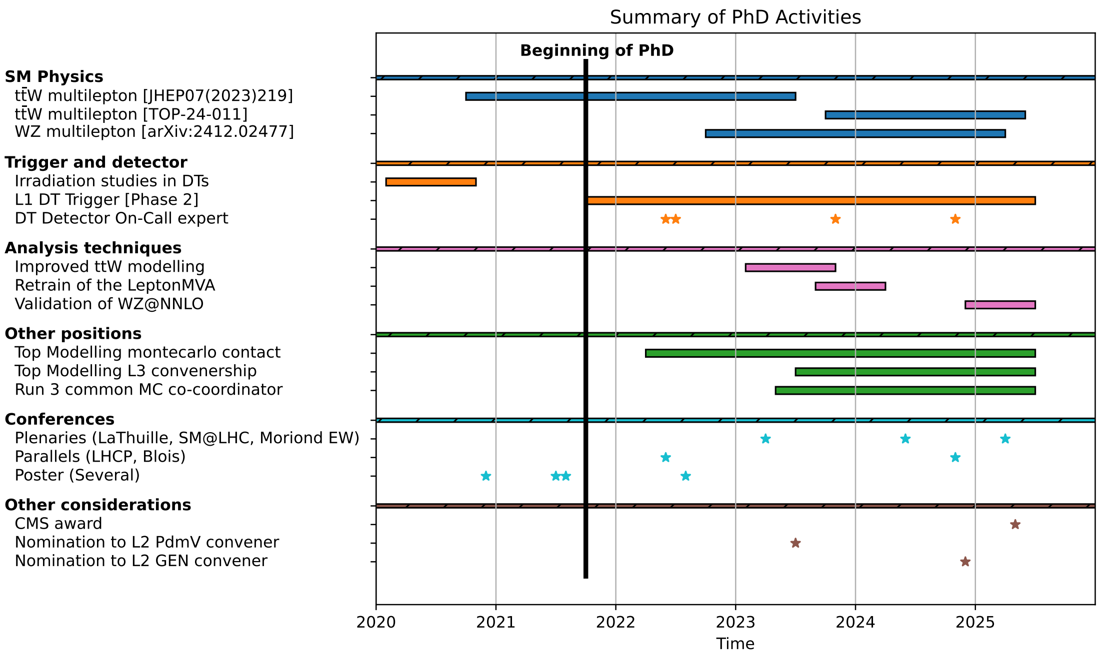

FIGURE. 1.1: Summary of the activities I have developed since the beginning of my PhD, including periods of overlap with my time as a master student at the University of Oviedo. The timelines for service work correspond either to the official appointment period or the duration of active involvement. Contributions that do not extend over a period larger than one month are represented as points at the time it happened.

2 Theoretical framework

In the early 20th century, the study of blackbody radiation by Max Planck introduced the concept of quantized energy emission, forming the basis of quantum mechanics. His work revolutionized physics and technology, explaining phenomena beyond classical theories. Quantum Field Theory (QFT) extends this framework, describing particles as excitations of quantum fields rather than separate entities.

Any QFT that aims to describe the quantum behavior of nature must satisfy mathematical consistency of the theory. In many cases, contributions to a given process can lead to the appearance of nonphysical divergences in calculations, which put at risk the validity of the theory and its predictive power. It is important to note that such divergencies are not a problem of the theory, but are intrinsic to the probabilistic nature of quantum mechanics. Divergences often arise in the treatment of different energy scales and can be understood through the Feynman path integral [18]. This formalism describes the evolution of a system as a sum over all possible paths between initial and final states, incorporating all quantum field configurations. At low energies, processes involving radiation at arbitrarily low (but nonzero) energy scales lead to infrared (IR) divergences. At high energies, divergences appear because the theory is extended to arbitrarily small distances, increasing the number of degrees of freedom indefinitely and causing the so-called ultraviolet (UV) divergences. Since experiments have consistently measured finite values for many properties that QFTs predict to diverge, quantum field theories must be renormalizable. Renormalizability is the property that allows a QFT to eliminate intrinsic IR and UV divergences, ensuring meaningful physical predictions. The concept of renormalizability will be of great importance in the following chapters, as it is one of the driving sources of uncertainty in many physics analyses.

In this chapter, the fundamental concepts of the SM are given, a renormalizable gauge theory that unifies the principles of special relativity and quantum mechanics to describe three of the four fundamental interactions: the strong, weak, and electromagnetic forces, is given.

2.1 Matter content of the SM

The SM has been extensively tested across a wide range of experiments, consistently demonstrating exceptional agreement between theoretical predictions and observed phenomena. Like any QFT, it is defined by a Lagrangian density, $\mathcal{L}$, which depends on a given set of fields, ψ_i, and their derivatives, $\partial_\mu \psi_i$, where i indexes ranges through all the field content of the SM. These fields are often referred to as "fundamental particles", as they are the mathematical depiction of the detectable particles in real experiments. In the following, the terms "field" and "particle" will be used interchangeably. As a quantum theory, the SM classifies particles primarily based on their spin. Particles with half-integer spin, which obey Fermi-Dirac statistics, are known as fermions. Particles with integer spin, which follow Bose-Einstein statistics, are known as bosons. Since the SM is also a relativistic theory, the fields ψ_i must transform under representations of the Lorentz group [19]. Specifically, fermions are described by spin-$\frac{1}{2}$ spinors, while bosons are represented as Lorentz vectors.

Fermions in the SM are divided into two families: leptons and quarks. The lepton family consists of three charged particles —the electron (e), muon (μ), and tau (τ), along with their corresponding neutral counterparts, the neutrinos (ν_{e}, ν_μ, and ν_τ). Quarks, in contrast, come in six different flavors. They are grouped based on their electric charge: up-type quarks (up u, charm c, and top t) carry a charge of $q = +\frac{2}{3}$, while down-type quarks (down d, strange s, and bottom b) have a charge of $q = -\frac{1}{3}$. Each family is at the same time organized in three generations, where the first generation is often composed by the lightest charged particles of each group, and their corresponding neutrinos in the case of the leptons: the e and ν_{e}, and the u and d in the case of the quarks. Similarly, the third generation is made up of the heaviest particles of each family: the τ and ν_τ in the case of the leptons, and the t and b in the case of the quarks. The remaining particles of the model are considered as the second generation.

2.2 Interactions and symmetries

Any QFT candidate to describe the nature of the high energy interactions must respect the experimentally confirmed conservation of certain quantities in specific types of interactions. This implies that the underlying theory describing these experimental results must remain invariant under both global and local transformations of the fermion fields present in the theory. We refer to these kinds of transformations as "gauge invariant transformations". While ensuring global symmetry is often straightforward, as it involves for instance a rotation of points in a field, maintaining local symmetry is more difficult. Following Noether's theorem [20], the most effective way to ensure local invariance under specific transformations is by introducing a vector field, known as boson field, that is used as a gauge to ensure the symmetry of the interaction. The emergence of bosons as in the SM is therefore natural in the theory and it is highly correlated with the existence of conserved quantities.

Bosons thus play a fundamental role in mediating interactions between particles. These interactions arise from local gauge symmetries of the $\mathrm{SU}_C(3)\times\mathrm{SU}_L(2)\times\mathrm{U}_\Upsilon(1)$group. The SM includes four types of gauge bosons, each associated with a fundamental symmetry, as well as one scalar boson. The gauge bosons include the photon (γ), which mediates the electromagnetic interaction associated with the $\mathrm{U}_\Upsilon(1)$ symmetry. The W^+, W^-, and Z bosons, collectively known as the weak bosons, mediate the weak interaction, which corresponds to the $\mathrm{SU}_L(2)$ symmetry of the SM. The $\mathrm{SU}_C(3)$ symmetry of the SM governs the strong interaction and introduces eight gauge bosons known as gluons (g). The Higgs boson (H) is the only scalar boson in the SM and has spin-0.

2.2.1 Quantum electrodynamics

The theory of quantum electrodynamics (QED) describes the local gauge symmetries of the SM associated with the $\mathrm{U}_\Upsilon(1)$ group. In the massless and free particle approximation, the Lagrangian density governing QED is given by equation 2.1:

$$\mathcal{L}_{\text{QED}}^{\text{free}} = \bar{\psi} i \gamma^\mu \partial_\mu \psi \tag{2.1}$$

where ψ represents the spinorial fields of charged fermions interacting via QED, γ^μ are the Dirac matrices. The $\mathrm{U}_\Upsilon(1)$ gauge symmetry manifests as a phase transformation of the spinor fields, as expressed in equation 2.2:

$$\psi(x) \to \psi'(x) = e^{i\alpha(x)}\psi(x) \tag{2.2}$$

where $\alpha(x)$ is an arbitrary real function that depends on spacetime position and, therefore, does not inherently preserve local gauge symmetry. To construct a gauge-invariant formulation of QED, one can apply Noether's second theorem, recognizing that the conserved current in QED corresponds to electric charge. This requires modifying the Lagrangian in equation 2.1 by introducing the covariant derivative, as defined in equation 2.3:

$$\partial_\mu \to \mathrm{D}_\mu = \partial_\mu - i\mathrm{e}\mathrm{A}_\mu \tag{2.3}$$

where e is the electric charge, and A_μ is the vector field that couples to the conserved currents in QED. Substituting this into the Lagrangian leads to the full QED Lagrangian, as expressed in equation 2.4:

$$\mathcal{L}_{\text{QED}} = -\frac{1}{4}\mathrm{F}^{\mu\nu}\mathrm{F}_{\mu\nu} + \bar{\psi}\left(i\gamma^\mu\partial_\mu - \mathrm{e}\gamma^\mu A_\mu\right)\psi \tag{2.4}$$

This Lagrangian includes two additional terms. The term $-\frac{1}{4}\mathrm{F}^{\mu\nu}\mathrm{F}_{\mu\nu}$ represents the kinetic term of the gauge field A_μ, where the field strength tensor is defined as $\mathrm{F}_{\mu\nu} = \partial_\mu \mathrm{A}_\nu - \partial_\nu \mathrm{A}_\mu$. The interaction term $e\bar{\psi}\gamma^\mu\psi A_\mu$ describes the coupling between QED fermions (charged particles) and the photon, which serves as the vector boson mediating QED interactions.

2.2.2 From QED to a unified electroweak theory

Glashow, Weinberg, and Salam first hypothesized that leptons not only interacted with photons but could also interact with the weak bosons, that are present for instance in the decay process of radioactive matter. This led to the idea that a unified theory could simultaneously describe both electromagnetic and weak interactions in a consistent framework.

Achieving a unified theory of electromagnetic and weak interactions —known as the EW interaction— requires constructing a Lagrangian density for the SM that preserves local gauge invariance under the $\mathrm{SU}_L(2) \times \mathrm{U}_\Upsilon(1)$ symmetry group. Because the weak force is a chiral interaction that does not transform equally right-handed and left-handed spinors, the chirality of the unified theory must be respected. Therefore fermion fields are represented by two different representations, known as Weyl spinors [21], represented in equation 2.5.

$$\mathrm{L} \equiv \frac{1}{2}\left(1+\gamma^5\right)\psi, \mathrm{R} \equiv \frac{1}{2}\left(1-\gamma^5\right)\psi \tag{2.5}$$

where $\gamma^5 = i\gamma^0\gamma^1\gamma^2\gamma^3$ is the fifth Dirac matrix, L represents a left-handed doublet, and R represents a right-handed singlet. In the SM, each particle can be described as either a right- or left-handed Weyl spinor, with the exception of neutrinos, which are exclusively left-handed Weyl spinors. The Lagrangian density in the free particle approximation can be expressed as shown in equation 2.6:

$$\begin{aligned}\mathcal{L}_{\text{EW}}^{\text{free}} = i\bar{\ell_{\mathrm{R}}}\gamma^\mu\partial_\mu\ell_{\mathrm{R}} + i\bar{\mathrm{q}_{\mathrm{R}}}\gamma^\mu\partial_\mu\mathrm{q}_{\mathrm{R}} + i\bar{\mathrm{a}_{\mathrm{L}}}\gamma^\mu\partial_\mu\mathrm{a}_{\mathrm{L}} + \\ \sum_{\psi=\ell_{\mathrm{R}},q_{\mathrm{R}},\mathrm{a}_L} \bar{\psi}\left(i\gamma^\mu\partial_\mu - m\right)\psi\end{aligned} \tag{2.6}$$

For simplicity, a minimal theory consisting of two right-handed spinors and a single left-handed spinor is considered. The first line of equation 2.6 corresponds to the Lagrangian density of the free particle $\mathrm{SU}_L(2)$ sector, while the second line corresponds to the $\mathrm{U}_\Upsilon(1)$ sector. One can construct covariant derivatives for each conserved current of the theory. In the case of $\mathrm{SU}_L(2) \times \mathrm{U}_\Upsilon(1)$, there are two conserved quantities: the weak isospin (I_a, where $a = 1, 2, 3$) associated with the $\mathrm{SU}_L(2)$ component, and the hypercharge (Υ) associated with the $\mathrm{U}_\Upsilon(1)$ component. The hypercharge is further related to the third component of the weak isospin via the relation: $\Upsilon = 2(Q - I_3)$. Following Noether's theorem there must be four gauge bosons associated to the theory. The complete and gauge invariant lagrangian can be expressed as in equation 2.7.

$$\mathcal{L}_{\text{EW}} = i\bar{\ell_{\text{R}}}\gamma^{\mu}\partial_{\mu}\ell_{\text{R}} + i\bar{\text{q}_{\text{R}}}\gamma^{\mu}\partial_{\mu}\text{q}_{\text{R}} + i\bar{\text{a}_{\text{L}}}\gamma^{\mu}\text{D}_{\mu}\text{a}_{\text{L}} + \sum_{\psi=\ell_{\text{R}},q_{\text{R}},\text{a}_L} \bar{\psi}\left(i\gamma^{\mu}\partial_{\mu} - \Upsilon g_{\Upsilon}\gamma^{\mu}B_{\mu}\right)\psi - \frac{1}{4}\text{W}_j^{\mu\nu}\text{W}^j_{\mu\nu} - \frac{1}{4}\text{B}^{\mu\nu}\text{B}_{\mu\nu} \tag{2.7}$$

Where the first three terms in the Lagrangian correspond to the kinetic terms of the fermions, the following term describes the coupling of the fermions to the gauge bosons, and ψ refers to a generic fermion field (lepton or quark). The first part, $i\gamma^{\mu}\partial_{\mu}$, is the usual kinetic term. The second part —$-\Upsilon g_{\Upsilon}\gamma^{\mu}B_{\mu}$— describes the interaction between the fermions and the $\text{U}_{\Upsilon}(1)$ gauge boson (B_{μ}), where Υ is the hypercharge of the fermion and g_{Υ} is the coupling constant associated with the $\text{U}_{\Upsilon}(1)$ symmetry. This term is responsible for the electromagnetic interaction between fermions through the exchange of a photon. The last two terms are the kinetic terms for the four gauge fields of the EW interaction. In particular, $\text{W}_j^{\mu\nu}$ is the field strength tensor for the three gauge bosons of the $\text{SU}_L(2)$ group, while B_{μ} is the gauge boson associated with the $\text{U}_{\Upsilon}(1)$ symmetry.

2.2.3 Quantum chromodynamics

Strong interactions in particle physics are described by Quantum Chromodynamics (QCD), which is associated with the $\text{SU}_C(3)$ component of the SM. Similar to the $\text{SU}_L(2) \times \text{U}_{\Upsilon}(1)$ symmetry framework that leads to the formal description of EW interactions, a gauge-invariant version of QCD can be derived starting from the free fermion approximation of the QCD Lagrangian density. For simplicity, a theory with two fermion fields corresponding to the up- and down-type quarks is considered. The Lagrangian density for such a theory is given in equation 2.8.

$$\mathcal{L}_{\text{QCD}}^{\text{free}} = \sum_{\psi=u,d} \bar{\psi} i\gamma^{\mu}\partial_{\mu}\psi \tag{2.8}$$

In this case, the u and d fields represent the quarks, which are components of the $\text{SU}_C(3)$ symmetry group. These quarks form triplets of fermion fields: q_1, q_2, and q_3, with $q = u, d$. The conserved quantity in QCD is known as the color charge, and each component of the triplet corresponds to a different color state of the quarks. As with the EW interaction, the color charge is a conserved quantity in QCD interactions, and thus it must be associated with a conserved current. The covariant derivative in QCD is given in equation 2.9.

$$G^a_{\mu\nu} = \partial_{\mu} - ig_s\frac{\lambda_a}{2}G^a_{\mu} \tag{2.9}$$

Here, G^a_{μ} represents the gauge fields associated with the $\text{SU}_C(3)$ symmetry group, and g_s is the strong coupling constant of QCD. The QCD theory has eight gauge bosons, known as gluons, which mediate the strong interaction. By introducing this expression into the Lagrangian for the free theory and extending it to all types of quarks in the SM, the full QCD Lagrangian density is obtained, as shown in equation 2.10.

$$\mathcal{L}_{\text{QCD}} = \sum_{\psi} \left[\bar{\psi} \left(i\gamma^{\mu}\partial_{\mu} \right) \psi + g_s \bar{\psi} \gamma^{\mu} \frac{\lambda_a}{2} \psi G^a_{\mu} - \frac{1}{4} G^a_{\mu\nu} G^{a,\mu\nu} \right] \tag{2.10}$$

In this expression, ψ runs over all types of quarks, which are the only fermions that interact via the strong force. The first term represents the free particle Lagrangian, the second term describes the interaction between quarks and gluons, and the last term accounts for the kinetic term of the eight gluon fields. In particular, the form of $G^a_{\mu\nu}$ is given by equation 2.11.

$$G^a_{\mu\nu} = \partial_{\mu} G^a_{\nu} - \partial_{\nu} G^a_{\mu} + g_s f_{abc} G^b_{\mu} G^c_{\nu} \tag{2.11}$$

Here, f_{abc} are the structure constants that define the commutation relations between the gauge fields of the theory. The third term shows that gluons can self-interact, a characteristic feature of non-abelian theories like QCD.

2.3 Electroweak Symmetry breaking and the Higgs mechanism

Since the symmetries of the SM are chiral, meaning they act differently on left- and right-handed fermions, any mass term of the form shown in equation 2.12 is forbidden, as these terms are not gauge invariant under transformations of the $\mathrm{SU}_L(2) \times \mathrm{U}_{\Upsilon}(1)$ group. As a result, the gauge invariance of the underlying theory is not preserved. A similar statement can be also made for the case of the boson vector fields.

$$\mathcal{L}_{\text{mass}} \sim m\bar{\psi}\psi = m \left(\bar{\psi}_{\mathrm{R}} \psi_{\mathrm{L}} + \bar{\psi}_{\mathrm{L}} \psi_{\mathrm{R}} \right) \tag{2.12}$$

However, experimental results from collider experiments, including direct measurements of SM particle masses, confirm that at least some of these particles must in fact be massive. This apparent contradiction is resolved through the Higgs-Brout-Englert (HBE) mechanism, which introduces spontaneous symmetry breaking in the electroweak sector (*Electroweak Symmetry Breaking*, EWSB) [22, 23] component of the SM.

To incorporate EWSB into the SM, a new scalar field, Φ, is introduced. This field is a doublet spinor composed of two scalar components, ϕ^+ and ϕ^0, and transforms under the spinor representation of the $\mathrm{SU}_L(2)$ symmetry group. The Lagrangian density associated with this new scalar field is given in equation 2.13.

$$\mathcal{L} = \left(\mathrm{D}_{\mu} \Phi \right)^{\dagger} \left(\mathrm{D}^{\mu} \Phi \right) + \frac{1}{2} \mu^2 \Phi^{\dagger} \Phi + \frac{\lambda}{2} \left(\Phi^{\dagger} \Phi \right)^2 \tag{2.13}$$

Where μ^2 and λ are free parameters representing the mass term and self-coupling constant of Φ, respectively. Note also that the theory is by construction gauge invariant,as the covariant derivatives D_μ, and scalar fields are always gauge invariant. To determine how Φ interacts with the vacuum, the vacuum expectation value (vev) by studying the extremes of the potential term, which is isolated in 2.14, is examined.

$$V(\Phi) = -\frac{1}{2}\mu^2\Phi^\dagger\Phi + \frac{\lambda}{2}\left(\Phi^\dagger\Phi\right)^2. \tag{2.14}$$

This potential has a trivial solution at $\Phi = 0$[1] and non-trivial local minima at $\Phi^\dagger\Phi = \frac{\mu^2}{\lambda}$. The existence of a non-zero vev implies that the assumed $\text{SU}_L(2)$ symmetry is not preserved in the vacuum state. However, this does not contradict the gauge invariance of the full $\text{SU}_L(2) \times \text{U}_\Upsilon(1)$ theory, as the Lagrangian remains gauge invariant even after including the Higgs mechanism. What is actually broken is the symmetry of the vacuum itself. By choosing Weinberg's unitarity gauge, one can see that the final form of the Φ doublet takes the form shown in equation 2.15.

$$\Phi = \frac{1}{\sqrt{2}}\begin{pmatrix} 0 \\ v + \text{H} \end{pmatrix} \tag{2.15}$$

In this case, v represents small fluctuations around the vacuum and is related to the nonzero vev derived earlier through the relation $v = \sqrt{\frac{2\mu^2}{\lambda}}$. The field H corresponds to the physical Higgs boson. Substituting this expression into the Lagrangian in equation 2.13, the Lagrangian density in equation 2.16 —now expressed in terms of the Higgs field and its interactions— is obtained.

$$\mathcal{L} = \left(D_\mu \text{H} D^\mu \text{H}\right) + \frac{1}{2}\mu^2\text{H}^2 + o(v\text{H}) + o(v^2) + o(H^3) \tag{2.16}$$

Here, the H^2 term in the Lagrangian indicates that the predicted Higgs boson is massive. Additionally, the terms $o(H^3)$ and higher-order contributions demonstrate that the Higgs is massive capable of couplings to itself.

The terms included in the covariant derivatives, as well as those of order $o(v\text{H})$, correspond to interactions between the EW gauge bosons and the Higgs field. These interactions describe how the Higgs boson couples to the gauge bosons, enabling processes such as Higgs boson production and decay in EW interactions. Furthermore, the terms of order $o(v^2)$ play a crucial role in generating mass terms for the EW gauge bosons. Specifically, these terms lead to the spontaneous breaking of the electroweak symmetry, giving mass to the W and Z bosons, as shown in equation 2.17:

[1] Here, zero refers to the spinor representation.

$$m_W = \frac{gv}{2}, \quad m_Z = \frac{v\sqrt{g_W^2 + g_\Upsilon^2}}{2} \tag{2.17}$$

Here, g and g_W, g_Υ are the coupling constants associated with the EW gauge interactions. Notably, the masses of the W and Z bosons are shown to be nonzero as soon as the Higgs mechanism is introduced, highlighting its essential role in properly predicting what is shown from experimental data. An important consequence of this mechanism is that the mass of the W and Z bosons is directly linked to the vev of the Higgs field. However, because λ is a free parameter of the theory, the mass of the Higgs boson itself remains an undetermined parameter within the theory and must be extracted from experimental measurements rather than derived from first principles. This leads to the so-called Hierarchy Mass Problem [24], which questions why the Higgs boson mass is stable despite large quantum corrections that, in principle, could drive it to much higher values.

3 The Large Hadron Collider and the CMS experiment

3.1 The Large Hadron Collider

The Large Hadron Collider (LHC) is the largest particle physics accelerator ever built. Beyond its technological achievements, the LHC and its experiments represent a global collaboration of scientists from hundreds of institutions worldwide that explore the fundamental interactions between elementary particles at an unprecedented energy regime. The accelerator is located at the CERN laboratory and is part of a larger accelerator complex, schematically represented in Figure 3.1.

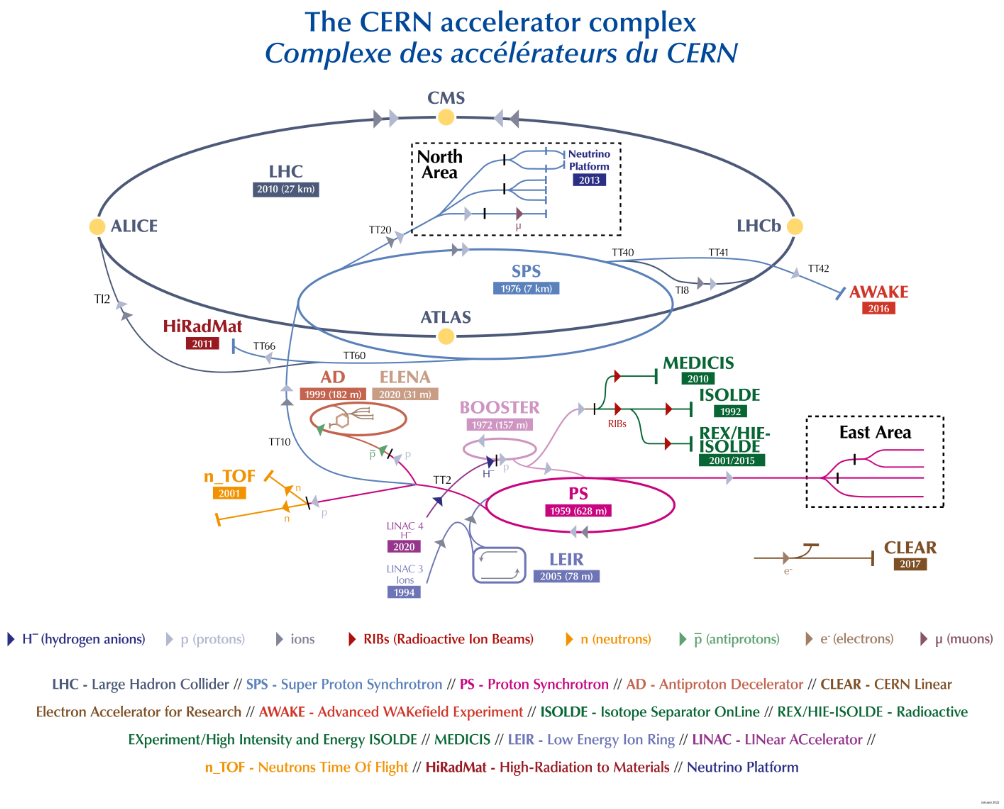

FIGURE. 3.1: Schematic of the entire accelerator complex located at CERN.

The operation of the LHC relies mostly on the collision of two proton beams accelerated to relativistic velocities. The acceleration process starts with hydrogen atoms extracted from a storage bottle and introduced into the LINAC 4 linear accelerator. The hydrogen atoms undergo a ionization process that effectively isolates the proton content. After ionization, LINAC 4 provides an initial energy of approximately 50 MeV to these protons, accelerating them to velocities corresponding to nearly one-third of the speed of light. This acceleration is achieved through the application of electric fields, which act on discrete bunches of protons.

Subsequent acceleration occurs within the Proton Synchrotron (PS), a synchrotron accelerator comprising multiple vertically stacked rings. The PS receives protons from LINAC 4 and further accelerates them along circular trajectories, guided by intense magnetic fields. To counteract potential energy losses due to synchrotron radiation emission, the PS incorporates pulsed electric fields within radiofrequency cavities. By the end of this phase, protons reach energies on the order of 1.4 GeV and reach velocities approximating 92% of the speed of light.

In the third acceleration phase, the protons are directly injected into the Proton Synchrotron Booster (PSB), where they reach energies of about 25 GeV and speeds of 99.9% of the speed of light. They are then sent to the Super Proton Synchrotron (SPS), a synchrotron accelerator with an even larger radius than its predecessors, where they reach energies of up to 450 GeV. Additionally, in the SPS, using magnetic fields with different polarizations, the beam is split into two distinct beams that will circulate in either a clockwise or counterclockwise direction through the ring. Once they have reached a sufficient energy level, the protons will proceed to their final acceleration phase in the 27 km ring that makes up the LHC, where they are expected to reach energies up to $6.8\ \mathrm{TeV}$. The beams intersect at four specific points along the LHC ring, corresponding to the locations of the ALICE, ATLAS, CMS, and LHCb experiments.

3.1.1 Luminosity, pileup, and the LHC dataset

Due to the probabilistic nature of the processes produced at the LHC, it is essential to collect a large dataset to ensure the statistical reliability of measurements. The instantaneous luminosity ($\mathcal{L}_{\mathrm{inst}}$) quantifies the rate of interactions occurring in a given process a, characterized by a cross-section σ_a. It is defined through the relation $N = \mathcal{L} \times \sigma_a$. Its precise definition in terms of parameters that characterize the functioning of the accelerator is given by equation 3.1.

$$\mathcal{L}_{\mathrm{inst}} = n_b \frac{N_1 N_2 l}{4\pi \sigma_x \sigma_y c}, \tag{3.1}$$

Where n_b is the number of proton bunches circulating in the LHC, N_1 and N_2 are the number of protons per bunch (on the order of 10^{11}), l is the circumference of the accelerator ring, and σ_x and σ_y represent the transverse dimensions of the proton bunches.

At the LHC, a given set of data taking runs of one of the detectors inside the LHC can last between 8-12 h, depending on the specific purpose of the runs. The instantaneous luminosity in a given data taking run is measured in units of $\mathrm{cm}^{-2}\mathrm{s}^{-1}$ and typically reaches values on the order of $\sim 10^{34}\ \mathrm{cm}^{-2}\mathrm{s}^{-1}$. During Run 2, the highest instantaneous luminosity ramped between 10^{34} cm^{-2}s^{-1} in 2016 and 2×10^{34} cm^{-2}s^{-1} by the end of 2018. In Run 3, the highest recorded peak up to 2022 reached 2.5×10^{34} cm^{-2}s^{-1} during the highest-performance periods that year.

Increasing the value of instantaneous luminosity carries important effects in the data taking. According to equation 3.1, l is a fixed quantity, σ_x and σ_y are constrained by the beam physics, and N_1 and N_2 are limited by the magnetic field strength of the LHC magnets. As a result, the primary way to increase $\mathcal{L}_{\text{inst}}$is by raising n_b. However, a higher n_b also leads to an increase in the number of additional simultaneous pp collisions, known as pileup (PU) interactions, occurring at the same time that the primary vertex (PV) interaction —the one that leads to the production of the most energetic process— occurs. This significantly complicates the reconstruction and identification of physical objects. The level of PU is typically estimated through the mean number of interaction vertices in a given data taking period. A summary of the pileup profile across different years is presented in Figure 3.2. During Run 2, the pileup profile peaked at approximately 35 interactions per crossing of the LHC. This value has doubled during the last year of Run 3 data taking in 2024.

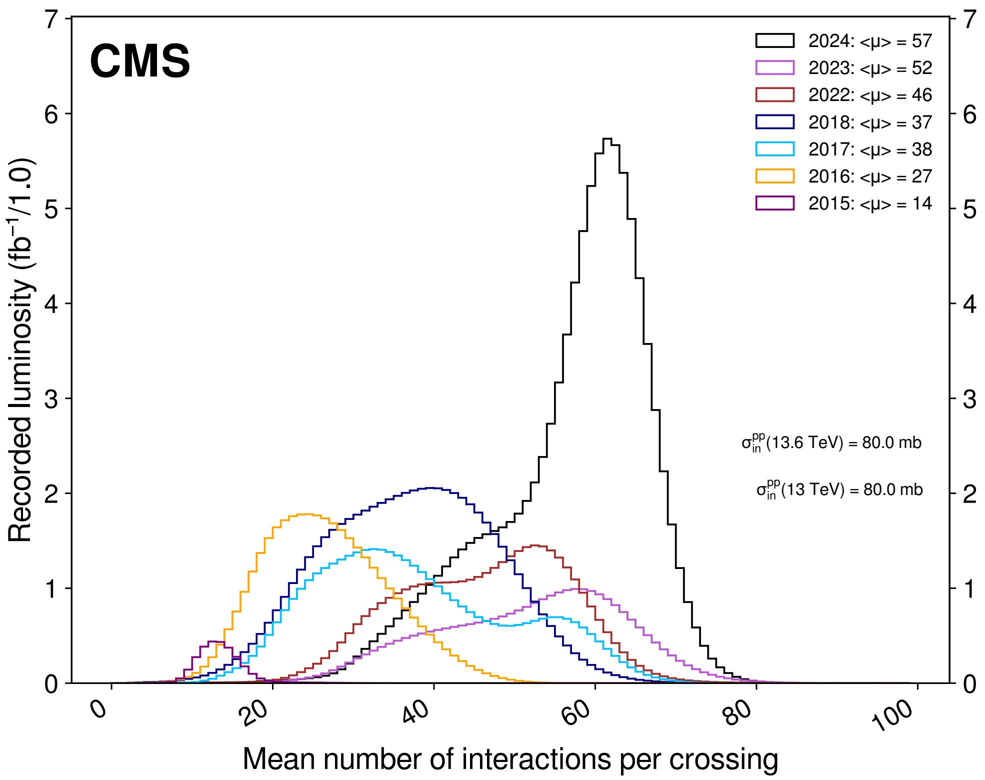

FIGURE. 3.2: Distribution of the average number of interactions per crossing (pileup) for pp collisions in Run 2 and 3. The plot also shows the overall cross section for the minimum bias sample, which is obtained from the PYTHIA8 prediction. The numbers associated to each year in the legend show the mean of each distribution.

When the instantaneous luminosity is integrated over a given period of time, the resulting quantity is known as the integrated luminosity (L). This quantity represents the total accumulated luminosity and serves as a key indicator of the amount of data collected. The integrated luminosity recorded by the CMS experiment per year of data taking, as well as the accumulated integrated luminosity delivered by the LHC and recorded by CMS, are shown in Figure 3.3. This quantity is typically measured in powers of *barn*, where $1 \text{ barn} = 10^{-28} \text{ m}^2$.

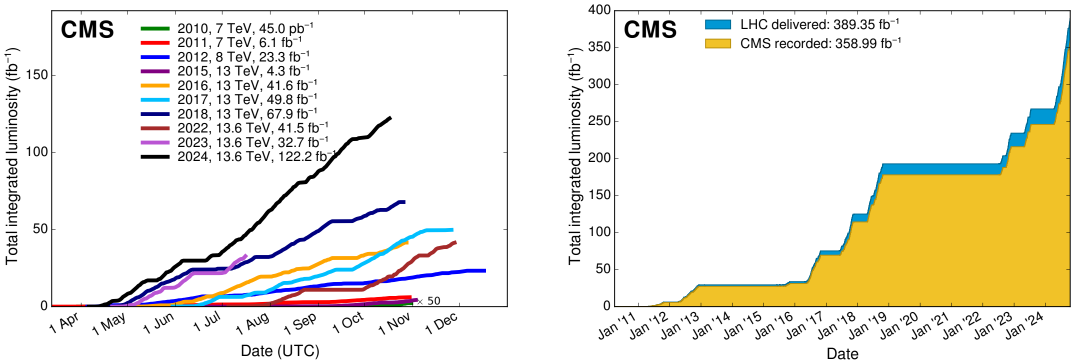

FIGURE. 3.3: Cumulative luminosity delivered to CMS during stable beams for pp collisions at different centre-of-mass energies, shown as a function of time from 2010 to 2024.

Over the past 15 years, the total integrated luminosity delivered by the LHC up to the time of writing this thesis is 389.35 fb^{-1}, of which the CMS experiment has recorded 358.99 fb^{-1}. The ratio between these two quantities, approximately 92%, highlights the excellent data-recording efficiency achieved by CMS. This dataset is 40 times larger than that of the Tevatron after its 20-year operation. This milestone is the result of the huge collaborative effort of the LHC community, that have enabled the collection of the largest dataset ever recorded in particle physics.

The content presented in this thesis uses 137 fb^{-1} of the recorded luminosity by the CMS experiment, which is the so-called full Run 2 dataset (from 2016 to 2018), and 34.7 fb^{-1} of the Run 3 dataset that was recorded during the first year of data taking in 2022. In total, this thesis presents results using more than 150 fb^{-1} of data, recorded over a period of more than 5 years .

3.2 The CMS experiment

The CMS collaboration is one of the four major experiments at the LHC. With more than 4000 collaborators, including senior researchers, technical personnel and a large fraction of PhD students, CMS has published more than 1300 peer-reviewed articles that explore different aspects of the pp collisions at the LHC.

As part of the milestones achieved by the collaboration, in 2012 the CMS experiment reported the first observation of Higgs boson production [11] in pp collisions at 7 TeV. Since then, and at the time of writing this document, the collaboration has continued to explore the Higgs mechanism, publishing nearly 200 results on various aspects of Higgs boson physics that are covered in a comprehensive review published in *Nature* [25], and the most precise measurement of the W boson mass [26] which has been recently submitted to *Nature*. These milestones could not have been achieved if it were not because of the more than 300 papers that CMS has released focusing on the research of the top quark and other SM bosons such as the W and Z bosons, which are equally relevant parts of the LHC and CMS physics programmes, and crucial for the correct understanding of the Higgs mechanism. These results are of particular relevance to this thesis.

The work of the CMS collaboration is based on data recorded by the CMS detector. In the following pages, a brief introduction to the technical aspects of the CMS detector is provided. A comprehensive description of its design and construction can be found in Refs. [27, 28].

3.3 Technical aspects of the CMS detector

The data considered in this thesis was recorded over a seven-year period (2016-2022). This period includes three years of data taking (2016-2018) at 13 TeV, a four-year-long shutdown (2018-2022), and one year of data taking that started in 2022 at 13.6 TeV, and finished in 2023. This period has therefore been marked by continuous evolution and improvement of the detector. For consistency in the descriptions, the CMS detector details presented in this thesis are based on its most recent configuration as of the Run 3 data taking period.

3.3.1 Coordinate system and overview

From a technical point of view, the task of the CMS detector is to reconstruct the trajectories of relativistic particles produced in LHC collisions. This is achieved by analyzing how different particles interact with the various materials of the detector. This information is correlated across the different subsystems that make up the CMS detector, and used to fully reconstruct the four-momentum of the particles.

The four-momentum of particles reconstructed in CMS are given in the CMS coordinate system. This coordinate system is defined such that the z-axis, representing the longitudinal direction, aligns with the LHC beam pipe. The x-y plane, known as the transverse plane, is oriented perpendicular to this axis. In this convention, the x-axis points radially towards the center of the LHC, while the y-axis is perpendicular to the Earth's surface. The relevant quantities that define the trajectory of a particle in the transverse plane are its transverse momentum (p_{T}), and the azimuthal angle (ϕ). In the longitudinal plane, the "pseudorapidity" (η) quantity is used instead of the typical polar angle (θ). This quantity is related to the polar angle through the relation in Eq. 3.2. The main advantage of using this quantity is its lorentz-invariance to boosts in the z-axis.

$$\eta = -\ln\left[\tan\left(\frac{\theta}{2}\right)\right] \tag{3.2}$$

The CMS detector is designed as a multi-layered, general-purpose instrument. In the CMS coordinate system, starting from the interaction point and moving outward in the transverse plane, the CMS detector consists of several subdetectors: the tracker system, the electromagnetic calorimeter, the hadronic calorimeter, the solenoid magnet, and the muon system. Each subdetector also extends along the longitudinal direction, contributing to the compactness of the detector, which allows it to nearly cover the entire solid angle around the interaction point. An schematic representation of the CMS detector can be found in Figure 3.4.

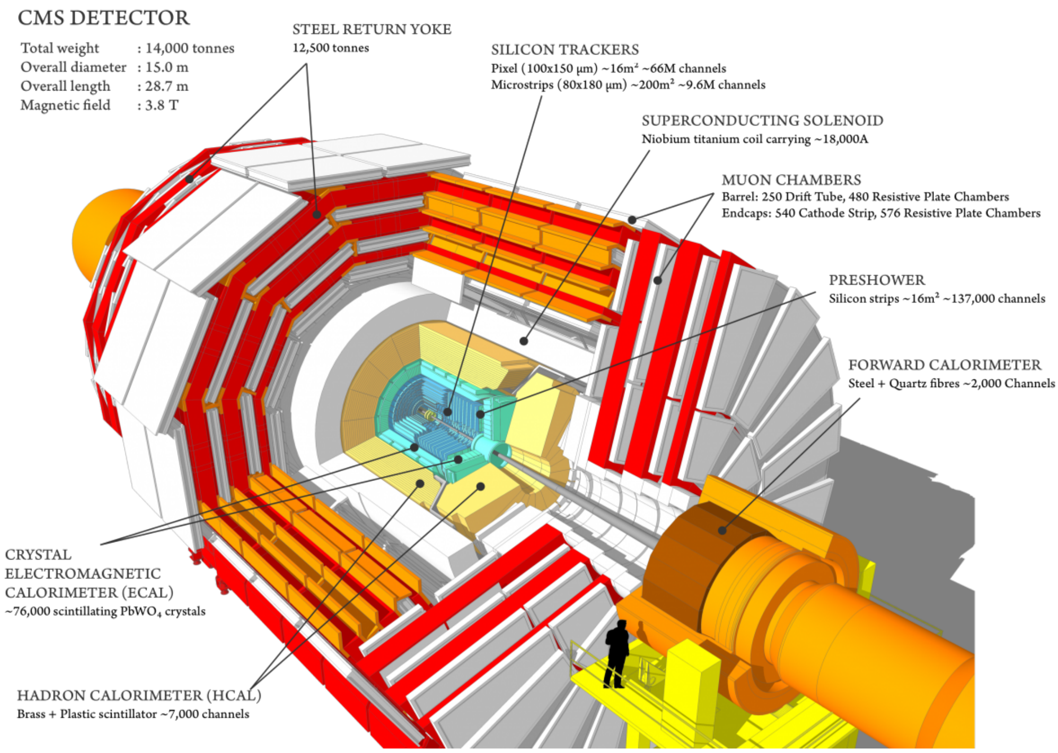

FIGURE. 3.4: [29] Schematic view of the CMS experiment and its subdetectors.

3.3.2 Tracking system

The tracking detector [30] in CMS has two distinct functions: tracking and vertexing. Tracking consists on the reconstruction of the trajectories of charged particles from pp collisions, while vertexing consists on disentangling the PV, defined as the one in which the most energetic collision occured, from PU vertices.

The tracker system comprises approximately 48 million silicon pixels, ensuring precise tracking in high-occupancy environments like pp collisions, and it is further optimized for coverage within $|\eta| < 2.5$, ensuring high precision in both the barrel and endcap regions. It consists of two main components: the Pixel Detector (PD) and the Silicon

Strip Detector (SSD). The PD, positioned closest to the interaction region, reconstructs the initial points of particle trajectories. It features four layers of silicon pixels in the barrel region, offering high spatial resolution, with layer distances between 20 and 160 mm. Additionally, three pixel disks extend into the forward region at 291, 396, and 516 mm. The SSD spans from about 200 mm to 1160 mm from the beam pipe, reaching the electromagnetic calorimeter.

Together, the PD and SSD allow the CMS tracker to provide high-precision measurements of charged particles, making them essential for the analysis of particle collisions at the LHC.

3.3.3 Electromagnetic calorimeter

The electromagnetic calorimeter (ECAL) is used to detect charged particles, with a specific focus on distinguishing between electrons and photons. It consists of around 6×10^4 lead tungstate ($\mathrm{PbWO_4}$) crystals positioned in the central barrel region of CMS and more than 7×10^3 additional crystals located in the endcaps. The $\mathrm{PbWO_4}$ material is characterized by a considerably high density, which facilitates the detection of electrons and photons by exploiting their strong ionization properties. Although nearly all particles produced in LHC collisions can interact with the $\mathrm{PbWO_4}$ crystals, mainly electrons and photons possess sufficient ionization capacity to deposit all their energy before passing completely through the calorimeter. In addition to its high density, the $\mathrm{PbWO_4}$ crystals also exhibit strong resistance to high-radiation environments, making them an ideal candidate material in highly active environments.

3.3.4 Hadronic calorimeter

The Hadronic Calorimeter (HCAL) surrounds the ECAL and plays a crucial role in measuring the energy of hadrons, including neutral hadrons, which cannot be detected by the ECAL. Due to spatial constraints between the ECAL and the solenoid, part of the HCAL is located outside the magnetic field of the solenoid. The HCAL is a sampling calorimeter, composed of brass layers interspersed with plastic scintillators, allowing for efficient energy measurement through the interaction of hadrons with the brass, while the scintillators detect the resulting shower of particles. This design maximizes the calorimeter's effectiveness in hadronic energy reconstruction.

3.3.5 Solenoid magnet

At the heart of CMS, just beyond the HCAL, lies a superconducting magnet measuring 13 m in length and 6 m in diameter, capable of generating a magnetic field up to 3.8 T. This powerful field bends the trajectories of charged particles, allowing for precise momentum measurements.

3.3.6 Muon spectrometers

Muons can generally travel long distances without interacting with the calorimeters. For this reason, muon detection subsystems are typically placed in the outermost region of the detectors. The strong magnetic field enables the integration of four specialized muon detection stations: drift tubes (DTs) in the barrel region, cathode strip chambers (CSCs) in the endcaps, resistive plate chambers (RPCs), and gas electron multipliers (GEMs). The GEM detectors enhance the muon detection coverage in the forward region, complementing the capabilities of the CSCs and RPCs. Together, the CMS muon system comprises 25,000 m^2 of detection planes, expanding over the whole barrel and endcap regions. These stations provide critical information for identifying and measuring muons produced in particle interactions.

The most common interaction mechanism for muons produced at the LHC is ionization, while radiative processes become increasingly significant at higher p_{T} [31]. As a result, muon detectors are predominantly designed as gaseous detectors, which respond to the ionization of the gas mixture caused by muons passing through. When a muon ionizes the gas, an avalanche of electrons drifts toward an anode wire positioned inside the gaseous detector. From the signals induced by this avalanche, the system can determine both the position and the time of its interaction with the gas. An overview of the CMS muon system can be seen in Fig. 3.5.

The CMS DT system consists of 250 stations distributed across the wheels of the CMS cylinder (Wh-2, Wh-1, Wh0, Wh$+1$, Wh$+2$), with Wh0 being the central wheel. Each wheel is further divided into twelve distinct sectors, containing four types of stations labeled MB1, MB2, MB3, and MB4, depending on their proximity to the interaction point, with MB1 being the closest and MB4 the farthest. Each station is divided into three groups of "super layers" (SL), each containing four layers of DT detection cells stacked on top of each other. Each detector cell is a gaseous detector composed of a two positively charged walls and a central anode wire.

In each chamber, the two outermost SLs are known as SL-ϕ (or SL1 and SL3), whereas the middle SL is referred to as SL-θ. The two SL-ϕ are used to locally reconstruct the azimuthal angle inside the chamber, whereas SL-θ is used to reconstruct the polar angle. The number of cells in each SL varies by chamber type. Generally, each layer of an MB1 chamber has 48 cells, each layer of an MB2 chamber has around 60 cells, each layer of an MB3 chamber has around 80 cells, and each MB4 chamber has 102 cells.

The CSC subsystem extends over the pseudorapidity range $|\eta| \in [0.9, 2.4]$. It consists of four different stations in each endcap (eight in total), with chambers positioned perpendicularly to the beam axis. Each CSC chamber is composed of six gas layers, where charged particles ionize the gas mixture. The electrons liberated by ionization drift towards the anode wires under an electric field, inducing signals on the strips, which allow precise position reconstruction. The overlapping strip and wire readout provides a

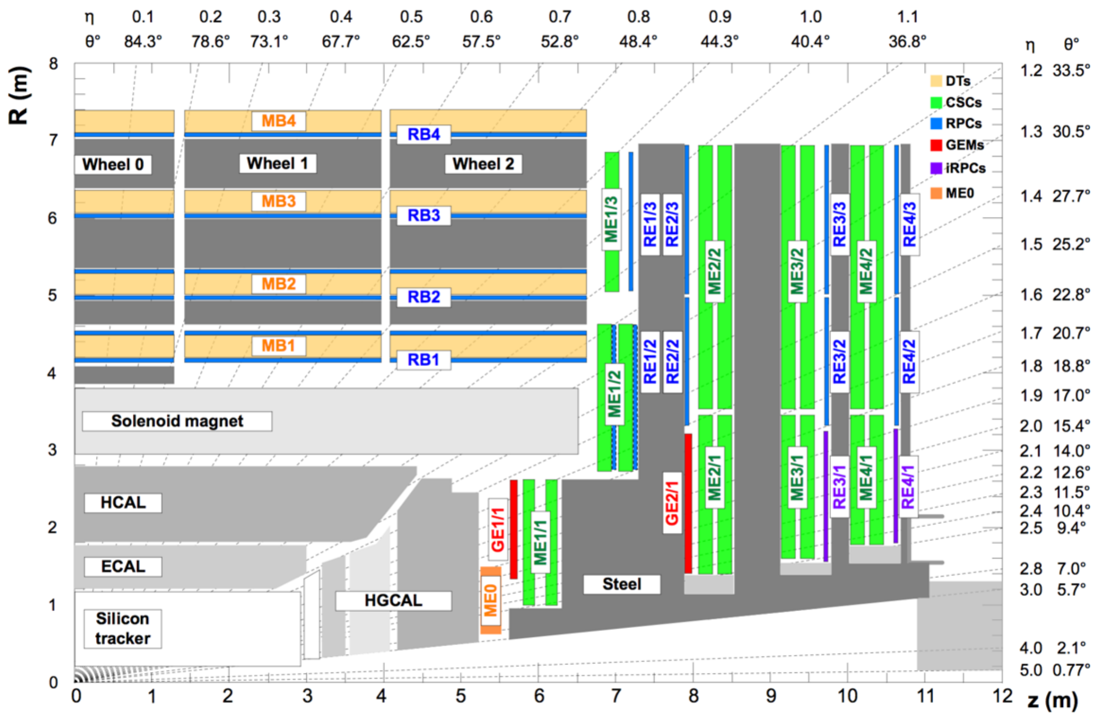

FIGURE. 3.5: A schematic representation of a quadrant of the CMS detector. The horizontal axis corresponds to the longitudinal plane, aligned with the beam axis, while the vertical axis represents the increasing distance from the beam. The interaction point is located at the lower-left corner. The positions of the various muon stations are indicated. The DTs are labeled MB (Muon Barrel), while the CSCs are labeled ME (Muon Endcap). RPCs are installed in both the barrel and endcap regions of CMS, where they are labeled RB and RE, respectively. GEM detectors are located in the forward region and labeled GE (GEM Endcap).

two-dimensional measurement of the muon trajectory. The CSC technology was chosen to instrument the CMS endcaps because it provides good position and time resolution, while performing well in large and non-uniform magnetic fields.

The RPC system is also a gaseous detector, consisting of a series of parallel plates separated by a thin gas gap. These chambers provide spatial and temporal resolution comparable to that of scintillators, making them crucial for the fast reconstruction of muons traversing the detector. The CMS RPC system is designed for high time resolution and efficient triggering, complementing the DTs and CSCs in identifying muons. Each RPC chamber consists of two resistive plates with a gas mixture in between. When a charged particle passes through, it ionizes the gas, triggering an avalanche effect under a strong electric field. The induced signal is read out by external pickup strips, allowing for precise timing measurements. The CMS RPC system consists of two modules separated by a gap. The total induced signal is the sum of the two signals from the gap, enabling each gap to operate with different gains while maintaining a higher total signal gain.

Finally, the GEM system is also a gaseous detector, based on thin foils perforated with a dense array of microscopic holes. These detectors offer excellent spatial resolution and can operate at high rates, making them ideal for precision tracking of muons in the forward region of CMS. Each GEM chamber typically consists of three GEM foils separated by gas gaps, forming a structure known as a triple-GEM. When a charged particle passes through, it ionizes the gas, and the resulting electrons are multiplied as they pass through the high electric fields inside the GEM holes. The amplified signal is then collected on readout strips or pads, allowing for precise position measurements.

3.4 Data acquisition in CMS

The mechanical detectors described in the previous section are designed to respond to the interactions of particles produced at the LHC as they pass through the detector. Each interaction is converted into electronic signals, which are collected by the CMS detector front-end (FE) electronics. These electronics act as the interface between the detector's mechanical structure and the CMS data acquisition (DAQ) system.

The CMS DAQ system is structured in multiple layers to efficiently process the data received from the detector. Once the data is captured by the FE electronics, it is transmitted via optical fibers to the back-end (BE) system through a network of readout electronics. This high-speed communication ensures quick data transfer and response. At the BE stage, the data is processed to reconstruct full event information, which occurs in several stages. These stages can be broadly categorized into the trigger, reconstruction and refined processing steps, which will be described in more detail in the following sections.

3.4.1 Trigger system

The LHC accelerator collides beams containing approximately 10^{11} protons each, at a frequency of 40 MHz. At the working instantaneous luminosity of the LHC, an average of 30-60 simultaneous collisions are expected to occur at each beam crossing. To cope with such a big amount of information, a sophisticated trigger system has been designed to select the most interesting events for the development of the CMS physics program. The CMS trigger [32] is therefore one of the most crucial tools, as its performance directly influences the physics discoveries that can be made. The CMS trigger system consists of two main components: the Level-1 trigger (L1T) and the High-Level Trigger (HLT).

The L1T is a hardware-based system designed to filter predefined events before performing detailed measurements of particle trajectories. This stage of the triggering process is divided into several steps. Initially, the information received from the FE electronics is processed locally by the trigger systems of each subdetector. The muon system attempts to reconstruct straight segments in the DTs and CSCs, while the ECAL and HCAL systems will focus on reconstructing energy clusters.

The local information is passed to the track finder and clustering algorithms, which correlate the information from several subdetectors in order to construct L1T objects. Each L1T object represents a first approximation of the properties of a given hadron, electron, photon, hadronic τ or muon candidate. The clustering algorithms compute an initial approximation of the total energy deposited in both the ECAL and HCAL, while the track-finding algorithms aim to reconstruct the trajectories of the muons using information from the DTs, RPCs, and CSCs. With this, a full event reconstruction is obtained considering L1T information.

Finally, the L1T event information is passed to a global trigger algorithm that makes the final decision. Because of the reduced quality of the L1T objects, the L1T global trigger tends to make a decision based on simple topologies consisting on the presence of one or two L1T objects that satisfy minimal kinematic requirements. Each L1T is assigned a bandwidth limit, which constrains the number of events it can accept and send to the HLT. The total bandwidth of the CMS L1T system is currently 105 kHz, and the overall time taken to give a final decision of the global trigger is at the order of $4\mu s$.

Events preselected by the L1T decision are passed to the HLT, along with the information used by the L1T to construct these objects. The HLT stage runs on computing farms outside the CMS detector and applies more refined reconstruction algorithms than those used in the L1T, though still constrained to specific detector regions and final-state topologies. The HLT logic is structured into "HLT paths," which together form the "HLT menu." Each HLT path is triggered by at least a L1T seed, initiating a sequence of reconstruction and filtering steps that ultimately lead to the formation of an HLT object.

The key advantage of HLT reconstruction over L1T is that, although a fast decision is still required, it does not need to be as immediate as the L1T decision. This additional processing time allows for significantly improved resolution of HLT tracking objects compared to those from L1T. During Run 3, the final DAQ bandwidth at the HLT stage is approximately 5 kHz. Since this bandwidth is shared among different trigger selections, the CMS HLT menu is currently able to include more than 600 distinct paths.

3.4.2 Event Reconstruction

The combined operation of the L1T, HLT, and CMS offline DAQ system reduces the initial 40 MHz collision rate from pp collisions to approximately 1 kHz during Run 2 [33], with an improved rate of 5 kHz in Run 3. Events selected by the HLT undergo further processing in a stage known as event reconstruction. The goal of this process is to provide a complete reconstruction of the kinematic properties of reconstructed objects, including muons, electrons, photons, charged hadrons, and neutral hadrons.

The process of obtaining physically meaningful properties of physics objects is typically divided into two main steps: *reconstruction* and *identification*. The reconstruction step employs subdetector-specific algorithms that are designed to target particular final-state topologies. For instance, the ECAL, HCAL, and muon systems each have dedicated reconstruction algorithms, which may focus primarily on their own detector data but can also incorporate information from other subsystems when needed.

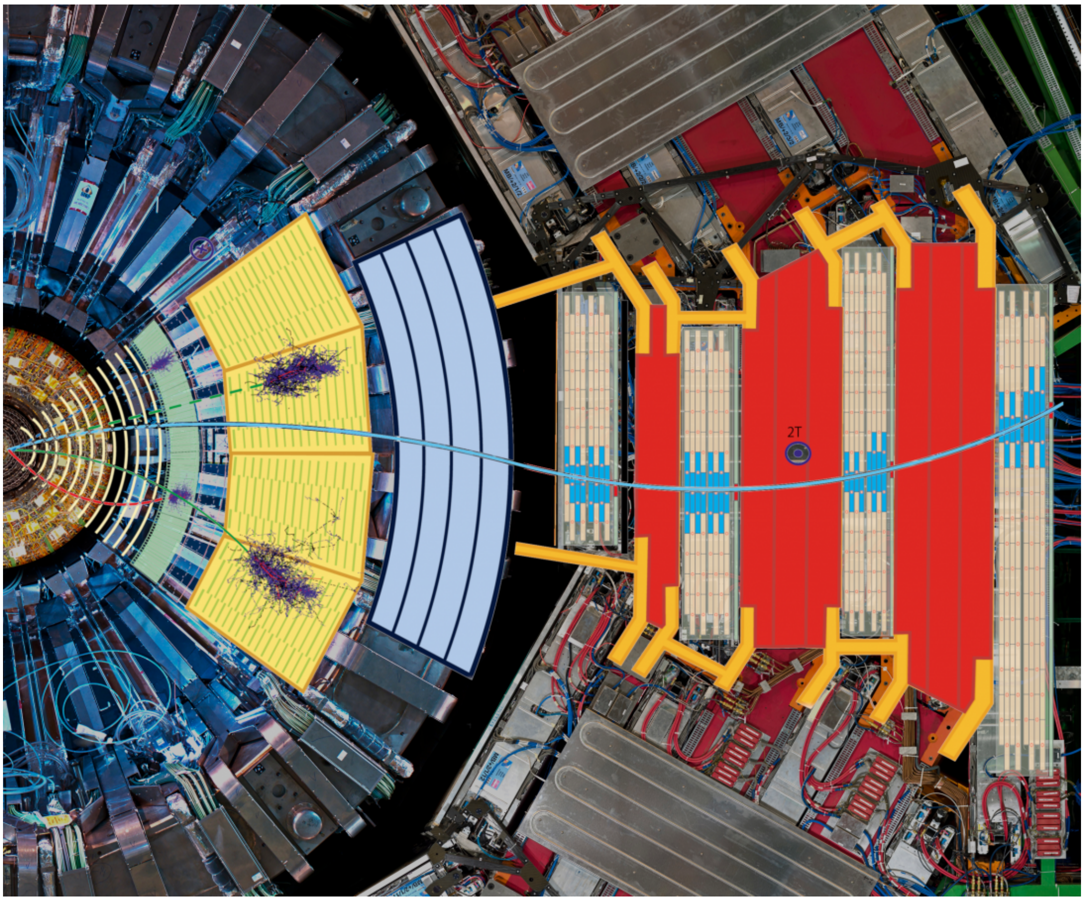

FIGURE. 3.6: A sketch of specific particle interactions in a transverse slice of the CMS detector, from the beam interaction region to the muon detector.

The final object definition is obtained using the particle-flow (PF) algorithm [34] that integrates information from all subdetectors to perform offline reconstruction of event properties. Specifically, the PF algorithm identifies electrons and photons as clusters of energy depositions in the ECAL. For electrons, these clusters are associated with a charged track in the tracker, while for photons, no track matches the cluster. Charged and neutral hadrons are reconstructed based on energy depositions in the HCAL. Charged hadrons are associated with tracks in the tracker, whereas neutral hadrons are identified from energy depositions in the HCAL that do not have matching tracks in the tracker. Muons primarily interact with the tracker and muon systems, and their reconstruction involves matching locally reconstructed segments in the muon system to charged tracks in the tracker. In the case of tau (τ) objects, when τ decays leptonically, the resulting decay products will either be reconstructed as an electron, a muon, or as a charged hadron if the decay is hadronic. An schematic representation of the signatures that different objects leave in the detector can be seen in Fig. 3.6. An overview of the reconstruction process within the PF algorithm is provided in the following pages.

3.4.2.1 Tracking and vertexing

The PF algorithm begins with the reconstruction of charged-particle tracks in the tracker. This process involves correlating locally reconstructed hits to build complete particle trajectories.

Track reconstruction follows the principle of iterative track finding, with each iteration employing a track-finding algorithm based on the Kalman Filter [35,36]. The process starts with a seed, typically a cluster of hits in the pixel detector. The algorithm then extrapolates from the seed to other nearby hit clusters. For each candidate track in this extrapolation step, a fit is performed to determine the track parameters. The candidate that best matches the expected trajectory of a charged particle through the tracker is selected, and the reconstructed track is used as the seed for the next iteration. Once no additional hit clusters remain for further extrapolation, the track-finding step concludes, and a new iteration of the iterative tracking procedure begins.

The key advantage of iterative track finding is its ability to first reconstruct tracks that are relatively easier to identify, typically those associated with particles of high p_{T} or those originating close to the collision region. Each iteration removes the hits already assigned to reconstructed tracks, therefore reducing the computational complexity for subsequent iterations. This approach significantly improves the reconstruction of low-p_{T} tracks and tracks from displaced vertices, which would otherwise be challenging to extract due to the high density of hits in the tracker.

Once the PF algorithm has reconstructed the tracks associated with charged particles, it proceeds to the vertexing step. The primary goal of this step is to estimate the location of the PV, as well as to identify secondary interaction points arising from PU interactions. Vertex reconstruction is performed by clustering tracks that are consistent with originating from the same interaction vertex. A fitting algorithm is then applied to determine the precise position of each vertex using the associated tracks.

3.4.2.2 Electrons and photons

The calorimetry reconstruction of electrons and photons is based on the reconstruction of shower-like signatures in the detectors.

Electrons and photons are generally highly radiative particles and undergo multiple interactions as they traverse the ECAL material. The most common interaction mechanism for electrons in the ECAL is the emission of bremsstrahlung photons, whereas for photons, the dominant process is photon conversion, in which the photon decays into an electron-positron pair. These secondary electrons interact with the ECAL in the same way as primary electrons.

The PF algorithm for electrons and photons begins with the formation of ECAL clusters, which are created by combining ECAL crystals that have recorded energy above a given threshold. The cluster with the highest energy serves as the seed for the subsequent reconstruction steps. Starting from this seed cluster, nearby clusters are combined to form the so-called superclusters (SCs).

In parallel to SC formation, an optimized tracking algorithm is employed to reconstruct electron tracks. This algorithm combines hits in the pixel detector to identify tracks compatible with the trajectory of an electron undergoing bremsstrahlung interactions. This tracking method, known as the Gaussian-Sum Filter (GSF) algorithm [37], is an extension of the Kalman Filter algorithm used in the tracker. The GSF algorithm refines the energy loss model of the Kalman Filter to better account for the radiative interactions that electrons experience in the ECAL material.

Once the ECAL SCs and GSF tracks are reconstructed, they are fed into the PF algorithm, which links them to form electron and photon objects. The kinematics of the resulting objects are obtained through a joint fit to the GSF track and the SC properties when available. A minimal selection criteria based on the kinematics of the reconstructed objects is used to enhance quality.

Finally, if a PF candidate is associated with both an ECAL SC and a GSF track, the reconstructed object is classified as an electron. Otherwise, if no GSF tracks are associated with the ECAL SC, the PF candidate is labeled as a photon.

3.4.2.3 Muons

Muon reconstruction in CMS relies on the signals collected by the muon spectrometer system, as detailed in Section 3.3.6.

The first step in muon reconstruction involves processing the information from hits recorded in different detector components: cells in the case of the DTs, strips in the case of the CSCs, and plates in the case of the RPCs. Hit reconstruction also requires applying timing corrections provided by the electronics. These corrections account for effects such as the critical paths between the electronic system and the detector, the time of flight from the originating vertex to the muon system, delays within the electronic system, and effects originating from the magnetic field which is not entirely uniform at increasing pseudorapidity.

The local information from these hits is then correlated within each subdetector to form straight segments, representing sections of the overall trajectory of the particle that triggered the muon system. The segments reconstructed in each subdetector are subsequently combined into a local reconstruction of the muon trajectory using a Kalman-Filter algorithm. The resulting objects from this reconstruction procedure are known as Standalone Muon tracks.

Once the standalone muons have been properly reconstructed, the information from the tracker is incorporated to obtain the full trajectory of the candidate muon. There are two different approaches to integrating the tracker information at this stage: inside-out and outside-in reconstruction. Inside-out reconstruction is performed by extrapolating tracker tracks to the muon system. If an extrapolated track matches a muon segment, the resulting object is labeled as a tracker muon. In the outside-in reconstruction, the procedure is reversed; muon segments are extrapolated back to the tracker system.

Due to the high efficiency of muon reconstruction in CMS, muons are typically reconstructed as both tracker muons and global muons. When this occurs, the two objects are merged into a single muon candidate. Muons obtained from this reconstruction are subsequently fed into the PF algorithm for combination with other reconstructed objects. In particular, for muons, the PF algorithm applies a set of minimal requirements designed to enhance the quality of the reconstructed object, ensuring its suitability for further analysis.

3.4.2.4 Hadrons and jets

Colored particles such as quarks and gluons, produced at the PV, are not detected directly as they promptly hadronize by combining with surrounding strongly interacting particles. The resulting hadrons undergo further decays and hadronization, creating an energy cascade that leaves signatures in both the ECAL and HCAL, with a total accumulated energy that, in the absence of energy loss because inefficiencies of the detector, corresponds to the summed energy of all hadrons in the decay chain.

The PF algorithm reconstructs hadrons by first removing electrons, ECAL photons, and muons. The remaining signatures correspond to charged and neutral hadrons, non-isolated photons from hadron decays, and a small fraction of non-isolated leptons. Within the tracker acceptance ($|\eta| < 2.5$), non-isolated photons from π_0 decays appear as unmatched ECAL clusters, while neutral hadrons are associated with HCAL clusters not associated with any tracks. Outside the tracker coverage, ECAL clusters linked to HCAL clusters originate from the same hadronic shower, whereas unmatched ECAL clusters are reconstructed as photons. The resulting objects are in any case known as calorimeter jets or simply Calo Jets. Calo jets candidates are assigned calorimetric energy by summing ECAL and HCAL cluster energies. This energy is then compared to the summed track momenta. Depending on the compatibility between the calibrated calorimetry energy and the summed track momenta, the energy of the PF hadron candidates is recalibrated.

The reconstructed PF hadron candidates are clustered using the anti-k$_T$ algorithm [38, 39], which groups them into cones of a given radius known as jets. The energy of a jet is defined as the sum of the energies of all PF hadron candidates within it, while its direction is determined by the cone axis. These quantities correlate with the direction and original energy of the particle produced at the PV. Jets are therefore spatially-grouped collections of particles whose properties resemble that of the initial partons that produced them. In average, 65% of the energy of a jet originates from charged hadron contributions, 25% is from photons, and the remaining 10% comes typically from neutral hadrons.

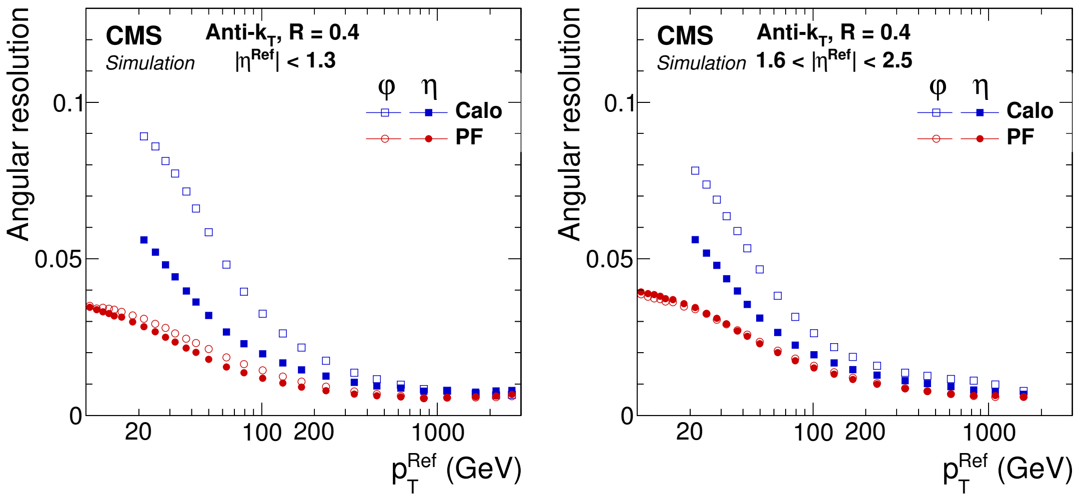

FIGURE. 3.7: [34] Resolution of the PF jet reconstruction algorithm using the anti-k$_T$ algorithm (red line) versus the calo jet reconstruction (blue lines) in the barrel (left) and endcap (right) regions of CMS.

The angular resolution of the PF anti-k$_T$ reconstruction, compared to that of calo jets, is shown in Figure 3.7 as a function of the reference jet p_T. Jets are reconstructed with a cone radius of $R = 0.4$. The reconstructed jets are obtained from detector-level quantities, whereas the reference jet is defined as the clustering of all generator-level particles, excluding neutrinos. All the jets used in this thesis have been clustered using this same algorithm.

3.4.2.5 Pileup mitigation

Particle interactions originating from PU vertices can affect the measurements of particle properties and lead to incorrect event interpretation. To address this issue, sophisticated algorithms are employed to distinguish between the signal and background components of the data. This section discusses the pileup mitigation techniques [40] used in the CMS experiment.

The pileup-per-particle identification (PUPPI) algorithm [41] is designed to mitigate the impact of pileup on jet property reconstruction. It achieves this by utilizing local shape information, event pileup characteristics, and tracking data. For each neutral particle, a local shape variable is computed based on the surrounding charged particles that are compatible with the PV within $|\eta| < 2.5$, as well as both charged and neutral particles outside the tracker coverage. This variable aids in distinguishing between collinear and soft diffuse distributions of objects surrounding the particle. Charged particles identified as originating from pileup vertices are removed from the analysis. The momenta of the neutral particles are then rescaled according to their likelihood of originating from the PV, derived from the local shape variable, thus eliminating the need for traditional jet-based pileup corrections.

Other algorithms such as Charged Hadron Subtraction (CHS) have also been used in the contents presented in this thesis. In the case of CHS, charged hadron contributions are removed from PU based on the vertex from which particles originate.

Throughout the course of this thesis, the term jet will used in general. For Run 2 analyses, the inherent algorithm for the jets is the CHS, whereas for Run 3 analysis the jets are reconstructed PUPPI.

3.4.2.6 Missing transverse energy

In high-energy physics experiments, not all particles produced in a collision interact with the detector. A prime example of this are the neutrinos, which are effectively invisible to the detector because of their weakly interacting nature. Despite this, energy conservation principles allow us to estimate the energy carried by these "invisible" particles. By summing the vector momenta of all detected particles in an event, the total momentum of the system can be calculated. Since the total momentum of the system must be zero in the laboratory frame, any imbalance in the measured transverse momentum can be attributed to the presence of undetected particles, such as neutrinos. This imbalance is referred to as the missing transverse momentum ($p_{\mathrm{T}}^{\mathrm{miss}}$).

In most events, the longitudinal component of momentum is not as relevant because the majority of the energy in high-energy collisions is carried transversely, perpendicular to the beam axis. Therefore, $p_{\mathrm{T}}^{\mathrm{miss}}$ is commonly defined as the modulus of the transverse component of the missing momentum vector. One exception to this general rule arises in studies of boosted topologies, where longitudinal momentum may play a more significant role, although such cases are not central to this thesis.

The $p_{\mathrm{T}}^{\mathrm{miss}}$ is calculated as the negative sum of the vector transverse momenta of all identified objects in the event. It will be referred to as PuppiMET, in case that the pileup mitigation has been treated using the PUPPI algorithm, or as CHS-$p_{\mathrm{T}}^{\mathrm{miss}}$ otherwise.

4 Monte Carlo modeling at CMS

In Chapter 2, it was shown how one can construct a gauge-invariant theory by using the symmetries observed in experiments. We primarily worked within the free-particle approximation, introducing interaction terms by enforcing gauge invariance. This approach provides a solid foundation for constructing the SM Lagrangian, from which theoretical predictions can be derived.

In HEP, the predictions of the theory are typically carried out using Monte Carlo (MC) generators. These programs encode the inner workings of the SM lagrangian, and are able to make predictions up to a given specified order in perturbation theory. Because of the complexity of higher-order calculations, it is currently impractical to compute them up to arbitrarily high orders, and thus these theories are approximated with perturbation techniques. Perturbation is usually performed in powers of either the strong coupling constant (α_s) or the weak coupling constant (α_{ew}).

Developers of MC generation software are typically not directly involved in the usage of these MC tools within experiments, as their focus lies primarily on the development of general-purpose frameworks and algorithms for MC generation. Consequently, the role of MC experts within CMS extends beyond the technical production of samples required for analyses. It also includes performing thorough validation studies of the produced samples, developing a deep understanding of which modeling techniques are best suited for specific physics processes, and identifying the technical limitations associated with certain sets of samples, which in some cases cannot be produced due to computational constraints. All these efforts are driven by the ultimate goal of MC experts in CMS, which is to ensure the reliability and validity of the physics content in all CMS publications, particularly regarding the modeling aspects.

A central feature of this thesis revolves around the generation of MC simulations. In particular, I have carried out validation studies of novel modeling approaches for the $\mathrm{t\bar{t}W}$ and WZ processes. The purpose of this section is to introduce a set of general concepts and techniques related to MC generation, which are essential for understanding the broader context of this work. These ideas will serve as a foundation for understanding the relevance and impact of the MC validation studies when interpreting the measurements presented throughout this thesis.

4.1 The SM at the LHC

Since protons are composite objects, the dynamics of proton collisions are much harder to predict than those of the fundamental particles. Furthermore, the non-Abelian gauge nature of QCD, added to the fact that gluons remain massless after EWSB, causes IR divergences in the QCD theory that make the usage of perturbative methods difficult. Renormalizability addresses this by introducing a characteristic energy scale, Λ_{QCD}. Above this scale, QCD can be treated perturbatively with a small strong coupling constant, while below it, QCD becomes non-perturbative, thus requiring alternative methods for describing it. Moreover, at energy scales above the Higgs mass, multiple interactions including electroweak corrections, loop effects, and higher-order QCD contributions become relevant, requiring precise calculations to accurately match experimental data.

As a result, describing LHC physics requires a deeper knowledge of QCD, parton-level modeling, and experimental corrections to extract meaningful results from collider data. In the following sections, the most important aspects about physics modeling in a LHC scenario will be covered.

4.1.1 Proton Parton distribution functions

According to the quark model from Gell-Mann [42], protons belong to the class of hadrons known as baryons. Specifically, at low scales, a proton is a bound state composed of two up quarks and one down quark (uud), known as the valence quarks. This quark content determines its fundamental properties: the total electric charge of the proton, which is $q_p = +1$, and its total angular momentum; $s_p = \pm\frac{1}{2}$. The latter result determines the that quarks are spin-$\frac{1}{2}$ fermions. In addition, and because quarks have non-zero colour charge, protons are "coloured" particles that are able to couple to QCD currents. This internal structure plays a crucial role in high-energy collisions, where the relevant interactions occur at the parton level rather than through elastic interactions between the protons, which are also accessible at the LHC, yet not of importance for the work presented here.

At energy scales significantly above the proton mass, the properties of the proton are no longer univocally determined by its valence quarks, and additional quantum effects become significant. Beyond the valence quarks, the structure of the proton is enriched by a dynamic "sea" of quark-antiquark pairs, gluons, and photons, which interact continuously with each other. As a consequence of energy and momentum conservation, the total energy of the proton is distributed among all its constituents. What was once a well-defined bound state of three quarks now follows a probabilistic description. In collisions between such protons, interactions can therefore occur between any parton within each proton.

In HEP, the nature of the proton is encoded in the parton distribution functions (PDFs), which describe the probability of finding a given parton carrying a fraction of the proton's total momentum at a specific energy scale. Because parton densities in the proton are inherently non-perturbative due to the fact that gluons are massless, the only proper way to model the PDFs of the proton is by extracting them from experimental data. Effectively, PDFs are used as an input when computing physics observables. For a generic observable, Θ depending on the initial state partons, its value can be computed as shown in equation 4.1.

$$\Theta = \sum_{i=0,1}^{N_f} \int dx_i dx_j f_i(x_i, \mu_F) f_j(x_j, \mu_F) \Theta(x_i, x_j, \mu_F) \tag{4.1}$$

Where N_f is equal to the number of parton flavours inside the proton, the indices i and j refer to the initial state partons, μ_F is the scale at which the collision occurs, $f_a(x_a, \mu_F)$ is the PDF of a parton of flavour $a = i, j$ carrying a fraction of the total momentum corresponding to x_a, and $\Theta(x_i, x_j, \mu_F)$ is the kernel used in the integration of the observable. Even though the whole computation directly depends in the scale at which the PDFs were measured, μ_F, thanks to the Dokshitzer-Gribov-Lipatov-Altarelli-Parisi [43–45] (DGLAP) equations, PDFs can be propagated to an arbitrary high-energy scale.

In all the MC simulations used in this thesis, PDFs are obtained from the NNPDF datasets. Specifically, the NNPDF3.0 [46] and NNPDF3.1 [47] sets are employed in the modeling of both the main signal samples and the relevant background processes. These two sets were the most precise descriptions of the proton PDFs at the time of developing the measurements presented in this thesis.

4.1.2 Physics of the hard scatter

The most energetic interaction between the partons from the two colliding protons is known as the *hard scatter*. Since the partons typically carry a large fraction of the total momentum of the protons, and the collisions occur at the TeV-scale, the dynamics of the hard scatter can be computed using perturbative methods. The goal is to determine the transition probability for an initial state, consisting of two incoming partons q_1 and q_2, to evolve into a final state f. This probability is generally given by equation 4.2.

$$\mathcal{P}(i \rightarrow f) = |\langle f|S|i\rangle|^2 \tag{4.2}$$

Here, $|i, j\rangle$ represents the quantum state of the initial partons, $\langle f|$ denotes the final state, and S is the scattering matrix (S-matrix). The key challenge is to compute the elements of the S-matrix, which encode the transition amplitudes from the initial state to the final state. One way of looking at the elements of the S-matrix in quantum mechanics is through the interaction picture, where the transition amplitude in equation 4.2 can also be expressed as in equation 4.3.

$$\langle f|S|i,j\rangle = \left\langle f \left| \int Te^{-i\int d^4x\mathcal{H}(x)} \right| i,j \right\rangle \tag{4.3}$$

Where $\mathcal{H}$ represents the Hamiltonian of the SM, and T is the T-matrix, which encodes the part of the S-matrix that is related to the interactions between particles. As mentioned before, because the computation of a transition occurs in a perturbative regime, one can expand this quantity using perturbative methods. The perturbative expansion up to the first two orders of the S-matrix can be found in 4.4.

$$S = 1 - i\int d^4x\mathcal{H}(x) + \frac{i^2}{2}\int d^4xd^4y\mathcal{H}(x)\mathcal{H}(y) + O(\mathcal{H}^3) \tag{4.4}$$

Computing these quantities in the interaction picture is generally not trivial, which is why the path integral formalism is often employed. This formalism is a reformulation of the integrals in equation 4.4 in terms of Green's functions. These Green's functions are computed from a generating functional, which itself encodes the dynamics of the field theory, using the Lehmann-Symanzik-Zimmermann (LSZ) reduction formula [48]. After applying the LSZ formula, the resulting Green functions can be diagrammatically represented as Feynman Diagrams [49].

Each Feynman diagram is therefore associated with an amplitude value known as the matrix element (ME). The value of $|\mathcal{M}_{i\to f}|^2$ gives the transition probability from an initial state i to a final state f. As a result, computing the elements of the S-matrix can be done by exactly computing all the Feynman diagrams contributing to the process $i \to f$. Equivalently, the computation up to a given order in perturbation theory is given by exactly computing only the Feynman diagrams contributing to that order.

The task of computing all relevant Feynman diagrams, and thus the task of integrating all the different MEs, is typically carried out by what are known as ME generators. These generators can also be employed to predict differential distributions of physical observables. This is achieved by using MC integration techniques. The procedure begins by sampling a specified phase space with different configurations of initial and final-state momenta. Each sample point in this phase space is referred to as an "event." For each event, a weight factor, derived from the matrix element calculation, is assigned. This weight indicates the relative importance of that event compared to others, and it is used for accurately describing physical observables at the differential level.

Some of the most widely used generators are POWHEG [50–53] and MADGRAPH5_AMC@NLO [54], both of which play a key role in this thesis. Both frameworks support calculations at different levels of perturbative accuracy, including Leading Order (LO) and Next-to-Leading Order (NLO) in QCD. Furthermore, POWHEG can achieve next-to-next-to-leading order (NNLO) accuracy in certain processes. Additionally, the MADGRAPH5_AMC@NLO framework has been extended to incorporate next-to-leading order (NLO) accuracies in the Electroweak (EW) expansion (NLO_{EW}) [55], enabling a more precise description of processes where EW effects play a significant role. These contributions are also frequently included in certain POWHEG processes.

4.1.3 Hadronization and parton shower

The convolution of PDFs and MEs for a given process provides insight into the physics of the hard scatter. For example, by interfacing the MADGRAPH5_AMC@NLO generator with a specific PDF, one can generate events for the $t\bar{t}W$ process, which can be symbolically described as $pp \rightarrow t\bar{t}W$.

It is important to note that neither POWHEG and MADGRAPH5_AMC@NLO, despite their accuracy at the ME level, are able to fully describe a given observable. This is because they lack the functionality to model the entire spectrum of radiation that normally originates from the parton shower. In order to interface these effects in MC generators, a tool that allows for the direct modification, or extension of the information provided by the matrix elements, must be used. Such tools are often grouped as "parton shower" (PS) models. A PS model includes all sorts of effects that complete the range of physics covered in a given MC sample. The list of different effects that are typically handled in the PS step during MC generation is summarized in Figure 4.1.

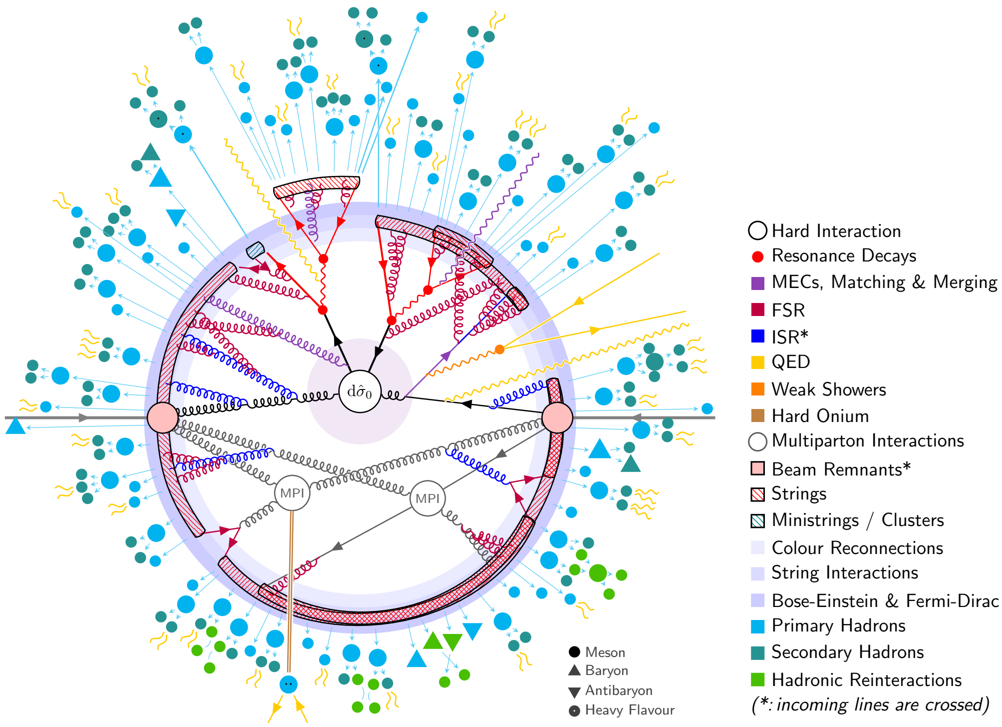

FIGURE. 4.1: [56] Schematic of the different processes that are normally modeled by PS models.

As a result, any process generated within these frameworks must be integrated into a PS. These PS generators account for soft (low energy) and collinear (very close to the particle that emmits the radiation) contributions, thus completing the predictions initially provided by the ME generators, which only cover the hard and non-collinear spectrum.

After a given ME is interfaced with a PS framework, the accuracy of the resulting observables that characterize a given process is promoted to F-LO + PS accuracy, where F stands for the amount of $\alpha_s$expansions taken in the perturbative QCD calculation. The achieved accuracy also depends on the configuration of the parton shower, which in the case of CMS relies on specific tuning settings, such as CUETP8M1 [57] and CP5 [58]. The tunings are normally derived based on ensuring good MC agreement in a $\mathrm{t\bar{t}}$ phase space, as the $\mathrm{t\bar{t}}$ observables such as its p_{T} or mass are sensitive to PS effects. Most of the MC samples used in this thesis are based on the CP5 tuning, while only a limited number of samples used for 2016 analyses employ the CUETP8M1 tuning.

4.2 Techniques used in MC generation

The ultimate goal of MC event generators is to predict the shape of a given observable at a differential level by generating events within a specified phase space, and integrating over all Feynman diagrams contributing to the process. The accuracy with which the predicted observables are represented is inherently limited by the precision of the generator itself. However, this accuracy is not guaranteed to be uniform across all observables. In particular, the precision of certain observables may be compromised due to the necessity of employing specific approximations in the calculations.

One of the most common examples of this effect arises in the interpretation of accuracy in NLO samples. The enhanced precision of NLO calculations compared to LO originates from the inclusion of additional higher-order corrections, which account for one-loop virtual corrections as well as real-emission contributions in some cases. In this context, inclusive observables are those that remain insensitive to the presence of additional emissions within a given phase-space region. An example of an inclusive observable in this case is the computation of cross-sections at different orders in QCD. The accuracy of these inclusive observables is generally well-controlled because the NLO calculation systematically ensures that divergences from the UV and the IR cancel once properly integrated over the final state. As a result, inclusive observables yield theoretical predictions with well-defined accuracy.

On the other hand, exclusive observables are explicitly sensitive to the presence or absence of additional radiation. These observables probe specific kinematic properties of the extra partons arising from real-emission corrections or those generated through parton showering. This discrepancy arises because the radiation contributions, which are necessary for NLO accuracy, can be distributed unevenly across phase space, leading to regions where approximations do not work properly. One of the most common examples of limitations regarding modeling the properties of the additional radiation is seen when looking at angular observables of very collinear radiation.

For instance, in the case of $\mathrm{t\bar{t}}$ generation within the MadGraph5_aMC@NLO framework, one would integrate the process following the syntax stated below,

```
generate p p > t t~ [QCD]
```

where the “generate” keyword will indicate to MadGraph5_aMC@NLO which process is to be integrated. The information that comes before the $>$ symbol indicates the initial state (pp), whereas the information after the $>$ symbol indicates the final state ($t\bar{t}$). The QCD keyword instructs MadGraph5_aMC@NLO to perform NLO calculations.

In this example, the total cross-section for the $pp \to t\bar{t}$ process is computed with full NLO accuracy by including: all LO contributions —known as the “Born” contributions—, the one-loop virtual corrections to the Born, as well as the real emission corrections to both. When interfaced with a PS, the framework ensures that the hardest radiation is picked from the NLO real emission matrix elements. Beyond this first emission, the parton shower performs resummation techniques to include contributions from additional soft and collinear emissions using leading-logarithmic (LL) accuracy, as implemented in frameworks like Pythia8. As a result, $t\bar{t}$ events with one jet in the final state receive NLO corrections from the matrix element, which are particularly relevant in the hard region of the jet p_T spectrum. In contrast, parton shower effects dominate in the soft region of the p_T spectrum and in narrower angular radiation distributions. The jet multiplicity distribution retains, however, full NLO+PS accuracy, as it correctly incorporates both real and virtual contributions in an inclusive manner.

The simultaneous usage of ME and PS accuracies is known as “matching matrix elements to parton showers”, and it is an extensively used technique in particle physics. This matching is performed internally using the MC@NLO formula in the case of the MadGraph5_aMC@NLO [54] samples. Similarly, it is also handled internally within the Powheg [51] framework for Powheg processes. All the samples used in this thesis are interfaced with Pythia8, although there are alternative choices such as Herwig or Sherpa that could also be used.

4.2.1 Multijet merging and matching

The accuracy of real emission contributions beyond just the hardest radiatio can be improved in frameworks such as MadGraph5_aMC@NLO by employing merging and improved matching techniques [59]. In this case, some ME contributions will receive NLO accuracy for additional real emissions, that can now be included as corrections to the 1-loop diagrams. This improves upon the accuracy of matched-only samples, which, as discussed earlier, can only guarantee NLO accuracy for inclusive observables.

One way to achieve this improvement in the case of $t\bar{t}$ production is by using the following syntax:

```
generate p p > t t~ [QCD] @0
add process p p > t t~ j [QCD] @1
```

Here, the second line instructs MadGraph5_aMC@NLO to also include real emission contributions beyond those incorporated in the one-loop amplitudes of the first Born process. A potential problem of double counting arises when considering the real emission terms in the one-loop amplitudes for @0 and the Born-level amplitudes for @1. To resolve this double counting, MADGRAPH5_AMC@NLO includes two algorithms specifically designed for this purpose: the MLM [60] algorithm for LO merged samples and the FXFX [59] algorithm for NLO merged samples. These matching and merging algorithms in MADGRAPH5_AMC@NLO effectively avoid double-counting between real emission terms from the ME and the PS. These techniques are of particular relevance to the modeling of the $t\bar{t}W$ process that will be covered in the following sections.

4.3 Modeling of the $t\bar{t}W$ and WZ signals

The use of MC generation techniques is fundamental for performing measurements, as it provides a systematic way to compare experimental data with theoretical predictions. These techniques are employed regardless of the specific scope or precision of the measurement. The reliability of any measurement is intrinsically tied to our understanding of the MC simulation; hence, it is essential to thoroughly understand the signal processes from the MC perspective as well.

Building upon the concepts introduced in the previous sections, this part now focuses on a more detailed discussion of the signal modeling for the processes under study in this thesis, namely the $t\bar{t}W$ and WZ production modes.

4.3.1 The $t\bar{t}W$ process

At LO in QCD, the contributions to the $t\bar{t}W$ account for approximately 56% of the total cross section. These contributions arise predominantly from quark-antiquark ($q\bar{q}$) annihilation diagrams, which are the only possible mechanisms for $t\bar{t}W$ production due to the electric charge of the W boson suppressing contributions from neutral initial states. As is common in many processes within the $t\bar{t}X$ family, NLO QCD corrections provide significant enhancements in the expected cross section. In particular, diagrams involving quark-gluon (qg) scattering begin to contribute at this order, increasing the total cross section by approximately 25%. At NNLO in QCD, two-loop contributions further enhance the cross section by an additional 12%, primarily due to the emergence of gluon-fusion diagrams, which are one of the dominant interaction mechanisms at the LHC due to the proton PDFs. Considering only QCD expansion terms, the total theoretical cross section for $t\bar{t}W$ production is predicted to be $\sigma_{t\bar{t}W} = 710.7 \pm 49$ fb.

These predictions are obtained considering only contributions that have a LO accuracy in the EW expansion. The impact of NLO EW corrections on $t\bar{t}W$ production has been extensively studied in the literature [61,62]. At this order, two distinct types of EW corrections are considered: leading and sub-leading contributions. The leading corrections, denoted as $\text{NLO}_{\text{EW}}^{\text{lead}}$, correspond to the next order in the EW coupling expansion relative to the LO QCD terms. These corrections reduce the $t\bar{t}W$ cross section by approximately 3%. The negative sign in these terms is primarily attributed to interference effects between EW loop corrections and the LO QCD contributions. On the other hand, the sub-leading corrections, denoted as $NLO_{EW}^{sublead}$, enhance the $t\bar{t}W$ cross section by approximately 10%. This significant increase arises from the appearance of tW scattering contributions, which are completely new to the calculation and therefore contribute positvely to the $t\bar{t}W$ cross section. Notably, these contributions are comparable in magnitude to the two-loop QCD corrections. A set of feynman diagrams contributing to the $t\bar{t}W$ cross section can be found in Figure 4.2.

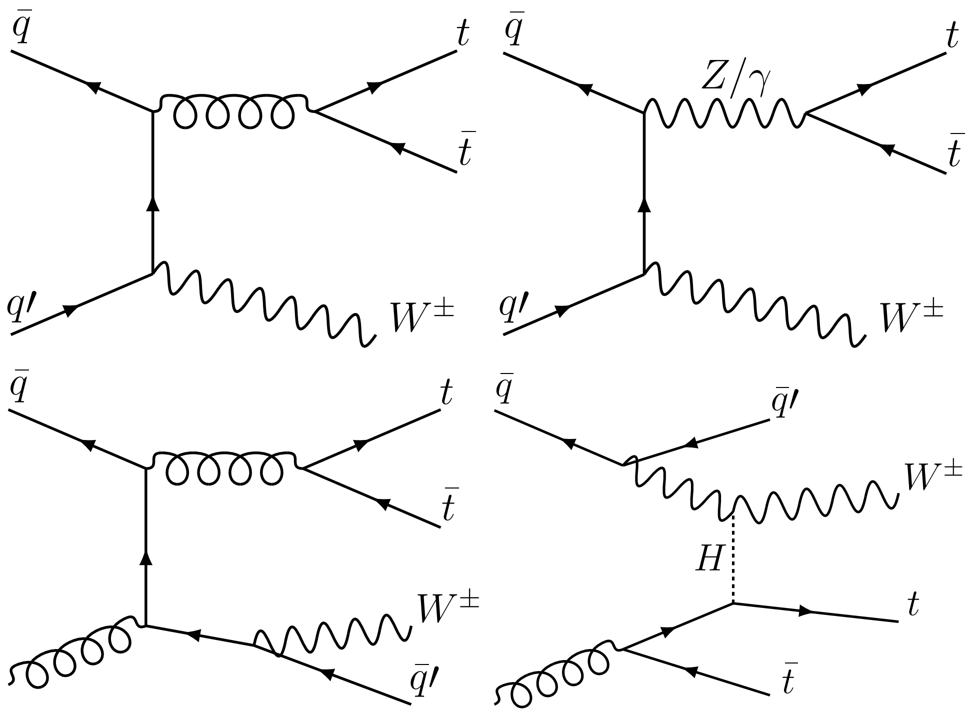

FIGURE. 4.2: [61] Representative Feynman diagrams for the LO QCD contributions to the $t\bar{t}W$ cross section are shown in the upper row, while the lower row represents the NLO QCD corrections. Additionally, the left diagrams display the LO EW contributions to the process, while the diagrams on the right illustrate the NLO corrections in the EW expansion. In particular, the diagram in the lower-right corner shows an example of the tW scattering contribution to the $t\bar{t}W$ process.

All in all, the state-of-the-art theoretical predictions for the $t\bar{t}W$ production cross section are known with remarkable precision. The cross section is computed at nearly NNLO accuracy in QCD, with the only missing contribution arising from the finite-part calculation of the two-loop corrections. This missing component is approximated using various methods, all of which yield consistent results. Additionally, the latest predictions incorporate NLO EW corrections [61, 62]. Including all the aforementioned terms, the predicted theoretical cross section for $t\bar{t}W$ is $\sigma_{t\bar{t}W} = 745.3 \pm 51$ fb [63], dominated by uncertainties due to the choice of renormalization and factorization scales.

In CMS, the $t\bar{t}W$ process is modeled at NLO in QCD using MADGRAPH5_AMC@NLO. The sample is generated with one extra emission in the matrix element, and the FXFX algorithm is used to properly account for possible double-counting effects. The syntax used for generating $\mathrm{t\bar{t}W}$ is shown below.

```
define ell+ = e+ mu+ ta+
define ell- = e- mu- ta-
define vll = ve vm vt
define vll~ = ve~ vm~ vt~

generate p p > t t~ ell+ vll [QCD] @0
add process p p > t t~ ell+ vll j [QCD] @1
add process p p > t t~ ell- vll~ [QCD] @2
add process p p > t t~ ell- vll~ j [QCD] @3
```

Where `ell+` and `ell−` refer to lepton final states. By using this syntax, all the non-resonant associated W contributions ttW are included in the modeling of $\mathrm{t\bar{t}W}$, without the need to approximate the decays, as in this case MADGRAPH5_AMC@NLO will compute all the matrix elements for $\mathrm{W}^{\pm} \to \ell^{\pm}\nu$. The decays of the top quarks are handled at LO using the MADSPIN package [64]. The decays are done inclusively, in order to include both the fully hadronic, semileptonic and multileptonic decay branchings for the $\mathrm{t\bar{t}}$ part of the $\mathrm{t\bar{t}W}$ process.

4.3.1.1 Improvements in the $\mathrm{t\bar{t}W}$ modeling

For the Run 2 analyses, the $\mathrm{t\bar{t}W}$ sample is modeled using version 2.6.5 of the MADGRAPH5_AMC@NLO generator. The predicted cross section for $\mathrm{t\bar{t}W}$ within this version, computed at NLO accuracy, is approximately 50% smaller than the predicted NNLO cross Section [63]. Even when including full parton shower resummation effects with fixed-order techniques from [65], the predicted cross section deviates notably from both the measurements and the NNLO predictions. In 2021, an improved version of the FXFX algorithm was released for MADGRAPH5_AMC@NLO versions beyond 3.3.0 [66]. This updated FXFX merging and matching procedure was specifically developed to include previously missing contributions in the $\mathrm{t\bar{t}W}$ process.

In qualitative terms, the new FXFX algorithm addresses an inaccuracy observed when merging $\mathrm{t\bar{t}W}$ samples at NLO accuracy in earlier versions of MADGRAPH5_AMC@NLO. Specifically, a discontinuity was identified at the merging scale, μ_{Q}, which determines how contributions are split between the ME and the PS. This discontinuity was reported by theorists and is illustrated in Figure 4.3.

At high values of μ_{Q}, the jet p_{T} spectrum displayed a discontinuity precisely at the scale in which the jet p_{T} was equal to the chosen μ_{Q}, leading to inconsistencies in the modeling of $\mathrm{t\bar{t}W}$. The initial workaround was to set a very low value for μ_{Q}, which effectively hid the discontinuity in a region dominated primarily by the PS effects. However, using low values of μ_{Q} resulted in unstable results, as the soft p_{T} spectrum of the hardest emission is typically not well modeled within MADGRAPH5_AMC@NLO.

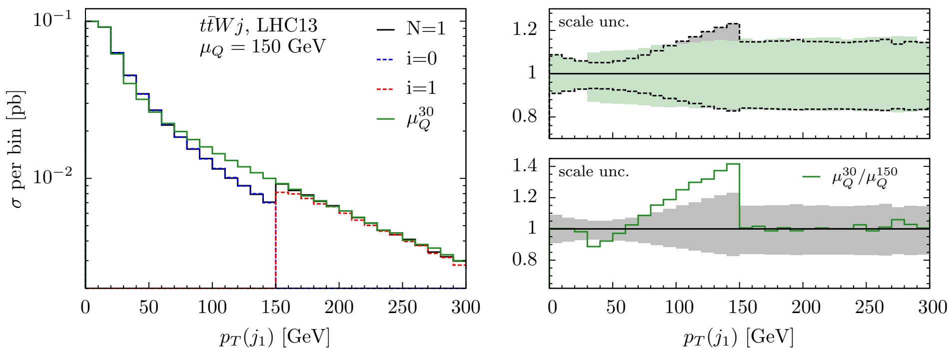

FIGURE. 4.3: [66] Differential distribution of the leading jet transverse momentum in a $t\bar{t}$W sample merged using the FXFX scheme with a merging scale of μ_Q = 150 GeV (left panel). The plot shows the complete prediction for the jet p_T in the case of the merged sample (N=1), as well as considering the lowest and highest jet multiplicity borns (i=0 and i=1, respectively). The ratio plots from the right show a comparison with the same distribution obtained using μ_Q = 30 GeV. The samples used for this comparison are generated with all resonances kept stable, and with hadronization and underlying event effects disabled. The matching and merging of matrix element and parton shower are performed using the FXFX prescription.

4.3.1.2 Implementation of the new FXFX procedure in CMS simulation

The problematic effect can be reproduced in the CMS $t\bar{t}$W sample by taking the same considerations as in Ref [66]. To do so, a $t\bar{t}$W sample in which resonances corresponding to the two top quarks and the W boson are kept stable is generated. In addition,both the hadronization and underlying event effects are disabled in the PS step to facilitate the study of just the radiation included in the ME. Jets are then clustered using the k_T algorithm with a cone parameter of $R = 1$, consistent with the clustering used in the FXFX matching procedure. Since any other additional radiation effect from the PS is turned off, the clustered jets should carry the same information as used in the FXFX matching.

Two generated samples are considered, each matched using a different value of μ_Q: 42 GeV, the standard value adopted by CMS for $t\bar{t}$W modeling, and 150 GeV, the default μ_Q value used by the theoretical authors. The results are shown in Fig. 4.4 for the distribution of the leading jet p_T, which is one of the main observables in which problems were observed. In the sample matched with μ_Q = 150 GeV, a clear discontinuity is observed at the merging scale. In contrast, the sample matched with μ_Q = 42 GeV shows no visible discontinuity, indicating a smoother merging between matrix element and parton shower contributions.

The discontinuity observed in the leading jet p_T spectrum was found to originate from an incomplete treatment of additional radiation in the $t\bar{t}$W process. In this process, extra radiation can arise either from standard QCD emissions attached to colored partons, or from EW emissions, where a W boson is radiated off one of the initial or final-state

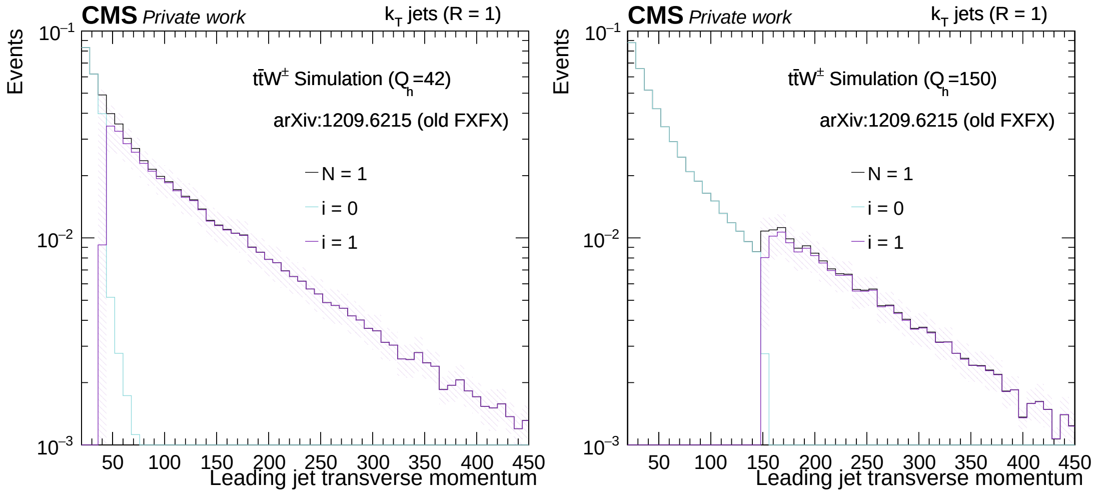

FIGURE. 4.4: Differential distribution of the leading jet transverse momentum in a $t\bar{t}W$ sample merged using the FXFX scheme with a merging scale of μ_Q = 42 GeV (left) and μ_Q =150 GeV (right). The plot shows the complete prediction for the jet p_T in the case of the merged sample (N=1), as well as considering the lowest and highest jet multiplicity borns (i=0 and i=1, respectively). The samples used for this comparison are generated with all resonances kept stable, and with hadronization and underlying event effects disabled. The matching and merging of matrix element and parton shower are performed using the FXFX prescription. These samples have been obtained using the CMS generation interface to MADGRAPH5_AMC@NLO.

partons. The latter type of emission is not accounted for by the parton shower, as most parton shower algorithms are designed to handle only QCD radiation. It was observed that when these EW contributions —which were IR due to the mass of the W boson— were being included as part of the matching in previous versions of the FXFX matching to the PS. By removing these jets from the matching, the discontinuity in the jet p_T spectrum was mitigated. Properly incorporating these EW radiations in the modeling of the $t\bar{t}W$ process ultimately resulted in a predicted cross section consistent with NNLO expectations.

The leading jet p_T distribution obtained using the improved FXFX matching scheme is shown in Figure 4.5. These results mirror those of Figure 4.4, except that the samples were generated using the updated FXFX implementation. This improved configuration was integrated into the CMS MC production workflow as part of the MC validation work developed during this thesis. In this updated setup, the discrepancy previously seen in the sample merged with μ_Q = 150 GeV has been significantly reduced. Additionally, contributions below the merging scale indicate the presence of EW radiation, which, in the older FXFX implementation were not properly accounted for. These effects are less prominent in the μ_Q = 42 GeV sample, as previously discussed, due to the lower merging scale pushing discontinuities into a region of phase space dominated by parton shower effects. The results shown here are consistent with the findings presented in Ref. [66].

Very high values of μ_Q may negatively affect the overall modeling of $t\bar{t}W$, since in

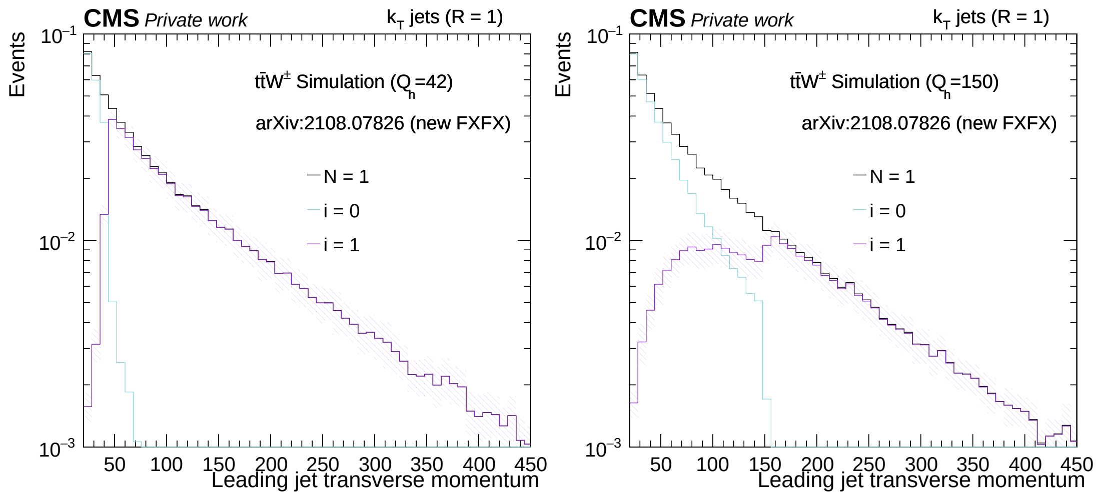

FIGURE. 4.5: Same distribution as Figure 4.4, this time considering the improved FXFX merging scheme.

that case, the bulk of the jet p_T—typically around 50 GeV in LHC collisions— would be modelled at LL accuracy by the PS, rather than at the higher accuracy achievable by MADGRAPH5_AMC@NLO. Conversely, low μ_Q values can obscure the impact of weak radiation in a kinematic regime where their contributions are significant. Therefore, it is crucial for experiments to carefully determine the μ_Q value that best fits $t\bar{t}W$ production data. Within CMS, a coordinated effort is, which will influence the future full Run 3 $t\bar{t}W$ measurement, has started.

4.3.1.3 Further validation at inclusive level

In addition to the problems in the prediction of the jet p_T spectrum, the previous FXFX modeling produced inconsistent results with large variations depending on the choice of the μ_Q scale. This issue was also resolved with the new FXFX modeling, where the predicted cross sections became more stable with respect to μ_Q. The evidence for this corrected behavior is shown in Figure 4.6, where the predicted cross sections for both the old and new FXFX implementations, within the CMS MC production framework, are compared.

The predictions shown correspond to the inclusive $t\bar{t}W$ production cross section, with the quoted uncertainties reflecting only the statistical component. Theoretical uncertainties, primarily due to scale variations, range from 7–9%, depending on the chosen merging scale. When using the updated FXFX implementation integrated into the CMS production workflow, the predicted cross sections exhibit a stable behavior consistent with the results presented in Ref. [66]. Slight differences in the overall normalization of the sample can be attributed to the different choice of PDFs between the CMS implementation and the one from the theorists. A much more pronounced non-stability of the predicted cross section when using the old FXFX, particularly at higher values of the merging scale, is also shown. These findings align well with the observations reported in

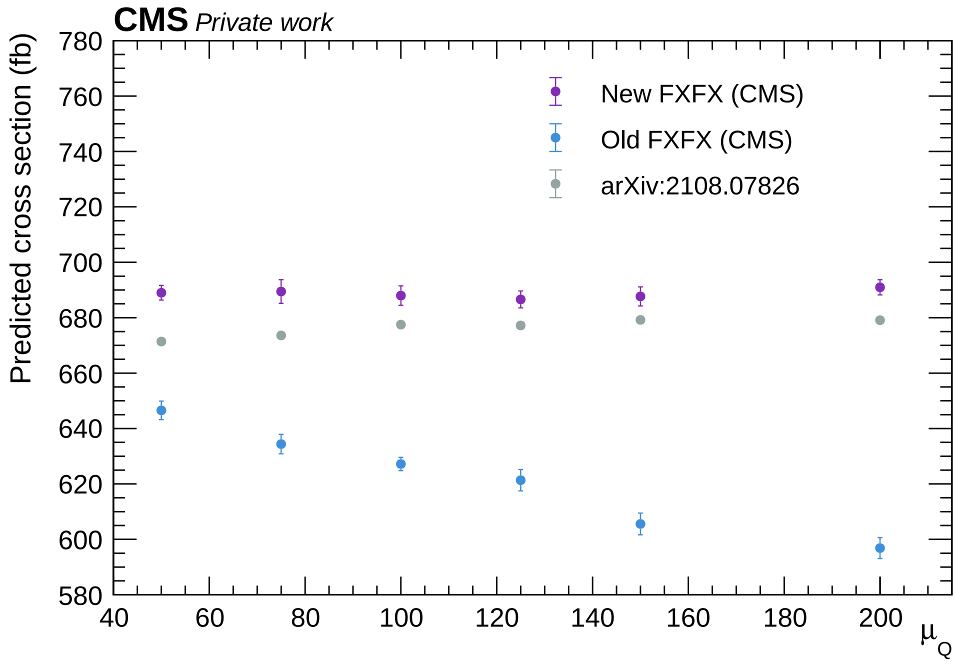

FIGURE. 4.6: Inclusive cross section predicted within MADGRAPH5_AMC@NLO considering the two available models for $\mathrm{t\bar{t}W}$. The predictions obtained using the CMS interface for generation, considering the old FXFX prediction (blue points), and the new FXFX (purple points). A comparison with the theoretical results reported in the theoretical paper (gray points) is also shown. The cross sections are in addition computed as a function of the μ_{Q} scale choice, ranging from 42 GeV (default value in CMS) up to 200 GeV. The uncertainties in these numbers do not account for theoretical sources, as the purpose is to compare the central values alone

the theoretical study.

4.3.1.4 Validation studies at the decay level

We further test the performance of the new $\mathrm{t\bar{t}W}$ modeling versus the old FXFX in final state topologies at the decay level. In this case, the goal is to reproduce the selection requirements from Ref. [66]. To do this, the nominal CMS configuration of the $\mathrm{t\bar{t}W}$ sample is considered. We produce four different samples, one for each tested value of μ_{Q} $\in$ $[42, 150]$ GeV, and each version of the FXFX algorithm. We check the difference at the generator level for several distributions. The most relevant ones can be found in Figure 4.7.

At the decay level, the results obtained using the different matching schemes do not exhibit significant discrepancies within the assigned theoretical uncertainties, which are predominantly driven by the choice of renormalization and factorization scales. However, these results are not yet fully conclusive. Further validation studies are currently ongoing as part of a coordinated effort between the CMS and ATLAS collaborations, with the goal of achieving a more comprehensive understanding of the impact of the updated FXFX implementation at this stage of the modeling.

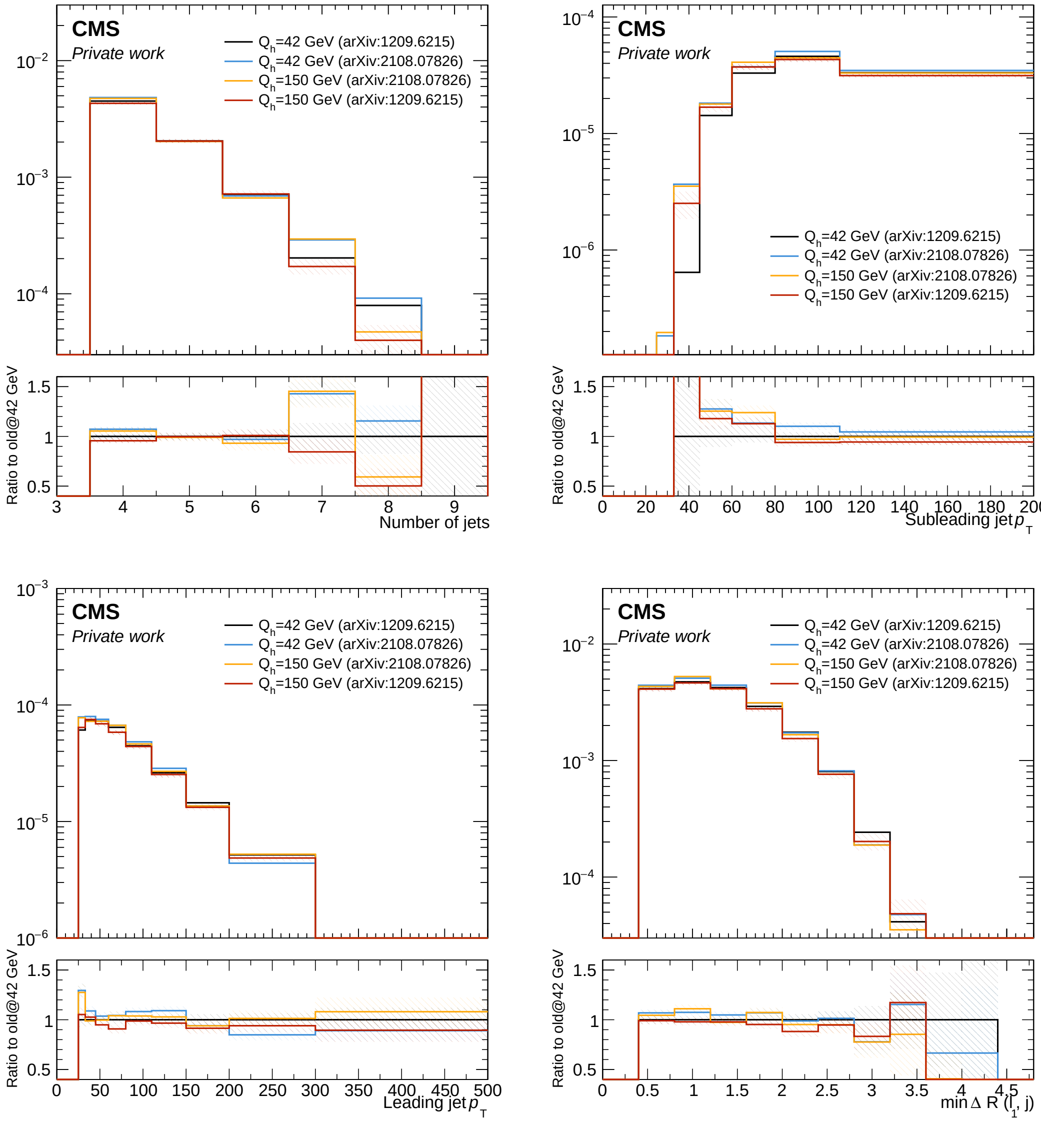

FIGURE. 4.7: Several observables at particle level for the fully generated $t\bar{t}\ell\nu$process, following a particle-level definition equivalent to that used in the theoretical paper. The distributions shown include: the jet multiplicity (upper left), transverse momentum of the leading jet (upper right), transverse momentum of the subleading jet (lower left), and the minimum ΔR distance between the leading lepton and any reconstructed jet in the event (lower right). Results are presented for two different merging schemes: the original and the improved FXFX prescriptions, each with two merging scale choices: μ_Q = 42 GeV and μ_Q = 150 GeV. The lower ratio panels display all distributions divided by the prediction obtained with the original FXFX setup and μ_Q = 42 GeV.

4.3.2 EW corrections to $t\bar{t}W$

In addition to the sample discussed previously, which models the bulk of the $t\bar{t}W$ spectrum by considering several expansions of the QCD perturbation series, $t\bar{t}W$ also receives significant contributions from EW processes. Specifically, the effects from the $\text{NLO}_{\text{EW}}^{\text{lead}}$ and $\text{NLO}_{\text{EW}}^{\text{sublead}}$ contributions must be taken into account.

The inclusion of the $\text{NLO}_{\text{EW}}^{\text{lead}}$ contribution can only be done at fixed order, as it is currently not possible to implement matching with the parton shower. Therefore, these contributions are incorporated as an initial normalization factor for the $t\bar{t}W$ process. On the other hand, the $\text{NLO}_{\text{EW}}^{\text{sublead}}$ contributions are modeled within MadGraph5_aMC@NLO at NLO accuracy in QCD, without additional parton merging. The full process is described below:

```
define ell+ = e+ mu+ ta+
define ell- = e- mu- ta-
define vll  = ve vm vt
define vll~ = ve~ vm~ vt~

generate p p > t t~ ell+ vll QCD=0 QED=4 [QCD] @0
add process p p > t t~ ell- vll~ QCD=0 QED=4 [QCD] @1
```

Here, the keywords `QCD=0 QED=4 [QCD]` instruct MadGraph5_aMC@NLO to include only LO terms in QCD and NLO terms in the EW expansion. Note that, because the sample is produced considering leptonic decays of the associated W boson, the leading order in this case is $\alpha_s\alpha^4$ instead of $\alpha_s\alpha^3$, as found in the literature for the case where the $t\bar{t}W$ process is not decayed. The additional α coupling arises from the decay of the W boson.

4.3.3 The WZ process

Similarly to the $t\bar{t}W$ process, the presence of a charged W boson in WZ production imposes constraints on the possible initial-state partons at LO in QCD. In particular, the LO diagrams are similarly dominated by $q\bar{q}$ annihilation channels, as gluon-initiated processes are absent at this order due to charge conservation.

As is common in diboson production, the WZ cross section receives sizable corrections from higher-order contributions, both in QCD and EW perturbation theory. Theoretical predictions for WZ production cross section have significantly improved over the years, and the inclusive cross section is currently known up to NNLO in QCD, complemented by NLO corrections in the EW expansion [67]. These higher-order contributions are essential for achieving a reliable prediction of the cross section, as they account for substantial effects such as soft and collinear QCD radiation, virtual loop corrections, and resummation effects in the EW sector, which become increasingly relevant at high energies. Moreover, the inclusion of NLO EW corrections is particularly important for precision measurements, as they can lead to negative contributions of several percent in certain regions of phase space, especially in the high-p_{T} tails of the vector boson spectra. Some diagrams contributing to the WZ process at LO, NLO, and NNLO used in the theoretical calculation of the WZ cross section can be found in Figure 4.8.

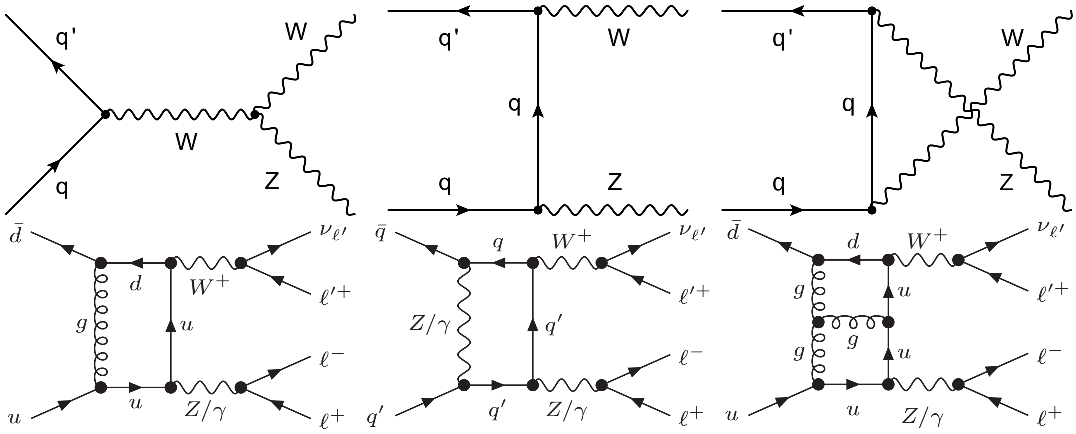

FIGURE. 4.8: Top row: Leading-order Feynman diagrams for WZ production in pp collisions from the s channel (left), t channel (center), and u channel (right). Bottom row: diagrams for the NLO QCD (left), NLO EW (center) and NNLO QCD (right) contributions to the WZ cross section.

These effects are crucial to consider when comparing theoretical predictions with data from Run 3, where experimental precision begins to reach the level of theoretical uncertainties. The accurate modeling of WZ production is also vital for probing anomalous triple gauge couplings (aTGCs) and for providing background estimates in searches for BSM physics.

4.3.3.1 Modeling of the WZ process

The most accurate MC prediction currently available within CMS for the WZ production process is based on calculations performed within the POWHEG [50–52,68,69] framework. This generator provides an NLO-accurate description of the hard scattering process, and is interfaced with PYTHIA8 for modeling of the PS.

In the generation of the WZ sample used in this thesis, the W and Z bosons are allowed to decay leptonically in a way that preserves full spin correlations in the decay products, which are important to proper modeling of angular correlations between the leptons. The factorization and renormalization scales are set in a dynamic way, by choosing event-by-event k_T scale proportional to the transverse mass of the diboson system. Electroweak corrections are not included in the event generation of this sample.

An alternative signal modeling based on MADGRAPH5_AMC@NLO is also available. In this case, the sample was generated including the full off-shell contributions of the WZ decays, thereby accounting for both resonant and non-resonant components. The generation was performed at NLO accuracy with FXFX multijet merging and matching, incorporating contributions with up to one additional jet. The older version of the FXFX scheme was used for this sample. It was employed solely to cross-check the dependence of the measurements presented in Chapter 7 on the choice of signal modeling.

Recently, the WZ process was implemented at NNLO QCD within the POWHEG framework by means of the Multi-scale Improved Next-to-Next-to-Leading Order (MiNNLO) method [70], which is a state-of-the-art approach for precision predictions in perturbative QCD, combining NNLO accuracy in total cross sections. It builds upon the POWHEG formalism by introducing a dynamic scale setting procedure and that allows to include higher-order corrections. This allows to generate fully exclusive events with NNLO accuracy for inclusive observables and improved modeling of soft and collinear emissions when considering parton shower interface with MECs. As a result, it provides a reliable and consistent interface between fixed-order calculations and parton shower simulations, making it particularly well-suited for precision measurements and new physics searches at the LHC. In addition to these, NLO EW accuracy is also achived for this new modeling of WZ.

The MiNNLO WZ sample is not yet available within CMS, as its release is relatively recent [71]. However, validation studies aimed at incorporating this process into the set of WZ modeling tools used by CMS are currently ongoing, and are part of the WZ-related contributions presented in this thesis. At present, the sample has not been fully integrated into the CMS framework due to computational limitations, as generating such high-precision processes is computationally intensive. Nonetheless, preliminary validation studies have been performed using events from Ref. [71], which were kindly provided by the authors. To initiate comparisons with the default CMS POWHEG sample, these events were showered using parton shower configurations specific to CMS.

So far, the validation studies have been about technicalities in the generation, such as making sure that the events could be properly matched to the PS interface available in CMS. A comparison of the invariant mass distributions for the dilepton and trilepton systems in WZ $\to 3\ell$ decays is presented in Figure 4.9, showing the first comparison of the two samples in the context of CMS MC generation.

Each distribution is normalized to the fiducial cross section of the samples, so normalization effects are included in the comparisons as well. The fact that the overall rate from MiNNLO is larger than the one from the POWHEG prediction is in line with the expected differences between NNLO and NLO predictions.

There is still significant work to do on this regard, but the first steps towards the implementation of the state-of-the-art MC modeling for WZ have been started as one of the main features of this thesis.

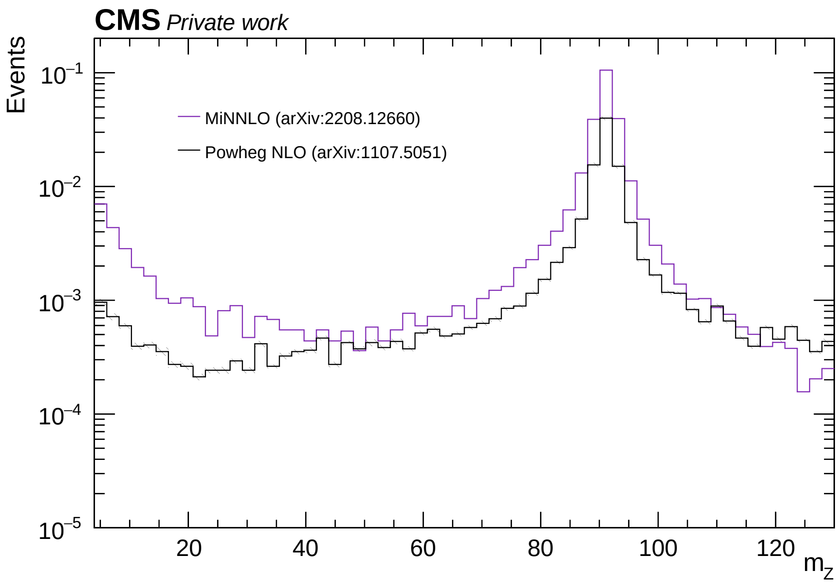

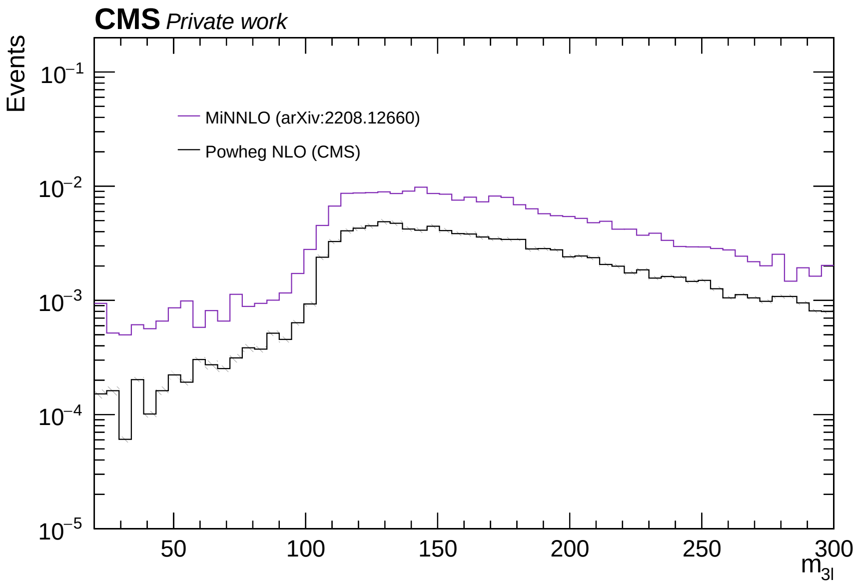

FIGURE. 4.9: Distribution of the line shapes (invariant masses of different composition of leptons) for the WZ multileptonic final states. The upper plot shows the mass spectrum for the Z resonance, whereas the bottom plot shows the invariant mass of the 3ℓ system, which is used as a proxy for the true mass of WZ. The MINNLO events, showered with the CP5 PS tuning used in CMS are shown in the purple line, and the nominal POWHEG prediction is shown as a black line. The uncertainties shown in the distributions account only for the ones arising from scale variations. Each distribution is normalized to its own fiducial cross section, so normalization effects between the two distributions are expected.

4.4 Monte Carlo production in CMS

As briefly introduced in Section 4.1, MC generation in high-energy physics is one of the most essential components of modern experimental analyses. Not only does it provide a crucial tool for comparing experimental data with theoretical predictions, but it also plays a fundamental role in the interpretation of results. This aspect has gained increasing relevance within the community as the precision of measurements at experiments such as CMS continues to improve. In many cases, the dominant limitations of these measurements arise from theoretical uncertainties directly connected to MC modeling. Moreover, feedback from the experimental community to MC developers is of great importance, as it fuels the continuous development of these simulation tools.

In the following pages, a detailed description of MC production within the context of the CMS collaboration, as well as a summary of my contributions to it, is presented.

4.4.1 Monte Carlo Production overview

The procedure to obtain a MC sample for data analysis in CMS starts with a formal request to the group responsible for producing the sample. The production of MC samples is typically organized according to the final state topology considered at the matrix element level, exploiting the expertise that different members of the several groups in CMS have. For instance, the generation of final states involving top quarks is usually handled by experts within the TOP group, while processes involving associated production with Higgs bosons are managed by the HIG group. Samples that predominantly cover EW phase spaces, such as WZ or ZZ, are generally produced by the Standard Model Physics group. Other scenarios, including Beyond the Standard Model (BSM) processes or less commonly used final states, are managed by other dedicated groups within CMS; however, these are less relevant in the context of this thesis.

In addition, all requests are coordinated and overseen by the generator (GEN) group of CMS, which holds broad expertise in the different physics groups. The GEN group ensures consistency and quality in the production of MC samples across the collaboration, supervising the contributions from all specialized teams. The Physics Data and Monte Carlo Validation group (PDMV) group is in charge of overseeing the production from the computing perspective.

As a member of the CMS collaboration, and given the central role that MC generation plays in all CMS results, I have been deeply involved in MC production activities within the collaboration. My primary responsibility has been serving as coordinator of the Top Modeling Group (TMG) in CMS, which operates within the TOP physics group. This group has contributed to the release of more than 150 publications on top-quark properties since the start of CMS. In addition, I have been one of the three members of the *common MC background* team, which is a group that cooperates with the GEN and PDMV groups, and it is in charge of coordinating the specific production of commonly used MC samples for Run 3 analyses. In addition, I have been candidate for the role of coordinator of the GEN and PDMV groups.

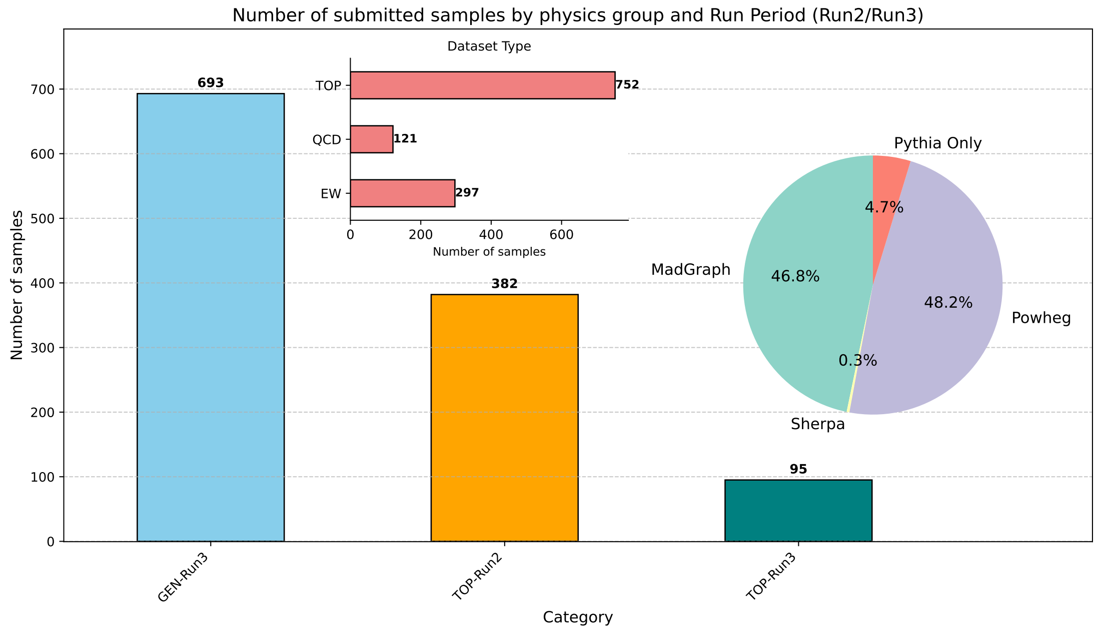

FIGURE. 4.10: Summary plot representing the total number of MC requests I have delivered to the collaboration. The main canvas displays a vertical bar graph, showing the distribution of requests split by dataset and physics group. Additionally, a horizontal bar graph, shown as an inset within the canvas, presents the breakdown by final state topology. A pie chart inset complements the figure by illustrating the fraction of requests according to the MC generation software employed.

Over the two years dedicated to this effort, I have not only worked as a coordinator, but I have also produced more than 1100 samples that are actively used by the collaboration. Breaking down the MC requests according to the target phase space, 752 of these correspond to TOP-like topologies, such as $\mathrm{t\bar{t}} + \mathrm{X}$ (where X denotes any particle except for a Higgs boson) and single top production modes. Approximately 100 samples focus on multijet final states (QCD), which are heavily used by groups to derive corrections on object identification, while nearly 300 are dedicated to EW final states, including processes such as WZ, ZZ, and Drell—Yan. Considering the distribution by dataset, and in line with the period when I joined the MC generation efforts in CMS, approximately 70% of my work has been dedicated to the production of Run 3 MC samples, and around 30%, has focused on providing physics samples for Run 2 analyses. Regarding MC generators, most of the samples I have produced were generated using POWHEG or MADGRAPH5_AMC@NLO, as these are the two most widely employed generators for TOP physics within CMS. A summary of my work in terms of MC generation is shown in Fig. 4.10.

5 Analysis techniques and the CMS dataset

5.1 Data quality issues

The operation of the detector is occasionally affected by issues that arise during data taking. Some of these problems arise from malfunctions within the data acquisition system, detector electronics, or human errors, while others originate from external factors such as power losses, leaks inside the CMS cavern, or other environmental conditions. Regardless of their origin, these issues impact data quality and must be accounted for during analysis. Despite these challenges, the CMS detector has operated smoothly throughout Run 2 and Run 3, and the issues discussed in this section do not compromise the overall quality of the recorded data.

5.1.1 Electron prefiring effects in Run 2

Due to the high number of pileup interactions in pp collisions, the innermost parts of the detectors are exposed to a harsh radiation environment. For this reason, detectors such as the tracker are constructed from radiation-resistant materials that, in principle, can maintain good performance even after years of data taking. However, outer detectors such as the calorimeters are generally less resilient to radiation and are therefore more susceptible to performance degradation due to ageing effects. In many cases, specific ageing studies are conducted to develop new methods for mitigating these effects, which are always present. Some of these ageing studies are discussed in Section 8.1.

In the case of the $PbWO_4$ crystals that form the ECAL, this material tends to lose its transparency, which is crucial for efficient electron and photon signature identification. As a result, increased noise levels in the detector can lead to spurious signals that trigger the L1 electronics prematurely. These noisy channels can interfere with the L1 reconstruction, causing incorrect timing assignments to reconstructed objects. This effect, known as "prefiring," leads to an efficiency loss ranging of a few percent in certain critical regions of the ECAL. Although other objects such as the muons can also lead to prefiring, the most problematic prefiring issue in Run 2 originated because the problems in the ECAL.

Since 2018, frequent updates to the detector timing have significantly mitigated this effect, reducing it to nearly negligible levels. Such effects are, in any, case included in the Run 2 analyses, particularly in the 2016 and 2017 data taking years, in which the prefiring effect was not corrected by default.

5.1.2 ECAL leakages during Run 3

During September 2022, an issue with high voltage in the power supply of the positive side of the endcap ECAL was reported. After investigation, it was determined that a leak had occurred in one of the cooling circuits of the ECAL supply system. As a result, approximately 7% of the ECAL channels had to be shut down, as the elevated voltage readings could significantly impact data collection in regions that, in principle, should not have been affected by the leakage. Until the faulty electronic component was identified and repaired, the ECAL channels directly affected by the leak remained off.

This effect was observed during data taking and, consequently, was not included in the simulations available at the time for data analysis. As a result, the MC simulations need to be corrected to remove electrons that could have been reconstructed in the problematic region of the detector. A correction method was developed by electron reconstruction experts and is applied to all Run 3 measurements that include the 2022 dataset.

In data, the effect of the leakage can be observed by examining the region with the affected crystals. This is illustrated in Figure 5.1, which shows the reconstructed electron distributions in $|\eta|$ and ϕ for two parts of the 2022 dataset—one from the first period (unaffected by the leakage) and another from the period affected by the leakage.

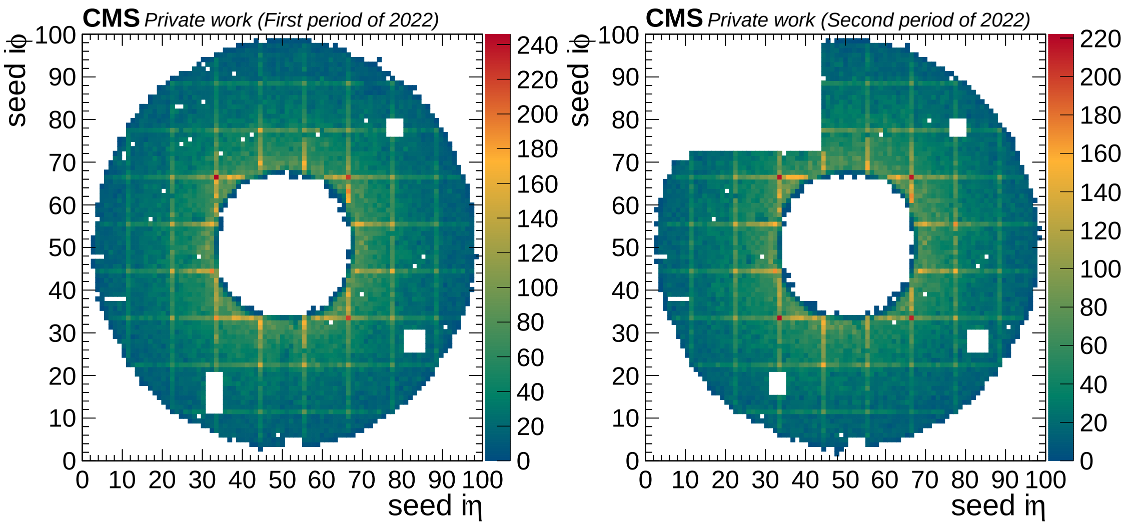

FIGURE. 5.1: Two-dimensional distributions of the position of the clusters in $|\eta|$ and ϕ in data in arbitrary units.

The affected region is also illustrated in Figure 5.2, which presents two-dimensional distributions of the reconstructed electron η and ϕ in simulation. As shown, only a limited region of the second period of 2022 is affected.

An additional consequence of this issue is the division of the 2022 dataset into two parts, separated by the time at which the leakage occurred.

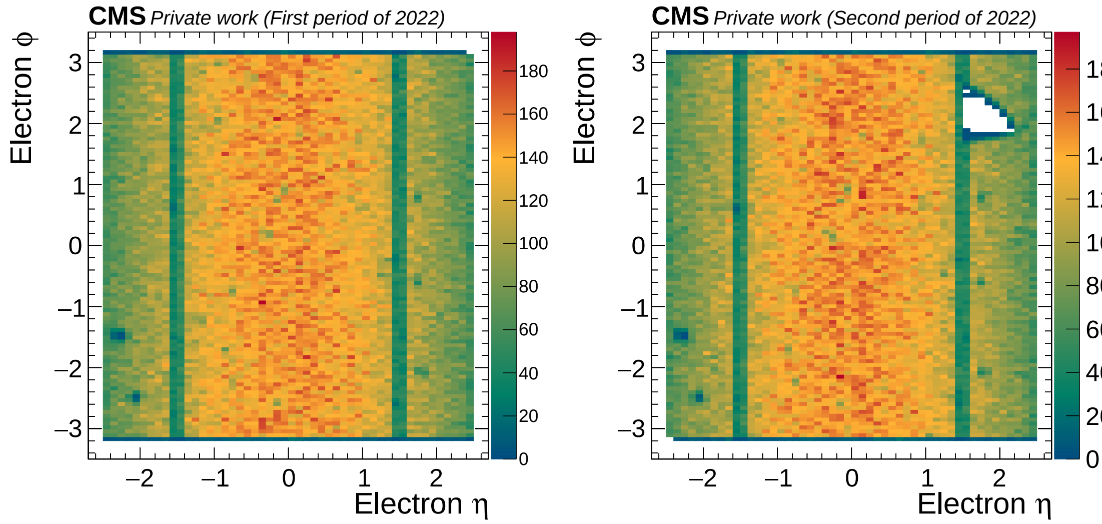

FIGURE. 5.2: Two-dimensional distributions of the reconstructed electron $|\eta|$ and ϕ in simulation for the first period of 2022 (left) and the second period of 2022 (right). Only the second part of 2022 is affected by this issue, and therefore the affected region is removed from the simulation.

5.1.3 Jet vetoes in Run 3

Additional issues were reported in the calorimeters during the second period of 2022 data taking that lead to inefficient performance of the calorimeters. These calibration effects are corrected by vetoing specific jets that have been reconstructed in "hot" zones of the detector, where the anomalous behaviour was observed. Figure 5.3 shows the result of applying these corrections in a MC simulation of WZ, for the first and second period of the 2022 data taking. As observed, only a relatively small region of the detector is affected by this issue, and the overall jet performance during Run 3 remains high.

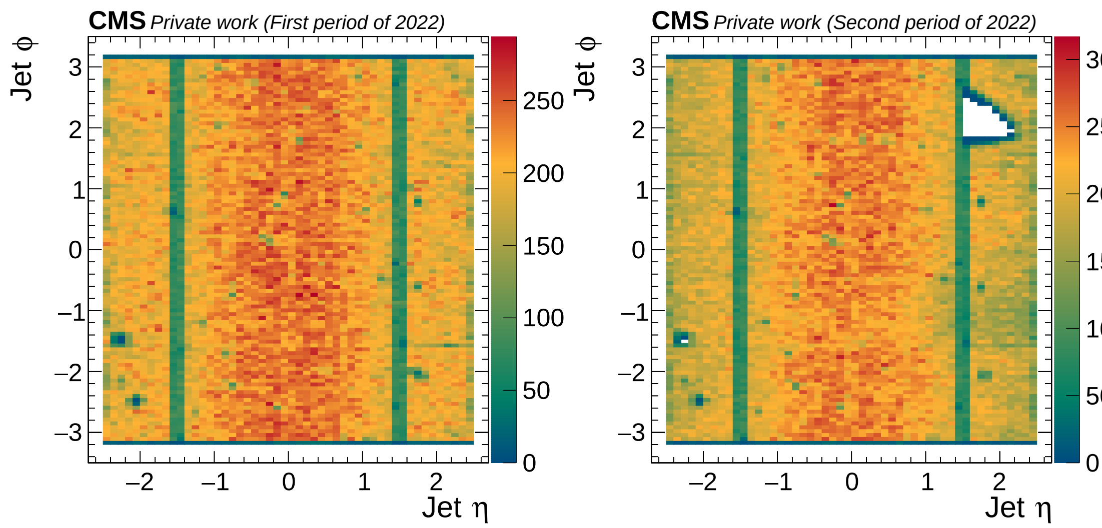

FIGURE. 5.3: Two dimensional representation of the reconstructed jet η and ϕ, including the veto maps used to account for the innefective areas of the HCAL. The plots correspond to the first (left) and second (right) periods of the 2022 data taking.

5.2 Object identification in Run 2 and Run 3

Because the requirements imposed by the trigger system and the offline reconstruction, described in Sections 3.4.1 and 3.4.2, are often based on simple conditions applied to a few kinematic properties of the reconstructed objects, these criteria are not always suitable for precision measurements. In contrast, it is necessary to distinguish between very similar processes, which requires exploiting subtle differences in the kinematics of the objects involved. Therefore, more refined selection strategies are typically employed at the analysis stage to enhance the sensitivity to the specific processes under study.

In this section, the detailed analysis strategies in terms of object identification are discussed. This chapter sets the baseline to perform the measurements that will be presented in the chapters.

5.2.1 Triggering on final states with multiple leptons

In Section 3.4.1, the concept of triggering was introduced as a key component of the data acquisition system in high-energy physics experiments such as CMS, which are required to handle the inherently large particle multiplicities produced in pp collisions. As a consequence, the trigger system plays a crucial role in selecting the most relevant events for further analysis. Events not selected by the trigger are permanently discarded, which implies that the design and performance of the trigger system directly influence the physics reach of the experiment.

In both data and simulation, all events contain boolean flags indicating whether a given event has fired a specific L1 and HLT path. Since HLT paths can only be activated if the corresponding L1 seed has been satisfied, the design of trigger selections at the analysis level typically focuses on choosing the HLT paths that maximize the efficiency for the targeted signatures. Although L1 seeds are a fundamental part of the trigger logic, their role in defining the final event selection is often less critical from an analysis perspective, as the primary constraints and efficiencies are usually determined by the HLT paths.

The analyses presented in this thesis focus on final states containing at least two leptons, commonly referred to as "multilepton" phase spaces. For such analyses, the HLT paths typically employed require the presence of at least one lepton (e, μ, or τ), subject to specific kinematic constraints on observables such as transverse momentum (p_{T}) and pseudorapidity (η). In addition to these kinematic selections, many HLT paths also impose quality requirements based on lepton isolation, which quantify how well-separated a lepton is from other particle candidates in the event. It is important to note that the list of triggers is often updated from year to year of data taking, resembling the continuous development of the trigger strategy in CMS.

The detailed list of triggers used, separated by data taking period, in the analyses presented in this thesis is provided in Table 5.2.1. In particular, the triggers listed under the Run 2 column are those employed in the analysis of the $t\bar{t}W$ process properties, presented in Chapter 6, whereas the set of triggers under the Run 3 column has been used in the measurement of the inclusive WZ production cross section, discussed in Chapter 7.

Table 5.2.1: Summary of HLT paths used in Run 2 and Run 3. A checkmark (✓) indicates the presence of the corresponding path in a given year.

Trigger group	HLT Path	Run 2			Run 3
		2016	2017	2018	2022
Single e	Tight e, $p_T^e > 27$ GeV	✓			
	Loose e, $p_T^e > 25$ GeV,$\|\eta\| < 2.1$	✓			
	Tight e, $p_T^e > 32$ GeV		✓	✓	✓
	Tight e, $p_T^e > 35$ GeV		✓		
Single μ	Isolated μ, $p_T^\mu > 24$ GeV	✓	✓	✓	✓
	Isolated μ, $p_T^\mu > 22$ GeV	✓			
	Isolated μ, $p_T^\mu > 22$ GeV,$\|\eta\| < 2.1$	✓			
	Isolated μ, $p_T^\mu > 27$ GeV		✓		
Double e	Two loose e, $p_T^e > 23, 12$ GeV	✓	✓	✓	✓
Double μ	Two isolated μ, $p_T^\mu > 17, 8$ GeV	✓			
	Two isolated μ, $p_T^\mu > 17, 8$ GeV, $\mathrm{m}_{\mu\mu} > 8$ GeV		✓		
	Two isolated μ, $p_T^\mu > 17, 8$ GeV, $\mathrm{m}_{\mu\mu} > 3.8$ GeV		✓	✓	✓
$e\mu$	Loose e and isolated μ, $p_T^e > 23$, $p_T^\mu > 8$ GeV	✓			
	Loose e and isolated μ, $p_T^e > 8$, $p_T^\mu > 23$ GeV	✓			
	Loose e and isolated μ, $p_T^e > 12$, $p_T^\mu 23$ GeV		✓	✓	✓
	Loose e and isolated μ, $p_T^e > 23$, $p_T^\mu > 12$ GeV		✓	✓	
Triple lepton (e, μ)	Three loose e, $p_T^e > 16, 12, 8$ GeV	✓	✓	✓	✓
	Three loose μ, $p_T^\mu > 12, 10, 5$ GeV	✓	✓	✓	✓
	Two loose e, one loose μ, $p_T^e > 12, 12, p_T^\mu > 8$	✓	✓	✓	✓
	Two loose μ, one loose e, $p_T^\mu > 9$ GeV, $p_T^e > 9$ GeV	✓		✓	✓

The logic of the trigger system is implemented using boolean logic. Events are selected if and only if at least one of the multiple HLT paths under consideration has been flagged as true by the trigger system. It is possible for a single event to simultaneously satisfy the requirements of multiple HLT paths. A typical example is an event containing one electron and one muon, both with p_T well above the thresholds imposed by the corresponding HLT paths. In such cases, the trigger system will flag both triggers as true. Since data events are stored in separate datasets according to which triggers have been activated, the same event may appear in multiple datasets. To prevent double counting, it is therefore essential to define a hierarchy among the triggers, ensuring that each event is assigned to a unique category. This procedure is commonly referred to as "overlap removal" and is systematically applied in the analyses to avoid event duplication.

An important consequence of this effect is that the overall efficiency of the full set of triggers employed in a given analysis must be explicitly evaluated. The trigger selection efficiency for each analysis presented in this thesis is discussed in the corresponding chapters. A comparison of trigger efficiencies between the 2018 and 2022 datasets is shown in Figure 5.4. The efficiency is measured using a simulation of the $WZ \to 3\ell + \nu$ process. For both datasets, the combined trigger set achieves an overall efficiency of more than 99% in the plateau.

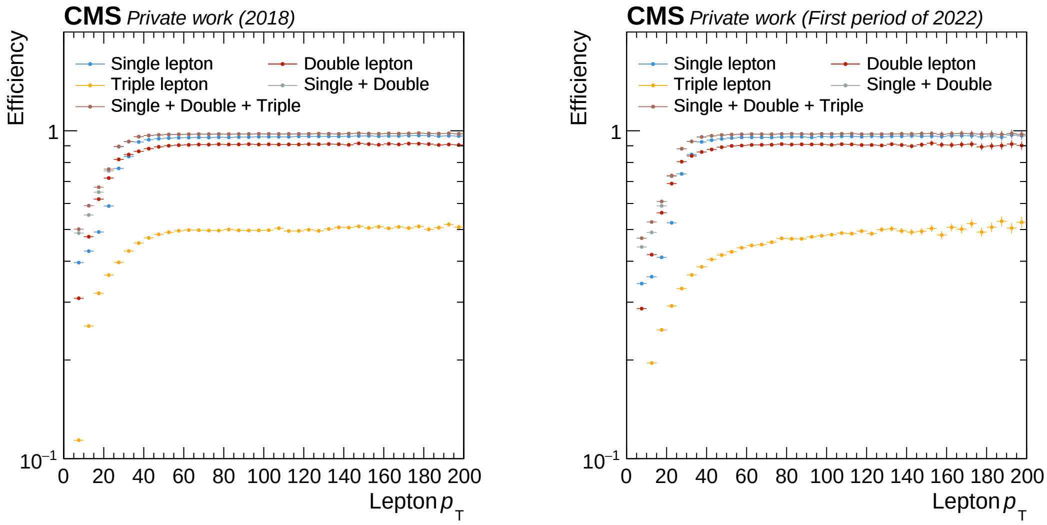

FIGURE. 5.4: Measured efficiency for different trigger selections as a function of the lepton p_T, estimated from MC simulation with 2018 (left) and 2022 (right) conditions. The total efficiency corresponds to the Double+Single+Triple lepton lines, and it is computed as the logical OR of all the different triggers. The efficiency per group of trigger is also shown with different colors in the plot.

5.2.2 Jets and flavour-tagging

Jets are incredibly useful objects for data analysis. Not only do they carry relevant information about the processes that occurred at the interaction point, but they also serve as a crucial handle for distinguishing between different processes that may exhibit varying properties, such as the expected jet multiplicity. As a result, applying minimal kinematic criteria to jets is often necessary to enhance the quality of those jets used in further analysis.

Beyond these minimal criteria, it is also important to identify the types of particles that contributed to their formation. The techniques used for this purpose are collectively known as *flavour-tagging* techniques and play a key role in many analyses. In CMS, flavour-tagging techniques are primarily focused on identifying jets originating from the production of a b-quark during a collision. This is because B-mesons, due to their relatively large mass, can travel a measurable distance before decaying. The CMS vertexing system can distinguish this displacement by identifying two distinct vertices along the particle's trajectory. This characteristic feature is one of the primary handles exploited by b tagging algorithms.

Over the years, the b-tagging experts of the CMS collaboration have developed multiple b tagging models. Some of these models, such as DEEPCSV [72] and DEEPJET [73], were extensively used throughout Run 2, while others, including ROBUSTPARTICLETRANSFORMER [74] and PARTICLENET [75], were developed in the more recent context of Run 3 data taking. All these algorithms are based on multivariate analysis (MVA) techniques, which correlate multiple input features to characterize the properties of the jets, with the target of assigning an score that represents how likely it is for the jet to be originating from a b quark.

The evolution of the performance of different b tagging algorithms used in the CMS experiment is summarized in Figure 5.5. The performance is evaluated using the Receiver Operating Characteristic (ROC) curve, which illustrates the probability of misidentifying a non-b jet as a b jet (Y-axis) versus the probability of correctly identifying a b jet as such.

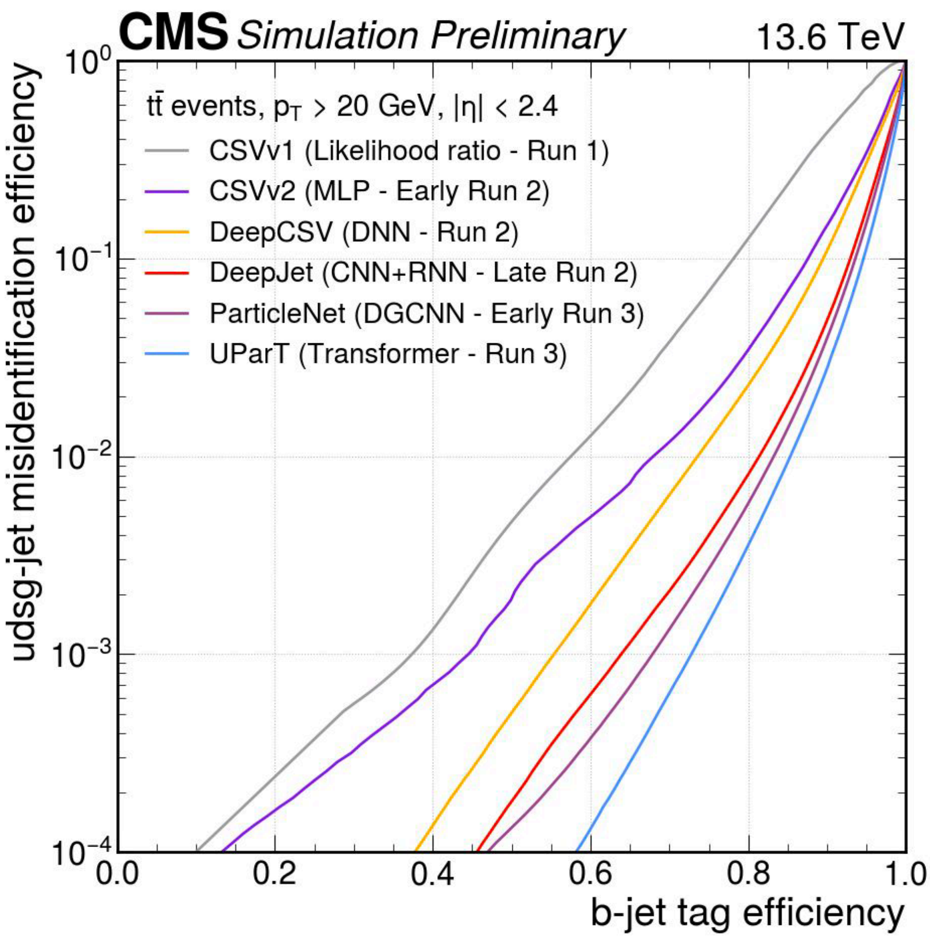

FIGURE. 5.5: [76] Evolution of b-tagging performance for jet flavor identification algorithms used in CMS since Run 1. In particular, the DEEPCSV and DEEPJET taggers are the primary algorithms used in this thesis.

These curves are commonly used as a reference to define an operating working point (WP) that ensures an approximately fixed signal and background efficiency. Any jet whose b tagging score is greater than the defined WP will be classified as b tag, and will be treated as if it were originated from a b jet. Table 5.2.2 summarizes the jet identification criteria, and b tagging WPs used in the two analyses that are presented in the following chapters. In addition to the criteria listed in the above paragraphs, jets that are within a cone of $\Delta R < 0.4$ with respect to a lepton are removed from the event.

	Criteria	Run 2	Run 3
Jets	Reconstruction algorithm	CHS	PUPPI
	p_T [GeV]	> 25	> 25
	$\|\eta\|$	< 2.5	< 4.7
	Minimum distance with any lepton	> 0.4	> 0.4
	PF quality	*Tight*	*Tight*
B tags	Identified as jet	✓	✓
	$\|\eta\|$	-	< 2.5
	B tagging algorithm	DEEPJET	DEEPJET
	B tagging WP	*Loose* or *Medium*	*Tight*

Table 5.2.2: Selection criteria for jets and b tags for the Run 2 and Run 3 analyses separately. The criteria for the b tags is only applied to identified jets. For b tags, a $-$ symbol indicates that no further requirement is applied, for those cases in which the selection criteria can overseed some of the requirements used on the jet object.

5.2.3 Lepton MVA for Run 3

The lepton selection is based on a MVA model known as the lepton MVA, a method extensively employed in several CMS Run 2 analyses, including the legacy results for the $t\bar{t}H$ [77] and WZ [78] processes. In particular, the strategy and performance of muon identification in Run 2 simulations have been documented in [79]. Due to its excellent performance, the lepton identification used in the $t\bar{t}W$ and WZ measurements, has also been based on this approach.

As the latter is performed using new data from 2022, the strategy was updated to accommodate the improvements in lepton reconstruction introduced since the version of the lepton MVA used in the legacy Run 2 results. This updated version of the MVA was particularly developed for the WZ measurement, and it is one of the main contributions that this thesis has provided to Run 3 object identification. This strategy presented in this section is now being used as a reference strategy in Run 3 analyses [80], and will be used in future Run 3 measurements of the CMS experiment.

5.2.3.1 Definition of prompt and nonprompt

Before delving into the details of lepton identification, it is important to emphasize that lepton identification relies on the premise that a given analysis targets a specific type of "signal" lepton, while aiming to avoid the selection of "background" leptons. Although the distinction between signal and background leptons can be somewhat diffuse and analysis-dependent, this classification is typically associated with the origin of the lepton. Leptons with signal-like properties are commonly referred to as "prompt" leptons, whereas those not produced through the same mechanisms as signal leptons are referred to as "nonprompt" leptons.

In the context of multilepton analyses, prompt leptons are normally defined as those originating from the decay of a W boson, Z boson, hadronic taus (τ_{h}), or H boson. Consequently, any lepton not produced in a prompt manner is referred to as a nonprompt lepton. Examples of nonprompt leptons include non-isolated leptons from heavy-flavour decays (such as B and C-hadrons), leptons from light hadron decays (such as pions or kaons), or hadrons that have been misidentified as leptons. The lepton identification used in analysis is therefore optimized to maximise the presence of prompt leptons over that of nonprompt leptons.

While nonprompt leptons have a well-defined physical origin, their presence in analyses primarily arises from the difficulty of distinguishing them from prompt sources. However, certain kinematic differences can be exploited to mitigate contamination from such backgrounds. This is illustrated in Figure 5.6, which shows the distributions of p_{T} and η for electrons and muons in a $\mathrm{t\bar{t}}$ simulation, where the total contribution is decomposed according to the origin of the leptons. As evident from these distributions, nonprompt leptons predominantly populate the low-p_{T} and high-η regions, distinguishing them from the prompt contribution.

A precise characterization of nonprompt leptons is a central challenge in any analysis, regardless of the number of selected leptons. Therefore, in the following pages details on how the lepton identification techniques have been optimized for the analyses presented in this thesis are given.

5.2.3.2 The prompt lepton MVA

The prompt lepton MVA, or simply lepton MVA, is a Machine Learning (ML) approach for lepton identification based on a Boosted Decision Tree (BDT). The model is trained using semileptonic $\mathrm{t\bar{t}}$ MC simulations, which simultaneously provide a source of both prompt and nonprompt leptons. This is achieved by matching reconstructed leptons to generator-level particles, exploiting the expected event topology: a prompt lepton originating from the $t \to \mathrm{W}b$ decay, two additional jets from the other top-quark decay, and possible initial- and final-state radiation (ISR/FSR) jets.

If the lepton from the $\mathrm{t\bar{t}}$ decay is properly reconstructed, it can be matched to its generator-level counterpart. However, in cases where the prompt lepton is lost due to misreconstruction, other leptons may still pass the selection criteria but remain unmatched to any generator-level particle. This matching strategy allows for a clear separation between prompt and nonprompt leptons, enabling a reliable training sample for the MVA.

Two different lepton MVAs are trained: one for electrons and another one for muons. The BDTs are trained using a preselection of leptons that must satisfy minimal identification criteria. The preselection imposes minimal kinematic requirements on the p_{T} and pseudorapidity η of the leptons, along with additional conditions ensuring that the tracks used for lepton reconstruction originate from the primary vertex. Since prompt leptons

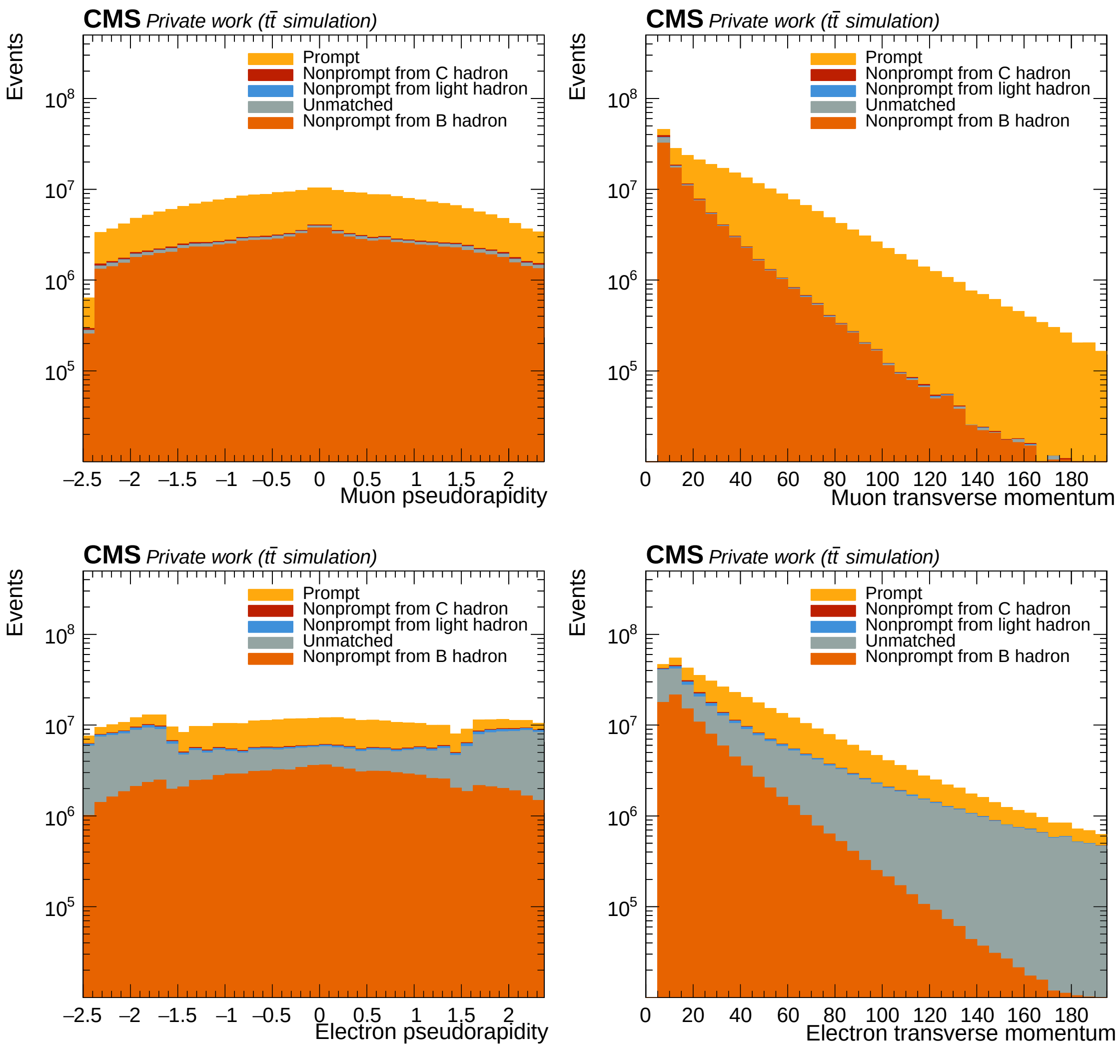

FIGURE. 5.6: Distribution of kinematic properties of the leptons split by their origin: prompt leptons, nonprompt leptons from B hadrons, nonprompt leptons from C hadrons, nonprompt leptons from light hadrons, and unmatched leptons. The unmatched category refers to cases where no generator-level particle is found to match with a reconstructed lepton. From upper left (muon η), upper right (muon p_{T}), lower left (electron η), and lower right (electron p_{T}). The plots are shown using $\mathrm{t\bar{t}}$ simulation, and the split is based on generator level information. No preselection of leptons has been included in these plots.

are expected to be isolated, in contrast to nonprompt leptons, which are typically accompanied by a jet, isolation is one of the most relevant variables for distinguishing between the two.

In this context, isolation is defined based on the sum of the scalar p_{T} of different charged and neutral particles reconstructed in the event. It is given by equation 5.1, where $\mathcal{R}$ denotes the cone size around the reconstructed lepton, ρ represents the energy density of neutral particles reconstructed within the tracker, and A is the effective area of the cone. The parameter $\mathcal{A}$ is extracted from simulation by studying the correlation between I_{ℓ} and ρ.

$$I_\ell = \sum_{\text{charged}} p_{\mathrm{T}} + max\left(0, \sum_{\text{neutrals}} p_{\mathrm{T}} - \rho \mathrm{A}\left(\frac{\mathcal{R}}{0.3}\right)^2\right) \tag{5.1}$$

A summary of all the quality requirements applied to preselected leptons is provided in Table 5.2.3.

	Electrons		Muons	
Criteria	Run 2	Run 3	Run 2	Run 3
p_{T} [GeV]	> 5	> 10	> 5	> 10
$\lvert\eta\rvert$	< 2.5	< 2.5	< 2.4	< 2.4
$\lvert d_{xy}\rvert$ [cm]	< 0.05	< 0.05	< 0.05	< 0.05
$\lvert d_z\rvert$ [cm]	< 0.1	< 0.1	< 0.1	< 0.1
d/σ_d	< 8	< 8	< 8	< 8
$I_\ell < 0.4 \times p_{\mathrm{T}}$	✓	✓	✓	✓
Missing hits	< 2	< 2	$-$	$-$
PF ID	*loose*	-	*medium*	*medium*

Table 5.2.3: Preselection criteria for electrons and muons in Run 2 and Run 3 analyses. Entries with a dash ($-$) mean that the selection was not included in the corresponding case.

The input variables used for the training include the lepton p_{T} and η, as well as the charged and neutral components of I_ℓ (first and second terms in equation 5.1). Additional variables account for the kinematic and identification properties of the lepton, such as the ratio of its transverse momentum and the nearest jet. The characteristics of the matched jet are also considered, including the b-tagging discriminant, and the number of charged particles within the jet. Furthermore, the training incorporates variables related to track impact parameters, such as the transverse and longitudinal impact parameters of the lepton track with respect to the PV and the signed three-dimensional impact parameter significance, d/σ_d. Additionally, in the case of muons, the compatibility of track segments in the muon system with the expected pattern of a minimum ionizing particle is also used. Some of the most discriminant observables used in the training are shown in Figure 5.7.

The discriminant resulting from the training performed for the Run 3 updated strategy is shown separately for muons and electrons in Figure 5.8. As observed in these distributions, the separation power achieved with this strategy allows for the definition of a working point of the lepton MVA that can reduce significantly nonprompt lepton contamination at analysis level.

The performance of the retrained lepton MVA was also compared to the previous version, as shown in Figure 5.9. The performance is evaluated using ROC curves, which illustrate the signal efficiency, defined as the probability of correctly identifying a prompt lepton, versus the background efficiency; that represents the probability of correctly identifying background leptons as such. Additionally, three alternative lepton selection strategies, widely used within the collaboration, are included in the comparison. These are re-

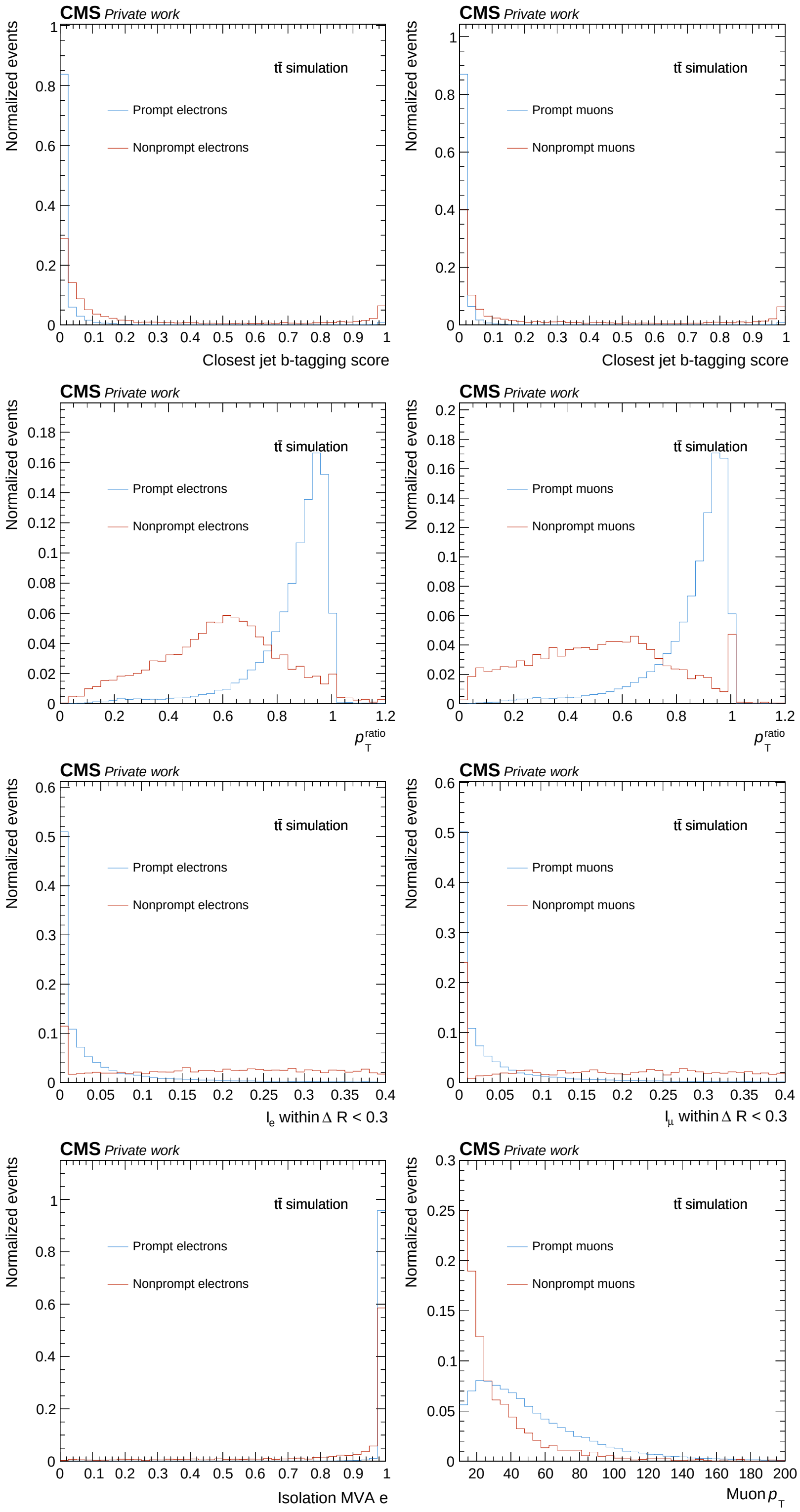

FIGURE. 5.7: Normalized distributions of the input variables used for the training of the prompt lepton MVA, considering the four leading input variables on each training. Plots in the left column show the distributions for the electron lepton MVA training, whereas distributions in the right column account for input variables of the muon lepton MVA. The contributions of the $t\bar{t}$ sample used for the training are splitted by the origin of the reconstructed leptons that are used in the training based on the generator level information.

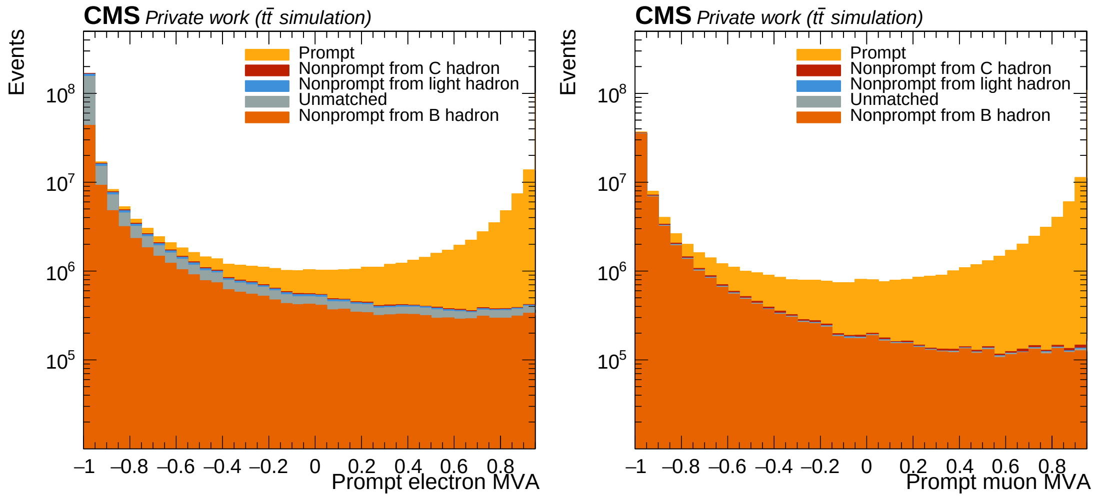

FIGURE. 5.8: Distribution of the MVA score for electrons (left) and muons (right), using $t\bar{t}$ simulation. The whole $t\bar{t}$ sample is split using generator-level information in terms of their origin: prompt leptons, nonprompt leptons from B hadrons, nonprompt leptons from C hadrons, nonprompt leptons from light hadrons, and unmatched leptons. The coloured histograms represent the different processes considered, stacked one top of each other. These plots include the preselection from Table 5.2.3 in order to be aligned with the preselection used for the training.

ferred to as the "cut-based" selectors. Unlike MVA-based approaches, cut-based selectors rely on sequential requirements imposed on lepton properties without employing a multivariate analysis. Since these selectors operate as boolean classifiers, their performance is measured only in terms of standalone signal and background efficiencies. The ROC curves for the prompt lepton MVA in both Run 2 and Run 3 are computed using only preselected leptons, as defined in Table 5.2.3.

As shown by the ROC curves, the retrained lepton MVA shows improved performance compared to the legacy version for both muons and electrons. A significant enhancement in prompt electron identification is achieved with the retrained model. This improvement arises from the fact that the Run 3 simulation used in the retraining incorporates a more accurate matching of prompt electrons. In previous versions, electrons that had radiated high energy photons were not always correctly classified as prompt. By including these electrons in the training, the lepton MVA recovers approximately 20% more signal efficiency on average, at the same background efficiency, a substantial improvement.

5.2.4 Lepton identification

The strategy for lepton identification relies on the lepton MVA approach described in the previous section. The lepton selection is built on top of the preselection requirements of the lepton MVA training, detailed in Table 5.2.3. The goal for these requirements is to reduce as much as possible the nonprompt lepton contamination at analysis level, while ensuring the highest signal efficiency possible. The detailed requirements for electrons

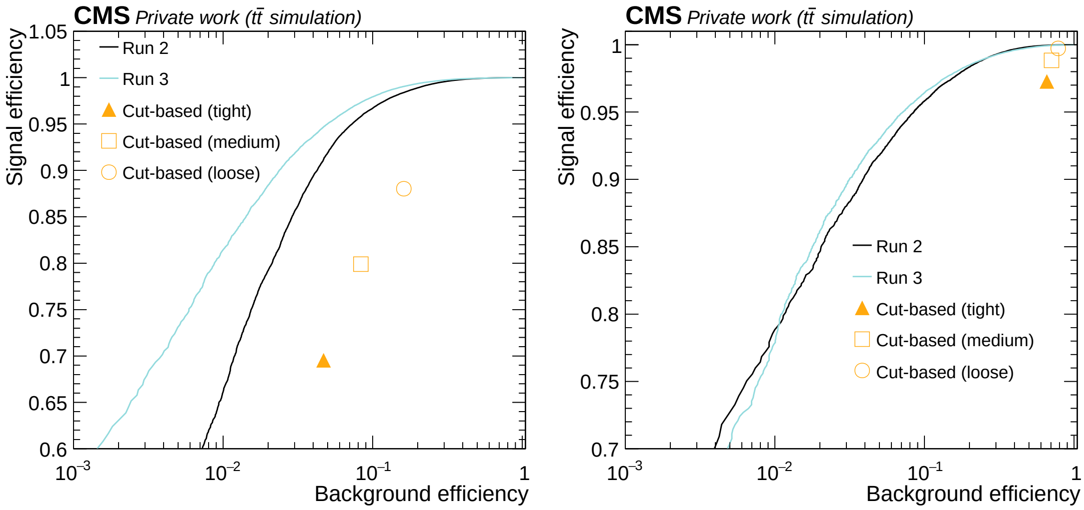

FIGURE. 5.9: Performance ROC curves comparing the previous version of the lepton MVA (black line) with the retrained version for Run 3 (light blue line) for electrons (left) and muons (right). Additionally, the performance of alternative lepton selection strategies in CMS is shown as points, representing the signal and background efficiencies for identifying prompt and nonprompt leptons. No event preselection is applied for these alternative strategies to ensure a fair comparison.

and muons in the Run 2 and Run 3 lepton definitions can be found in Table 5.2.4. In the case of the prompt MVA requirement for Run 2, two values of the WP were considered in different analyses. The smaller value of the lepton MVA focuses on maximizing signal efficiency, at the cost of also enhancing the presence of backgrounds; while the higher value is used for analyses that aim to supress the contributions from the background as much as possible.

This selection criterion ensures a very high prompt selection efficiency while maintaining a stable nonprompt selection rate of less than 10^{-2}. The signal efficiency corresponding to this nonprompt rate is 82% for preselected muons in Run 2 and 83% for preselected muons in Run 3. For preselected electrons, the efficiencies are 41% in Run 2 and 63% in Run 3. An exception occurs in the differential measurements of the $t\bar{t}W$ process, where the efficiency is also 63%, even thoough the measurement is performed with the Run 2. This improvement is due to a similarly retrained lepton MVA in Run 2, which was not available at the time of the inclusive cross-section measurement. The details will be discussed in the corresponding chapters.

5.2.5 Object identification in $t\bar{t}W$ and WZ

The efficiency and performance for object identification studies is generally measured in fixed phase spaces, which are useful for deriving corrections and evaluating efficiencies. Since the processes studied in this thesis differ from those typically used for this purpose, this section aims to reproduce some of the performance studies developed by object experts, using MC simulations of the $t\bar{t}W$ and WZ processes. The goal is to assess

Table 5.2.4: Selection criteria for electrons and muons in Run 2 and Run 3 analyses. Entries with a dash (−) mean that the selection was not included in the corresponding case. In the case of the prompt MVA requirement for Run 2, two values of the WP were considered in different analyses.

	Electrons		Muons	
Criteria	Run 2	Run 3	Run 2	Run 3
Is *loose*[1]	✓	✓	✓	✓
$\sigma_{i\eta i\eta}$	< { 0.011 / 0.030 }[2]	< { 0.011 / 0.030 }[2]	−	−
H/E	< 0.10	< 0.10	−	−
1/E - 1/p	> -0.04	> -0.04	−	−
Conversion rejection	✓	✓	−	−
Missing hits	< 1	< 1	−	−
Deep Jet of nearby jet	<WP-medium[3]	<WP-medium[3]	<WP-medium[3]	<WP-medium[3]
Jet relative isolation[3]	< 0.7	< 0.7	< 0.5	< 0.5
Lepton prompt MVA	$> 0.80/0.40$	> 0.90	$> 0.85/0.4$	> 0.64

[1] According to Table 5.2.3
[2] First number indicates the requirement for leptons in the barrel, wheras the second one for leptons in the endcaps.
[3] As defined by the CMS b tagging group.

the degree of extrapolation assumed when applying these techniques to other processes. In general, this extrapolation is not large, and therefore the techniques are found to be applicable.

5.2.5.1 Lepton identification

For prompt lepton identification, the physics of the involved leptons is relatively similar across WZ, $\mathrm{t\bar{t}}$, and $\mathrm{t\bar{t}W}$. This is because, in all three processes, prompt leptons originate from the decay of an on-shell W or Z boson, resulting in comparable p_{T} spectra. However, slight differences in the performance of the lepton MVA might be expected due to variations in the relative isolation of these leptons. In top-quark-related processes such as $\mathrm{t\bar{t}}$ and $\mathrm{t\bar{t}W}$, the higher jet multiplicity leads to increased hadronic activity around the leptons, making their isolation slightly different from that in WZ events. Additionally, in the specific phase spaces considered in these analyses, the origin of nonprompt leptons can also impact overall performance. These aspects will be discussed in detail in the corresponding chapters.

5.2.5.2 Flavour tagging

The b-tagged jets from $\mathrm{t\bar{t}W}$ are typically similar to those from $\mathrm{t\bar{t}}$, meaning that the b-tagging efficiencies measured in $\mathrm{t\bar{t}}$ and $\mathrm{t\bar{t}W}$ do not differ significantly. This similarity arises because in both cases the leading b quarks identified in the analysis originate from the decay of a top quark into a W boson and a b quark, which is the primary decay mode of the top quark. In contrast, b quarks in WZ events usually originate from gluon radiation in the initial state, which subsequently decays into a pair of b quarks ($g \to \mathrm{b\bar{b}}$).

As a result, the b tagging performance in $t\bar{t}$ and WZ differs significantly. This effect can be observed in Figure 5.10, which shows the b tagging performance in terms of correct identification versus misidentification for the three considered processes: $t\bar{t}$, $t\bar{t}W$, and WZ.

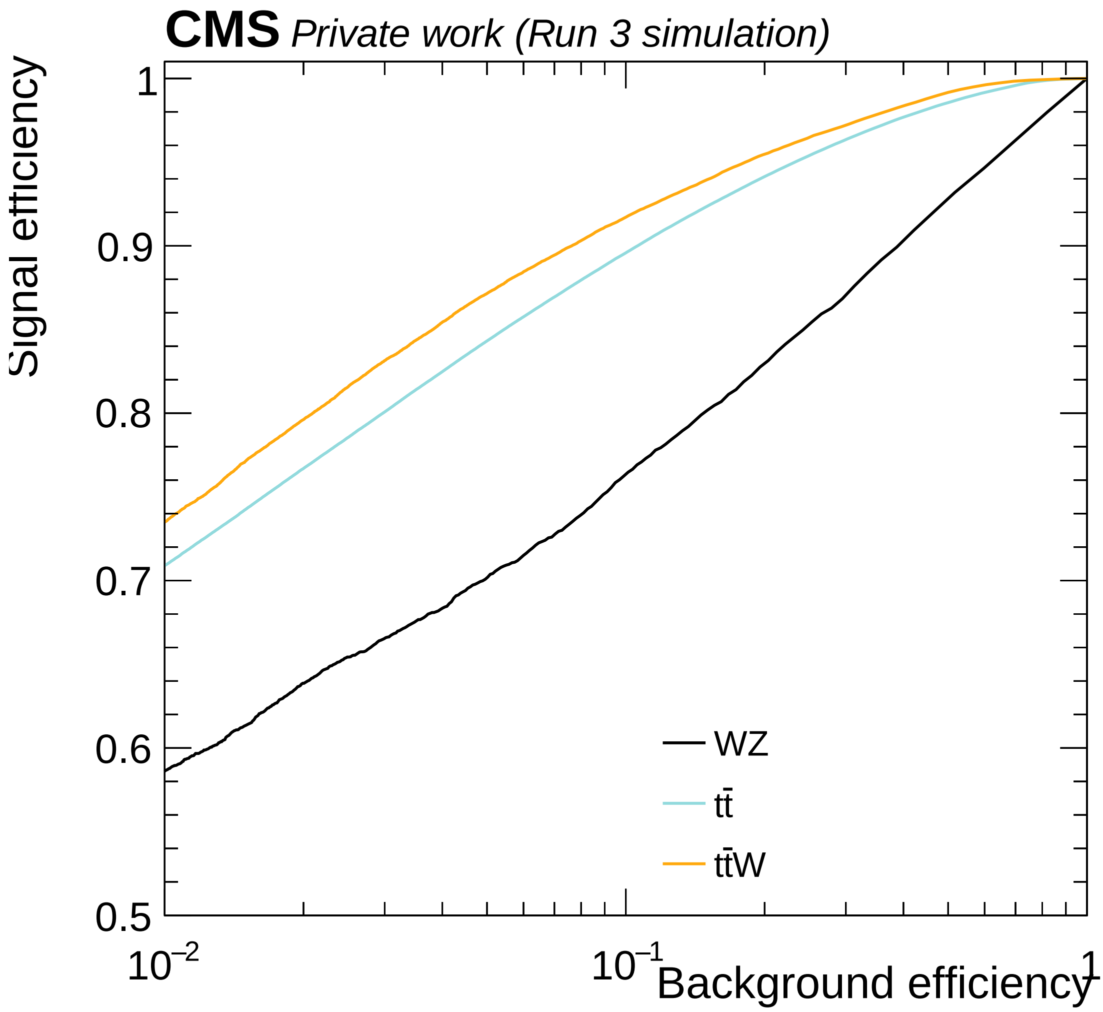

FIGURE. 5.10: b-tagging efficiency for the DEEPJET tagger using Run 3 simulation of WZ (black line), $t\bar{t}W$ (orange line), and $t\bar{t}$ (light blue line). The performance is evaluated as the probability of correctly identifying a *b* jet (b-tagging efficiency) versus the probability of misidentifying a non-b jet as a b jet. Only jets with $p_T > 30$ GeV and $|\eta| < 2.4$ are considered in these curves. These plots are only used for illustrative purposes to showcase the performance on the processes analyzed in this thesis in a particular phase space.

At the same background efficiency, the signal efficiency for $t\bar{t}$ and $t\bar{t}W$ is higher than for WZ. This feature is a key consideration in defining the analysis strategy to effectively reduce contributions from SM processes involving top quark production. The specific details about how b tags are identified will be discussed in the corresponding chapters.

5.3 Corrections to the Monte Carlo simulation

While the knowledge of the CMS collaboration regarding the operation, performance, and details of the detector is well extended among experts and documented in several references, the need to compare data against theoretical simulations based on MC imposes the need of an emulator of the CMS detector. However, exact emulation of the detector is often impractical, as it would not only require encoding all electronic delays and physical constraints into a software package, but also to be constantly updated, as the data taking conditions can vary from run to run. Consequently, MC simulations used in analyses typically require corrections to properly emulate the recorded data at reconstruction level. In the following sections details on the different corrections are given.

5.3.1 Trigger efficiency corrections

Trigger efficiencies and scale factors are measured in a data-driven manner using the reference trigger method. The underlying hypothesis is that data events can be selected using reference trigger paths that are uncorrelated with the ones used in the analysis event selection. The reference trigger provides a set of data events in which the efficiency of the measured paths can be estimated. However, this approach comes at the cost of reduced statistical power due to the additional constraints imposed by the reference trigger criteria. To ensure orthogonality in event selection, a dataset that is enriched in events with high jet and $p_{\mathrm{T}}^{\mathrm{miss}}$ activity is used to perform trigger efficiency measurements across all data taking years.

Events that pass the reference trigger HLT requirements from Section 5.2.1 must also contain the same number of leptons, with the same p_{T} requirements that mimic those of the leptons used in the measurement for which the trigger efficiencies need to be derived. Since reference triggers often rely on orthogonal datasets with events triggered by $p_{\mathrm{T}}^{\mathrm{miss}}$, it is essential to select events with a minimum $p_{\mathrm{T}}^{\mathrm{miss}}$ equal to the threshold used in the triggers defining the reference dataset. This selection defines the preselection region (PR). No additional kinematic cuts are applied in the PR to maximize statistical power in the measurement. The efficiency of the measured trigger, $\epsilon(HLT)$, is then computed as shown in Equation 5.2.

$$\epsilon(HLT) = \frac{\text{Events passing HLT and PR}}{\text{Events passing PR}} \tag{5.2}$$

Using this method the efficiencies are measured both in data and MC sample, and a scale factor can be derived to correct for the difference in MC events. The statistical uncertainty due to the limited size of the preselected data sample is propagated through this scale factor to the final measurement. Additional systematic uncertainties are derived from this method. The resulting trigger efficiencies and corrections are particular of each analysis, and are therefore detailed in the corresponding chapters.

5.3.2 Pileup simulation in MC

Because PU interactions are an experimental effect arising from multiple bunch crossings at the LHC, they are not included in the event generation of MC simulations. However, PU is inherently present in the recorded data, and therefore must be incorporated into the MC simulations. There are two main approaches to achieve this, both of which rely on mixing a target MC sample with a minimum bias (MB) sample. The MB sample is superimposed onto the MC sample to introduce PU effects before the digitization and reconstruction of the main sample.

Since Run 2, the CMS experiment has predominantly used the premixing technique for PU simulation. In premixing, PU events are generated in advance in a way that allows events from the MB sample to be retrieved dynamically during processing. For each generated event in a given MC sample used for analysis, a corresponding event from the premixing library is selected. These two events are then overlaid, ensuring that the generated sample retains its intended physics content (e.g., all particles from the matrix element and parton shower in a $\mathrm{t\bar{t}}$ sample), while also including additional particles that model PU effects. Once the samples are mixed, they proceed through the production chain described in Section 4.4 for further processing.

The MB sample is typically generated before the end of a given data taking period, assuming an expected PU profile. However, this profile often differs from the one ultimately observed in the data, as it is impractical to update the premixing library continuously. As a result, one of the corrections that need to be applied to the MC is the so-called pile-up corrections, which are derived by experts within the collaboration to adapt the simulations to the correct profile for a given data taking period. Figure 5.11 shows the number of reconstructed vertices before and after applying the PU corrections, in the context of the WZ analysis. Good agreement between the data and simulation is observed after applying these corrections.

This effect is typically one of the first corrections applied at the analysis level in any CMS analysis.

5.3.3 Jets, b-tagged jets and missing energy

Simulating the true detector response in the reconstruction of MC events is a complex task, and typically, the efficiencies and resolutions with which jets are reconstructed in simulations are more optimistic than in real data. As a result, proper calibration of the jets is essential to ensure that the MC accurately reflects the energy and momentum of the reconstructed jets in data. In many analyses that rely on event categorization based on jet properties, the effects originating from jet energy calibration are among the leading sources of systematic uncertainty. It is important to note that, since jets are typically selected based on their kinematic properties, any significant effect on the momentum resolution can cause substantial migrations between event categories, thus increasing the

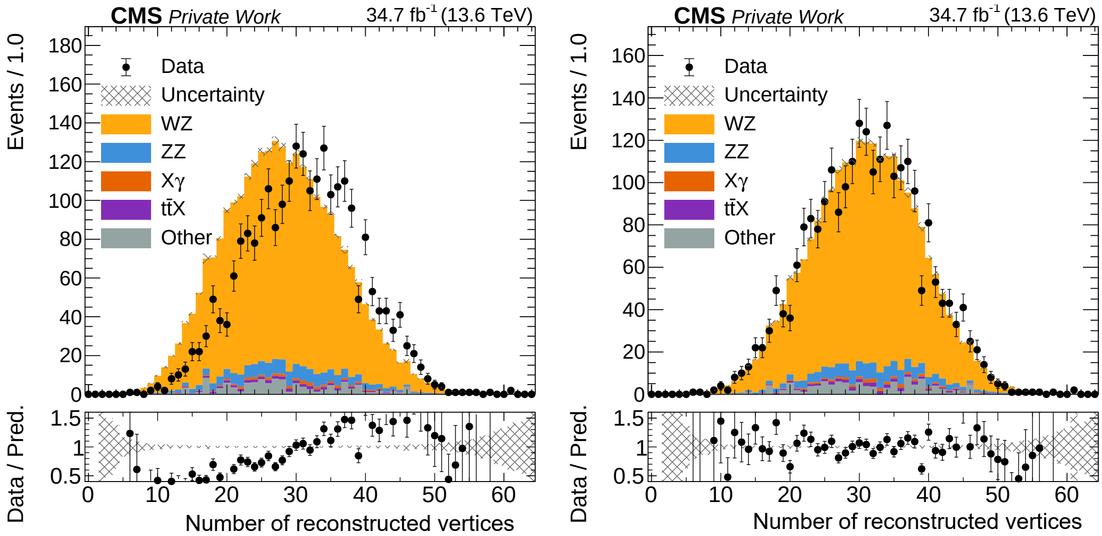

FIGURE. 5.11: Distribution of the number of reconstructed vertices before (left) and after (right) applying the PU corrections. The coloured histograms represent the different processes considered, stacked one top of each other, whereas the black markers represent the data. The distributions are obtained from data taken in Run 3 and are compared to the PU profile obtained from simulations used in the WZ analysis. The ratio panels show the ratio between data with respect to the sum of the predicted distributions. The vertical lines on the data points represent the statistical uncertainty in the data and the hatched band corresponds to the total uncertainty in the prediction..

uncertainty of the analysis.

The procedure for applying these corrections is documented in [81]. In summary, there are two types of calibrations in CMS: those that aim to properly model scaling effects (jet energy scale calibration) and those that aim to calibrate resolution effects (jet energy resolution calibration). Jet energy scales are derived using a factorized approach in which each level of correction is applied sequentially. Each step in the chain applies a scaling factor, dependent on the properties of the jet, that modifies the jet's four-momentum. Subsequently, the output of each step serves as the input for the next. On the other hand, jet energy resolutions are applied using a smearing procedure, which makes the p_{T} resolution in MC more similar to the real resolution achieved in data.

These corrections not only impact the jets but must also be propagated to other objects that depend on the jets. For instance, because the missing transverse energy is computed as a balance to achieve energy conservation, it is highly dependent on the energy associated with each jet. As a result, $p_{\mathrm{T}}^{\mathrm{miss}}$ must also be corrected for these effects. Similarly, the performance of b tagging, which depends on the kinematic properties of the jets, must account for these corrections as well.

5.3.4 Leptons

Similarly to jets, selection efficiency and resolution in the case of leptons tend to perform better in simulation than in data, and as a result, corrections must be applied. In the case of the leptons, there are several components to these corrections: reconstruction, identification, isolation and scale. In the case of the first three, these are normally subject to the definition of prompt lepton used in the analysis, which as detailed in Section 5.2.4, is based on the requirements imposed primarily by the prompt lepton MVA for both electrons and muons. In the case of the scale corrections, these aim at matching the resolution effects of the detector in properly measuring the momentum of the leptons. In this section the most relevant corrections are detailed.

Corrections to the MC are derived by considering the ratio of efficiencies measured in data and MC. This ratio is applied as an additional weight to properly normalize the MC by considering an additional per-event weight which is computed as multiplicative corrections for each lepton.

5.3.4.1 Lepton reconstruction

Reconstruction corrections are generally small, and have been relatively stable in both Run 2 and Run 3. In Figure 5.12, the correction factors for the electron reconstruction efficiencies are shown for the two periods of the 2022 data taking.

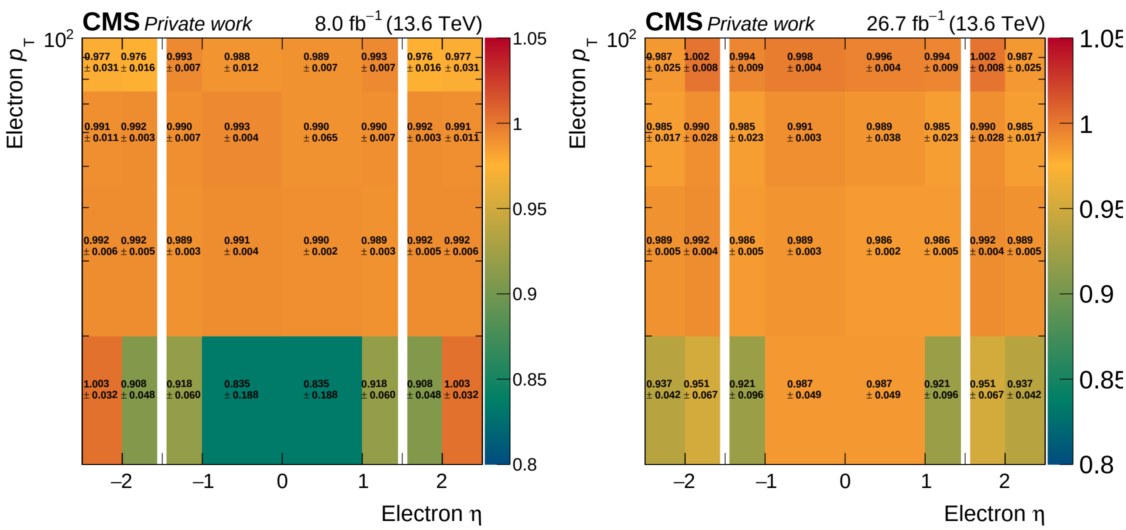

FIGURE. 5.12: Electron reconstruction corrections shown as a two-dimensional map as a function of η and p_T of the identified electron. Each bin represents the weight correction applied to the MC and the corresponding uncertainty. Corrections are shown for the first (left) and second (right) periods of 2022.

In the case of muons, the reconstruction corrections are often close to unity, thanks to the excellent muon reconstruction performance of CMS. Because of this, these corrections are often neglected.

5.3.4.2 Lepton identification and isolation

Isolation criteria, such as those used to train the prompt lepton MVA, are notably different between data and simulation. This is partly due to the intrinsic challenges in prop-

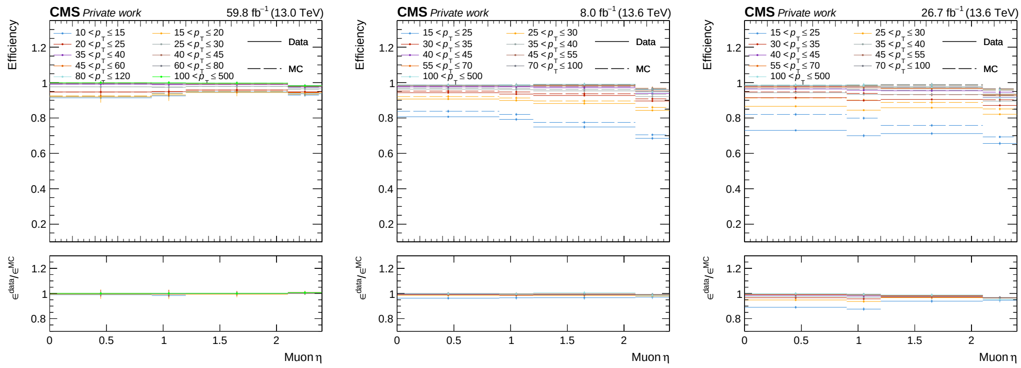

FIGURE. 5.13: Muon identification efficiencies obtained from the tag-and-probe method for the last year of Run 2 data taking (left), and the two data taking periods of 2022, shown separately for the first (middle) and second (right) periods of 2022. The efficiencies are shown separately for Data and MC in the upper pads of each plot, and have been estimated using $Z \to \ell\ell$ events with the tag-and-probe technique. Ratio plots show the ratio between the data and MC efficiencies.

erly modeling lepton isolation. To address these discrepancies, specific corrections are derived to account for potential mismatches arising from the lepton definition.

The lepton identification and isolation efficiencies are estimated using the tag-and-probe technique [82] and are derived using data in $\mathrm{Z} \to \ell^+\ell^-$ enriched regions. Events containing a pair of same-flavor, oppositely charged leptons with an invariant mass close to that of the Z boson are selected. One lepton must pass the tight selection criteria (tag) described in Table 5.2.4, while the other is required to satisfy only the loose selection criteria (probe) described in Table 5.2.3. The efficiency of the tight selection is then determined as the fraction of probe leptons that also pass the tight criteria.

Signal and background contributions are estimated via a template fit to the invariant mass distribution of the lepton pair. Efficiencies are derived in a two-dimensional (p_T, η) binning scheme, using four bins in $|\eta|$ spanning from 0 to 2.5, and nine bins in p_T covering the range from 10 to 120 GeV, to account for variations in detector geometry and response across different momentum ranges. The lepton identification efficiencies for the data taking year of 2018, and the two different periods of 2022, are presented in Figures 5.13 and 5.14 for muons and electrons, respectively. The efficiencies are shown separately for data and MC. The corrections for 2022 were specifically derived for the WZ measurement using Run 3 data.

Excellent performance is generally observed for both muons and electrons during the 2018 data taking period, which serves as a reference for comparison with the 2022 results. This behavior is expected, given that the 2018 data taking was already stable due to several preceding years of operation. In 2022, good performance is also observed for muons and electrons; however, in the case of electrons, leakage effects in the ECAL have a notably effects, as indicated by the larger difference in efficiencies at lower $|\eta|$. The two-dimensional correction maps, showing both the per-lepton weight as well as the uncertainty associated to the method, are shown for muons and electrons in 2022 are

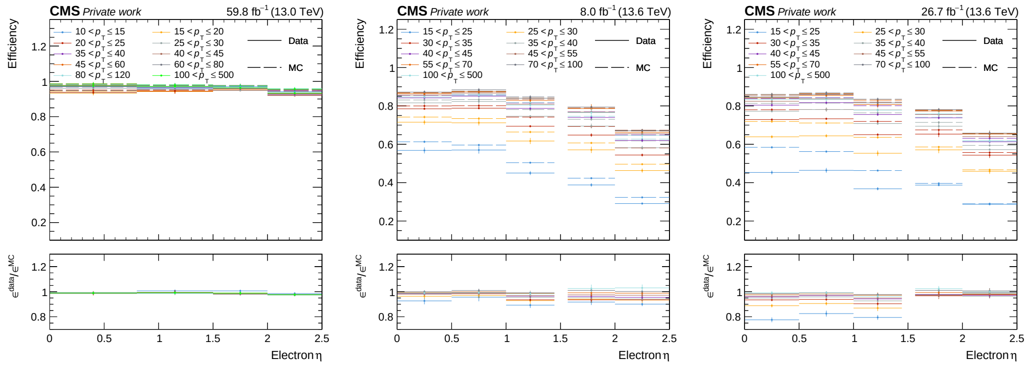

FIGURE. 5.14: Electron identification efficiencies obtained from the tag-and-probe method for the last year of Run 2 data taking (left), and the two data taking periods of 2022, shown separately for the first (middle) and second (right) periods of 2022. The efficiencies are shown separately for Data and MC in the upper pads of each plot, and have been estimated using $Z \to \ell\ell$ events with the tag-and-probe technique. Ratio plots show the ratio between the data and MC efficiencies. The regions between $|\eta|$ 1.44 and 1.56 that do not show any correction correspond to gaps in detector material, which were explicitly removed for the 2022 corrections.

shown in Figures 5.15 and 5.16, respectively.

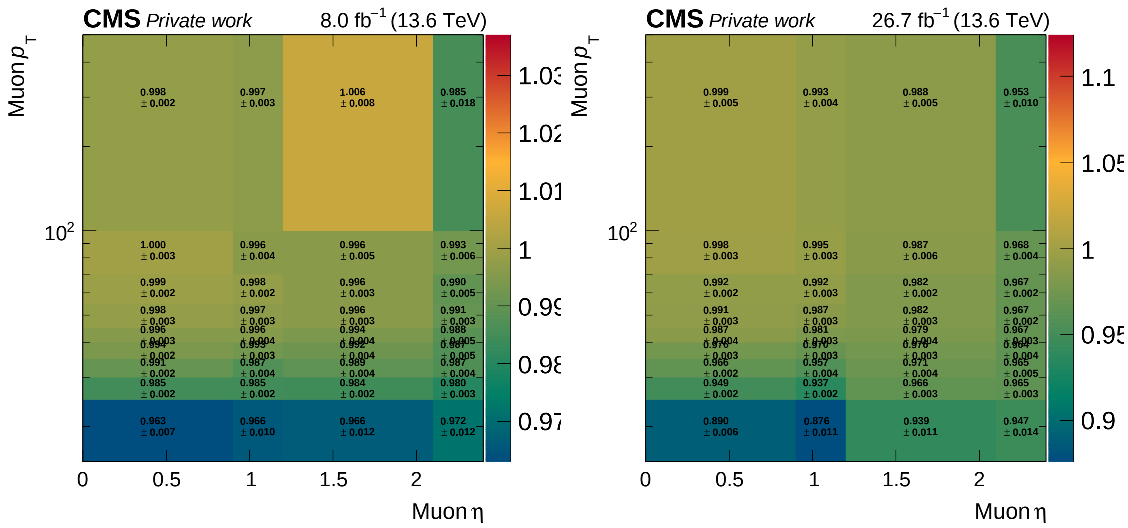

FIGURE. 5.15: Muon identification corrections shown as a two-dimensional map as a function of $|\eta|$ and p_T of the identified muon. Each bin represents the weight correction applied to the MC and the corresponding uncertainty. Corrections are shown for the first (left) and second (right) periods of 2022.

5.3.5 Lepton distributions

In the previous section, it was stated that most corrections related to lepton identification are derived from comparisons between $Z \to \ell^+\ell^-$ simulations and data. Once these corrections are applied, their validity can be tested by comparing the corrected MC simulation with data in the same region where the corrections were originally derived from. This procedure, known as a closure test, ensures that the applied corrections properly

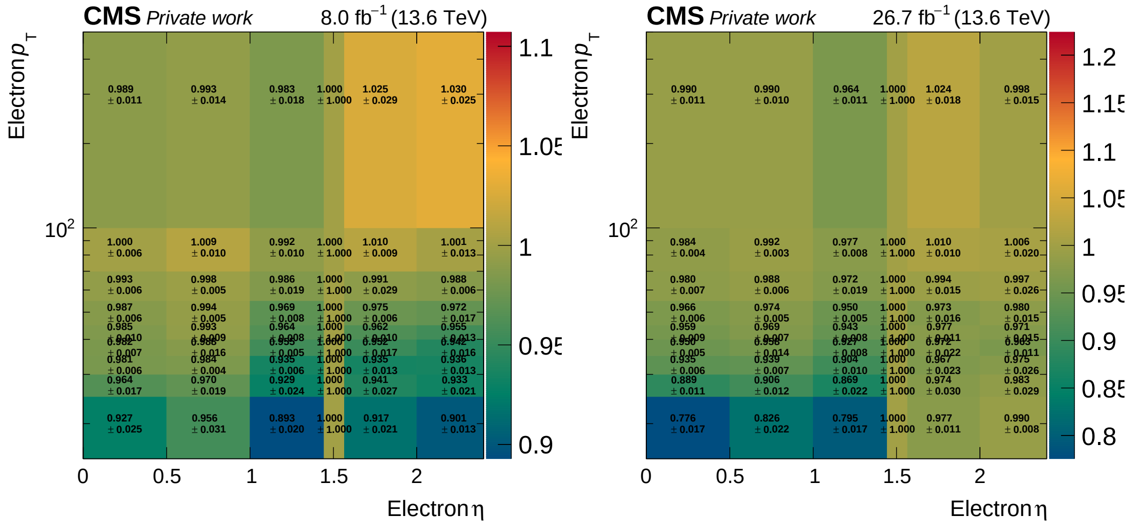

FIGURE. 5.16: Electron identification corrections shown as a two-dimensional map as a function of $|\eta|$ and p_{T} of the identified electron. Each bin represents the weight correction applied to the MC and the corresponding uncertainty. Corrections are shown for the first (left) and second (right) periods of 2022.

account for discrepancies between simulation and data. Figure 5.17 presents the closure test performed on $\mathrm{Z} \to \mathrm{ee}$ and $\mathrm{Z} \to \mu\mu$ events. The selections are designed to mimic the properties of the leptons that will be used later in the analysis. The closure test is shown specifically for the Run 3 corrections. However, the performance in the Run 2 dataset behaves in a very similar way.

Additionally, the closure test is performed by studying the invariant mass distribution of the two leptons from $\mathrm{Z} \to \ell^{+}\ell^{-}$ decays. This distribution is particularly sensitive to reconstruction, identification, and isolation efficiencies, but more importantly to scale correction effects. The corresponding distributions are shown in Figure 5.18.

Overall, good agreement is observed in these distributions, and good performance for the lepton identification is validated.

5.4 Statistical analysis of High Energy Physics data

The framework for measuring production cross sections is built on the fundamental idea that the observation of a physical process can be framed as a counting experiment, and this relation can be established by means of equation 5.3, where $\sigma\,(\mathrm{pp} \to \mathrm{X})$ is the cross section for the process X, and $N(\mathrm{X})$ is the number of events that are produced in a given dataset of size L.

$$\sigma\,(\mathrm{pp} \to \mathrm{X}) = \frac{N(X)}{\mathrm{L}} \tag{5.3}$$

Statistical methods are also used to extract meaningful features from data by com-

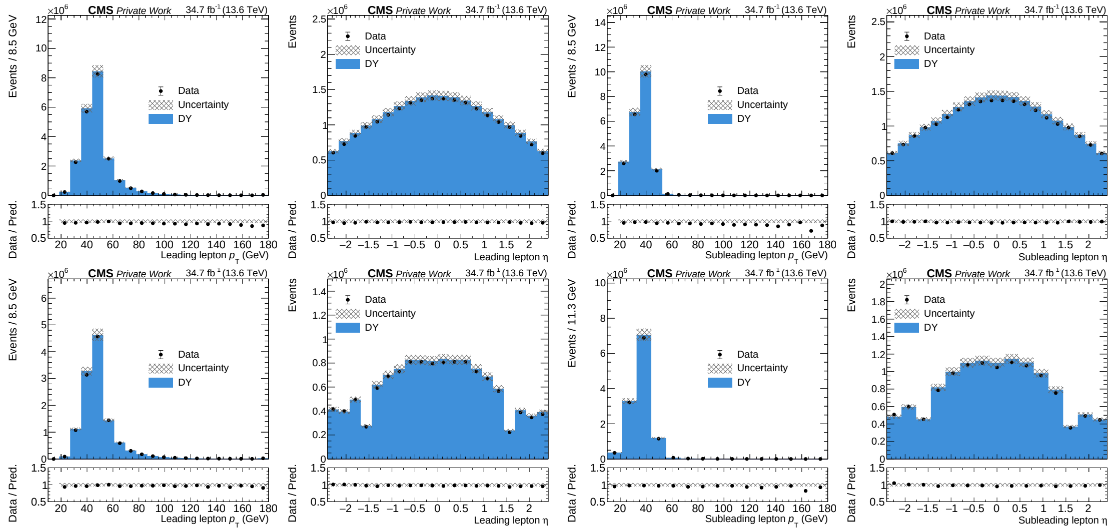

FIGURE. 5.17: Distributions of p_{T} and η for the selected leptons after applying all corrections, using the full 2022 dataset. The upper row corresponds to muons, while the lower row corresponds to electrons. Within each row, the first two plots show the p_{T} and η distributions for the leading (most energetic) lepton, while the last two plots correspond to the subleading lepton. The lower panels in each plot display the ratio of data to simulation, with uncertainty bands being the ones derived from the different methodologies.

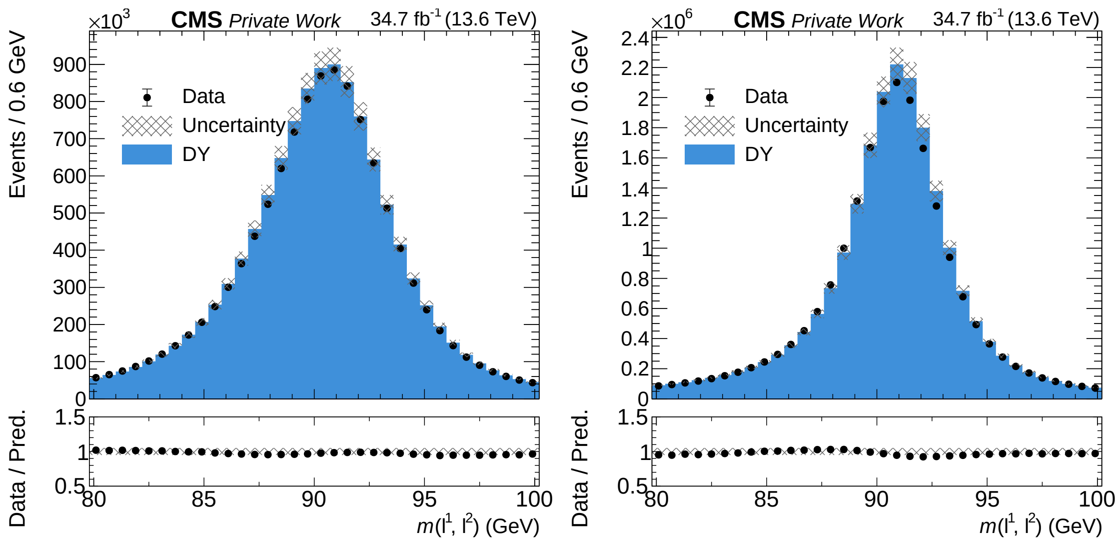

FIGURE. 5.18: Distributions of the invariant mass of the selected leptons after applying all corrections, using the full 2022 dataset. The left plot corresponds to electrons, while the right plot corresponds to muons. The lower panels in each plot display the ratio of data to simulation, with uncertainty bands being the ones derived from the different methodologies

paring observed results with the expected behavior, which is derived from the MC generation methods outlined in 4.4. This section provides a general overview of the key concepts regarding the statistical analysis used in the measurements presented in this thesis.

5.4.1 Fiducial volume and the cross section formula

Measuring the cross section for a given process involves determining how many events of the signal process (X) are observed in a given dataset. To do so in an unbiased way, one typically estimates the background processes (any process that does not contribute to the signal) and compares these estimates to the observed data. The difference between the data and the predicted background corresponds to the observed signal in the dataset.

The concept of signal is subject to the target phase space that that is aimed to measure. If a general "total phase space" is defined as the complete set of theoretically accessible configurations that allow to produce the process of interest, then a reasonable definition of the fiducial volume would be the subset of these configurations that are actually measurable by experiments. The fiducial volume can be defined either using reconstructed-level quantities, by applying specific requirements on the reconstructed object kinematics, or even generator-level quantities. Regardless of the choice, it is important to note that measurements are always performed within the fiducial volume. Once fiducial quantities are properly measured, they can be extrapolated to a much wider phase space or even to the total phase space.

For instance, in a $\mathrm{t\bar{t}}$ measurement, the total phase space includes all possible top quark pair production events, but a much more practical fiducial volume might only consider events with a single lepton in the final state. While the former is more general, it is not accessible due to the fact that top quarks are not possible to detect because of their short lifespan. By measuring the fiducial cross section of the latter, one can easily extrapolate to the total phase space.

To extrapolate from the fiducial volume to the total phase space and obtain the true number of events, $N(\mathrm{X})$, one must account for detector effects such as reconstruction, identification, and calibration; as these effects reduce the number of selected events with respect to the ones predicted from the theory. Additionally, if the fiducial volume is defined by generator-level selections, their efficiencies must also be considered, as they directly impact the cross section. The general relationship for obtaining the true number of events is given by Eq. 5.4:

$$N(X) \cdot [\epsilon \times \mathcal{A}] = N_{\text{fid}}^{\text{obs}}(X) \tag{5.4}$$

Here, ϵ represents the efficiency of selection criteria applied at the reconstructed level, while $\mathcal{A}$ accounts for the efficiency of the generator-level requirements. The quantity

$N_{\text{fid}}^{\text{obs}}(X)$ corresponds to the number of events *observed* in the fiducial volume at analysis level. Dividing this expression by the luminosity, one obtains the formula for what is known as the *fiducial cross section*.

$$\sigma_{\text{fid}}^{\text{obs}}(X) = \frac{N(X) \cdot [\epsilon \times \mathcal{A}]}{\text{L}} \tag{5.5}$$

The fiducial cross section is the parameter that is actually accessible in experiments, and it is therefore the quantity that is generally measured. The problem of measuring a cross section is therefore determined by the proper estimation of the number of observed signal events, proper calibration of the ingredients used in the analysis, and full consideration of all the theoretical constraints imposed by the signal modeling.

5.4.2 Signal extraction in likelihood fits

The observation of $N(X)$ signal events in a counting experiment is inherently probabilistic. Therefore, assigning a confidence level to the likelihood of observing the same result in an independent experiment is necessary to assess the statistical significance of the measurement. The statistical model that is used in the context of this thesis is implemented under the set of tools known as COMBINE [83].

The COMBINE model is essentially based on the idea that the probability of observing $N(X)$ signal events in a dataset containing $s + b$ events, where s and b are the expected signal and background yields, respectively, follows a Poisson-like distribution with mean $s + b$. Based on this premise, COMBINE builds a likelihood function as the one shown in equation 5.6.

$$\mathcal{L}(\Phi) = \prod_d \left[p\left(\vec{x}_d; \mu, \vec{\nu}\right) \prod_k p_k\left(y_k; \nu_k\right) \right] \tag{5.6}$$

This extended likelihood models several effects relevant for shape-based analyses in particle physics. The vector $\vec{x}$ represents the different —statistically independent— observations in the fiducial volume for a given set of events. These observations are parametrized by the measured parameter of interest, μ. Additionally, the likelihood incorporates sources of systematic uncertainties affecting the observed phase space, represented by the vector of nuisance parameters, $\vec{\nu}$. These parameters are typically given a central value ν_i, which is intrinsically related to the efficiency term in the cross section formula. They are also assigned a confidence level range that quantifies the uncertainty in their measurement. The uncertainty parametrization is provided by the term $p_k\left(y_k; \nu_k\right)$.

The complete likelihood, $p\left(\vec{x}_d; \mu, \vec{\nu}\right) \prod_k p_k\left(y_k; \nu_k\right)$, describes the probability of observing the set of parameters $\vec{x}$, given a signal strength μ, a vector of nuisance parameters fixed at their central values, and the uncertainty associated with each parameter of interest. The final component of the likelihood formula is a product of individual likelihoods, which allows for the definition of an extended likelihood function suitable for binned analyses. In these analyses, events are classified into bins of a histogram, with the parameter d indexing all different observations.

The measurement of the parameter μ and its uncertainties is carried out through a fit to the data, assuming that the predictions follow this statistical model. In this fit, the values of μ and $\vec{\nu}$ are estimated by maximizing the likelihood. The uncertainty on the measured parameters is quantified as a confidence interval, derived from a profiled likelihood fit. In this method, the test statistic

$$\Lambda\left(\mu\right) = \frac{\mathcal{L}(\vec{x};\mu,\vec{\nu})}{\mathcal{L}(\vec{x};\mu,\hat{\vec{\nu}})}$$

is profiled for different values of the observed μ. For each tested hypothesis, the nuisance parameters are maximized. The resulting value that minimizes Λ corresponds to the central value of the parameter, and the uncertainty is obtained from the profiled likelihood. The confidence interval is derived under the assumption that $-2\log(\Lambda)$ follows a χ^2 distribution.

Moreover, the parameter μ can be physically interpreted as the *signal strength* within the fiducial phase space, defined as:

$$\mu = \frac{\sigma_{\text{fid}}}{\sigma_{\text{theo}}},$$

where σ_{fid} is the fiducial cross section and σ_{theo} is the theoretical prediction for the cross section. The signal strength parameter introduces a degree of freedom to the likelihood that measures how the initial normalization assumption for the signal compares to the actual measured value.

5.4.3 Sources of uncertainty in experimental measurements

In any analysis, several factors, which may not be precisely known or accurately simulated, can influence both the event yield of the signal and the background processes, as well as the shape of the distributions in the key observables used for signal extraction. These effects are collectively accounted for as systematic uncertainties, which arise from various sources such as limitations in simulation models, uncertainties in the measurements of detector performance, and theoretical approximations.

Systematic uncertainties can be broadly categorized into two main sources: experimental and theoretical. The theoretical uncertainties stem from the different assumptions, choices, and limitations inherent in the event generators used to simulate the processes, or in the normalization factors used to estimate their cross section. These uncertainties can have a significant (and sometimes limiting) effect on the measurements, as the generators may not fully capture all relevant physics effects. On the other hand, experimental uncertainties arise from the various corrections and detector effects discussed in Section 5.3, which impact how well the detector response and the final event yields are modeled. These effects are modeled as nuisance parameters in the likelihood fits used to performed the measurements, following the premises detailed in Section 5.4.

Both experimental and theoretical sources of uncertainty are common to most analyses and, in the context of this thesis, are treated similarly in both the $\mathrm{t\bar{t}W}$ and WZ measurements. For this reason, this section provides a general description of the systematic uncertainties considered in both analyses. Any analysis-specific details are discussed in the relevant chapters.

5.4.3.1 Experimental uncertainties

Luminosity: the integrated luminosities for the 2016, 2017, 2018, and 2022 data taking periods are individually measured, with corresponding uncertainties of 1.2%, 2.3%, 2.5%, and 1.4%, respectively [84–87].

Pileup reweighting: the pileup reweighting technique, detailed in Section 5.3.2, carries an associated uncertainty of 4.6%. This uncertainty is derived by varying the minimum bias cross section by the given percentage.

Trigger: the uncertainty due to trigger efficiency is estimated by varying the trigger corrections within the uncertainties determined from the method used to derive the corrections.

Lepton reconstruction: the derivation of the electron reconstruction efficiencies described in 5.3.4 carry out a modest uncertainty that is applied in bins of the electron p_{T}, for electrons with $p_{\mathrm{T}} < 20$ GeV, $p_{\mathrm{T}} \in$[20, 75) GeV and $p_{\mathrm{T}} \geq 75$ GeV. The uncertainties are the ones shown in the maps from Figure 5.12.

Lepton identification: the lepton identification and isolation efficiencies are estimated using the tag-and-probe technique and are affected by the size of the data set in $\mathrm{Z} \rightarrow \ell\ell$ enriched regions, where the efficiencies are derived. Systematic uncertainties affecting this procedure are estimated through the variation of different parameters in the fitting templates as well as in the tag selection criteria. These uncertainties are applied in the same way as the corrections described in Section 5.3.4. The statistical component of these uncertainties, corresponding to the size of the data set in which the tag-and-probe technique has been applied, is also included as a component of these uncertainties. The uncertainties are the ones shown in the maps from Figure 5.15 and 5.16 for muons and electrons, respectively. Uncertainties average approximately 1% per electron and 0.5% per muon. The statistical component of these uncertainties, corresponding to the size of the data set used for the tag-and-probe technique, is also included in the evaluation. These corrections are one of the main sources of uncertainty in multileptonic analyses.

Lepton energy corrections: uncertainties in the energy scale of the leptons introduce a smaller effect which induces variations in the lepton p_{T}. Although these variations are negligible for muons, they are considered in the 2016, 2017 and 2018 datasets.

Jet energy corrections: several uncorrelated sources of uncertainty related to jet energy corrections are considered. The jet energy scale (JES) and jet energy resolution (JER) uncertainties are evaluated by shifting the corrections applied to the reconstructed jets by one standard deviation, both up and down. The events are then re-analyzed, with the re-application of the jet-based selection and the recalculation of all relevant kinematic quantities, to obtain the varied kinematic distributions. These distributions are incorporated as shape uncertainties, which include both rate and shape effects.

b tagging: the b tagging veto efficiencies are corrected according to the latest available b tagging corrections. Historically, b tagging corrections are estimated by fitting five independent measurements, aiming to evaluate the b tagging performance in different phase spaces and minimize bias from the region in which the discriminator is trained. Uncertainties in the b tag scale factors are propagated as event weights using an event reweighting method, which adjusts the weight of the selected simulated events to predict the correct event yield in data.

5.4.3.2 Theoretical uncertainties

Uncertainties in the modeling of signal and background processes can affect acceptance and selection efficiencies, the shape of kinematic distributions, and the predicted cross sections used for the normalization of simulated event samples. All theoretical uncertainties are normally treated as correlated across data taking years.

Renormalization and factorization scales: uncertainties due to missing higher-order corrections are estimated by varying the renormalization (μ_R) and factorization (μ_F) scales from the event generators independently up and down by a factor of two from their nominal values. The impact on the acceptance (shape of distributions) is considered separately from the effect on the overall cross-section (normalization). For the signal processes, only the acceptance effects are included, as normalization uncertainties on the signal would be inconsistent with the goal of measuring the signal cross section itself.

Choice of PDFs: the uncertainty associated with PDFs is evaluated using NNPDF replicas [47] following the procedure described in Refs. [88, 89]. This results in 100 individual variations, which are simultaneously assessed for the main processes, and some dominant backgrounds depending on the analysis. Additionally, two variations in the strong coupling constant (α_s) are considered.

ISR/FSR: For signal processes, the effect of ISR and FSR in the parton shower simulation is accounted for by varying the parton shower weights up and down by a factor of two.

All sources of systematic uncertainties are included as parameters to be evaluated in the statistical analysis conducted for experimental measurements.

6 Measurements of the $\mathrm{t\bar{t}W}$ properties at 13 TeV

Similar to $\mathrm{t\bar{t}}$, the $\mathrm{t\bar{t}W}$ process is characterized by the presence of two top quarks in the final state. However, a distinctive feature in this case is that the top-antitop pair is produced in association with a W boson. Figure 6.1 presents a summary of the cross sections of various top-quark-related processes measured by the CMS experiment, including their comparison to different theory predictions. At a centre-of-mass energy of 13 TeV, the $\mathrm{t\bar{t}}$ production cross section surpasses that of $\mathrm{t\bar{t}W}$ by approximately three orders of magnitude. Therefore, the $\mathrm{t\bar{t}W}$ process lies in the category of rare top-quark production processes, alongside $\mathrm{t\bar{t}H}$, $\mathrm{t\bar{t}Z}$, and $\mathrm{t\bar{t}}\gamma$, which themselves constitute the primary backgrounds to $\mathrm{t\bar{t}W}$.

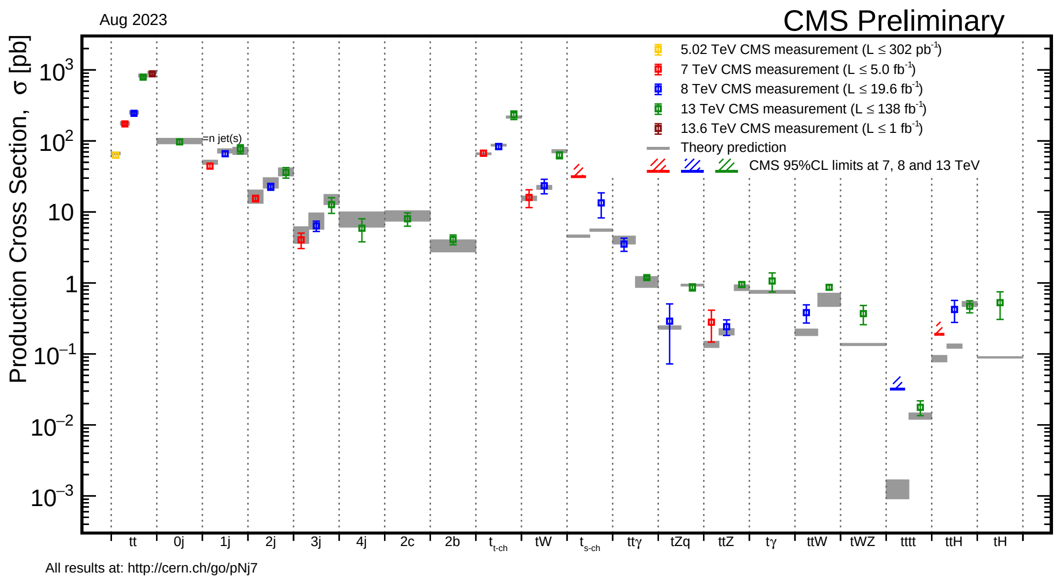

FIGURE. 6.1: Summary of production cross sections for top-quark-related processes, as measured by the CMS TOP physics group, including their comparison to different theory predictions.

Given that $\mathrm{t\bar{t}W}$ production constitutes the central focus of this thesis, this chapter is entirely dedicated to its study. In particular, the two measurements that constitute the core of this thesis will be reviewed. First, its inclusive cross section measurement is obtained using the full Run 2 dataset of the CMS experiment [14]. This measurement confirms previously reported tensions between the predicted $\mathrm{t\bar{t}W}$ cross section and the SM, and it is up to date the most precise measurement of this quantity.

In light of the persistent tensions between the measured $\mathrm{t\bar{t}W}$ inclusive cross section and the latest SM predictions —consistently observed by both the CMS and ATLAS experiments— differential measurements of the $t\bar{t}W$ process have also been carried out using the full Run 2 dataset. The aim of these measurements is to identify observables that could provide further insight into the origin of these discrepancies with respect to the SM. The results have been made publicly available to the scientific community in Ref. [15].

6.1 Analysis strategy

The properties of the $t\bar{t}W$ process are studied in the context of multilepton final states. Consequently, the $t\bar{t}W$ analysis builds upon the concepts outlined in Chapter 5, which discusses the essential components of a multilepton analysis. The requirements detailed in the aforementioned chapter focus on general aspects such as object identification, corrections, and overall considerations. However, since the $t\bar{t}W$ process is characterized by a relatively low cross section, even when using the full Run 2 dataset, and due to the considerable presence of backgrounds such as $t\bar{t}H$, $t\bar{t}Z$, and $t\bar{t}\gamma$, a more refined strategy is required to achieve an accurate measurement. The details of this strategy are presented in this section.

Some differences in the overall analysis strategy, particularly concerning the lepton selection, should be noted between the inclusive and differential $t\bar{t}W$ measurements. The inclusive measurement aims to maximize the number of selected signal events by applying looser lepton selection criteria, as defined by lower lepton MVA requirements in Table 5.2.4. In contrast, the differential measurement focuses on enhancing background suppression by employing the tighter lepton MVA requirements. In the following, the term "tight lepton" will be used consistently to refer to the definition appropriate for each analysis context. Additional differences in the overall selection strategies between the two approaches will also be discussed in this section.

Throughout the following pages, the strategy used for the inclusive cross section will be refered to as the "loose" method, and to the strategy used for the differential measurements as the "tight" method. Specific differences between the loose and tight methods at different parts of the descriptions will be highlighted in the text where relevant.

6.1.1 Event Selection

Two distinct signal regions (SRs) are defined, both based on the presence of at least two tightly identified leptons, following the object definitions described for the case of Run 2 analysis in Section 5.2.

The first SR is defined by the presence of at least two leptons with the same electrical charge and is referred to as the two-lepton same-sign region (2ℓss). Only events containing exactly two tight leptons are selected. These leptons are ordered by p_T, with the highest-p_T lepton labeled as the leading lepton (ℓ_1) and the second-highest as the subleading lepton (ℓ_2). Events with additional leptons that do not satisfy the tight selection criteria are vetoed. The leading lepton must have $p_\mathrm{T} \geq 25$ GeV, while the subleading lepton must satisfy $p_\mathrm{T} \geq 15$ GeV. To reduce contributions from low-mass resonances, the invariant mass of the same-sign dilepton pair must be greater than 30 GeV. Additionally, to suppress backgrounds from Z boson production, events are required to satisfy that the invariant mass of the two selected leptons must not fall within 10 GeV of the Z boson mass peak. A similar veto is applied to same-flavor, opposite-sign lepton pairs. The central value of the Z mass is taken from the Particle Data Group (PDG) world average, based on the latest LEP measurements [90]. These requirements are particularly effective in reducing backgrounds from $\mathrm{t\bar{t}Z}$ production, where either a lepton charge is misidentified or a non-tight lepton, when combined with a tight lepton, reconstructs an invariant mass close to the Z boson mass. To further suppress charge misidentification backgrounds, all reconstructed leptons must satisfy consistency across three independent charge sign measurements, following the "selective algorithm" described in [91]. Finally, selected events must contain at least three jets, with at least two identified as b-tagged jets, based on the loose WP definitions outlined in Section 5.2.2.

An additional signal region, characterized by the presence of at least three tight leptons (3ℓ), is defined. In this region, the leading lepton must have $p_\mathrm{T} \geq 25$ GeV, while the subleading and third-leading leptons are required to satisfy $p_\mathrm{T} \geq 15$ GeV. The same criteria used to suppress low-mass resonances and backgrounds involving resonant Z production in the 2ℓss signal region are also applied here. Additionally, charge consistency is enforced by requiring the sum of the lepton charges to be exactly one. Finally, selected events must contain at least two jets, with a minimum of two identified as loose b-tagged jets.

All the selection requirements described in this section are applied to the differential measurements of the $\mathrm{t\bar{t}W}$ process. For the inclusive measurement, some selection criteria are slightly modified. The complete set of selection requirements for both the inclusive and differential cross-section measurements, in the 2ℓss and 3ℓ channels, is summarized in Table 6.1.1.

6.2 Background estimation

The measurement of low cross-section processes such as $\mathrm{t\bar{t}W}$ requires refined background estimation techniques, as these measurements are typically background-dominated. Backgrounds in any analysis are generally classified into two main categories. First, "reducible backgrounds" arise due to non-performant behaviour in detector reconstruction or identification of analysis objects. In multilepton analyses, the dominant reducible background is the presence of nonprompt leptons, described in Section 5.2.3, and "charge misidentification" backgrounds; which arise due to the charge of a reconstructed lepton being incorrectly assigned.

Backgrounds which are not produced in this way are known as "irreducible backgrounds", or simply prompt backgrounds. They originate from processes that produce

Table 6.1.1: Event selections applied in the 2ℓss and 3ℓ channels. The p_{T} thresholds applied to the highest, second-highest, and third-highest p_{T} leptons are separated by commas. The symbol "-" indicates that no requirement is applied. Objects in parentheses refer to selections that were applied in the inclusive cross section measurement, and not in the differential measurements. The symbols ℓ_1 and ℓ_2 refer only to tight leptons.

Selection step	2ℓss	3ℓ
Number of leptons†	≥ 2	≥ 3
Number of tight leptons	$= 2$	$= 3$
Lepton p_{T} (GeV)	$25(30), 15(20)$	$25, 15, 15$
Charge requirements	$q_{\ell_1} = q_{\ell_2}$	$\sum_{\ell} q_\ell = \pm 1$
Number of central jets	≥ 3	≥ 2
b tag requirements	≥ 2 loose (≥ 1 medium or ≥ 2 loose)	
$\lvert m_{\ell_1\ell_2} - m_{\mathrm{Z}} \rvert$ (GeV)‡	$> 10(15)$	> 10
$m_{\ell\ell'}$ (GeV)	> 30 (12)	> 30 (12)
$p_{\mathrm{T}}^{\mathrm{miss}}$(LD) (GeV)	$-$ (12)	$-$ (12)

† Includes both tight and non-tight leptons.
‡ Applied to all SFOS lepton pairs and to same-sign electron pairs.

prompt leptons in a way similar to $\mathrm{t\bar{t}W}$, and thus require exploiting subtle kinematic differences in order to distinguish them from the signal. In the $\mathrm{t\bar{t}W}$ analysis, the dominant irreducible backgrounds are $\mathrm{t\bar{t}H}$ and $\mathrm{t\bar{t}Z}$, as both processes can produce final states with multiple prompt leptons with relatively similar properties. Additionally, several subdominant prompt contributions, when considered collectively, play a significant role in the final selection and must be properly accounted for. By carefully modeling both reducible and irreducible backgrounds, the analysis aims to enhance the presence of $\mathrm{t\bar{t}W}$ while minimizing contamination from background processes.

Regardless of their origin, specific choices must be made regarding how to predict background contamination in a given selection. This involves not only estimating the shape of the background distributions but also determining their normalizations, i.e., the expected number of background events of each type. Typically, prompt backgrounds are estimated using MC simulations, as their contributions arise from well-defined physical processes. The shapes of these backgrounds are generally well modeled by MC generators, while their normalization can even be refined by applying higher-order corrections that are calculated at fixed order. For reducible backgrounds, however, simulation is less reliable due to the more ambiguous nature of their origin, making data-driven estimation techniques preferable. The primary advantage of data-driven methods is that they do not depend on potentially inaccurate simulations for normalization; instead, the total background yield is extracted directly from data, improving the robustness of the estimation.

In this section, the various estimation techniques for the main backgrounds in the $\mathrm{t\bar{t}W}$ analysis are discussed. Beyond estimating the background contributions to predict the amount of background in a given phase space, these methods also introduce additional systematic uncertainties that affect the final measurements. These uncertainties arise from the choices made throughout the estimation process. A detailed discussion of the associated systematics is provided in Section 6.4. The treatment of the backgrounds is something common to both the loose and tight methods used for the inclusive and differential cross sections, respectively, and therefore are described only once.

6.2.1 Prompt backgrounds

All the backgrounds that originate from prompt sources in the analysis are estimated using MC simulations.

The samples used to estimate the yields and observables of different background sources is calculated at various levels of accuracy, primarily using the MADGRAPH5_AMC@NLO and POWHEG generators. The dominant backgrounds fall into the $\mathrm{t\bar{t}X}$ category, which mainly consists of $\mathrm{t\bar{t}H}$ and $\mathrm{t\bar{t}Z}$ processes. For $\mathrm{t\bar{t}H}$, the modeling is obtained using the POWHEG generator, incorporating NLO accuracy in QCD, including contributions from up to one additional real radiation emission [92] in the matrix element. In the case of $\mathrm{t\bar{t}Z}$, the generation is carried out using MADGRAPH5_AMC@NLO, considering terms up to NLO in QCD. Unlike $\mathrm{t\bar{t}H}$, no additional jets are included in the matrix element calculations.

The second most significant background source arises from diboson production mechanisms such as WZ, ZZ, and WW, which are collectively categorized as the diboson background. These processes contribute to events with multiple leptons and missing transverse momentum, making them an important component of the overall background estimation. All diboson samples are generated at NLO using the POWHEG generator [68].

Additionally, a distinct category labeled as "other" is introduced to account for subdominant background processes in terms of cross section and number of selected events. This includes single top production modes in association with a H or Z boson (tHq, tHW, tZq), as well as rarer processes such as $\mathrm{t\bar{t}XX}$, where X represents any boson. Furthermore, triboson production (VVV), featuring three vector bosons in the final state, is included in this category. All these backgrounds are modeled using MADGRAPH5_AMC@NLO at different orders of accuracy in the QCD expansion.

Lastly, a smaller but non-negligible contribution comes from conversion backgrounds, where photons that have undergone a conversion due to the interactions with the detector lead to undesired lepton contamination. While less dominant than the previously mentioned sources, these processes are still taken into account to ensure a comprehensive background modeling in the analysis. The conversion background is taken from simulation of several processes that include an associated γ that has lead to a conversion, and are generally modeled using MADGRAPH5_AMC@NLO.

6.2.2 Nonprompt backgrounds

The estimation of the nonprompt background is performed using the nonprompt-rate (NR) method. This approach aims to determine the true nonprompt contamination in various analysis regions by measuring the fraction of nonprompt leptons that pass the tight selection criteria, relative to the total number of selected leptons. The latter includes not only those that pass the tight selection but also leptons that fail the tight requirement while remaining sufficiently isolated, potentially mimicking the characteristics of prompt leptons.

This measurement is performed in a phase space dominated entirely by nonprompt contributions, known as the measurement region (MR). The strategy relies on selecting events containing a single genuine nonprompt lepton that is not close to a nearby jet within the same event in a cone of $\Delta R > 0.7$. This selection is designed to replicate the characteristics of nonprompt leptons that ultimately enter the SR selections, which primarily consist of isolated leptons well separated from jets. Notably, this approach does not use triggers that rely on isolation, as any isolation requirement applied to the selected leptons would introduce a bias in the NRs.

The NR is then extracted by computing ratio of the number of leptons passing the tight selection criteria to those passing a relaxed selection with respect to the one used for analysis. The relaxed criteria is defined by dropping the requirement on the prompt MVA discriminant for muons and electrons, and instead using tighter requirements on the jet relative isolation, which is defined as shown in equation 6.1.

$$\text{Jet relative isolation} = \begin{cases} \frac{p_T^{\text{j}}}{p_T^{\ell}} - 1, \text{if the reconstructed jet is matched to a generator level jet} \\ \text{PF relative isolation within } \Delta R = 0.4, \text{otherwise} \end{cases} \quad (6.1)$$

The NRs are extracted in bins of the lepton kinematics, specifically in bins of cone-p_{T} and η. The cone-p_{T} observable serves as a useful proxy for the true p_{T} of the parton that originated the nonprompt lepton. It is defined as the p_{T} of the lepton, if it passes the tight identification criteria, and as 90% of the p_{T} of the closest jet accompanying the lepton if it does not. This choice of cone-p_{T}, rather than p_{T}, helps mitigate biases arising from the fact that p_{T} values are often stricter than cone-p_{T}. As a result, using p_{T} directly could lead to the unintentional exclusion of non-isolated leptons that should be accounted for in the MR.

For each bin of lepton cone-p_{T}, the numerator and denominator values for the NR are extracted through a maximum likelihood fit to the $m_{\mathrm{T}}^{\mathrm{fix}}$ observable, as defined in equation 6.2. Here, $p_{\mathrm{T}}^{\mathrm{fix}}$ is fixed at a constant value of 35 GeV, and $\Delta\phi$ refers to the transverse angle between the lepton momentum and the $\vec{p}_{\mathrm{T}}^{\mathrm{miss}}$ vector.

$$m_{\mathrm{T}}^{\mathrm{fix}} = \sqrt{2 \cdot p_{\mathrm{T}}^{\mathrm{fix}} \cdot p_{\mathrm{T}}^{\mathrm{miss}} \cdot \left[1 - \cos\left(\Delta\phi\right)\right]} \tag{6.2}$$

This observable is chosen because its dependence on $p_{\mathrm{T}}^{\mathrm{miss}}$, combined with the fixed value of $p_{\mathrm{T}}^{\mathrm{fix}}$, results in a rapidly falling distribution that effectively discriminates between nonprompt and prompt backgrounds. Below the W mass scale, most contributions arise from nonprompt sources such as QCD, whereas above this scale, prompt contributions, primarily from W+jets, become more relevant. This behavior occurs because high-$p_{\mathrm{T}}^{\mathrm{miss}}$ QCD events are typically due to resolution effects from the detector, which are relatively rare. As a result, the contributions of QCD events at high $p_{\mathrm{T}}^{\mathrm{miss}}$ (or high $m_{\mathrm{T}}^{\mathrm{fix}}$) are less common. In contrast, W+jets production typically involves a neutrino, leading to very high $p_{\mathrm{T}}^{\mathrm{miss}}$ values, making it a more frequent contribution at higher $p_{\mathrm{T}}^{\mathrm{miss}}$.

The number of selected leptons of each type is then used to extract the NR factor, f_i, following equation 6.3. Once the NRs are derived, the nonprompt contribution is estimated by weighting data events in a sideband region of the SR, known as the application region (AR). This region is defined using the same selection criteria as the SR but requires that at least one of the two leptons satisfies the relaxed tight criteria, while at least one fails the tight selection.

$$f_i = \frac{N_{\mathrm{tight}}}{N_{\mathrm{tight}} + N_{\mathrm{not\text{-}tight}}} \tag{6.3}$$

To estimate the nonprompt background in the SR, the derived weights are extrapolated from the AR. However, the extrapolation must account for the fact that, by construction, the origin of the nonprompt lepton in the SR is unknown. Consequently, the weighting procedure must consider the various combinatorial possibilities for identifying which lepton is nonprompt in the SR. Moreover, the complexity of this combinatorial approach increases with the number of selected leptons, as the number of possible configurations grows. A compact and mathematically elegant expression for computing this extrapolation factor was derived in Ref. [93] and is adopted in this thesis. For completeness, the formula is reproduced in equation 6.4.

$$N_{T_1,\ldots,T_N} = -\sum_{t \in \mathbb{Z}_2^N, t \neq 0} \left[\prod_{i=1}^{N} \left((-1)^{t[i]} \frac{f_i^{t[i]}}{1 - f_i^{t[i]}} \right) \cdot N_t \right] \tag{6.4}$$

Here, $\mathbb{Z}_2^N$ denotes the product space of N individual $\mathbb{Z}_2$ subspaces, where each $\mathbb{Z}_2$ represents the two possible states of a given lepton: either passing or failing the tight selection criteria. The variable t specifies the configuration of leptons that pass or fail the tight requirements in the AR. Additionally, $N_{T_1,\ldots,T_N}$ represents the predicted number of nonprompt leptons that pass the tight criteria in the SR, while N_t corresponds to the number of events with the same configuration of tight and not-tight leptons, arranged in the exact positions defined by t.

As a result of these considerations, the NR can be interpreted as the probability that a given reconstructed lepton is nonprompt, with this probability being influenced by the lepton kinematics. This behavior is expected, as discussed in Section 5.2.3, since nonprompt leptons tend to be softer than prompt ones; and the measurement accounts for this effect accordingly.

6.2.3 Charge misidentification background

Charge misidentification is particularly relevant in the $\mathrm{t\bar{t}W}$ analysis, as the defining feature of the 2ℓss region is the requirement for two same-sign leptons. This distinction is crucial for separating multilepton $\mathrm{t\bar{t}W}$ events from the much more abundant dileptonic $\mathrm{t\bar{t}}$ events, which typically produce opposite-sign lepton pairs. Given that the $\mathrm{t\bar{t}}$ dilepton production cross-section is approximately three orders of magnitude larger than that of $\mathrm{t\bar{t}W}$, it is essential to control charge misidentification to prevent overwhelming contamination from $\mathrm{t\bar{t}}$ events.

The 2ℓss signal region receives a contribution from events with an opposite-sign lepton pair in which the electric charge of one of the leptons has been mismeasured. This charge is determined by the curvature of the tracks traversing the detector, and any mismeasurement of this curvature can result in a misassignment of the charge of the lepton. Electrons interact with the detector through Bremsstrahlung, emitting photons that alter the curvature of the track. These radiated photons can also convert into an electron-photon pair, further distorting the curvature measurement. Although these effects are largely suppressed by the triple charge consistency requirement detailed in Section 6.1.1, a significant electron charge misidentification rate remains.

The charge misidentification rate is measured by comparing the true and reconstructed charge for leptons in $\mathrm{Z} \to \ell^+\ell^-$ and $\mathrm{t\bar{t}}$ MC samples, for leptons that pass the tight selection criteria outlined in Section 5.2.4, in events containing two such leptons. The charge misidentification rate is defined as the probability that the reconstructed charge of a lepton differs from its charge at the generator level. It is parameterized as a function of lepton p_T and $|\eta|$. The charge misidentification contribution is determined by scaling opposite-sign events in this region by the charge misidentification rates. The factor for an event is given by the probability that the charge of one electron is incorrectly measured, while the charge of the other selected electron is correctly measured. Based on this premise, the event weight from equation 6.5 is derived.

$$w = p_1(1 - p_2) + p_2(1 - p_1) \tag{6.5}$$

Here, p_1 is the probability that the charge of the first electron is assigned the wrong charge, and p_2 is the probability that the charge of the second electron is mismeasured. Since the charge misidentification probabilities for muons are negligible, the misidentification probabilities for muons are set to zero.

6.3 Validation of the background estimations

To ensure that the background estimation techniques perform as expected and do not introduce biases in the signal extraction, several validation regions (VRs) are defined. The primary objective of these VRs is to establish an orthogonal phase space to the SR, where the dominant contribution originates from the background rather than the signal. This approach is a standard practice in the early stages of an analysis, as it provides a robust way to compare predictions with data without looking at signal-enriched regions.

The VRs are categorized based on the number of selected leptons, considering cases with 2ℓ, 3ℓ, and 4ℓ. Each VR is designed to specifically target a dominant background process, allowing for a systematic validation of the estimation techniques. Some of these VRs also serve as a basis for defining control regions (CRs), which play a crucial role during signal extraction. Unlike VRs, which are primarily used for checking the overall agreement of a certain background dominated phase space with the data, CRs are actively incorporated into the signal extraction process to constrain the dominant backgrounds and mitigate their impact on the SR.

A detailed breakdown of the validation and control regions, including their specific definitions and intended roles in the analysis, is provided in the following subsections. The regions that are described in this section have been used in both the inclusive and differential measurements. For illustration purposes, only the results for the tight method are shown.

6.3.1 Backgrounds with 2ℓ

The purpose of the 2ℓ validation region is to assess the accuracy of the nonprompt background prediction. This region is defined by inverting the selection requirement on the number of central jets that was originally used to define the 2ℓss region in Table 6.1.1. In addition, the b tag requirement is made so that at least one of the selected jets passes the medium WP.

Several key distributions illustrating the level of agreement between the predicted and observed nonprompt background contributions are shown in Figure 6.2, demonstrating the reliability of the method. The observed agreement serves as a proof that the method is properly predicting the amount of nonprompt, and that any discrepancy with the data is fairly covered by the considered uncertainties, which are further discussed in Section 6.4.

Similarly, the predictions for the charge misidentification background are validated using a dedicated validation region. This region uses a similar selection to the one in the 2ℓss signal region. In this case, both leptons are required to be electrons, and instead of

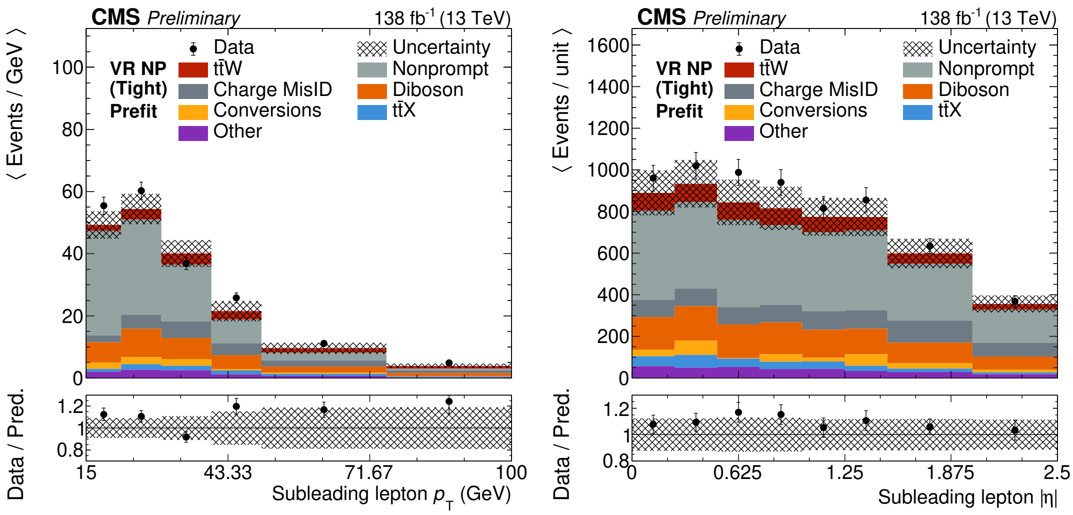

FIGURE. 6.2: Distributions of the lepton p_T (left) and $|\eta|$ (right) for the subleading lepton in the 2ℓ validation region. The coloured histograms represent the different processes considered, stacked one top of each other, whereas the black markers represent the data. The ratio panels show the ratio between data with respect to the sum of the predicted distributions. The vertical lines on the data points represent the statistical uncertainty in the data and the hatched band corresponds to the total uncertainty in the prediction.

vetoing events where the mass of the two electrons is within the Z mass peak, the mass of the di-electron system is required to be within 10 GeV of the Z mass. The jet multiplicity and b tag multiplicity requirements are also dropped. Figure 6.3 shows some kinematic variables in the validation region after the weight factors detailed in Section 5.2.3.1 are applied, demonstrating good agreement between data and prediction both in the total rate and the kinematic distributions.

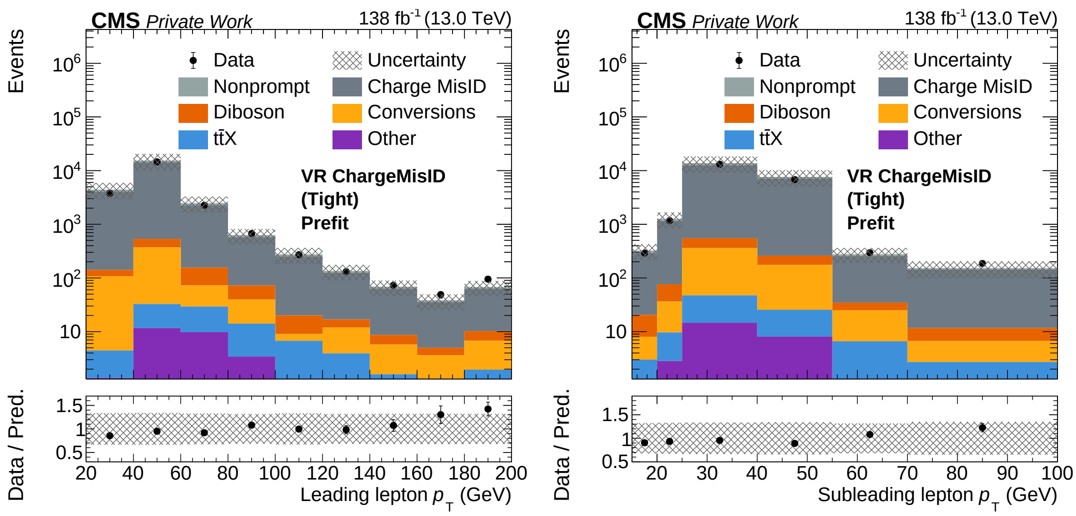

FIGURE. 6.3: Distributions of the cone-p_T (left) for the leading (left) and subleading (right) lepton in the 2ℓ validation region for the charge misidentification background. The ratio panels show the ratio between data with respect to the sum of the predicted distributions. The vertical lines on the data points represent the statistical uncertainty in the data and the hatched band corresponds to the total uncertainty in the prediction.

6.3.2 Backgrounds with 3ℓ and 4ℓ

A VR is built upon the 3ℓ selections of the 3ℓ SR, considering in this case the inversion of Z veto as the requirement used to orthogonalize the selection with respect to the SR. These considerations allow for an enrichment on diboson and $t\bar{t}Z$ backgrounds. Several kinematic observables of interest for the leptons are shown in Figure 6.4, separated into regions of low and high jet multiplicities, which are enriched in WZ and $t\bar{t}Z$, respectively. In both cases, the validation region selections are inclusive in terms of the number of b tags. The results demonstrate overall good agreement between the data and the predictions across all the observables, confirming the validity of the background control strategy.

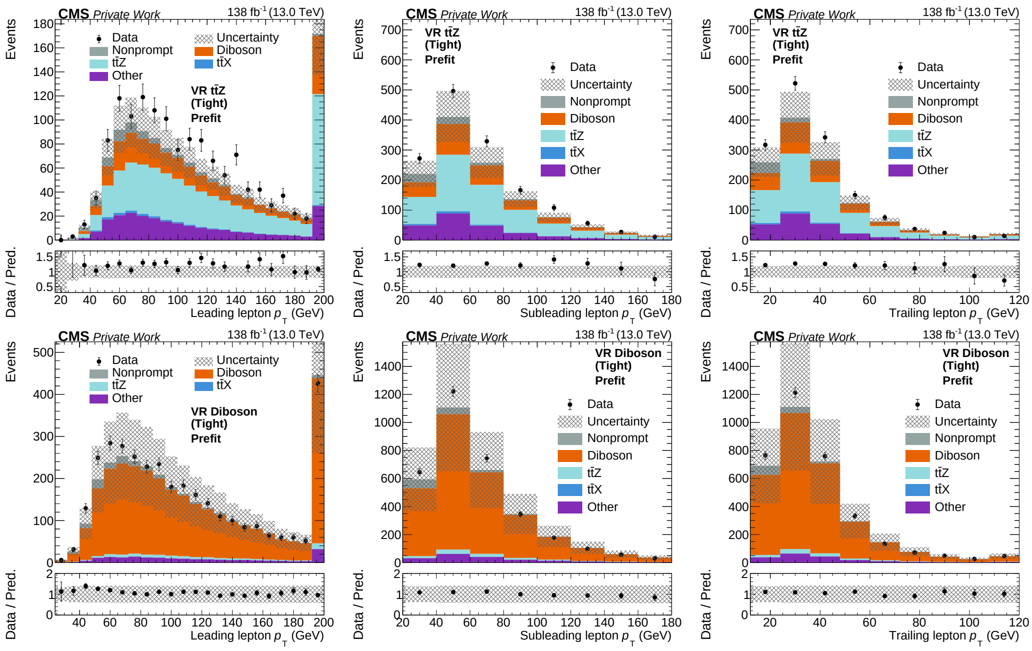

FIGURE. 6.4: Distributions of the lepton cone p_T for the first (left column), second (middle column), and third (right column) leptons in the 3ℓ VR. The coloured histograms represent the different processes considered, stacked one top of each other, whereas the black markers represent the data. The ratio panels show the ratio between data with respect to the sum of the predicted distributions. The vertical lines on the data points represent the statistical uncertainty in the data and the hatched band corresponds to the total uncertainty in the prediction. The upper row correspond to high jet multiplicity bins, dominated by $t\bar{t}Z$ background, while the bottom row correspond to low jet multiplicity bins, dominated by WZ background.

A control region to monitor the contributions of the WZ and $t\bar{t}Z$ backgrounds is derived from this validation region. This region is defined by relaxing the specific requirements on the jet multiplicity and b tagging, allowing for a broader phase space where both backgrounds can be more clearly distinguished. Events are then categorized based on the number of jets and b tags in the final state, exploiting the distinct jet and b tag multiplicities between the $t\bar{t}Z$ and WZ backgrounds.

In addition, a CR with 4ℓ in the final state is defined to constraint the effect of the ZZ background, as well as a minor component of $t\bar{t}Z$. This region is extremely pure in ZZ, with almost no contribution from other processes. A similar classification based on the number of reconstructed Z candidates (with a minimum requirement of one Z candidate), and the number of jets and b tags, is used. The used distributions, in this case for the loose method selections, can be found in Figure 6.5.

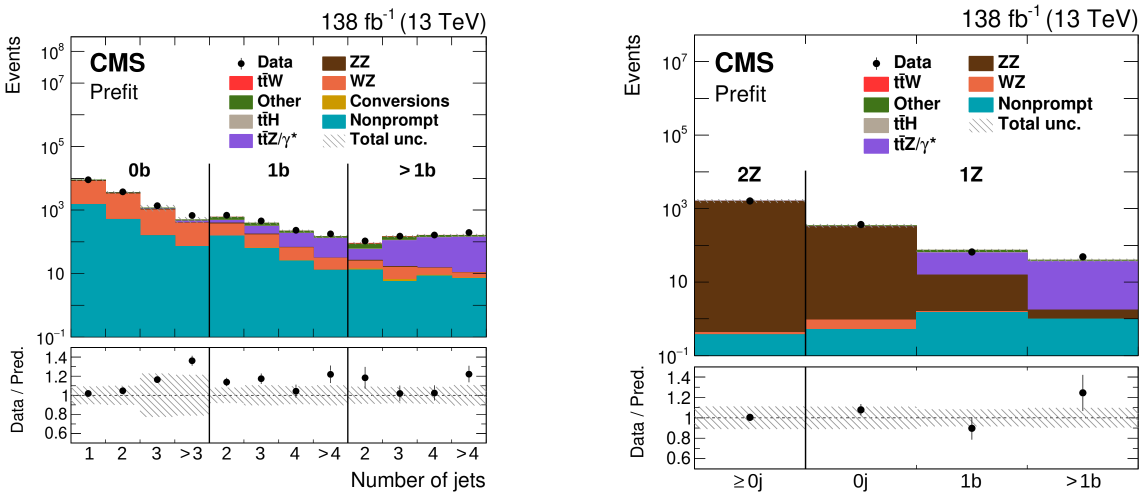

FIGURE. 6.5: Distribution for the number of selected jets and b tagged jets in the CRs for 3ℓ (left) and 4ℓ (right). The coloured histograms represent the different processes considered, stacked one top of each other, whereas the black markers represent the data. The ratio panels show the ratio between data with respect to the sum of the predicted distributions. The vertical lines on the data points represent the statistical uncertainty in the data and the hatched band corresponds to the total uncertainty in the prediction. For the 3ℓ CR, events with no b-tagged jets are classified into bins 1 to 4, events with one b-tagged jet into bins 5 to 8, and events with more than one b tag into bins 9 to 12. In the case of the 4ℓ CR, the first bin contains events with two reconstructed Z, and the last three bins contain events where at least there is one reconstructed Z boson.

6.4 Systematic uncertainties

In addition to the systematic uncertainties discussed in Section 5.4.3, further sources of uncertainty arise in the $t\bar{t}W$ measurement, primarily due to the different background estimation techniques employed. The treatment of the systematic uncertainties is also shared between the inclusive and differential cross section measurements, so the descriptions provided in the following are valid for both.

A major source of systematic uncertainty stems from the estimation of the nonprompt background. A key contribution to this uncertainty originates from the contamination of the NR measurement by residual prompt processes when fitting $m_{\mathrm{T}}^{\mathrm{fix}}$. To account for this, three independent methods are used to subtract the prompt contributions. While these methods generally yield consistent results within statistical uncertainties, driven by the dataset size in the AR, an additional systematic uncertainty is assigned as a function of the lepton cone-p_{T} and η. These effects are included as shape uncertainties that range from 10% to 40%, depending on the lepton p_{T}, η, and flavour. Additionally, the statistical uncertainty from the limited dataset size in the MR is propagated as an extra component of the nonprompt background uncertainty. Finally, non-closure effects observed in simulation contribute an additional uncertainty, ranging from 5% to 30%, applied as a flat uncertainty depending on the lepton flavor.

The uncertainty on the charge misidentification prediction, derived from data, is assigned a flat 30% uncertainty, independent of electron kinematics. This choice accounts for observed discrepancies between data and simulation when applying the charge misidentification rates in the validation regions, as described in Section 6.3.

Two additional sources of uncertainty are included to account for the mismodeling of the WZ and ZZ processes as a function of the number of jets and b-tagged jets, as observed in the three-lepton and four-lepton CRs [94], and confirmed from Figure 6.5. The first introduces a 10% uncertainty per selected jet, up to a maximum of 50%. The second applies a 10% uncertainty on event yields for events with zero or one b-tagged jet and a 40% uncertainty for events with two or more b-tagged jets.

The normalizations for the WZ, $\mathrm{t\bar{t}Z}$, and ZZ backgrounds are parametrized in the likelihood as freely floating parameters, which are then constrained by data from the CRs defined in Section 6.3. This approach allows to mitigate potential biases in the signal extraction performed in the SR due to possible mismodelings on these backgrounds, while also enabling the estimation of the final impact of their normalizations through the post-fit uncertainties obtained in the profiled likelihood fit.

Several rate uncertainties are considered for the background normalization. The dominant background, $\mathrm{t\bar{t}H}$, is constrained within 20% [94]. The $\mathrm{t\bar{t}}\gamma$ normalization includes an 8% uncertainty [95], with an additional 30% uncertainty for photon conversion mismodeling [96]. The tHq and tHW backgrounds each carry a 50% uncertainty [25], while tZq has a 10% uncertainty [97]. The $\mathrm{t\bar{t}XX}$, (dominated by four-top production) and triboson (dominated by WWW) backgrounds are assigned 50% uncertainties, reflecting experimental precision at the time [98, 99]. Other minor backgrounds are also constrained within 50%, conservatively accounting for extrapolation effects in kinematic regions with high jet and b tag multiplicities.

6.5 Inclusive $\mathrm{t\bar{t}W}$ cross section measurement

The measurement of the $\mathrm{t\bar{t}W}$ inclusive cross section represents the most precise measurement of this quantity, and it is performed using the full Run 2 dataset of the CMS experiment, and the considerations for the loose method that were described in the previous sections. The relevance of this measurement stems from previously reported discrepancies between the latest theoretical predictions for $\mathrm{t\bar{t}W}$ production and experimental data, which are confirmed by these results. Moreover, this result is in good agreement with the corresponding measurement from ATLAS [100].

6.5.1 Signal extraction methodology

After properly addressing all aspects of the analysis strategy, including object definition, phase space definition through an event selection strategy, and the treatment of systematic uncertainties, one needs to define the approach in which signal will be discriminated from background. Specifically, the inclusive cross-section measurement is performed using a simultaneous likelihood fit to both the 2ℓss and 3ℓ regions detailed in Section 6.1.1. Additionally, the fit incorporates the three-lepton and four-lepton control regions discussed in Section 6.3.

6.5.1.1 Signal discrimination in the 2ℓss channel

In the 2ℓss channel, a multivariate approach is employed to enhance the separation between signal and background. At the early stages of the measurement, two optimization methodologies were explored to maximize the signal sensitivity: a BDT and a neural network (NN) with multiple output nodes. Both models were trained using a set of discriminating variables that included the reconstructed kinematics of leptons and jets, the presence of additional jets, and their b tagging scores. Although the performance gains were marginal, the final decision was to use the NN-based approach. Some of the input variables that were used in the training can be found in Figure 6.6. Overall agreement is observed in the input variables.

The neural network was designed to differentiate the signal process from the two dominant background contributions: nonprompt leptons (primarily from semileptonic $\mathrm{t\bar{t}}$ decays) and other $\mathrm{t\bar{t}X}$ processes ($\mathrm{t\bar{t}H}$, $\mathrm{t\bar{t}Z}$, and $\mathrm{t\bar{t}}\gamma$). To ensure unbiased results, 20% of the signal and 15% of the background simulated samples were reserved exclusively for training and excluded from the rest of the measurement.

The NN architecture consists of two hidden layers with 128 and 64 nodes, respectively, followed by an output layer with four nodes, corresponding to nonprompt leptons, $\mathrm{t\bar{t}X}$ ($\mathrm{t\bar{t}Z}$ and $\mathrm{t\bar{t}H}$), $\mathrm{t\bar{t}}\gamma$, and $\mathrm{t\bar{t}W}$ processes. The hidden layers use the rectified linear unit (RELU) activation function, which outputs the input value when positive and zero otherwise. The output layer employs a SOFTMAX activation function, ensuring that the outputs are positive and sum to one. To mitigate overtraining, a dropout layer is applied after the hidden layers, randomly setting half of the inputs to zero during training. The neural network is optimized using the ADAM algorithm with a learning rate of 0.0015, minimizing the categorical cross-entropy loss function over 20 epochs. Finally, the classifier output is transformed based on the quantiles of the total expected background, ensuring that the background distribution decreases linearly. This transformation is applied to optimize the binning of the final discriminant.

The output distribution of the NN is categorized into 12 different channels, defined by lepton flavor (e, μ) and final-state charge ($++$, $---$), considering only light leptons. Figure 6.7 shows distributions of the NN output score for the $\mathrm{t\bar{t}W}$ node, where for

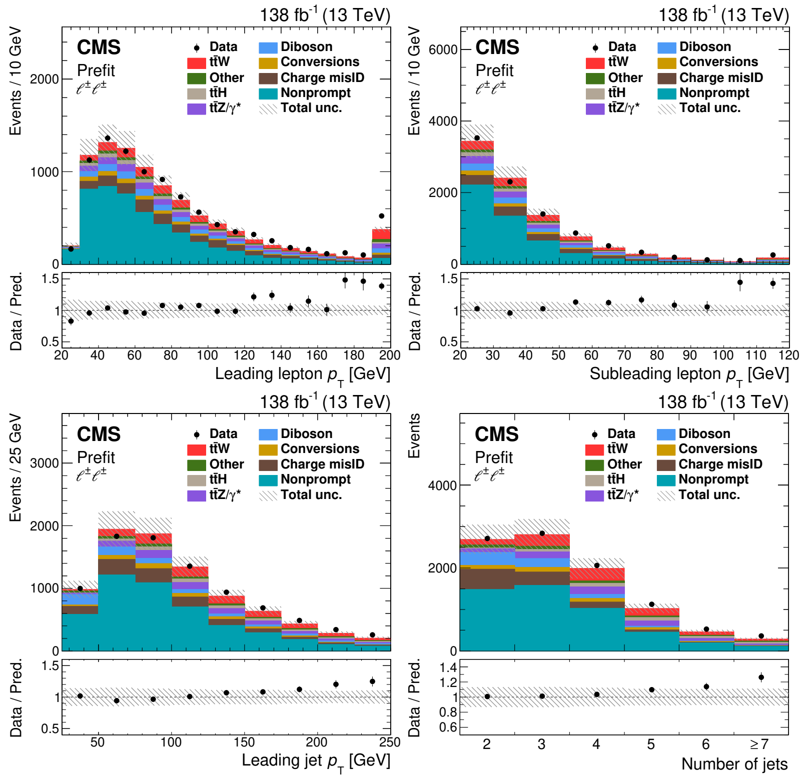

FIGURE. 6.6: Distributions of the leading (upper left) and subleading (upper right) lepton p_{T}, the leading jet p_{T} (lower left), and the number of jets (lower right) in the 2ℓss SR used for the inclusive measurement. The coloured histograms represent the different processes considered, stacked one top of each other, whereas the black markers represent the data. The ratio panels show the ratio between data with respect to the sum of the predicted distributions. The vertical lines on the data points represent the statistical uncertainty in the data and the hatched band corresponds to the total uncertainty in the prediction.

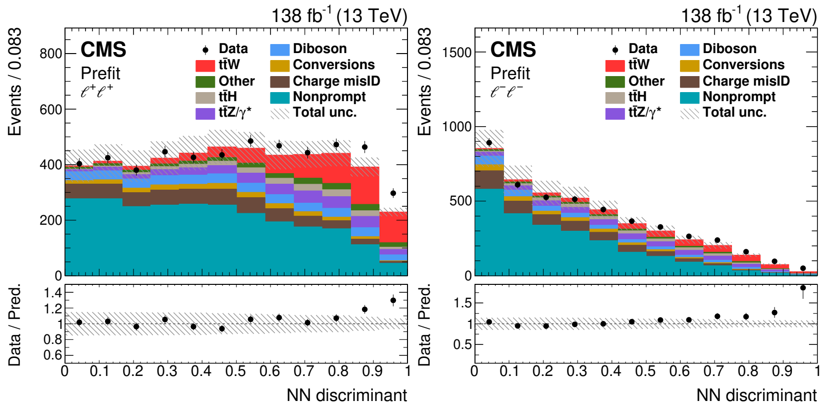

FIGURE. 6.7: Distributions of the NN output score shown separately for final states with two positively charged leptons (left), and two negatively charged leptons (right), in the 2ℓss SR used for the inclusive measurement. The coloured histograms represent the different processes considered, stacked one top of each other, whereas the black markers represent the data. The ratio panels show the ratio between data with respect to the sum of the predicted distributions. The vertical lines on the data points represent the statistical uncertainty in the data and the hatched band corresponds to the total uncertainty in the prediction.

illustration purposes, events are grouped based solely on final-state charge, without distinguishing lepton flavors. These distributions serve as inputs for the signal extraction fit performed in the 2ℓss region.

6.5.1.2 Strategy for the 3ℓ channel

The amount of background processes that can yield three prompt leptons in the final state is limited. Given the excellent performance of the CMS detector, it is also highly unlikely that background processes such as semileptonic $\mathrm{t\bar{t}}$ or QCD-like backgrounds contaminate these selections. In contrast, due to the relatively low branching ratio of $\mathrm{W} \to \ell\nu$, the 3ℓ signal region is more statistically limited than the 2ℓss region. Therefore, the analysis strategy must be adapted to ensure good sensitivity despite the reduced event yield.

The strategy for the 3ℓ channel relies on a categorization approach based on the number of jets, medium b tags, and the total lepton charge of the final-state leptons. This results in subcategories with different sensitivity and background composition. A total of 12 categories are defined, as shown in Fig. 6.8.

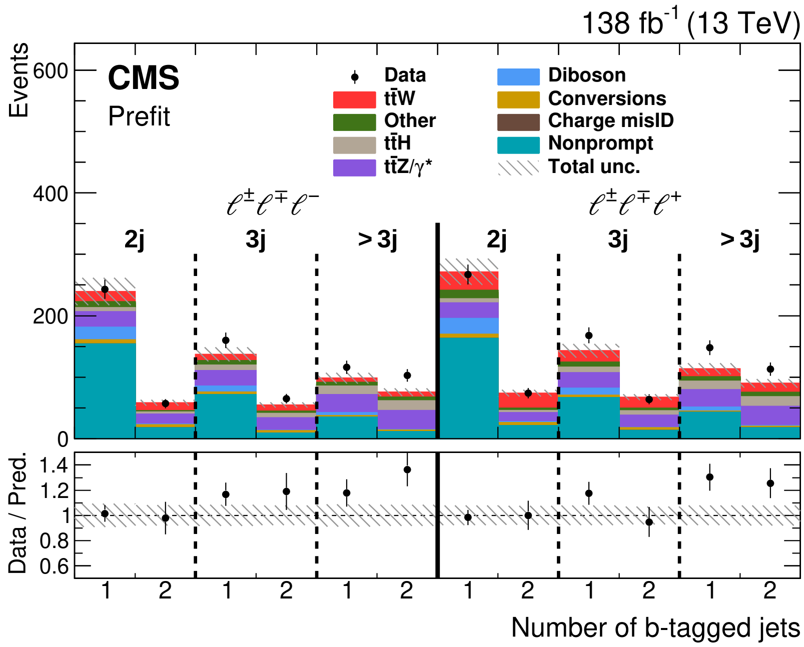

FIGURE. 6.8: Distribution of the number of medium b-tagged jets for events in the 3ℓ SR, for different numbers of jets. Events with total 3ℓ charge -1 and $+1$ are shown in the left and right halves of the plot, respectively. The coloured histograms represent the different processes considered, stacked one top of each other, whereas the black markers represent the data. The ratio panels show the ratio between data with respect to the sum of the predicted distributions. The vertical lines on the data points represent the statistical uncertainty in the data and the hatched band corresponds to the total uncertainty in the prediction.

For each category, a common single discriminant variable and binning are chosen across all subcategories and years to define the set of bins used for the joint maximum likelihood fit employed in the signal extraction. Several observables have been studied as

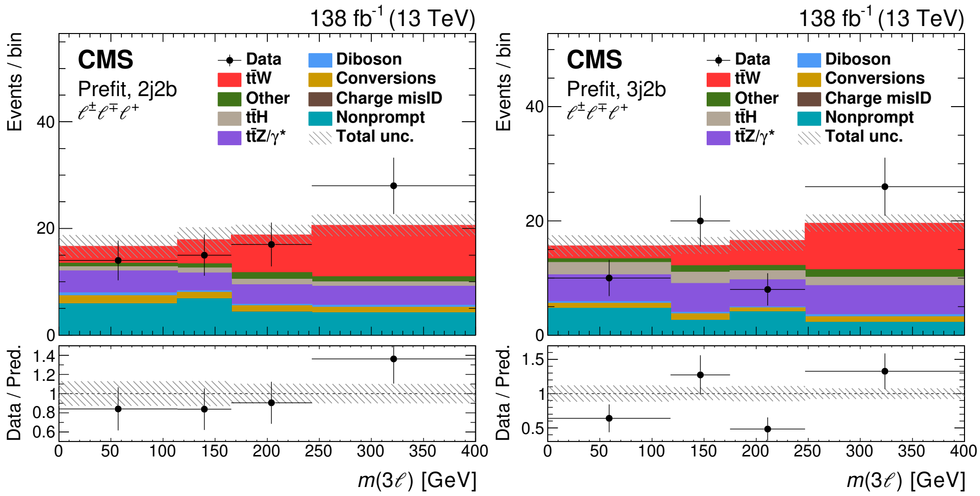

FIGURE. 6.9: Distributions of the three-lepton invariant mass are displayed in final states with two (left) and three (right) jets, of which exactly two pass the medium b tagging requirements, in the 3ℓ SR of the inclusive measurement. The coloured histograms represent the different processes considered, stacked one top of each other, whereas the black markers represent the data. The ratio panels show the ratio between data with respect to the sum of the predicted distributions. The vertical lines on the data points represent the statistical uncertainty in the data and the hatched band corresponds to the total uncertainty in the prediction.

potential discriminant variables for this channel, and the most sensitive observable has been chosen for the final measurement in combination with the dilepton channel. The observables that were tested included: $p_{\mathrm{T}}^{\mathrm{miss}}$, the sum of the transverse momentum of the three leptons (p_{T}^{3l}), the invariant mass of the three leptons (m_{3l}), the sum of the transverse momentum of the jets ($\mathrm{H_T}$), and the minimal distance between leptons ($\min \Delta R$).

The sensitivity studies included a rebinning-based strategy in which the binning of the different observables was recomputed based on a flat profiling of the backgrounds across their spectrum. The goal was to minimize the number of bins in each observable to reduce statistical uncertainties in this channel, and to maximize profiling of the signal by leaving background contributions approximately flat. A compromise exists between the number of bins and the number of MC events per bin, ensuring that the chosen binning minimizes uncertainty while avoiding statistical limitations. Finally, the m_{3l} distribution, rebinned to consider four bins, was used for signal extraction in the 3ℓ channel. Figure 6.9 shows the m_{3l} distribution (four bins) for the most significant categories with two and three jets with two b-jets, split by lepton total charge.

6.5.2 Cross section results

The final $\mathrm{t\bar{t}W}$ cross section is extracted from a maximum likelihood fit to the 8 different NN distributions from the 2ℓss SR, the 12 $m_{3\ell}$ distributions in the 3ℓ SR, as well as the 3ℓ and 4ℓ CRs from Figure 6.5.

To account for potential discrepancies across different data taking years, the fit is performed separating the dataset in the 2016, 2017, and 2018 datasets. All systematic uncertainties are treated as *a priori* uncorrelated sources of uncertainty in the final result. The importance of each source of uncertainty, the average uncertainties from different sources are shown in Table 6.5.2. The total systematic uncertainty is 5.8%, with the dominant source being the non-prompt background estimation, followed by the charge misidentification uncertainty, and the modeling of low cross-section processes (grouped in the "Other" category).

The cross-section results for each separate 2ℓss and 3ℓ channel, in all cases considering the three- and four-lepton control regions, are shown in Figure 6.10.

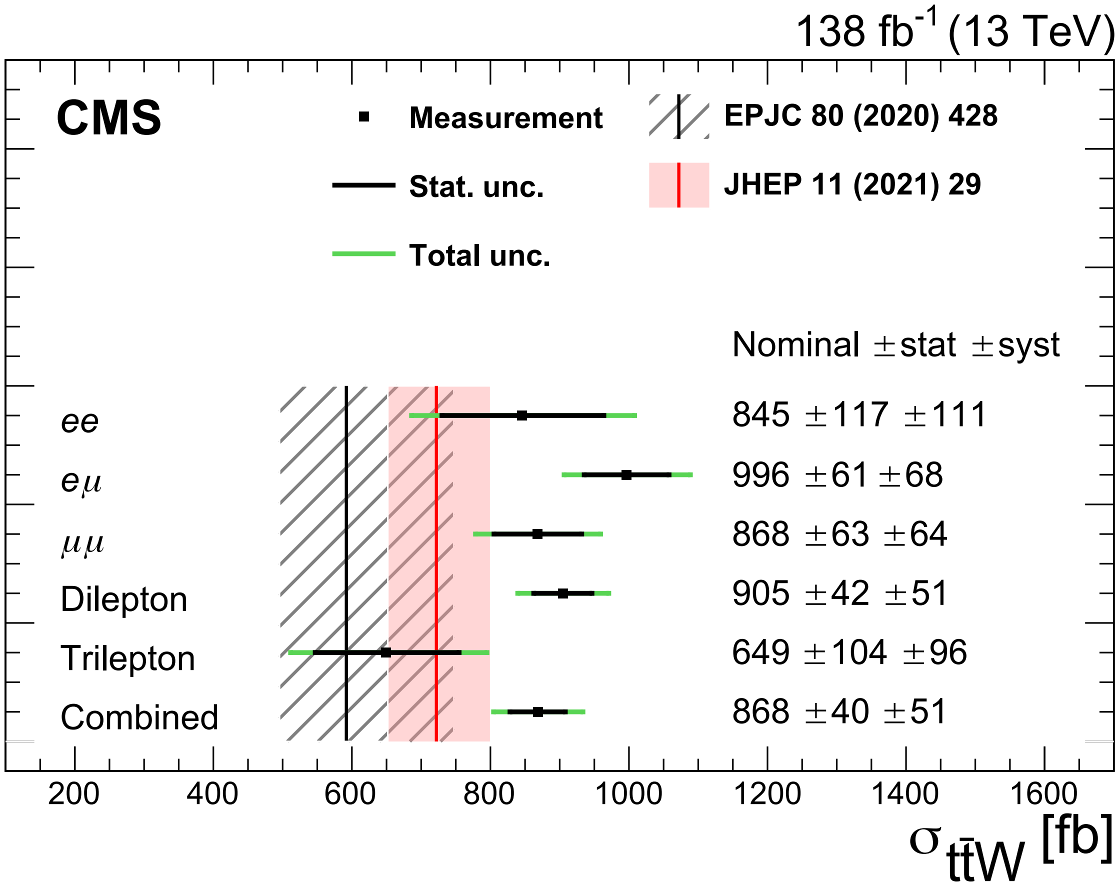

FIGURE. 6.10: Measured $t\bar{t}W$ production cross section for the individual dilepton (ee, eμ, $\mu\mu$, and combined) channels and the trilepton channel, as well as their combination. The inner black bars show the statistical uncertainty, and the outer green bars give the total uncertainty. The predictions from two SM calculations are shown by the black and red vertical lines, with the associated bands corresponding to the total uncertainty.

The combined result is found to be consistent with the measurements performed in each separate channel, within the uncertainties. Furthermore, the result exhibits a slight tension with the latest theoretical predictions for the $t\bar{t}W$ process at the time of publication.

Table 6.5.2: Sources of systematic uncertainty in the predicted signal and background event yields with their impact on the measured $t\bar{t}W$ production cross section, estimated after the fit to the data. Only systematic uncertainty sources with values greater than 0.1% are included in the table. The production cross sections of the $t\bar{t}W$, WZ, ZZ, and $t\bar{t}Z$ processes are simultaneously constrained in the fit. The second-to-last row refers to the statistical uncertainty in the simulated event samples.

Source	Uncertainty [%]
Experimental uncertainties	
Integrated luminosity	1.9
b tagging efficiency	1.6
Trigger efficiency	1.2
Pileup reweighting	1.0
L1 inefficiency	0.7
Jet energy scale	0.6
Jet energy resolution	0.4
Lepton selection efficiency	0.4
Background uncertainties	
$t\bar{t}H$ normalization	2.6
Charge misidentification	1.6
Nonprompt leptons	1.3
VVV normalization	1.2
$t\bar{t}XX$ normalization	1.2
Conversions normalization	0.7
$t\bar{t}\gamma$ normalization	0.6
ZZ normalization	0.6
Other normalizations	0.5
$t\bar{t}Z$ normalization	0.3
WZ normalization	0.2
tZq normalization	0.2
tHq normalization	0.2
Modeling uncertainties	
$t\bar{t}W$ scale	1.8
$t\bar{t}W$ color reconnection	1.0
ISR & FSR scale for $t\bar{t}W$	0.8
$t\bar{t}\gamma$ scale	0.4
VVV scale	0.3
$t\bar{t}H$ scale	0.2
Conversions	0.2
Simulation statistical uncertainty	1.8
Total systematic uncertainty	5.8

6.6 Differential $t\bar{t}W$ cross section measurement

Following the inclusive cross section measurement, which confirmed mild tensions between experiment and theory, differential measurements were performed. The goal of doing differential measurements is to parametrize detector effects in a way that allows for an accurate reconstruction of the true value of the observables at the time where the particle was produced. The procedure of extracting true level quantities (defined at generator level) from reconstructed level quantities (defined at detector level) is known as "unfolding". The idea of the unfolding is to parametrize discrete observables, represented as histograms, following equation 6.6

$$y_i = A_{ij} x_j \tag{6.6}$$

where y_i and x_j are the observables, under a histogram representation, at the detector and unfolded level, respectively. A_{ij} is known as the response matrix, and it is used to parametrize the response of the detector. It gives the probability for an event generated in the bin j of the generator level distribution to be measured in the bin i of the detector-level distribution.

The unfolding can be performed at different stages of the generator level steps, typically at the "parton level" or "particle level." Parton-level unfolding reconstructs the kinematics of objects produced in the hard scatter before they decay into final-state particles. Examples include the transverse momentum of the top quarks in $t\bar{t}$ or the transverse mass of the $t\bar{t}W$ system. Conversely, particle-level unfolding focuses on observables of objects produced after these decays, such as the kinematics of leptons from top quarks and W bosons, jet kinematics, and particle multiplicities based on flavor.

For the measurement presented in Ref. [15], a particle-level unfolding approach was adopted. As far as object and event selection, treatment of uncertainties and background estimation methods, the differential measurements are built upon the considerations that were given in the previous sections. Therefore, this section focuses on outlining the unfolding procedure in detail, and to present the results from said unfolding.

The signal model that is used to parametrize the response matrix is chosen based on the same signal sample that was outlined in Section 4.3.1, using the old FXFX merging scheme. Comparisons at generator level with the sample produced using the new FXFX scheme are presented for the first time in any analysis. For consistency among the comparisons, both samples are generated using a merging scale μ_Q =42 GeV, which is the nominal value used by CMS.

6.6.1 Unfolding procedure

The unfolding procedure is limited by the ability to invert the response matrix, A_{ij}. The response matrix may have a large dimension or be highly non-diagonal, making its diagonalization numerically complex. Several approaches can be employed to address this issue. In this analysis, a maximum-likelihood fit is chosen. The response matrix is indirectly applied or "unrolled" in the distribution to be unfolded. This is achieved by splitting the signal process into different particle-level bins for each detector-level bin, thus encoding all the information related to the response matrix in an indirect manner.

A key distinction from the inclusive cross-section measurement is that, in this case, each signal process defined at the particle level is associated with a parameter of interest in the likelihood fit, as described in Section 5.4. Instead of having a single parameter of interest that scales the $\mathrm{t\bar{t}W}$ normalization, there is a parameter of interest for each particle-level bin that scales the $\mathrm{t\bar{t}W}$ contribution. Apart from this conceptual difference, each parameter is treated in the same way. In this case, each observable is unfolded in a given SR, either 2ℓss or 3ℓ, but not both. In all cases including the CRs for 3ℓ and 4ℓ in the fit. The likelihood also incorporates all sources of uncertainty described in Section 6.4.

The main gain in using maximum-likelihood based unfolding, instead of other techniques normally used in particle physics, originates from the fact that in likelihood fits one is able to use the full power of the covariance matrix, which encodes not only the diagonal terms of the uncertainty, but also the correlation between the different nuisance parameters. This is particularly relevant in differential measurement, where the achieving good precision is extremely challenging.

6.6.2 Definition of the particle level

Unfolding is performed in a fiducial volume that matches the target signal definition. The definition of the fiducial region is designed to closely match the event selection criteria used in the analysis, thereby minimizing uncertainties associated with extrapolating from the folded to the unfolded phase spaces. This is done separately for the dilepton and trilepton signal regions, where the differential measurements are performed.

At the generator level, objects are defined using generator-level quantities. Generator leptons are "dressed" with nearby photons, close by $\Delta R < 0.1$, to recover the true momentum of those leptons that may have radiated photons. These leptons are referred to as "dressed" leptons. Generator-level jets are clustered using the same anti-k_T algorithm configuration as that used for detector-level jets. B quarks at this level are identified using a ghost-matching algorithm, which tags generator-level jets as b jets based on the presence of a b quark within the jet. The specific selection criteria for each region are summarized in Table 6.6.3.

It is possible that some events selected at the reconstructed level do not pass the fidu-

Table 6.6.3: Definition of the fiducial selection. The lepton related quantities refer to "dressed" leptons.

Requirement	2ℓss	3ℓ
Lepton definition	Dressed (e, μ)	Dressed (e, μ)
N_ℓ	2	3
$q_{\ell_1} = q_{\ell_2}$	✓	-
Lepton p_T (GeV)	$25, 15$	$25, 15, 15$
Number of jets	≥3	≥2
Number of b jets	≥1	≥1

cial level requirements. In such cases, $t\bar{t}W$ events that pass the detector-level requirements but fail to meet the fiducial level criteria are treated as a background source in the likelihood fits used for unfolding.

6.6.3 Selection of observables

The choice of observables is guided by their relevance in improving the understanding of the modeling of the $t\bar{t}W$ process. The complete list of observables that were considered is shown in Table 6.6.4.

Table 6.6.4: List of variables to be unfolded for both the 2ℓss and 3ℓ channels.

Variable	Description
Angles between objects	
$\lvert\Delta\eta(\ell_1, \ell_2)\rvert$	absolute difference in pseudorapidity between the two leading leptons
$\Delta R(\ell_1, \ell_2)$	separation in (η, ϕ) space between the two leading leptons
$\Delta R(\ell_1, \text{jet})$	separation in (η, ϕ) space between the leading lepton and its closest jet
Jet-related variables	
H_T	scalar sum of jet p_T
leading jet $\lvert\eta\rvert$	$\lvert\eta\rvert$ of the jet with highest p_T
leading jet p_T	p_T of the jet with highest p_T
subleading jet $\lvert\eta\rvert$	$\lvert\eta\rvert$ of the jet with next-to-highest p_T
subleading jet p_T	p_T of the jet with next-to-highest p_T
Lepton-related variables	
leading lepton p_T	p_T of the lepton with highest p_T
subleading lepton p_T	p_T of the lepton with next-to-highest p_T
lepton maximum $\lvert\eta\rvert$	maximum $\lvert\eta\rvert$ among the leptons
$\sum$ lepton p_T	sum of the lepton p_T's
m(ℓ_1, ℓ_2)	invariant mass of the system of the two leading leptons
Object multiplicity	
Jet multiplicity	number of jets

Angular observables, particularly those involving jets, provide sensitivity to the merging scheme used in the modeling of $t\bar{t}W$ production.

Jet-related observables primarily probe the accuracy of higher-order perturbative corrections. For instance, the p_T spectrum of the first few jets in $t\bar{t}W$ production is modeled with exclusive accuracy at NLO over most parts of the phase space, at scales higher than the merging scale. In contrast, the low p_{T} regime of the jet p_{T} should be modeled at LO by the real emission contributions in the lowest jet multiplicity sample that composes the $\mathrm{t\bar{t}W}$ sample. Because the new FXFX merging and matching scheme affected the region right below the merging scale, which in this case is set to μ_{Q} =42 GeV, it is of particular importance to look at these observables.

Lepton-related observables also exhibit sensitivity to higher-order QCD effects. Radiation emitted in the event alters the kinematics of the recoiling particles, thus impacting the energy available for lepton production. This is particularly relevant in the softer regime of lepton p_{T} distributions, where NLO effects play a significant role in shaping the spectrum.

Finally, **jet multiplicity** is a key observable in $\mathrm{t\bar{t}W}$ production, as it is directly influenced by the treatment of additional QCD radiation. One of the major improvements in the new FXFX merging scheme was its impact on this observable, allowing for a more accurate description of events with high jet multiplicities by incorporating additional radiation effects. Studying this observable provides insights into the effectiveness of these modeling improvements.

For illustration purposes, the unfolded results for a subset of the distributions considered in the measurements is presented. The observables shown were selected based on either their relevance to understanding the modeling of $\mathrm{t\bar{t}W}$, or the precision with which they are measured.

6.6.4 Validation of the binning

One of the most important aspects to ensure in the unfolding procedure is the diagonality of the response matrix, which can be optimized by selecting an appropriate binning strategy for both detector- and particle-level quantities. The choice of binning is validated by evaluating the purity and stability of the different unfolded distributions. Given a response matrix, $M(i, j)$, where i corresponds to a given particle-level bin and j corresponds to a given detector-level bin, the *purity* quantity is defined as the fraction of events in a given particle-level bin that are reconstructed within the corresponding detector-level bin. Similarly, *stability* is defined as the fraction of events in a detector-level bin that originate from the corresponding particle-level bin. These quantities are optimized in order to choose an optimal binning to perform the unfolding.

The response matrices for several observables measured in this thesis can be found in Figures 6.11 and 6.12 for the 2ℓss SR, and in Figure 6.13 for the two observables measured in the 3ℓ SR. The response matrices are reasonably diagonal, and no need of alternative techniques such as regularization is needed to ensure the stability of the unfolding. Slightly stronger migrations are reported in jet related observables, which originate mainly from resolution effects in the detector when measuring jets.

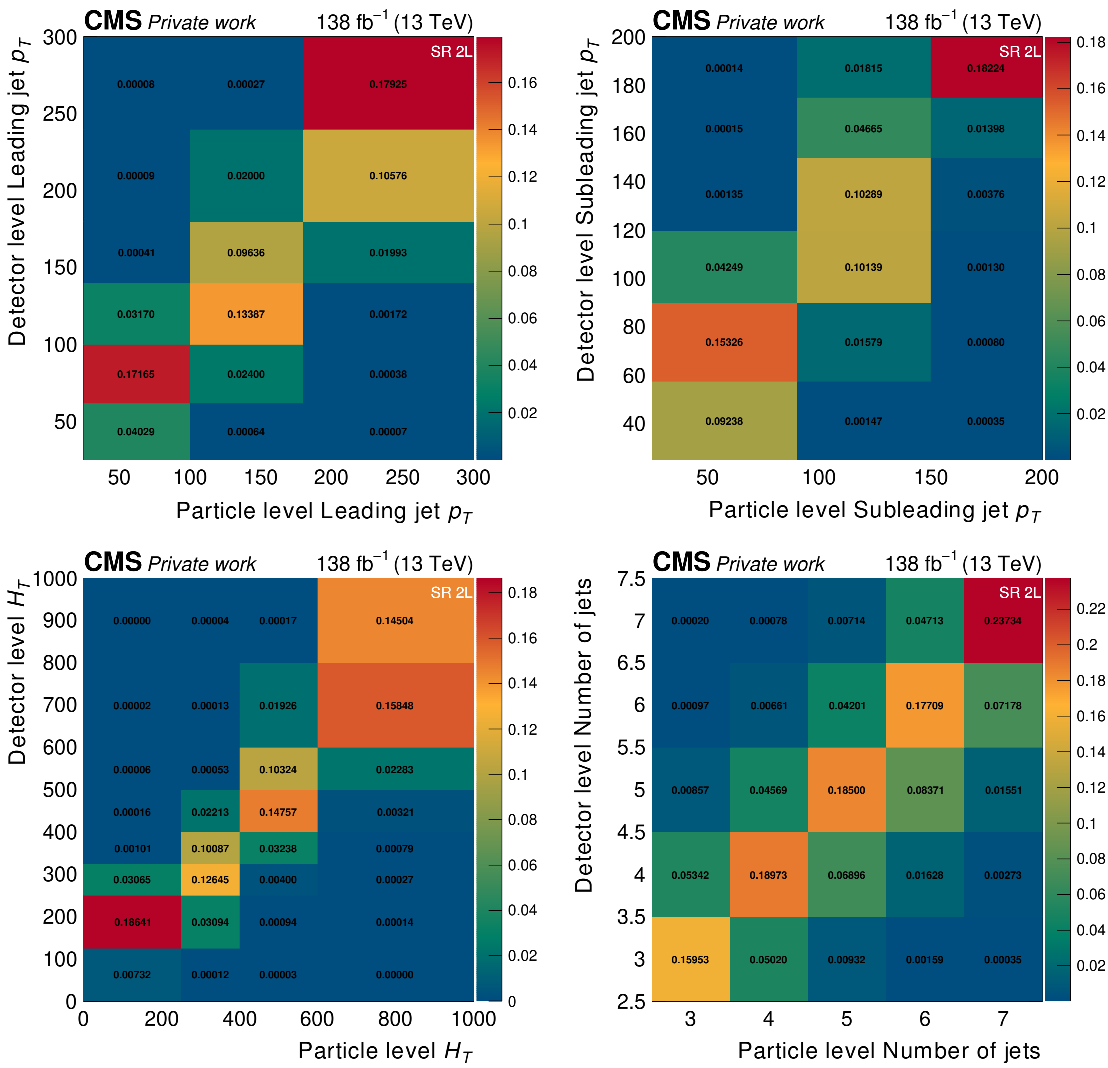

FIGURE. 6.11: Response matrices for four different observables unfolded to the particle level in the 2ℓss signal region. Observables are: leading jet p_T (top left), subleading jet p_T (top right), $\mathrm{H_T}$(lower left), and number of jets (lower right).

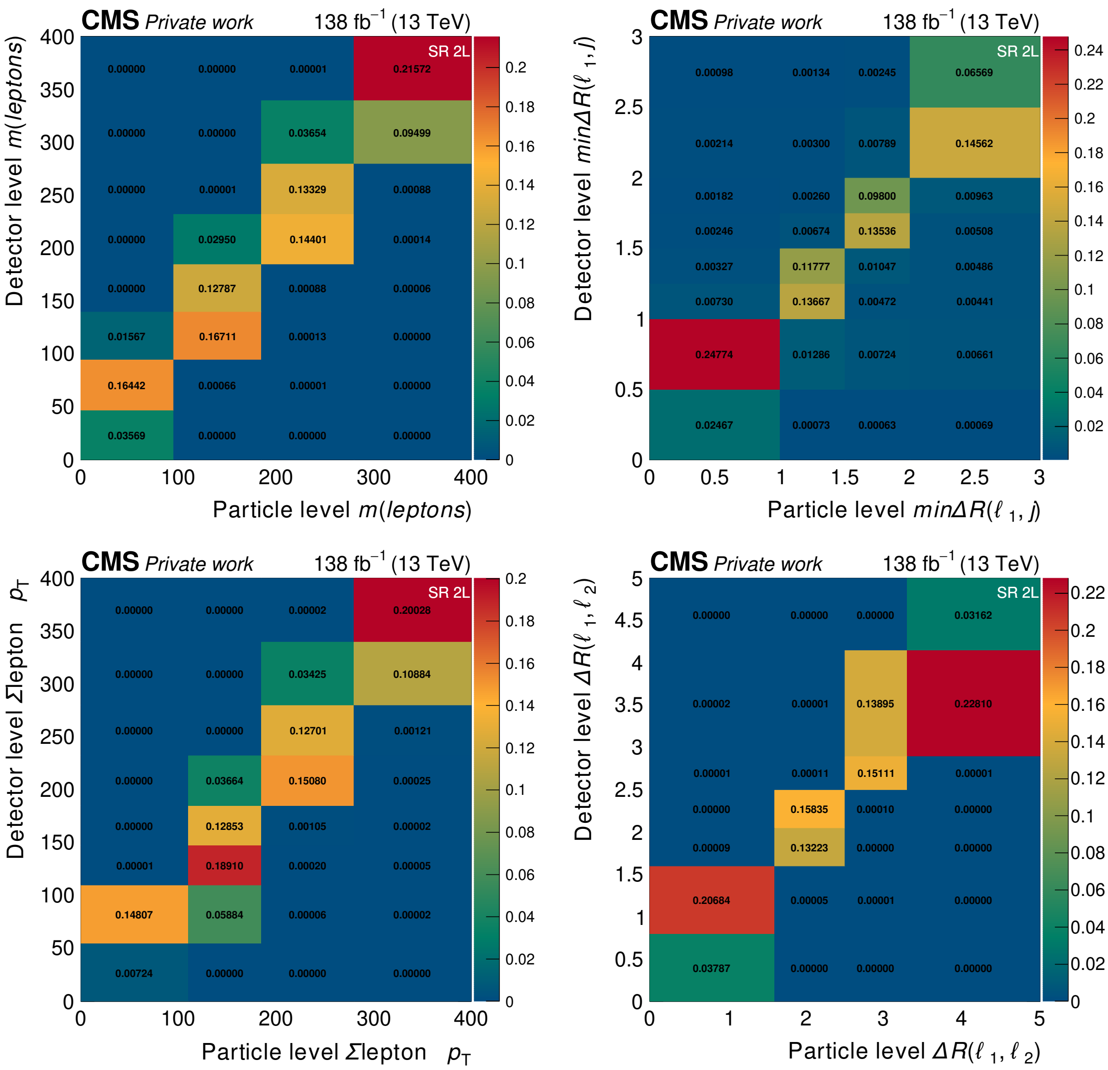

FIGURE. 6.12: Response matrices for four different observables unfolded to the particle level in the 2ℓss signal region. Observables are: invariant mass of the dilepton system (top left), minimum ΔR between the leading lepton and the jets (top right), summed p_{T} of the dilepton system (lower left), and ΔR between the two leptons (lower right).

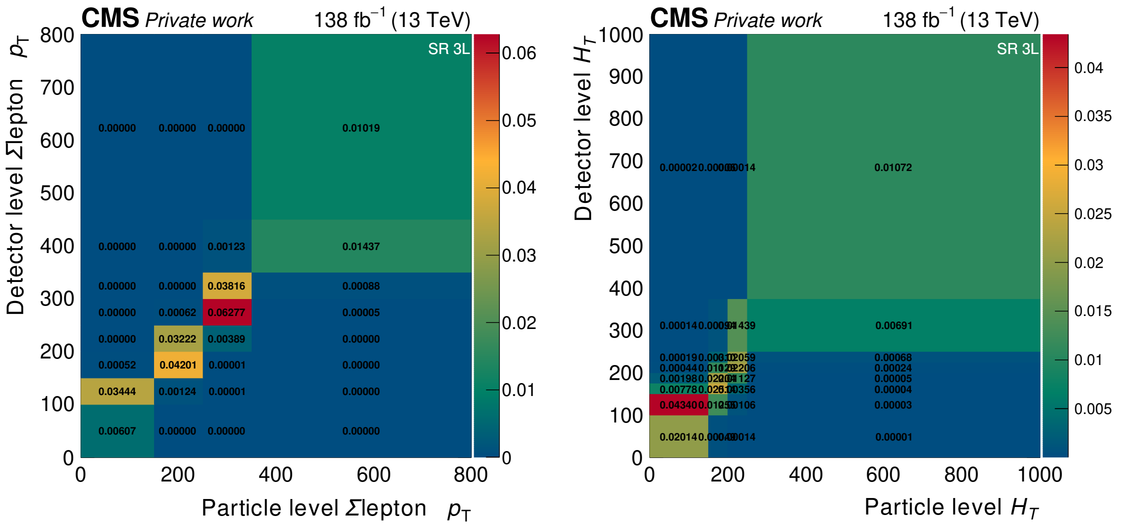

FIGURE. 6.13: Response matrices for four different observables unfolded to the particle level in the 3ℓ signal region. Observables are: summed p_{T} of the three lepton system (left), and $\mathrm{H_T}$(right).

6.6.5 Unfolding of observables

Before presenting the unfolding results, the observables at the detector level are examined. To do this, a likelihood fit is performed, as outlined in Section 6.6.1, to extract the scaling parameters for each of the generator-level signals modeling the $\mathrm{t\bar{t}W}$ contributions, as well as the postfit values of the nuisance parameters. The results of this fit are then propagated to the detector-level observables by scaling the signal contributions according to the scaling parameters derived from the likelihood fit performed in the main measurement, as well as by adjusting the background normalizations, which are also extracted from the same fit. Additionally, the full covariance matrix is considered in the propagation of uncertainties. This approach allows us to observe how the scaling of the signal influences the agreement at the detector level. Figure 6.14 shows the distributions for the same observables for which the response matrices were presented in the 2ℓss. Overall, a good level of agreement across all distributions is observed, even before any fit to the data has been applied. The signal contributions get scaled by an overall normalization factor of $\sim$20%, which is in agreement with the reported $\mathrm{t\bar{t}W}$ excess that was also shown in the inclusive cross section measurement.

The results for the unfolding of the same set of observables are shown in Figures 6.15 and 6.16, for the absolute and normalized differential cross section per measured bin, respectively. All the results are compared with the latest theory prediction that was covered in Section 4.3.1. The results are generally in agreement with the standard model prediction, within the allocated uncertainties, which are dominated by the statistical component. The unfolded data is in extremely close agreement with the newest $\mathrm{t\bar{t}W}$ modeling, which hints that further studies must be performed in order to find the reason for the mild tensions that are reported.

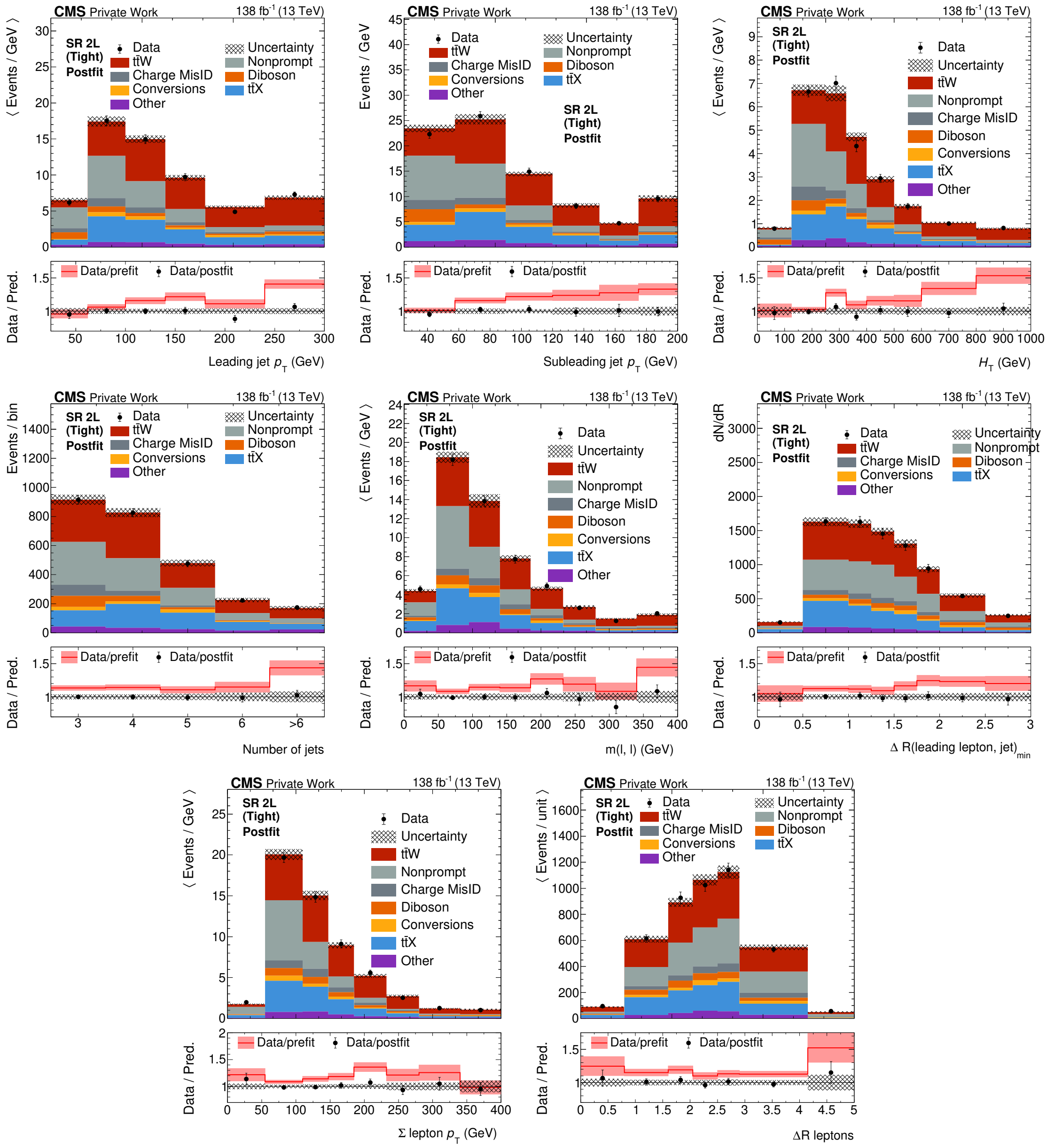

FIGURE. 6.14: Distributions for the leading jet p_{T} (upper left), subleading jet p_{T} (upper center), $\mathrm{H_T}$ (upper right), number of selected jets (middle left), invariant mass of the two lepton system (middle center), minimum ΔR between the leading lepton and the jets (middle right), summed p_{T} of the dilepton system (bottom left), and ΔR between the two leptons (bottom right). All distributions are shown after the fit to the data in the 2ℓss region, including the CRs for the main backgrounds. The coloured histograms represent the different processes considered, stacked one top of each other, whereas the black markers represent the data. The ratio panels show the ratio between data and total prediction before to the fit to the data (red line), with respect to the sum of the predicted distributions after the fit to the data. The vertical lines on the data points represent the statistical uncertainty in the data, and the hatched (filled) band corresponds to the total uncertainty in the prediction after (before) the fit to the data.

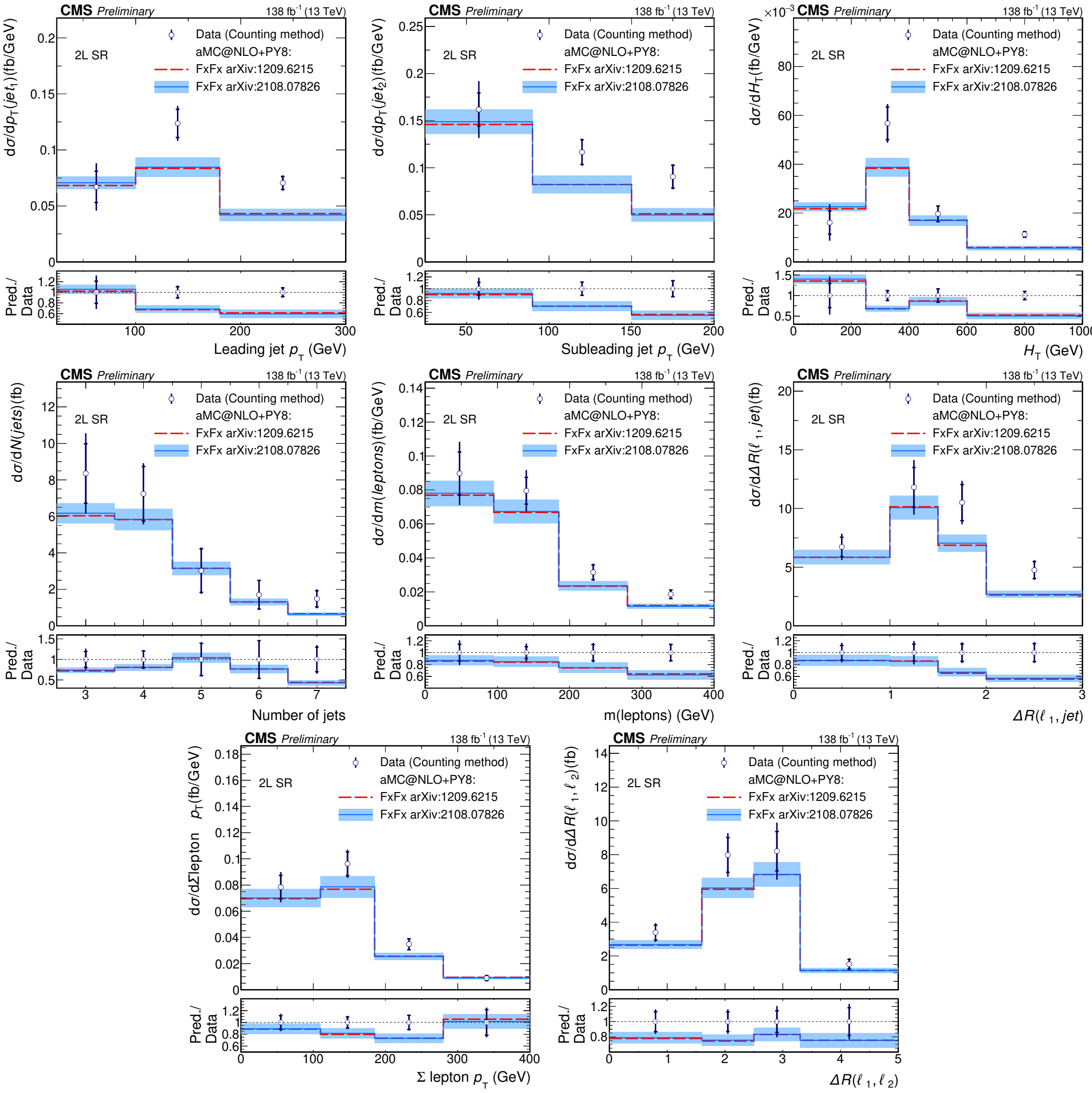

FIGURE. 6.15: Absolute differential cross sections for the leading jet p_T (upper left), subleading jet p_T (upper center), H_T (upper right), number of selected jets (middle left), invariant mass of the two lepton system (middle center), minimum ΔR between the leading lepton and the jets (middle right), summed p_T of the dilepton system (bottom left), and ΔR between the two leptons (bottom right). All distributions are obtained from the unfolding of these observables in the 2ℓss channel of the differential measurement. The lower panels show the ratio between the predictions and the measurement. The vertical lines on the unfolded data points represent the total experimental uncertainty of the unfolded cross section, while the horizontal bars show the statistical component of the uncertainty.

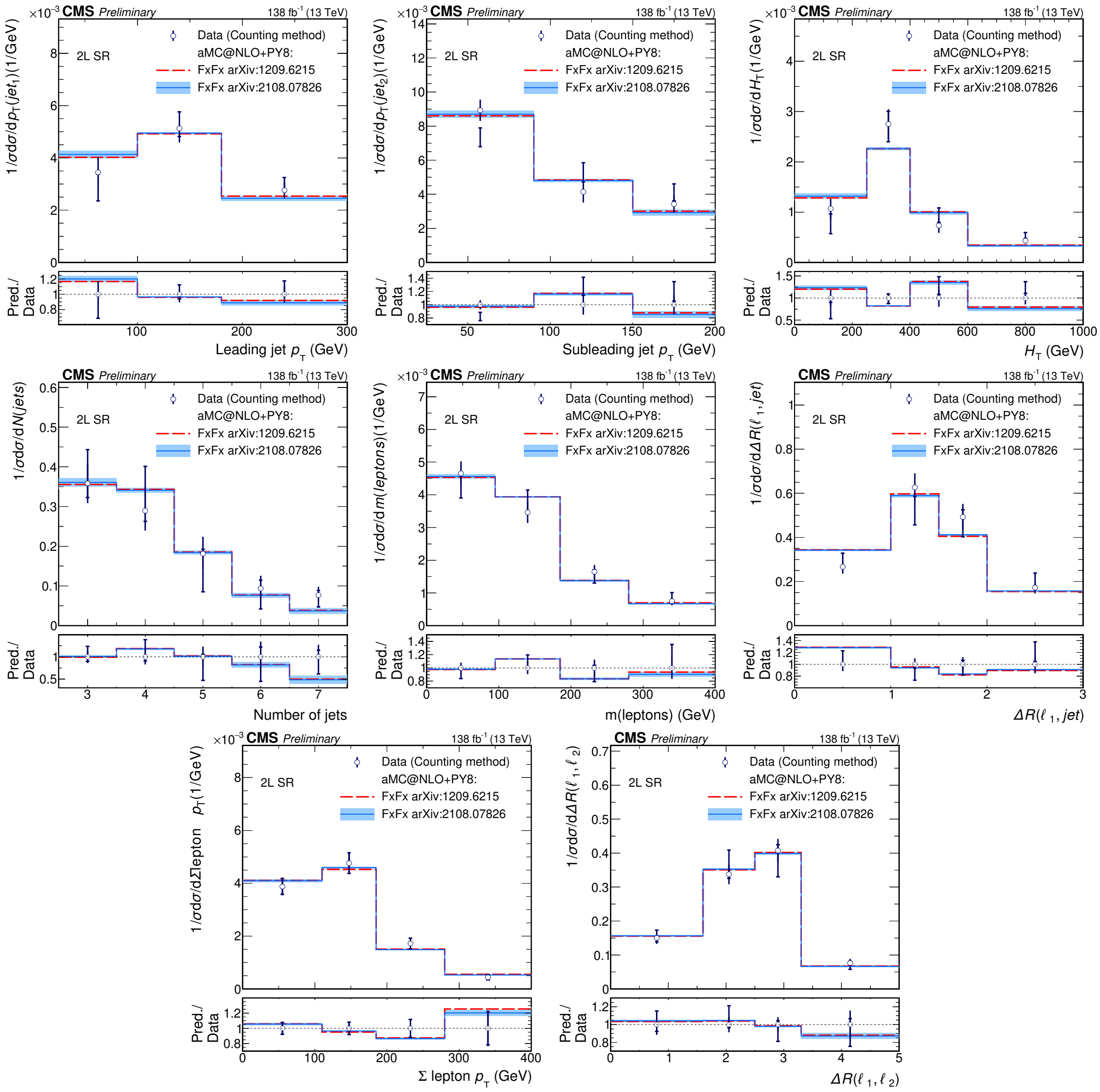

FIGURE. 6.16: Normalized differential cross sections for the leading jet p_{T} (upper left), subleading jet p_{T} (upper center), $\mathrm{H_T}$ (upper right), number of selected jets (middle left), invariant mass of the two lepton system (middle center), minimum ΔR between the leading lepton and the jets (middle right), summed p_{T} of the dilepton system (bottom left), and ΔR between the two leptons (bottom right). All distributions are obtained from the unfolding of these observables in the 2ℓss channel of the differential measurement. The lower panels show the ratio between the predictions and the measurement. The vertical lines on the unfolded data points represent the total experimental uncertainty of the unfolded cross section, while the horizontal bars show the statistical component of the uncertainty.

Similarly, Figure 6.17 shows the results obtained in the 3ℓ channel, including the distributions before the unfolding. The unfolded results in the case of the 3ℓ channel are shown in Figures 6.18 and 6.19 for both the absolute and normalized differential cross sections, respectively.

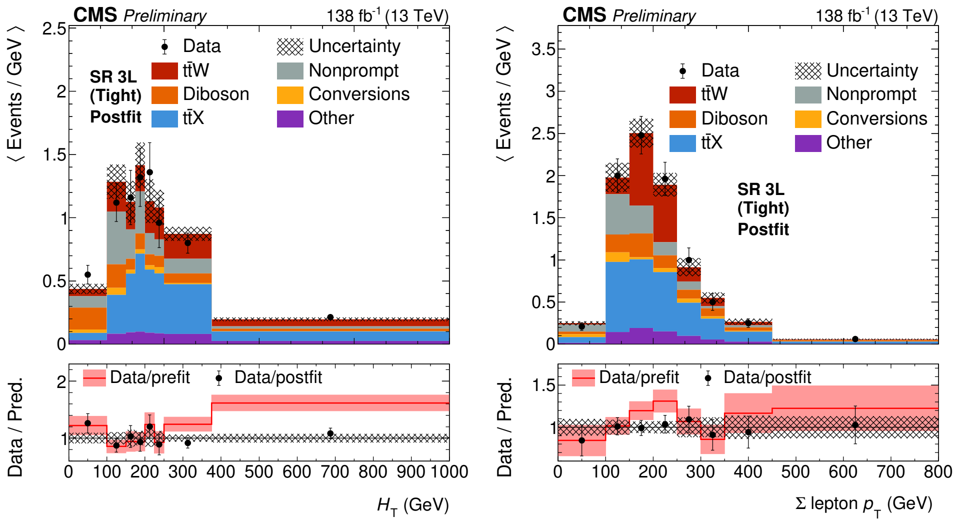

FIGURE. 6.17: Distributions for H_T(left), and the summed p_T of the 3ℓ system (right). All distributions are shown after the fit to the data in the 3ℓ region, including the CRs for the main backgrounds. The coloured histograms represent the different processes considered, stacked one top of each other, whereas the black markers represent the data. The ratio panels show the ratio between data and total prediction before to the fit to the data (red line), with respect to the sum of the predicted distributions after the fit to the data. The vertical lines on the data points represent the statistical uncertainty in the data, and the hatched (filled) band corresponds to the total uncertainty in the prediction after (before) the fit to the data.

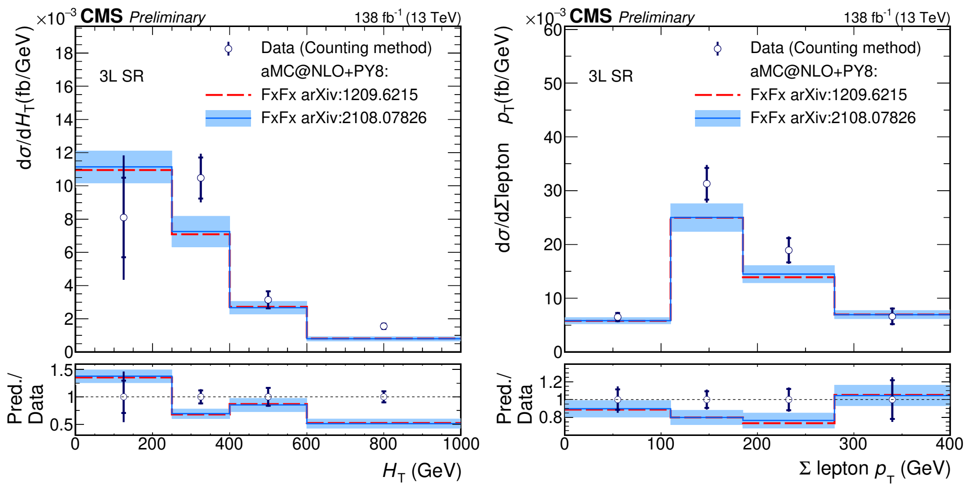

FIGURE. 6.18: Absolute differential cross sections for H_T(left), and the summed p_T of the 3ℓ system (right). All distributions are obtained from the unfolding of these observables in the 3ℓ channel of the differential measurement. The lower panels show the ratio between the predictions and the measurement. The vertical lines on the unfolded data points represent the total experimental uncertainty of the unfolded cross section, while the horizontal bars show the statistical component of the uncertainty.

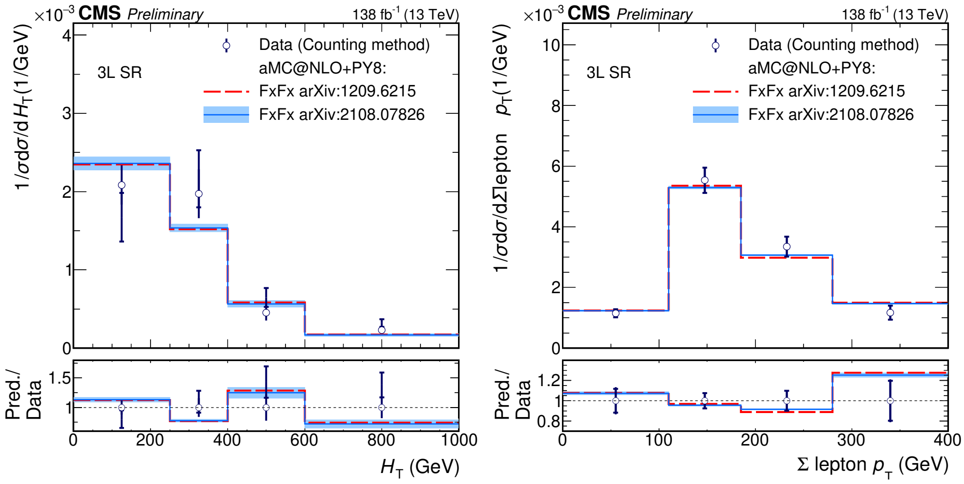

FIGURE. 6.19: Normalized differential cross sections for H_T(left), and the summed p_T of the 3ℓ system (right). All distributions are obtained from the unfolding of these observables in the 3ℓ channel of the differential measurement. The lower panels show the ratio between the predictions and the measurement. The vertical lines on the unfolded data points represent the total experimental uncertainty of the unfolded cross section, while the horizontal bars show the statistical component of the uncertainty.

The measurements are generally dominated by systematic uncertainties, with the uncertainties from the NR estimation, detailed in Section 6.2, being the largest ones. A non-negligible component of statistical uncertainty is also observed, particularly in the 3ℓ unfolded results.

6.7 Summary and prospects

In this chapter, two of the most important measurements related to $t\bar{t}W$ studies at the LHC have been presented. The inclusive cross-section measurements confirmed the mild tensions previously reported in dedicated $t\bar{t}H$ measurements, with much better accuracy. Additionally, particle level distributions for several observables that are relevant to the $t\bar{t}W$ process have been presented. These differential measurements were performed through unfolding of the same signal process used for the $t\bar{t}W$ inclusive cross-section measurement and were compared at the generator level with the latest MC simulations.

An alternative methodology for unfolding the $t\bar{t}W$ signal —not covered in this thesis— is also included in the measurements from Ref. [15]. This alternative approach is based on the loose selection that was used for the inclusive measurement. In this case, background contributions are suppresed through the use of an MVA selector that is unrolled in different particle level bins. The unfolding is then performed through a maximum likelihood fits to the unrolled MVAs, and the results are then compared with the ones obtained from the tight method presented in my work. Both results, which are statistically uncorrelated, are found to be in good agreement; therefore confirming the robustness of the method.

Both results are of key importance to the community from an experimental perspective, as all relevant experimental effects that must be accounted for in the measurement have been thoroughly detailed. From a theoretical perspective, the unfolded results are crucial for MC developers to continue improving the simulations available for experiments, which, in the case of $t\bar{t}W$, are still in tension with the data.

There are still improvements to be made in future iterations of the $t\bar{t}W$ measurements. One limiting factor in the inclusive cross-section measurement was the contribution from very low cross-section backgrounds. Surprisingly, processes contributing only a few events, orders of magnitude below the signal, had a large impact on the final uncertainty. This was studied during the measurement, and it was found that these contributions were mainly concentrated in NN bins that were signal-dominated. While the NN approach effectively distinguished $t\bar{t}W$ from other backgrounds, it struggled to separate $t\bar{t}W$ from these very low cross-section processes such as $t\bar{t}XX$ or VVV. As a result, the fit could not constrain the theoretical uncertainties, leading to a significant impact on the measurement.

The solution lies in improved MC modeling. A sensitivity level has been reached that requires the measurement of these very low cross-section processes, in order to provide input that can be used by the theory community to further refine the modeling of these process. Understanding the differences between $t\bar{t}W$ and these processes will greatly help improve the precision with which its properties are measured.

For the part on the $t\bar{t}W$ modeling, the differential measurement results still present slight tensions with the data, even when comparing the latest theory predictions, which were expected to fix at least part of the discrepancies. This has to be taken again as a motivation to further study the modeling of $t\bar{t}W$. In particular, several studies are being conducted within the LHC community to find new approaches to understand the properties of this complicated process.

The work presented in this thesis also contributes to future measurements at the LHC, since now the new FXFX modeling of $t\bar{t}W$, specifically developed for this thesis, is being used as the nominal signal modeling during the current Run 3 measurements.

7 Measurement of WZ production at 13.6 TeV

In contrast to $t\bar{t}X$ processes, diboson production cross sections are among the most accessible processes at the typical operating energies of the LHC. In particular, the associated production of a W and a Z boson (WZ) has been extensively studied since the discovery of the W and Z bosons. The properties of this process have been measured multiple times at different center of mass energies by the Tevatron [101, 102], using $p\bar{p}$ collision data, as well as in pp collisions by both the ATLAS [103–111] and CMS [78, 112–123] experiments.

The most recent addition to this set of measurements uses pp collision data collected during Run 3 of the LHC by the CMS experiment [17], and it is one of the main results of this thesis. At the time of writing this chapter, the corresponding publication has been accepted by the *Journal of High Energy Physics*. Notably, this result provides the first measurement of the inclusive WZ cross section at $\sqrt{s} = 13.6$ TeV. Furthermore, it stands among the first ten results released with LHC Run 3 data, including different measurements from both the ATLAS and CMS collaborations.

In the following sections, the methodology of the measurement, as well as the presentation and detailed discussion of the results, are presented.

7.1 Event selection

Similarly to the $t\bar{t}W$ measurement presented in Chapter 6, the WZ measurement relies on multilepton final states. Object definitions, including those for leptons, jets, and b tagging, follow the identification criteria outlined in Chapter 5, considering the specific adaptations to Run 3 analyses in this case.

The event selection for the SR targets the leptonic decay channels of both the W and Z bosons. Unlike the case of the $t\bar{t}W$ measurement, where determining the true origin of the leptons can be challenging due to the presence of additional neutrinos from multiple W decays, the WZ phase space benefits from a distinct final state. In this case, a dedicated tagging strategy is employed, in which each of the selected leptons is assigned to its corresponding parent boson based on kinematic criteria. This approach allows for a more accurate reconstruction of the event topology and improves the discrimination between signal and background.

The tagging algorithm proceeds as follows. Starting from events with at least three leptons in the final state —corresponding to the leptonic decays of the W boson ($W^{\pm} \rightarrow$

$\ell^{\pm}\nu$) and the Z boson ($Z \to \ell^{+}\ell^{-}$)— all possible pairs of leptons are constructed. These lepton pairs are sorted according to the absolute difference between their invariant mass and the Z boson mass, which, as in the $t\bar{t}W$ measurement, is taken from LEP measurements [90]. The pair with the invariant mass closest to the nominal Z boson mass is selected and identified as originating from the Z decay. These two leptons are labeled ℓ_{Z_1} and ℓ_{Z_2}, with ℓ_{Z_1} denoting the more energetic (leading) lepton of the pair, and ℓ_{Z_2} the subleading one. Among the remaining leptons in the event, the one with the highest transverse momentum is assumed to originate from the W boson decay and is labeled ℓ_{W}.

Once the leptons are properly tagged, additional identification and kinematic requirements are imposed. First, selected events must contain exactly three leptons that satisfy the tight identification criteria defined in Table 5.2.4, and any event containing additional leptons is vetoed. Since the WZ signal targets resonant Z boson production, the invariant mass of the two leptons tagged as originating from the Z decay (ℓ_{Z_1} and ℓ_{Z_2}) is required to lie within a 15 GeV window around the reference Z boson mass used in the tagging algorithm. Furthermore, a minimum invariant mass requirement on the full three-lepton system is applied: $m(\ell_{Z_1}, \ell_{Z_2}, \ell_{W}) \geq 100$ GeV. To account for the expected missing energy from the neutrino in the W boson decay, a requirement of $p_{T}^{miss} > 35$ GeV is imposed.

Events containing at least one b-tagged jet passing the tight identification criteria of the DEEPJET algorithm are vetoed from the selection. Additionally, the presence of at least one opposite-sign same-flavour (OSSF) lepton pair in the final state is required. Finally, to remain consistent with the generator-level phase space definition of the signal MC samples described in Chapter 4, a minimum dilepton mass requirement of $\min(m(\ell, \ell')) > 4$ GeV is applied to all lepton pairs in the event. The complete set of requirements that are imposed to define the SR in the WZ measurement can be found in Table 7.1.1.

Table 7.1.1: Selection requirements for the SR of the analysis. The requirements on the p_T are applied in order for for ℓ_{Z_1},ℓ_{Z_2}, and ℓ_{W}, respectively.

Variable	Requirement
Number of tight leptons	$= 3$
Lepton p_T	$> \{25, 15, 25\}$ GeV
N_{OSSF}	≥ 1
$\lvert m(\ell, \ell') - m_Z \rvert$	< 15 GeV
p_{T}^{miss}	> 35 GeV
Number of b tags	$= 0$
$\min(m(\ell, \ell'))$	> 4 GeV
$m(\ell_{Z_1}, \ell_{Z_2}, \ell_{W})$	> 100 GeV

Several observables relevant to the measurement are shown in Figure 7.1, and good agreement is observed across all the considered observables. Additionally, the purity of the selected events —defined as the fraction of events originating from WZ production relative to the total number of selected events— is approximately 86%, indicating that the signal region is strongly dominated by the WZ signal.

7.2 Background estimation

All background contributions are modeled using MC simulation. Within the SR, where the background constitutes approximately 15% of the total event yield, the three most significant prompt background sources —ranked by their relative contribution— are as follows: ZZ, contributing about 6%; $\mathrm{t\bar{t}Z}$, contributing roughly 2%; and $\mathrm{X}\gamma$, also contributing around 2%. Additionally, backgrounds arising from nonprompt leptons account for approximately 3%. The remaining contributions come from processes with low production cross sections, such as VVV or $\mathrm{t\bar{t}XX}$, where X can be any vector boson.

One of the most interesting aspects of this measurement is that the SR can be slightly modified to define multiple orthogonal selections. These alternative selections enable further suppression of background contributions and improve the signal extraction. As a result, several CRs are introduced in the analysis, each targeting a specific background component that is relevant to the measurement. The methodology for controlling each background type is discussed in detail in the following sections.

7.2.1 Prompt backgrounds

The ZZ background is largely suppressed by the requirement of exactly three leptons, since this process typically results in four prompt leptons in the final state. Nonetheless, a non-negligible contribution remains due to cases where one of the leptons falls outside the acceptance of the selection criteria. The $\mathrm{t\bar{t}X}$ backgrounds are primarily reduced through the veto on b-tagged jets, as the b tagging algorithms used in CMS are generally efficient in identifying at least one of the two b jets from $\mathrm{t\bar{t}}$ decays. The $\mathrm{X}\gamma$ background, which is dominated by associated $\mathrm{Z}\gamma$ production (around 99% of the expected events), also includes smaller contributions from $\mathrm{W}\gamma$, $\mathrm{t\bar{t}}\gamma$, and $\mathrm{WZ}\gamma$ production. This background is significantly mitigated by the requirement on the invariant mass of the three-lepton system, since electrons from photon conversions are usually not energetic enough to yield the high invariant masses characteristic of genuine WZ events.

To control these backgrounds, three orthogonal CRs are defined. A ZZ CR is defined by increasing the lepton multiplicity requirement to exactly four leptons, rather than three. The hardest lepton not belonging to the best OSSF pair is referred to as ℓ_3 in this region. An additional fourth lepton is required to pass the tight identification criteria and have $p_{\mathrm{T}} > 15\mathrm{GeV}$. In addition, a $\mathrm{t\bar{t}Z}$ CR targets top-related backgrounds, and is defined by inverting the b tag veto applied in the SR. Due to the Z mass window selection, this region is primarily dominated by $\mathrm{t\bar{t}Z}$ and tZq backgrounds, followed by $\mathrm{t\bar{t}W}$ and $\mathrm{t\bar{t}H}$. Finally, a $\mathrm{X}\gamma$ CR is defined by inverting the requirements on both the invariant mass of the three-lepton system, $m(\ell_{\mathrm{Z}_1}, \ell_{\mathrm{Z}_2}, \ell_{\mathrm{W}})$, and the missing transverse momentum, $p_{\mathrm{T}}^{\mathrm{miss}}$.

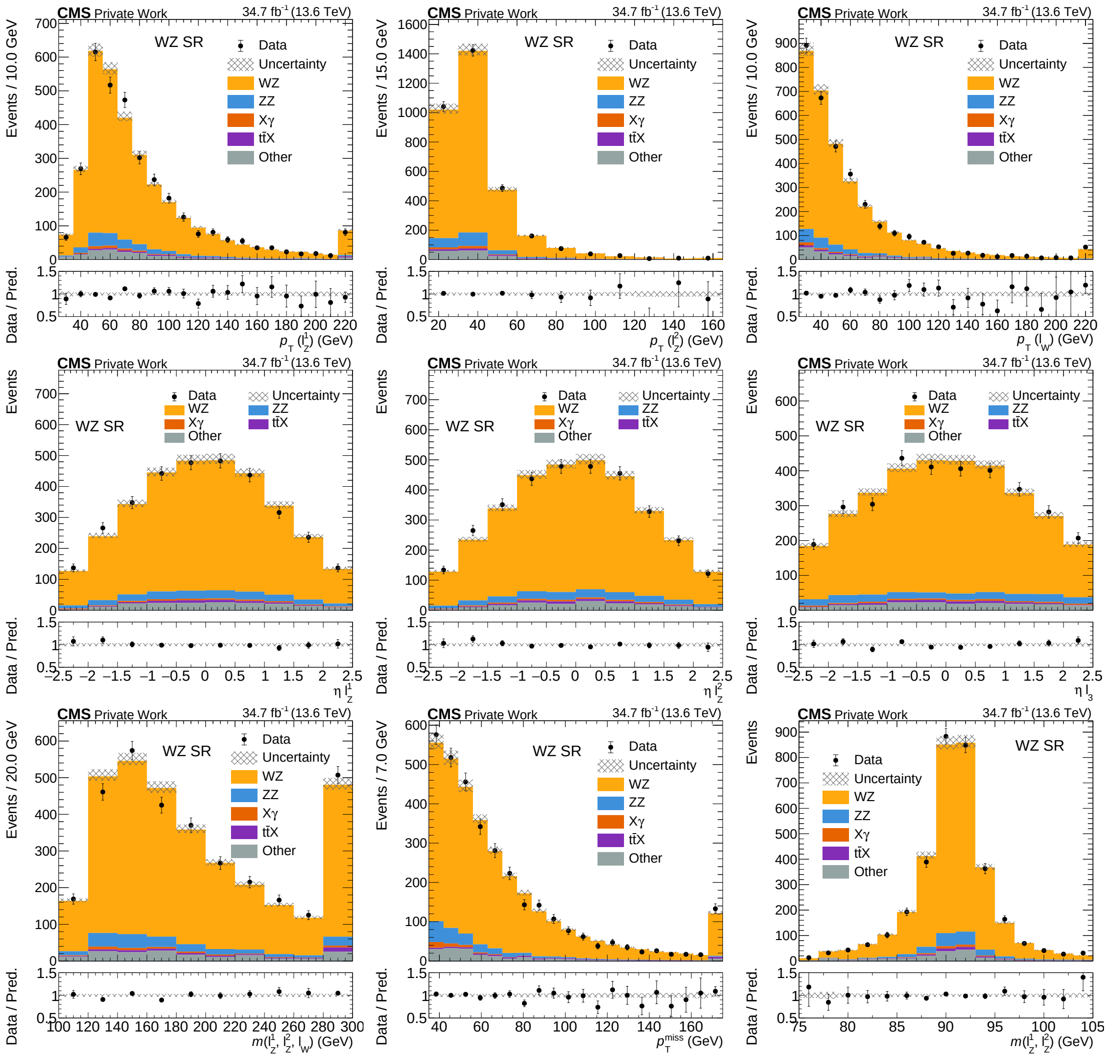

FIGURE. 7.1: Distributions of several observables in the SR. The first and second rows show the p_T and η of ℓ_{Z_1} (left), ℓ_{Z_2} (middle) and ℓ_W (right), respectively. The last row shows other kinematic observables of interest, namely the invariant mass of the 3ℓ system (left), p_T^{miss} (middle), and the invariant mass of the system formed by ℓ_{Z_1} and ℓ_{Z_1}. The coloured histograms represent the different processes considered, stacked one top of each other, whereas the black markers represent the data. The ratio panels show the ratio between data with respect to the sum of the predicted distributions. The vertical lines on the data points represent the statistical uncertainty in the data and the hatched band corresponds to the total uncertainty in the prediction. Processes with a small contribution to this region are grouped in the "Other" category.

This selection enhances the contribution of background events with asymmetric photon conversions. The complete set of requirements for each CR can be found in Table 7.2.2

Table 7.2.2: Requirements for the definition of the control regions of the analysis. Objects in parentheses relate to the ZZ CR.

Region	Number of tight leptons	$p_{\mathrm{T}}\{\ell_{\mathrm{Z}_1}, \ell_{\mathrm{Z}_2}, \ell_{\mathrm{W}}(\ell_3), (\ell_4)\}$ (GeV)	N_{OSSF}	$\lvert m(\ell_{\mathrm{Z}_1}, \ell_{\mathrm{Z}_2}) - m_{\mathrm{Z}}\rvert$ (GeV)	$p_{\mathrm{T}}^{\mathrm{miss}}$ (GeV)	$N_{b\ \mathrm{tag}}$	$\min(m(\ell, \ell'))$ (GeV)	$m(\ell_{\mathrm{Z}_1}, \ell_{\mathrm{Z}_2}, \ell_{\mathrm{W}}(\ell_3))$ (GeV)
ZZ CR	=4	$>\{25, 15, 25, 15\}$	≥1	<15	-	=0	>4	>100
$\mathrm{t\bar{t}Z}$ CR	=3	$>\{25, 15, 25\}$	≥1	<15	>35	>0	>4	>100
$\mathrm{X}\gamma$ CR	=3	$>\{25, 15, 25\}$	≥1	-	≤35	=0	>4	<100

To validate the modeling of these backgrounds in the CRs, lepton kinematic observables are displayed in Figure 7.2, for the three control regions defined in the analysis. Overall, good agreement between data and simulation is observed, even before performing any fit to the data.

Additionally, the ZZ CR is also used to validate lepton resolution effects. This is achieved by studying the invariant mass of the most energetic OSSF lepton pair separately for muons and electrons. The results are shown in Figure 7.3, and again show good agreement between data and simulation.

7.2.2 Nonprompt backgrounds

In contrast to the $\mathrm{t\bar{t}W}$ measurement, where the dominant sources of background arise from semileptonic $\mathrm{t\bar{t}}$ events and QCD-like processes, the nonprompt background in the WZ measurement is primarily due to Z +jets events. In these cases, a jet from the initial state is misidentified as a lepton. Secondary contributions from $\mathrm{t\bar{t}}$ and single top production are efficiently suppressed by the b tag veto applied in the SR. Additionally, the WP used for the lepton MVA selection provides strong discrimination against these backgrounds, ultimately reducing the nonprompt contamination to approximately 3% of the total yield in the SR. Consequently, the nonprompt background is modeled entirely using MC simulation, both in terms of normalization and shape.

To validate this MC-based estimation, a sideband region enriched in nonprompt leptons is defined. This region is constructed following the same principles as the AR used in the $\mathrm{t\bar{t}W}$ nonprompt background estimation. It requires three final-state leptons with kinematic selections closely matching those of the SR. Due to the tagging algorithm and the on-shell Z requirement, the leptons identified as ℓ_{Z_1} and ℓ_{Z_2} are highly likely to be prompt. Therefore, the lepton tagged as ℓ_{W} is the most probable candidate to be the nonprompt lepton. Based on this assumption, the tight selection criteria is dropped for the ℓ_{W} candidate to define the validation region.

With this definition, a relatively pure validation region is obtained. It consists of approximately 72% nonprompt background, 15% signal, and 13% other prompt processes. Within the nonprompt category, 98% originates from Z +jets events, with the remaining 2% mainly stemming from dileptonic $\mathrm{t\bar{t}}$ production. To evaluate how well the MC models the data in this region, the kinematic distributions of the nonprompt lepton candidate

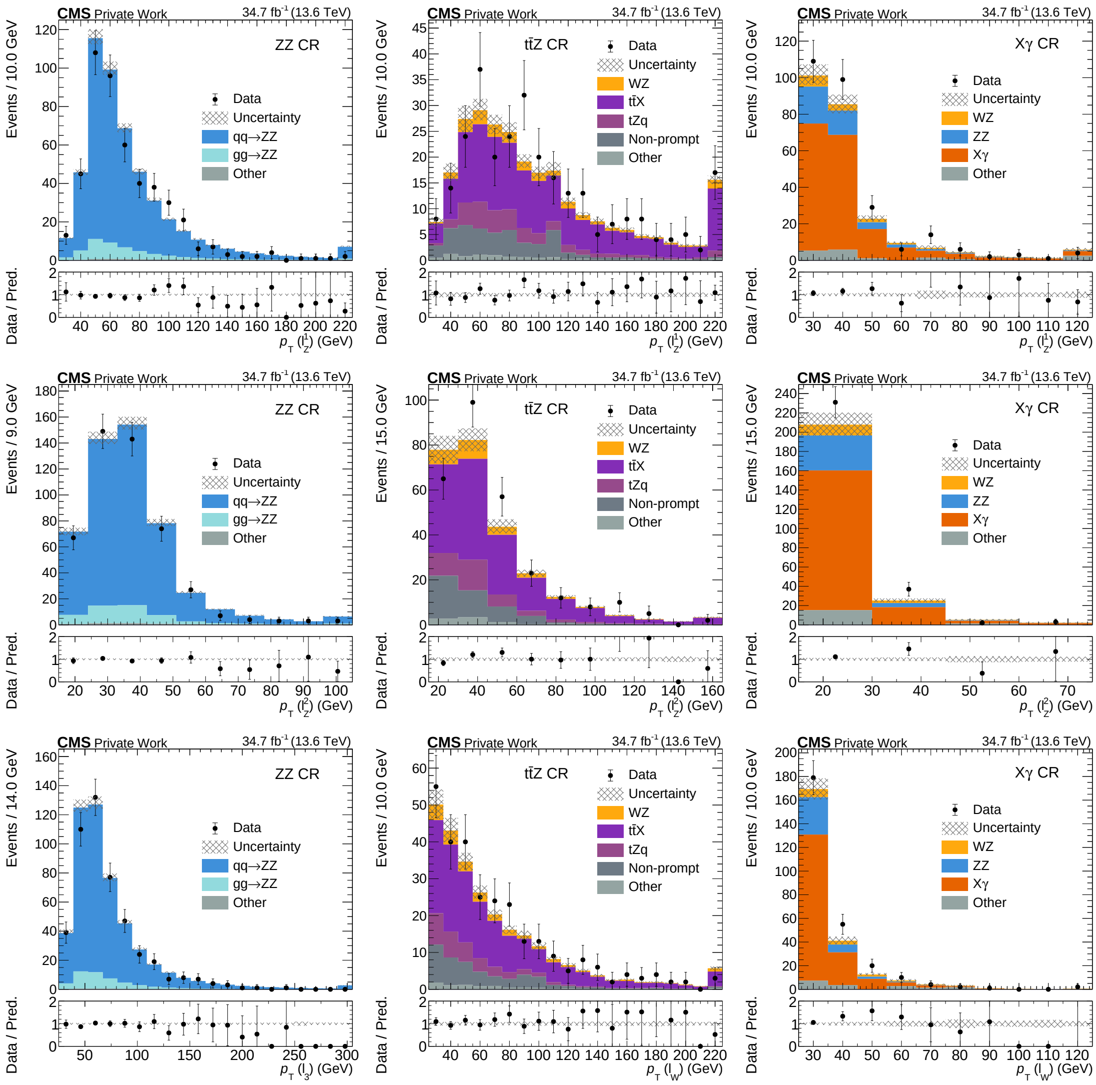

FIGURE. 7.2: Distribution of observables in the ZZ (left column), $t\bar{t}Z$ (middle column) and $X\gamma$ (right column). For each column, the p_T of ℓ_{Z_1} (upper row), ℓ_{Z_2} (middle row) and ℓ_W (lower row) is shown. The coloured histograms represent the different processes considered, stacked one top of each other, whereas the black markers represent the data. The ratio panels show the ratio between data with respect to the sum of the predicted distributions after the fit to the data. The vertical lines on the data points represent the statistical uncertainty in the data, and the hatched band corresponds to the total uncertainty in the prediction after the fit to the data. Processes with a small contribution to this region are grouped in the "Other" category.

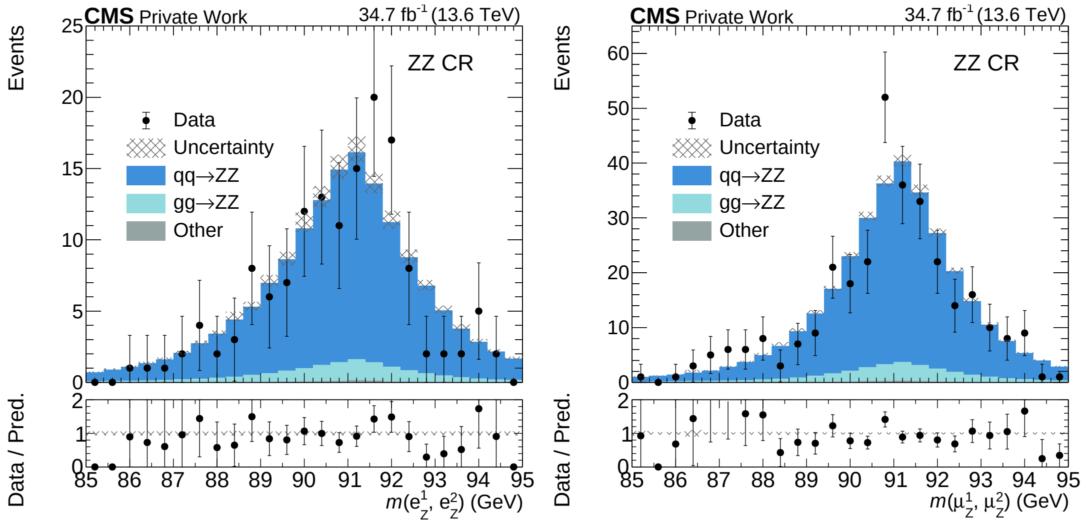

FIGURE. 7.3: Invariant mass of the pair of leptons with the highest invariant mass in the ZZ CR, shown separately for OSSF pairs of electrons (left) and muons (right). The coloured histograms represent the different processes considered, stacked one top of each other, whereas the black markers represent the data. The ratio panels show the ratio between data with respect to the sum of the predicted distributions. The vertical lines on the data points represent the statistical uncertainty in the data and the hatched band corresponds to the total uncertainty in the prediction.

are examined, as shown in Figure 7.4. Overall agreement is observed, supporting the reliability of the MC-based modeling of nonprompt backgrounds in 3ℓ final states. To account for discrepancies observed at low p_{T} and high $|\eta|$, a 30% flat uncertainty is assigned to the nonprompt background estimate in the SR.

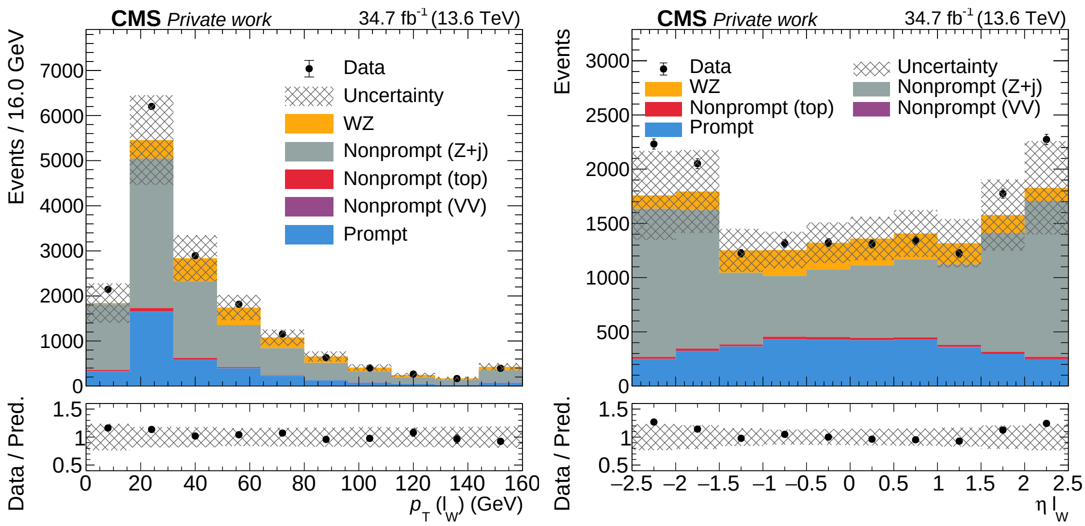

FIGURE. 7.4: Kinematic distributions of the ℓ_{W} candidate in the nonprompt-enriched validation region. The coloured histograms represent the different processes considered, stacked one top of each other, whereas the black markers represent the data. The ratio panels show the ratio between data with respect to the sum of the predicted distributions. The vertical lines on the data points represent the statistical uncertainty in the data and the hatched band corresponds to the total uncertainty in the prediction.

7.3 Systematic uncertainties

Similarly to the $t\bar{t}W$ measurement, the majority of systematic uncertainties affecting the extraction of the WZ cross section are discussed in Section 5.4.3. This section focuses on uncertainties that are specific to the WZ analysis, which primarily arise from the background estimation techniques and theoretical modeling of both the signal and background processes.

The total uncertainty associated with the trigger efficiency is divided into two components: a systematic component accounting for potential biases in the selection of the control dataset, and a statistical component resulting from the limited size of this dataset. These two sources are treated as uncorrelated and applied independently across the dataset. The systematic uncertainty ranges from 0.5% to 1.0%, while the statistical component varies between 0.5% and 1.6%.

The normalizations of the main background contributions —ZZ, $t\bar{t}X$, and $X\gamma$— are extracted from the fit to data. Consequently, their impact on the final measurement is determined from the post-fit constraints provided by the likelihood fit. The nonprompt background normalization is constrained within a 30% uncertainty band, as motivated by the mismodeling effects discussed in Section 7.2.2. Other subdominant backgrounds, which contribute negligibly to the overall yield, are assigned a conservative 50% uncertainty.

A summary of all the input uncertainties considered in the analysis is shown in Table 7.3.3.

7.4 Inclusive cross section results

Two sets of measurements for the WZ production cross section are reported, each corresponding to a different definition of the signal phase space. In both cases, the regions in which the WZ signal is extracted is defined using generator-level quantities, following the same principles as the ones discussed in the $t\bar{t}W$ differential measurements, particularly in Section 6.6.2.

The first measurement targets a fiducial volume referred to as the "fiducial region" (FR), defined at particle level using generator-level quantities. The FR is constructed by selecting events that contain at least three dressed leptons at generator level, excluding τ leptons. These leptons are associated to their parent bosons using the same tagging algorithm as in the SR, and are labeled as $\ell_{Z_1}^{\text{Dressed}}$, $\ell_{Z_2}^{\text{Dressed}}$, and $\ell_{W}^{\text{Dressed}}$. Once the leptons are tagged, the full set of kinematic requirements used in the SR is applied at generator level, including the requirement of at least one OSSF lepton pair.

The second measurement is performed in a broader phase space referred to as the "total region" (TR), which extends the FR by relaxing some of its selection criteria. In

Table 7.3.3: Summary of the input relative uncertainties. Numbers are presented in percentages over the predicted signal yields of the associated process on which they have an effect. All uncertainties are treated as shape variations on the templates used for the fit, with the exception of the normalization uncertainties in the backgrounds that are treated as flat variations of the corresponding yield. Single numbers refer to the maximum uncertainty associated to a given input, whereas ranges refer to values that may vary depending on different parts of the dataset.

Source	Uncertainty (%)	Processes
Integrated luminosity	1.4	All MC
Trigger efficiencies	0.5—1.6	All MC
b tagging (heavy)	0.1	All MC
b tagging (light/gluon)	<0.1	All MC
Pileup	0.4—1.7	All MC
Jet energy scale	1.1	All MC
Electron reconstruction	3.8	All MC
Electron ident. efficiency	3.5	All MC
Electron energy scale	0.3	All MC
Muon efficiencies	1.1	All MC
Non-prompt bkg. normalization	30	Non-prompt
VVV normalization	50	VVV
tZq normalization	15	tZq
VH normalization	25	VH
ISR	0.1	WZ
FSR	0.8	WZ
WZ theory (μ_{R}, μ_{F}, PDF)	0.6	WZ

particular, events involving WZ $\rightarrow \tau + \mathrm{X}$ decays are also included as part of the signal definition. Additionally, the requirements on lepton kinematics and the number of OSSF pairs are dropped. The only kinematic requirement retained in the TR is the presence of a resonant Z boson, and the presence of exactly three leptons in the final state.

The TR is designed to provide a more inclusive measurement of the WZ cross section, with fewer requirements on the properties of the process. In contrast, the FR is motivated by the aim to reduce as comprehensively as possible the detector acceptance effects on the theoretical uncertainties that affect the measurement. The complete list of selections used for the FR and TR definitions can be found in Table 7.4.4.

The signal strength of the WZ process is extracted through a maximum likelihood fit to the number of observed events in four exclusive categories, defined by the flavour composition of the three reconstructed leptons: eee, $\mathrm{ee}\mu$, $\mu\mu\mathrm{e}$, and $\mu\mu\mu$. In addition to the individual fits in each channel, a combined fit across all four categories is also performed. The same observable used to extract the signal in the SR is also employed to extract the normalization of the main backgrounds for which a CR was defined in Section 7.2. The input observables used in the fit for each region are shown in Figure 7.5.

For each measurement, the total number of WZ events passing the detector-level SR requirements is further split according to whether they satisfy the generator-level defi-

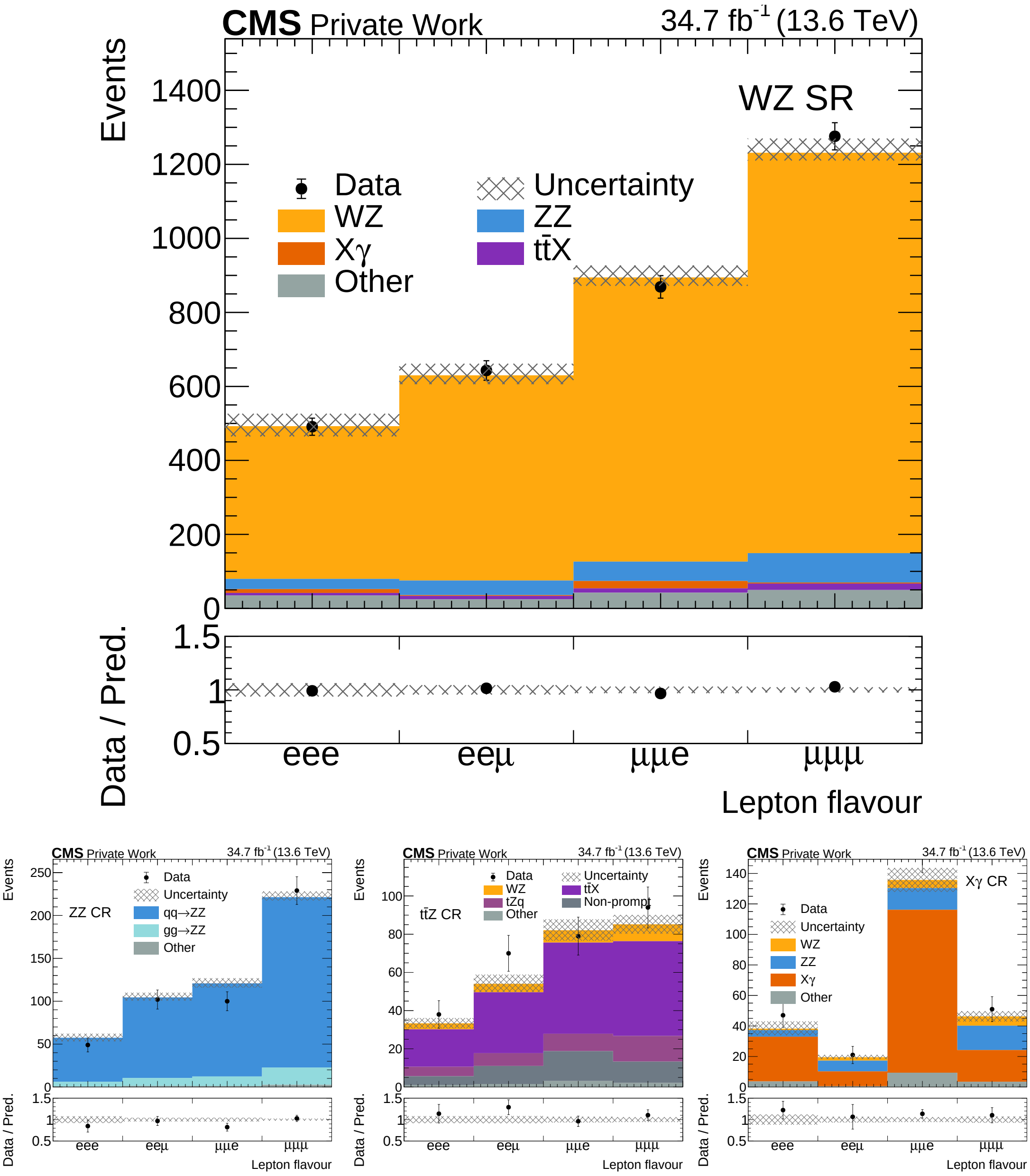

FIGURE. 7.5: Distributions of the flavour composition distributions in the SR (top), and the ZZ (left), $t\bar{t}Z$ (middle), and $X\gamma$ (right) CRs. The coloured histograms represent the different processes considered, stacked one top of each other, whereas the black markers represent the data. The ratio panels show the ratio between data with respect to the sum of the predicted distributions. The vertical lines on the data points represent the statistical uncertainty in the data and the hatched band corresponds to the total uncertainty in the prediction. Minor background contributions are grouped under the “Other” label. The definition of “Other” may vary between different regions.

Table 7.4.4: Definition of the fiducial and total regions. The lepton related quantities refer to "dressed" leptons. A dash symbol is used in cases the selection is not considered for the corresponding phase space.

Region	Fiducial	Total
Lepton definition	Dressed (e, μ)	Dressed (e, μ, τ)
$N_\ell = 3$	✓	✓
$p_\mathrm{T}\{\ell_{\mathrm{Z}_1}, \ell_{\mathrm{Z}_2}, \ell_\mathrm{W}\} > \{25, 15, 25\}\mathrm{GeV}$	✓	-
$\lvert\eta\rvert\,\{\ell_{\mathrm{Z}_1}, \ell_{\mathrm{Z}_2}, \ell_\mathrm{W}\} < \{2.5, 2.5, 2.5\}$	✓	-
$N_\mathrm{OSSF} = 1$	✓	✓
$60 < m(\ell_{\mathrm{Z}_1}, \ell_{\mathrm{Z}_2}) < 120\mathrm{GeV}$	✓	✓
$\min(m(\ell, \ell')) > 4\mathrm{GeV}$	✓	✓
$m(\ell_{\mathrm{Z}_1}, \ell_{\mathrm{Z}_2}, \ell_\mathrm{W}) > 100\mathrm{GeV}$	✓	-

nitions of the fiducial (FR) or total (TR) phase spaces. Events that pass the SR selection but fail both FR and TR generator-level requirements are classified as "non-fiducial" contributions. These non-fiducial events are not scaled with the signal strength in the fit, and instead they are treated as an additional background component. All systematic uncertainties discussed in Section 7.3 are incorporated into the likelihood as nuisance parameters, except for the normalizations of the main backgrounds, which are included directly in the fit by promoting them to additional parameters of interest in the likelihood model.

A breakdown of the different sources of systematic uncertainty and their impact on the result after the fit to data is presented in Table 7.4.5. The normalization parameters obtained in the combined fit —performed according to the total region definition— for the individual background processes are: $r_{\mathrm{ZZ}} = 0.96 \pm 0.06$, $r_{\mathrm{t\bar{t}Z}} = 1.18 \pm 0.15$, and $r_{\mathrm{X}\gamma} = 1.10 \pm 0.13$. The final uncertainty on the predicted WZ cross section amounts to 3.4% for the inclusive measurement in the total region, and 3.3% for the fiducial measurement. In both cases, the overall sensitivity is primarily driven by the $\mu\mu\mu$ and $\mu\mu\mathrm{e}$ channels.

The results from the fit are also extrapolated to observables that do not directly enter the likelihood, in order to verify that no significant bias is introduced in other kinematic distributions by fitting to the number of observed events in the different lepton flavour categories. This serves as a cross-check of the robustness of the fit strategy. The results of this validation are shown in Figure 7.6 for several observables of interest, and in Figure 7.7 for the particular case of the invariant mass of the 3ℓ system, which is one of the most important observables in WZ, as it provides sensitivity to searches for new physics, in the context of aTGC theories. Excellent agreement is observed between data and the post-fit prediction across all the observed distributions.

7.4.1 Results in the fiducial region

The measured fiducial cross sections are reported in Table 7.4.6 for the different flavour channels, including a comparison with theoretical predictions computed from the signal POWHEG sample, as well as the next-to-NLO (NNLO) QCD and NNLO QCD $\times$ NLO EW

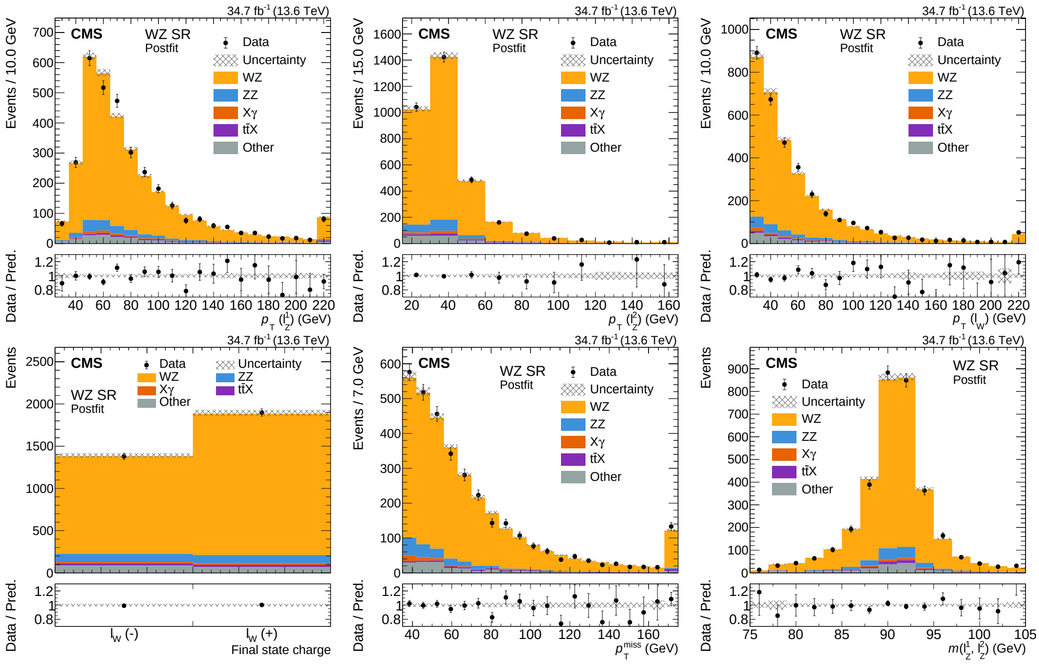

FIGURE. 7.6: Distributions of several observables in the SR accounting for the fit to data. From upper left (p_T of ℓ_{Z_1}), upper middle (p_T of ℓ_{Z_1}), upper right (p_T of ℓ_W), bottom left (final state charge), bottom middle (p_T^{miss}), and bottom right (invariant mass of the ℓ_{Z_1} and ℓ_{Z_2} pair). The coloured histograms represent the different processes considered, stacked one top of each other, whereas the black markers represent the data. The ratio panels show the ratio between data with respect to the sum of the predicted distributions. The vertical lines on the data points represent the statistical uncertainty in the data and the hatched band corresponds to the total uncertainty in the prediction. Processes with a small contribution to this region are grouped in the "Other" category.

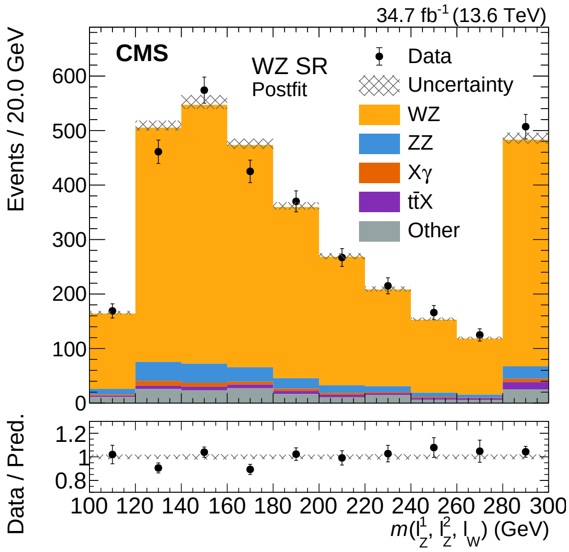

FIGURE. 7.7: Distributions of the invariant mass of the 3ℓ system in the SR. The coloured histograms represent the different processes considered, stacked one top of each other, whereas the black markers represent the data. The ratio panels show the ratio between data with respect to the sum of the predicted distributions. The vertical lines on the data points represent the statistical uncertainty in the data and the hatched band corresponds to the total uncertainty in the prediction. Processes with a small contribution to this region are grouped in the "Other" category.

Table 7.4.5: Breakdown of different sources of systematic uncertainties and their relative impact in each channel, as well as in the inclusive measurement; as a percentage of the total uncertainty. The dash symbol indicates that the specific uncertainty does not apply.

Source	Inclusive (%)	eee (%)	eeμ (%)	$\mu\mu$e (%)	$\mu\mu\mu$ (%)
Integrated luminosity	1.5	1.5	1.4	1.4	1.5
Trigger efficiencies	0.5	1.0	1.0	1.0	0.7
b tagging	0.1	0.1	0.1	0.1	0.1
Pileup	0.4	0.6	0.8	0.2	0.4
Jet energy scales	0.9	1.3	0.7	1.1	0.7
Electron reconstruction	1.2	4.0	2.9	1.1	-
Electron ident. efficiencies	0.7	3.6	2.4	1.1	-
Electron energy scale	0.1	0.1	0.1	0.0	-
Muon efficiencies	0.7	-	0.3	0.8	1.2
Non-prompt bkg. normalization	0.7	1.6	0.5	0.7	0.7
VVV normalization	0.4	0.4	0.4	0.4	0.4
tZq normalization	0.1	0.1	0.1	0.1	0.1
ZZ normalization	0.3	0.8	0.7	0.5	0.5
$t\bar{t}Z$ normalization	0.3	0.7	0.6	0.4	0.5
Xγ normalization	0.2	0.7	0.3	0.4	0.2
VH normalization	0.2	0.2	0.2	0.1	0.2
ISR/FSR	0.3	0.5	0.2	0.4	0.3
WZ theory (μ_R, μ_F, PDF)	0.6	0.6	0.6	0.6	0.6
MC statistical	0.5	1.9	0.9	1.0	0.9
Statistical	2.0	5.3	4.6	3.8	3.3
Total	3.4	8.5	6.5	5.0	4.3

prediction from MATRIX [67]. In all MATRIX predictions the main setup for the SM parameters, scale and PDF choices, was adopted; and only the requirements of the leptons in order to mimic either the fiducial or total definitions were modified.

There are slight differences between the results obtained in channels with three leptons of the same flavour (eee and $\mu\mu\mu$) and those with mixed flavours (eeμ and $\mu\mu$e). These differences arise primarily from additional contributions present in the same-flavour final states, which are absent or suppressed in the mixed-flavour channels. Specifically, the eee and $\mu\mu\mu$ channels receive interference contributions from diagrams involving the exchange of identical final-state leptons, leading to a slight enhancement in the total amplitude. Furthermore, the presence of two same-charge leptons of the same flavour increases the number of possible lepton combinations that satisfy the event selection criteria, resulting in a larger effective cross section. These effects, while relatively small, are consistently accounted for in the MATRIX predictions. They are not considered, however, in the POWHEG fixed order predictions. In the final selection defined with detector level quantities, these effects are further mitigated by the lepton identification efficiencies.

Table 7.4.6: Measured fiducial cross sections and their corresponding uncertainties for the flavour-exclusive and flavour-inclusive categories. The predictions from both POWHEG at NLO in QCD and LO EW as well as several ones obtained from MATRIX (NLO QCD, NNLO QCD, NNLO QCD $\times$ NLO EW) are also included.

Category	Accuracy	Fiducial cross section (fb)
eee	POWHEG , NLO QCD	$68.0^{+2.3}_{-2.1}$ (scale) $\pm$ 1.0 (PDF)
	MATRIX, NLO QCD	$69.9^{+3.9}_{-3.1}$ (scale)
	MATRIX, NNLO QCD	$77.0^{+1.8}_{-1.7}$ (scale)
	MATRIX, NNLO QCD $\times$ NLO EW	$75.4^{+1.7}_{-1.6}$ (scale)
	Measured	72.0 $\pm$ 4.0 (stat) $\pm$ 4.5 (syst) $\pm$ 1.0 (lumi) $\pm$ 0.4 (theo)
eeμ	POWHEG , NLO QCD	$68.0^{+2.3}_{-2.1}$ (scale) $\pm$ 1.0 (PDF)
	MATRIX, NLO QCD	$68.7^{+3.8}_{-3.0}$ (scale)
	MATRIX, NNLO QCD	$75.0^{+1.8}_{-1.6}$ (scale)
	MATRIX, NNLO QCD $\times$ NLO EW	$73.4^{+1.7}_{-1.5}$ (scale)
	Measured	73.9 $\pm$ 3.5 (stat) $\pm$ 3.1 (syst) $\pm$ 1.1 (lumi) $\pm$ 0.4 (theo)
$\mu\mu$e	POWHEG , NLO QCD	$68.0^{+2.3}_{-2.1}$ (scale) $\pm$ 1.0 (PDF)
	MATRIX, NLO QCD	$68.7^{+3.8}_{-3.0}$ (scale)
	MATRIX, NNLO QCD	$75.0^{+1.8}_{-1.6}$ (scale)
	MATRIX, NNLO QCD $\times$ NLO EW	$73.4^{+1.7}_{-1.5}$ (scale)
	Measured	71.2 $\pm$ 2.9 (stat) $\pm$ 2.0 (syst) $\pm$ 1.0 (lumi) $\pm$ 0.4 (theo)
$\mu\mu\mu$	POWHEG , NLO QCD	$68.0^{+2.3}_{-2.1}$ (scale) $\pm$ 1.0 (PDF)
	MATRIX, NLO QCD	$69.9^{+3.9}_{-3.1}$ (scale)
	MATRIX, NNLO QCD	$77.0^{+1.8}_{-1.7}$ (scale)
	MATRIX, NNLO QCD $\times$ NLO EW	$75.4^{+1.7}_{-1.6}$ (scale)
	Measured	75.3 $\pm$ 2.5 (stat) $\pm$ 1.5 (syst) $\pm$ 1.1 (lumi) $\pm$ 0.4 (theo)
Inclusive	POWHEG , NLO QCD	$271.9^{+9.0}_{-8.5}$ (scale) $\pm$ 3.8 (PDF)
	MATRIX, NLO QCD	$277.1^{+15.3}_{-12.3}$ (scale)
	MATRIX, NNLO QCD	$304.0^{+7.1}_{-6.6}$ (scale)
	MATRIX, NNLO QCD $\times$ NLO EW	$297.7^{+6.8}_{-6.3}$ (scale)
	Measured	297.6 $\pm$ 6.4 (stat) $\pm$ 6.4 (syst) $\pm$ 4.2 (lumi) $\pm$ 1.5 (theo)

7.4.2 Results in the total region

The results for the total cross section measurement of the WZ process, along with their comparison to theoretical predictions computed at various orders in the QCD and EW perturbative expansions, are presented in Table 7.4.7 and Figure 7.8. The uncertainty on the measured cross section values is breakdown into their associated statistical, systematic, luminosity, and theoretical components.

As a cross-check, the measured cross sections were independently validated using an alternative strategy based on the fiducial cross section formula. In this approach, the likelihood fit was used only to extract the post-fit yields of the WZ signal in each final state. These post-fit yields were then used to compute the fiducial and total cross sections via the fiducial cross section formula from equation 5.5. In this method, theoretical systematic uncertainties were not included as nuisance parameters in the fit but were instead propagated separately to the final measurement through the acceptance correction factor. This strategy was additionally tested using an alternative signal modeling based on the MADGRAPH5_AMC@NLO generator. In both cases the resulting cross section measurements were found to be consistent with those obtained using the main analysis strategy,

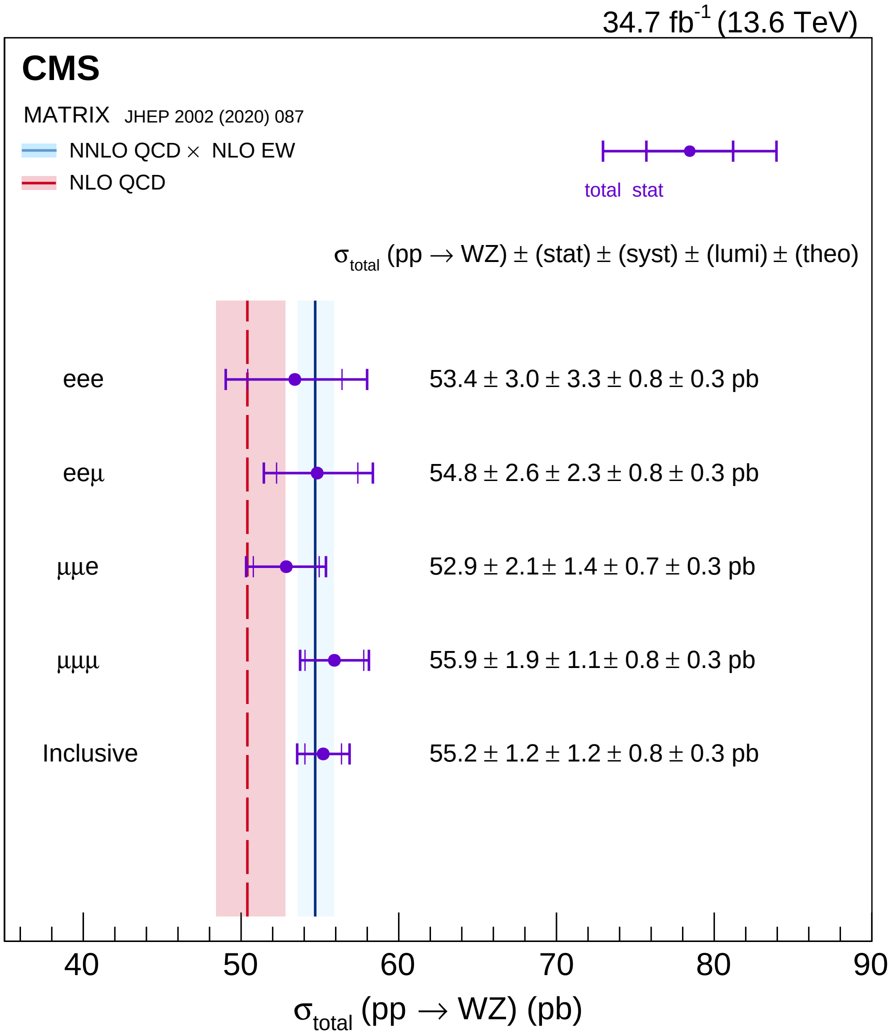

FIGURE. 7.8: Total WZ production cross section for each of the flavour-exclusive and for the flavour-inclusive categories. The vertical bands show different theoretical predictions for the WZ cross section at NLO in QCD (red dashed line) and NNLO QCD × NLO EW (blue solid line), as well as their corresponding scale uncertainties. For each measurement, the best fit value is denoted with a purple point, with two delimiters on the error bars that account for the statistical and total uncertainties.

thereby reinforcing the reliability of the results.

Table 7.4.7: Flavour-inclusive total cross section result. The predictions from both POWHEG at NLO in QCD and LO EW as well as several ones obtained from MATRIX (NLO QCD, NNLO QCD, NNLO QCD × NLO EW) are also included.

Accuracy	Total cross section (pb)
POWHEG , NLO QCD	$50.5\,^{+2.6}_{-2.1}$ (scale) $\pm$ 1.1 (PDF)
MATRIX, NLO QCD	$50.4\,^{+2.3}_{-2.0}$ (scale)
MATRIX, NNLO QCD	$55.0\,^{+1.2}_{-1.1}$ (scale)
MATRIX, NNLO QCD × NLO EW	$54.7\,^{+1.2}_{-1.1}$ (scale)
Inclusive (Measured)	55.2 $\pm$ 1.2 (stat) $\pm$ 1.2 (syst) $\pm$ 0.8 (lumi) $\pm$ 0.3 (theo)

7.5 Summary and Prospects

In this chapter, I have presented the first measurement of the WZ production cross section in pp collisions at a centre-of-mass energy of 13.6 TeV, using data collected in 2022 by the CMS detector, corresponding to an integrated luminosity of 34.7 fb^{-1}. The analysis focuses on final states where the W and resonant Z bosons decay leptonically into light leptons, e or μ. Events are categorized according to the flavour composition of the three final-state leptons, and this classification is used to extract the signal strength of the WZ process, as well as to constrain the normalisation of the dominant background contributions.

Two measurements are reported: one in a fiducial phase space designed to closely match the detector acceptance and minimize theoretical extrapolation, and another extrapolated to a broader total phase space, allowing for direct comparison with more general theoretical predictions. The production cross sections are measured inclusively, as well as for each of the four flavour combinations of the final-state leptons. All results are found to be in excellent agreement with the Standard Model predictions at NNLO QCD × NLO EW accuracy. The measured values are:

$$\sigma_{\text{fiducial}}(\mathrm{pp} \to \mathrm{WZ}) = 297.6 \pm 6.4\,(\text{stat}) \pm 6.4\,(\text{syst}) \pm 4.2\,(\text{lumi}) \pm 1.5\,(\text{theo})\ \text{fb},$$
$$\sigma_{\text{total}}(\mathrm{pp} \to \mathrm{WZ}) = 55.2 \pm 1.2\,(\text{stat}) \pm 1.2\,(\text{syst}) \pm 0.8\,(\text{lumi}) \pm 0.3\,(\text{theo})\ \text{pb}.$$

These results have been accepted for publication in the *Journal of High Energy Physics* and have been presented at major conferences, including the 42nd International Conference on High Energy Physics (ICHEP) in the summer of 2024, and the 59th Rencontres de Moriond 2025: Electroweak Interactions & Unified Theories conference. All numerical results are available on the HEPDATA repository [124], so that they can be used by theorists for future developments in WZ signal modeling.

Looking ahead, the WZ process continues to offer a rich testing ground for SM predictions at the LHC. With anticipated improvements in detector performance during by the end of Run 3, the accumulation of larger datasets, and potential combinations with Run 2 results, more precise measurements of the WZ properties are expected. Current signal modeling relies on MC simulations at NLO accuracy; however, NNLO generators are now available and will be crucial in reducing theoretical uncertainties —currently among the dominant sources of systematic uncertainty. The effort to include these simulations in the CMS production workflow has also been started as part of the work presented in this thesis, and more particularly in the context of WZ measurements. Incorporating these advancements will be essential for the next generation of WZ measurements, pushing the precision frontier even further.

8 Muon detection at the High-Luminosity LHC

Shifting towards a more detector-oriented focus, the present chapter explores various aspects regarding muon detection with the CMS DT system that have been developed throughout the course of this thesis. In particular, the work presented here is framed within the Phase-2 upgrade plans for the CMS experiment in preparation for the High-Luminosity LHC (HL-LHC). Approved in 2013, the HL-LHC establishes to a major upgrade of the detectors, enabling it to operate at peak instantaneous luminosities up to three times higher than the maximum achieved during Run 2, which is about $2 \times 10^{34}\ \mathrm{cm}^{-2}\mathrm{s}^{-1}$. The current plan is to start the high luminosity era between 2030 and 2031. By the end of 2042, the expected dataset size recorded at the HL-LHC is expected to be 3000 fb^{-1}, ten times larger than the expected with the full Run 2 and Run 3 datasets together.

Such a goal represents a challenge not only for accelerator physics but also for the experiments. The increase in instantaneous luminosity will significantly impact the PU conditions, which are projected to reach approximately 140 interaction vertices per bunch crossing at the start of the HL-LHC, nearly twice the highest PU observed during Run 3. Moreover, the HL-LHC will provide the largest dataset ever recorded and will likely represent the final dataset recorded at LHC. As a result, Phase-2 marks a crucial opportunity for experiments to maximize their physics reach. This requires a highly inclusive approach to detection, covering as much detector acceptance as possible. Furthermore, the increased instantaneous luminosity will substantially raise the radiation levels absorbed by the detectors, which will consequently need to operate in a significantly more challenging operating environment.

To overcome these challenges, the CMS experiment has developed upgrade plans aimed at enhancing its detection capabilities. My contributions to these developments are contextualized within the upgrade of the DT detectors, in particular through the characterization of the effects of irradiation on muon detection with the DT chambers, as well as with the development of innovative triggering approaches that can be implemented at the L1 trigger. The upgrade plans for the CMS DT system have been thoroughly reviewed in the technical design reports for the trigger [125], and the DT [126, 127].

8.1 Irradiation studies

During the HL-LHC, the CMS experiment will not change the DT chambers, and therefore the continuous operation of the DT stations will led to deterioration of the wires connected to the electronics. Malfunctioning cables can negatively impact detection efficiency, since a damaged wire may fail to trigger when a muon passes by, which, in turn, can affect the local segment reconstruction efficiency.

aging effects are crucial to ensure long-term operation. For the DTs, dedicated longevity studies were conducted at the Gamma Irradiation Facility (GIF++), a CERN installation designed for studying radiation effects on detectors. The aim of these studies was to expose a spare MB2 chamber from the CMS experiment to a ^{137}Cs radiation source to assess how performance could degrade based on the total dose absorbed by the various wires in the spare MB2. The ^{137}Cs source was selected because its primary γ-emission peak occurs at $E_\gamma = 661.657$ KeV, which is sufficient to ionize the chamber gas and generate a current in the anodes that could emulate the exposure to radiation at the HL-LHC. Previous studies performed in a spare MB1 chamber were presented in Ref. [128].

8.1.1 Time of exposure

The chamber was irradiated for nearly two years, with weekly irradiation runs that systematically exposed the chamber to the radiation effects. The aging process was controlled by adjusting the low- and high-voltages of the DT wires. The low-voltage regulates the ability to trigger the electronics and is typically set to 20 mV during data taking. The high voltage, on the other hand, determines the overall gain of the gas mixture used for detection, with a standard operating value of 3550 V at the time of the experiment. To establish a reference, some of wires were turned off during the irradiation period, to remove aging effects from the exposure to the radiation. This setup allowed for a direct comparison of hit detection efficiency between aged and non-aged wires, providing a clear measure of aging effects. The wires in SL1-L1 and SL1-L4 were selected for aging, while those in SL1-L2, SL1-L3, SL2, and SL3 served as reference wires.

By the end of the irradiation period, the aged wires had absorbed a total radiation dose of 2500 mGy. This dose is equivalent to the amount of dose that is expected to be absorbed by the DT system, after recording approximately 5000 fb^{-1}, which is 1.5 times the anticipated integrated luminosity of the HL-LHC. This can be seen in Figure 8.1, where the recorded integrated luminosity and accumulated dose over different time periods are reported.

8.1.2 Efficiency measurements

The performance of the DT system in an aged scenario is estimated in terms of hit efficiency. The hit efficiency is defined as the ratio between the number of correctly identified hits in the DTs, over the total number of hits that triggered the chamber.

To measure the efficiency, two sources of muons were used: cosmic and beam muons. Cosmic muons, which result from cosmic rays interacting with the atmosphere, are more common and arrive from all directions, leading to a uniform signal distribution across

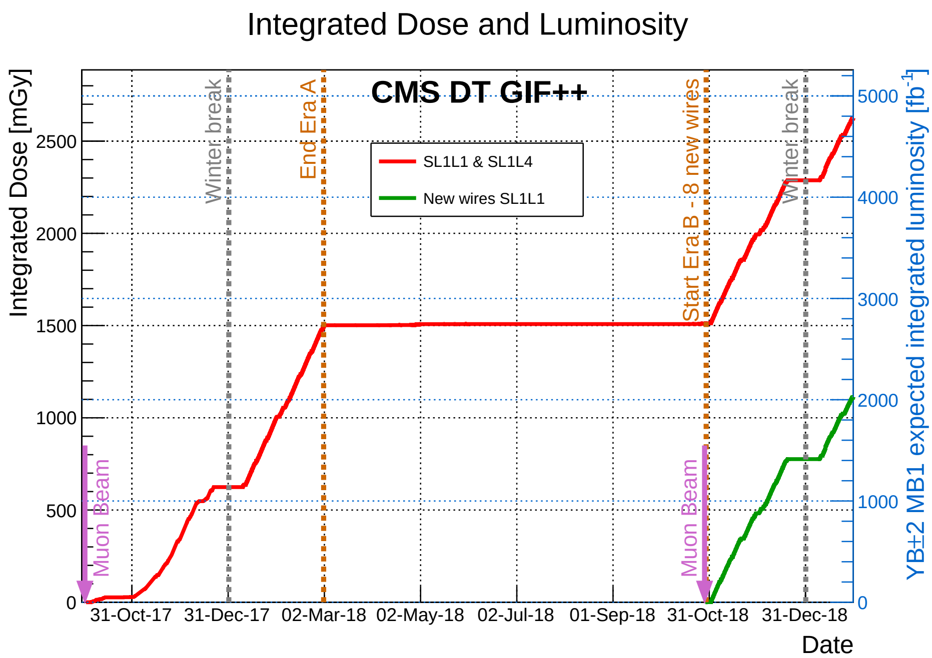

FIGURE. 8.1: [129] Integrated dose, in mGy, as a function of time for the irradiation period of the CMS DT spare chamber "MB2" at GIF++. The right y-axis represents the equivalent integrated luminosity, computed using a dose-to-luminosity conversion factor, while the left y-axis corresponds to the expected integrated luminosity for a given accumulated dose.

the chamber. Beam muons, in contrast, are produced by directing a proton beam onto a fixed target. The proton collisions generate pions, which decay into muons in about 99% of cases. Unlike cosmic muons, beam muons are concentrated in specific regions of the irradiated chamber.

Figure 8.2 shows the hit efficiency as a function of the expected instantaneous and integrated luminosities at the HL-LHC. The former provides insight into the hit efficiency conditions during data taking, while the latter reflects the expected efficiency degradation due to aging over years of operation.

A maximum drop of 20% in hit detection efficiency is observed at instantaneous luminosity values corresponding to the HL-LHC design, attributed to aging effects in both aged layers. The efficiency loss in the SL1-L4 aged wires is less pronounced than in SL1-L1 due to the experimental setup. The radiative source was positioned closer to the L1 wires, resulting in a slightly higher radiation exposure compared to SL1-L4. This trend is also expected in the HL-LHC scenario: since MB2 chambers are the second closest to the beam, where most of the radiation originates, they are expected to experience more aging than MB3 and MB4 chambers, which are farther from the beam, but less than MB1 chambers, which are the closest to the beam. In terms of hit detection performance at the end of the HL-LHC, a 50% drop of efficiency is expected by the end of the HL-LHC.

While hit detection efficiency provides insight into performance loss within a given DT chamber, it does not necessarily imply a strong correlation with the loss of muon

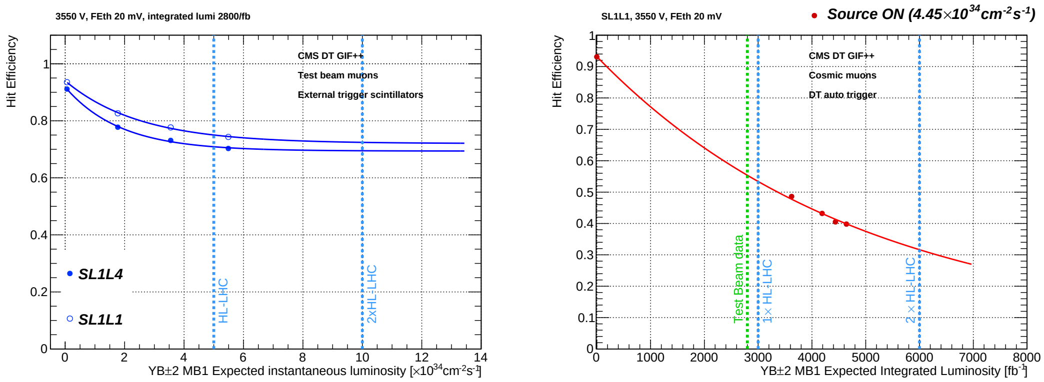

FIGURE. 8.2: [129] Left: Hit efficiency for test beam muons as a function of instantaneous luminosity for the aged layers. Right: Hit efficiency for cosmic muons as a function of integrated luminosity for the aged layer only. Each of these points corresponds to a different date during the whole irradiation period in which the hit efficiency was measured at normal operating values of the low and high voltages. The data are fitted using an exponential model.

reconstruction performance. This is because the efficiency loss because malfunctioning wires within individual DT chambers can generally be recovered by exploiting the large coverage of the DT system and the redundancy of the reconstruction algorithms, that normally combine the information from all DT chambers. Moreover, not all chambers are equally affected by radiation. For instance, chambers located in the central wheel of CMS experience less radiation compared to those in the forward region, where beam-induced radiation is more significant.

To evaluate this effect, the muon reconstruction efficiency as a function of the pseudorapidity at which the muon is reconstructed was measured under different aging scenarios. The aging model was derived from the results obtained at GIF++ and implemented in the detector simulation as a random loss of channels available for triggering. As shown in Figure 8.3, these studies indicate that aging effects have only a minor impact on muon reconstruction due to the built-in redundancy of the system.

As a result of these studies, it was concluded that the DT system is well-prepared to withstand the challenging environmental conditions of the HL-LHC in terms of both detector longevity and reconstruction efficiency.

8.2 Upgrade of the CMS trigger in Phase-2

The Phase-2 upgrade of the L1 system requires reaching technological milestones to improve physics sensitivity at the hardware level. The system will need to deal with 200 simultaneous collisions per beam crossing. The information from the whole CMS detector, including the tracking and high-granularity calorimeter information will now be part of the information available at the L1 for the first time. The target latency and maximum ouput bandwidth for the L1T decission are 12.5μs and 750 kHz, respectively. As a result,

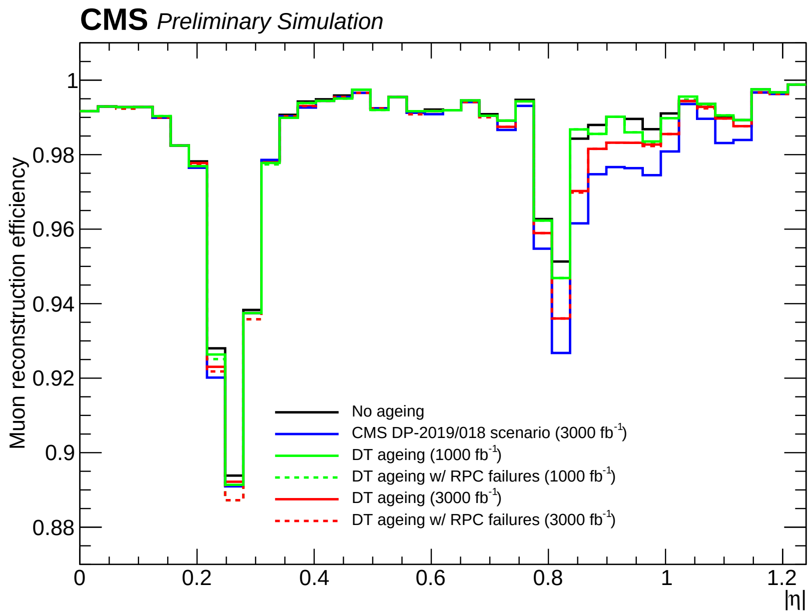

FIGURE. 8.3: [129] Muon reconstruction efficiency comparison as a function of the pseudorapidity. These efficiencies have been computed using generated dimuon events and considering different DT aging scenarios. The depletion observed $|\eta| = 0.3$ and 0.9 is not due to aging effects, but rather due to geometric limitations of the detector.

the L1 trigger architecture will be completely replaced for the Phase-2 of the CMS experiment. These updates aim to enhance algorithmic performance in terms of efficiency, rate, and throughput. Focusing on the L1 trigger upgrade for Phase-2, the proposed logic architecture is schematically summarized in Figure 8.4.

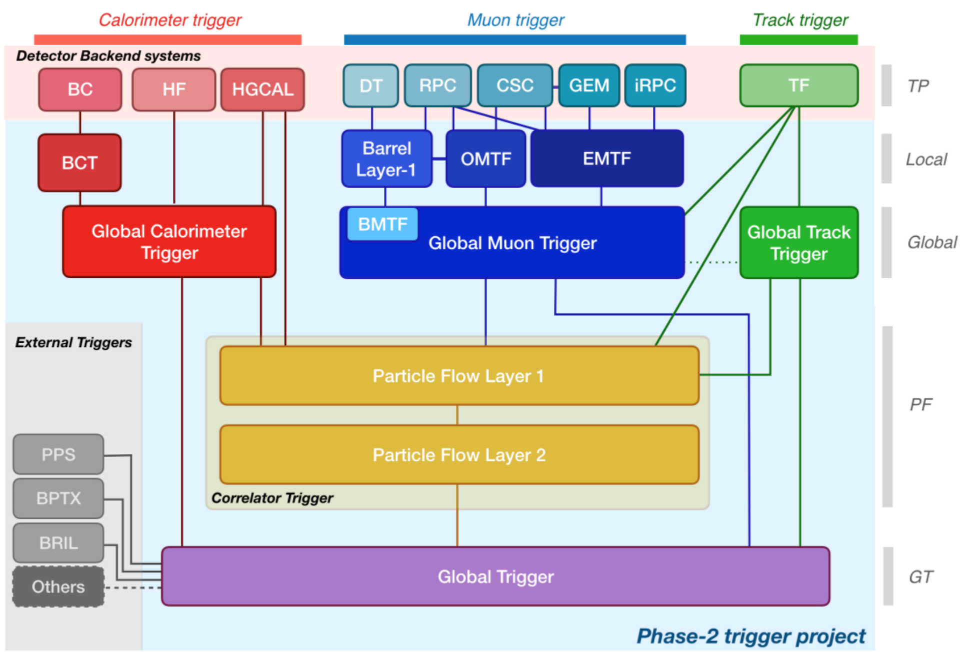

FIGURE. 8.4: [125] Functional diagram of the CMS L1 Phase-2 upgraded trigger design. A detailed description of this conceptual design is provided in the main text.

Inputs from each subsystem are processed by three dedicated global triggers: the global calorimeter trigger (GCT), the global muon trigger (GMT), and the global track trigger (GTT). The calorimeter trigger receives signals from the barrel calorimeter, the new high-granularity calorimeter (HGCAL), and the hadron forward calorimeter (HF). Data is first processed by the barrel calorimeter trigger (BCT) before being merged by the GCT.

The underlying logic of the muon trigger follows the same principles as in the legacy system, which is to processes signals from the muon sub-detectors, and feed this information into the muon track finders (TFs). The TFs are organized by pseudorapidity regions, as in the current system: the barrel muon TF (BMTF), endcap muon TF (EMTF), and overlap muon TF (OMTF). Their role is to correlate inputs from different subsystems to estimate local muon trajectories within the muon system. The TF outputs are sent to the global muon trigger (GMT), where track trigger information is also incorporated. The GMT then reconstructs complete muon trajectories with offline resolution. Finally, data from the GMT and calorimeter triggers are processed in the correlator trigger (CT), which performs a particle-flow-like reconstruction. The final decision on event selection is made by the global trigger (GT), similar to the legacy system.

My main contributions to the trigger upgrade have focused on improvements to the trigger strategy in the first layer of the DT trigger logic. To provide context for this work, the following sections will outline the specific upgrade plans for the DT system, with an emphasis on the electronics upgrade for muon identification using DT chambers, and how the newly developed triggering strategies fit within this framework.

8.2.1 Upgrade of the DT electronics

As part of the upgrade plans, the DT subsystem will experience a full replacement of the electronics used for both signal processing and triggering.

From the point of view of the triggering procedure, the DT system can be broadly seen as a two-tier layered system that consists of a front-end, a back-end. The front-end electronics act as the first interface between the DT instrumentation and the trigger system. When a muon ionizes the gas chambers, the deposited charge in the DT anode cable triggers the front-end electronics, which then send a signal indicating detection. The back-end electronics act as the interface between the front-end electronics (that triggered the signals), and the trigger system. Finally, the DT triggering system uses the information received from the back-end to locally reconstruct the information that triggered the front-end.

The back-end system of the DTs is renewed for Phase-2, replacing the legacy ASIC-based triggering electronics with a more flexible FPGA-based architecture. In the new system, the Barrel Muon Trigger Layer 1 (BMTL1) board takes over the functionalities previously handled by the unch Track Identifier (BTI) and Track Correlator (TRACO), and the TwinMux boards, which were in charge of performing pattern recognition, correlation and concentration of muon trigger primitives. Similarly, on the front-end side, the legacy ASIC-based readout is replaced by the On-Detector Board for Drift Tubes (OBDT) [130], which integrates FPGA technology to interface the DTs with the trigger and readout systems. These upgrades enable enhanced performance, increased adaptability, and better integration with the Phase-2 trigger architecture.

The new trigger system for Phase-2 will rely on Field Programmable Gate Array (FPGA) based architectures. The main reason for this shift lies in the unique flexibility offered by FPGAs. FPGAs, on the other hand, are designed to be reprogrammable. This means that the internal configuration of the FPGA can be changed at any time, even during the operation of the system. In other words, the FPGA internal connections between different electronic systems (such as flip-flops or memories) can be changed at will. The programming or design of an FPGA is achieved through the use of specialized hardware design languages, such as Hardware Description Language (HDL).

Solutions based on FPGAs are extremely suited for evolving projects such as the CMS trigger, as they allow for frequent updates and optimizations, ensuring that the trigger architecture evolves with new algorithms or requirements without needing to replace the entire hardware. Moreover, FPGAs provide a level of parallel processing that allows multiple tasks to be performed simultaneously, making them well-suited for the high-speed demands of particle detection and trigger decision-making. This flexibility, combined with continuous improvements in FPGA performance, makes them a strong alternative to ASICs in modern particle physics experiments.

Finally, the fact that FPGAs are programmed rather than being designed for a specific, fixed purpose allows multiple algorithms to be implemented on a single board. This flexibility aligns perfectly with one of the primary goals of the upgrade, which is to extend the range of covered phase spaces at the trigger stage. Most of the work that has been developed in the context of this thesis has been devoted to the development of new algorithms that could be implemented in the BMTL1 electronics, with the goal of triggering on different signals that can be identified within the muon DT system.

8.3 Muon triggering in Phase-2

The current method for triggering based on muon signatures at the BMTL1 is known as the Analytical Method (AM) [131]. In the Phase-2 architecture, the information provided to the AM comes directly from the OBDT. Each BX, the OBDT will be allowed to send up to 8 hits per BX to the BMTL1. This information is buffered in the board, and used to generate TPs that are subsequently fed into the TFs. The AM then employs an algorithm that works on a per-SL basis. For each SL, the AM thoroughly analyzes all possible combinations of three and four hits that are compatible with a straight line within the given SL. The AM later correlates the information from each SL to form high-level TPs that are consistent with a muon traversing up two SLs in the ϕ view. In the case of the θ

SL, since there is no correlation with adjacent chambers, the maximum amount of hits is still 4. Several approaches have been tested as alternative methods to the AM, and none of them lead to better efficiencies, rates or time resolution. Thus, the AM was chosen to be the main Phase-2 algorithm for the DT Trigger step performed at the BMTL1.

8.4 Triggering on high p_{T} muons in Phase-2

In pp collisions, reconstructed muons in CMS can reach energies as low as a few GeV and can go as high as energy conservation laws allow. For this energy range, there are two primary sources of interaction: ionization and radiative energy losses (bremsstrahlung). The Bethe-Bloch formula generally describes the different energy loss mechanisms that a given charged particle can undergo due to the interaction of this particle with a given material. The type of interactions normally depend on several aspects of both the projectile (the particle) and the target (the material). The formula presented in 8.1 gives the rate of energy loss $-\frac{dE}{dx}$ for a charged particle traversing through a given material, considering the contributions from ionization and bremsstrahlung mechanisms only.

$$-\frac{dE}{dx} = -\frac{4\pi z^2 e^4}{m_\mu c^2 \beta^2}\left[\ln\left(\frac{2mc^2\beta^2}{I}\right) - \beta^2\right] - E \times \frac{4\alpha r_e^2 z^2 n}{m_\mu^2}\ln\left(\frac{183}{Z^{1/3}}\right) \tag{8.1}$$

Here, z is the charge of the incident particle, e is the elementary charge, m is the mass, c is the speed of light, I is the mean excitation energy of the medium, and $\beta = v/c$ is the velocity of the particle relative to the speed of light, r_e is the classical electron radius, m_μ is the mass of the muon, and Z is the atomic number of the target material. The first term represents the energy loss rate due to ionization, whereas the second term amounts the energy losses due to bremsstrahlung. As the speed of the particle increases, approaching the speed of light, the ionization interaction mechanisms are less frequent. At the same time, radiative losses due to bremsstrahlung become a much more relevant contribution to the energy loss of a charged particle. While these interactions are typically suppressed by the mass of the projectile, high-energy muons can still undergo substantial bremsstrahlung.

8.4.1 Physics use case

In case there is no bremsstrahlung, the signature observed in the DTs typically consists of 3-5 hits per SL, depending on the how inclined the muon trajectory is when entering the chamber. In contrast, when the muon produces bremsstrahlung radiation, for instance, through interactions with the iron between MB1 and MB2, the emitted radiation can either interact with electrons in the iron or lead to electron-positron pair production via conversion mechanisms. In either case, the produced electrons from the electromagnetic shower can reach a nearby SL in another chamber, causing ionization of the gas. This results in a higher multiplicity of hits, which can trigger the electronics and be sent to the

BMTL1 for processing. Figure 8.5 shows an schematic representation on how these two cases could be seen from the detector point of view.

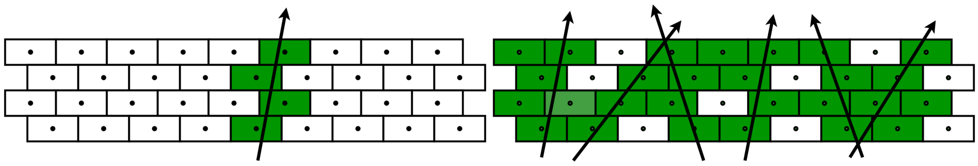

FIGURE. 8.5: [132] Comparison of hit multiplicity in a given DT SL for two scenarios: (left) a non-radiative muon passing through the chamber, and (right) a muon that has showered, presumably in the iron before the chamber, resulting in a significantly higher hit multiplicity in the SL.

During Run 2, it was demonstrated that showering effects significantly affected reconstruction efficiency [133]. A shower identification algorithm was developed to tag showering events based on the multiplicity of segments in DT or RPC stations. The study analyzed L1 inefficiencies by correlating the number of reconstructed showers with trigger performance. Two efficiency measurements were compared: one based on shower tagging and another by direct matching of reconstructed muons to L1 objects. Figure 8.6 illustrates this efficiency loss as a function of muon momentum. The results confirm a clear drop in L1 efficiency at high p_T due to showering, which the L1 trigger cannot recover.

This inefficiency will also be present in Phase-2 due to a limitation of the AM. This limitation stems from the fact that, regardless of the number of hits arriving at the BMTL1, all reconstructed TPs must be delivered within a fixed time window. This window is constrained by the time resolution of the AM, which is on the order of a few nanoseconds. When a muon showers, the increased hit multiplicity can exceed the processing capacity of the AM, leading to inefficiencies in reconstruction. As result, the the accuracy of the TFs in reconstructing the trajectory of high-p_T muons is negatively affected, as there is not enough information to properly determine the true momentum of the showering muon. Furthermore, the kick from the radiation makes the available information somwewhat misleading in many cases. As a result, a showering muon may be reconstructed with a lower momentum than the L1T threshold, preventing the event from being triggered.

If the event is triggered despite the showering, its efficiency can be recovered through shower identification in the offline reconstruction. However, if the momentum assignment of showering muons is incorrect, the efficiency loss occurs at the L1 trigger level, making the event unrecoverable. As a result of these studies, new innovative approaches to trigger on such signatures have been developed, particularly in this thesis. These studies are presented in the following pages.

8.4.2 The hit counting algorithm

The strategy for triggering on high-p_T muons is designed to be implemented within the BMTL1, where the AM also operates. This approach builds upon the findings of

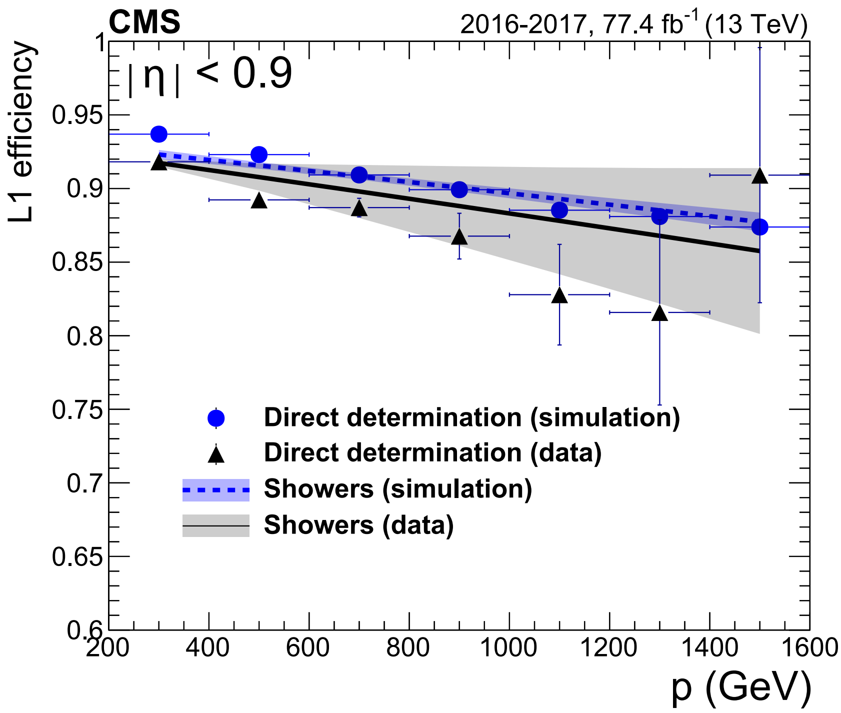

FIGURE. 8.6: [133] The L1 efficiency in the barrel measured with two different approaches. The plots show a comparison between directly determining the efficiency from simulation (blue dots) and from data (black triangles), with respect to calculating it from shower multiplicity, both in 2016+2017 combined data (black line) and 2017 simulation (dashed blue line). The shaded bands represent the statistical uncertainties of the measurements and the systematic uncertainty of the showering probability determination.

Ref. [133], as well as on a similar implementation included in the Run 3 trigger menu, which targeted muon showers in the endcap regions of CMS through the use of the High Multiciplity Trigger (HMT) algorithm [134]. The new algorithm is specifically developed to target such signatures in the barrel region, thereby extending the geometrical acceptance for muon shower triggering.

The algorithm is based on establishing a correlation between the presence of a muon shower and the number of identified hits in a given DT chamber. The main principle of the algorithm is to count the number of hits within a given time window, which accounts for the maximum time in which the outputs from the BMTL1 must be fed into the next stage of the L1 trigger. If the number of hits in a given chamber exceeds a predefined threshold within this window, the shower trigger is activated, and a flag is sent to the next layers of trigger so further considerations could be taken into account. At this level, the following constraints are considered:

- **Number of hits**: Since the algorithm requires counting hits within a given time window, it must account for the fact that hits are sent in batches per BX from the OBDT. Consequently, part of the allocated latency is dedicated to buffering hits.
- **Buffering constraints**: A single hit can only be kept in the buffer for up to 16 BXs

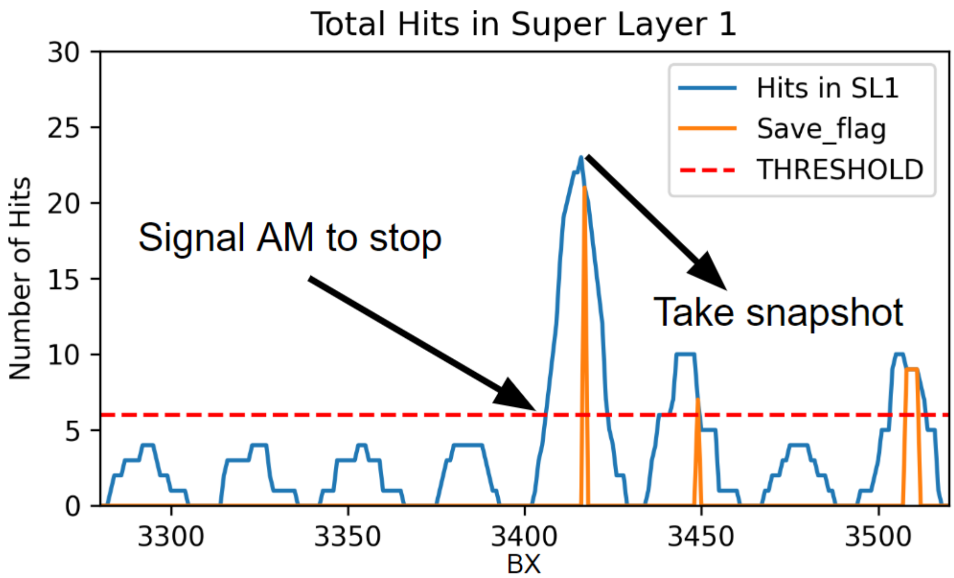

FIGURE. 8.7: Distribution of the number of hits per BX for a set of simulated events containing showering and non-showering muons. The blue line represents the hit count per BX, the orange line indicates instances where the muon shower triggers the system, and the red line marks the triggering threshold.

due to memory limitations in the firmware. Therefore, the algorithm must consider this time window to estimate the maximum number of recorded hits.

- **Readout**: The algorithm is designed to read hits from one SL at a time (similarly to the AM). Multiple instances of the same algorithm can be implemented within the BMTL1 to enable the readout of multiple SLs simultaneously.

With these technical constraints, the appearance of a shower in the trigger system would resemble what is shown in Figure 8.7, which illustrates the number of hits recorded in SL1 of a given MB1 chamber. For non-showering events the maximum recorded hits in the SL typically range between 4 and 5. This corresponds to one hit per layer of the SL, with occasional additional hits arising from delta-ray effects or noise fluctuations. In contrast, for showering events, the hit multiplicity increases significantly, reaching peaks of over 20 hits in a single SL. The width of each peak in this distribution corresponds to the 16 BX time window constraint that limits the time that one is able to buffer hits in the FPGA.

The proposed algorithm is refered to in this document as the Hit Counting Algorithm (HCA), and it is designed to identify peaks in the hit distribution. When the number of recorded hits exceeds a predefined threshold (typically 5 or 6), the event is classified as a showering event and is subsequently triggered. This signal might be used to inform the AM, which operates on the same board, that the event contains a shower. Consequently, the AM can account for this information when computing the TPs.

Once the shower algorithm is triggered, a snapshot of the event is taken, and a Shower-TP is sent as an output. This additional information can be utilized in later stages of the trigger to enhance the reconstruction of showering muons.

8.4.3 Validation of the HCA in simulation

The performance of the algorithm has been tested in two different simulations. The first simulation was produced with a private GEANT4 simulation of a DT chamber in which muons target towards a general MB2 chamber used to simulate the effects of the shower. Muons were generated with a p_{T} of 2 TeV, so that it could be in the regime in which the major interaction mechanism for the muons was through bremsstrahlung. Because the bremsstrahlung is often produced in the interaction with the iron, the same simulation could be used to test the performance of the HCA in case of non-shower topologies.

The true presence of a shower is obtained by tracking the history of the GEANT4 simulation. Each hit generated by the electromagnetic shower is assigned a unique numerical identifier, distinguishing it from hits originating from the interaction with a muon. By tracking these identifiers, one can clearly define a "true" shower, which can then be compared with the objects reconstructed by the HCA. The performance of the algorithm using this simulation is shown in Figure 8.8, for the measurement of confusion metrics. The confusion is obtained by counting the number of times that the algorithm triggers the event because it detected a shower, depending on whether a true shower occurred or not.

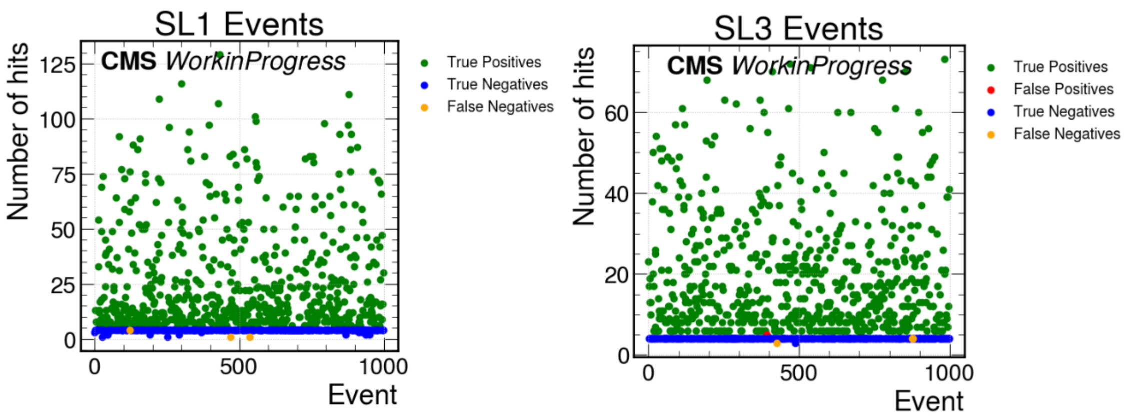

FIGURE. 8.8: Confusion metrics for the HCA measured in SL1 (left) and SL3 (right) of the simulated DT chamber. The green points (true positives) indicate cases where a true showering muon was present, and the algorithm successfully triggered the event. The blue points (false negatives) represent instances where a showering muon was present, but the algorithm failed to trigger. The red (false positives) and orange (true negatives) points correspond to cases where the trigger was activated despite no true showering muon in the respective SL.

The results of this algorithm implementation shows remarkable performance in properly identifying showers. Notably, events classified as true negatives, false positives, or false negatives are predominantly concentrated in the regime below 10 hits. Above this threshold, all events triggered by the algorithm correspond to true showering events.

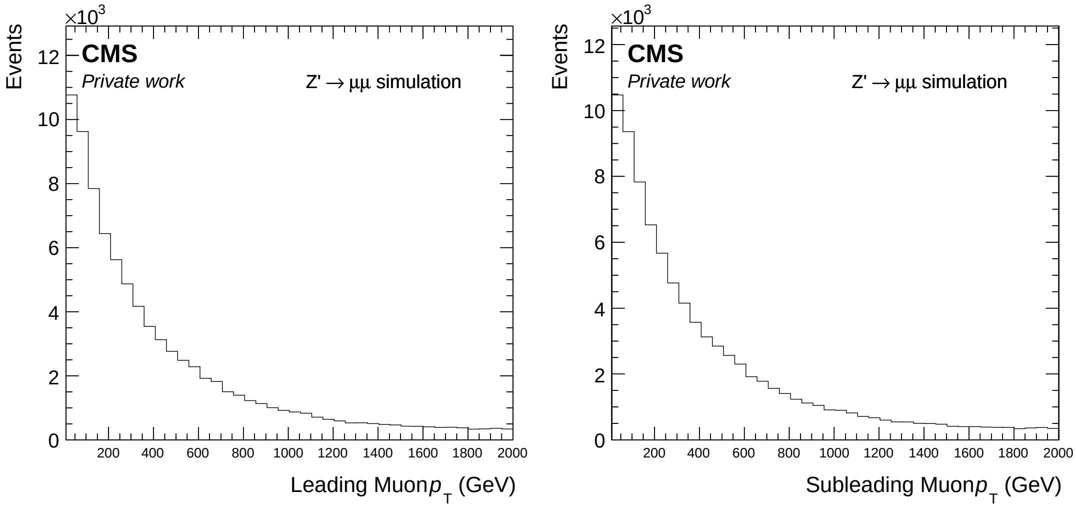

FIGURE. 8.9: Distribution of the muon p_T in the case of the two muons from the Z′ decay.

8.4.3.1 Results in real physics use cases

The second set of validation studies were also performed using a MC simulation of Z′ production, in which the mass of the Z′ has an invariant mass of 6 TeV. The Z′ candidates of this sample are generated with an invariant mass of 6 TeV, and are decayed to two energetic leptons, as shown in Figure 8.9, where the p_T of the two muons is shown. The samples are generated with a PU profile of 200, which is the expected profile by the end of the HL-LHC, which constitutes the dominant source of background hits for the HCA when using this sample.

To evaluate the performance of the algorithm, the HCA is applied to each event in the Z′ sample. Event triggering is based on whether the number of hits exceeds a configurable threshold, which serves as a parameter in the algorithm. The performance of the HCA, in terms of triggering efficiency on different types of chambers, is shown in Figure 8.10, integrated over all sectors, and for each wheel of the CMS detector. Efficiency is computed as the ratio of events that triggered the HCA to the total number of events processed. Additionally, the performance is evaluated as a function of the threshold used to define the HCA trigger.

For each wheel, the efficiency increases as in the outtermost DT stations. This behavior arises because the electromagnetic showers that trigger the HCA are limited by the amount of material the muon traverses as it passes through the detector. As a result, the outermost chambers are more sensitive to higher hit counts than the innermost ones, since these interactions typically occur in the iron between the chambers. Moreover, for a given chamber, the efficiency increases in the central wheel of CMS. This is expected, as in the Z′ sample, the most energetic muons are generally more central. Consequently, these muons are more likely to interact in the central region of the detector.

Additionally, these results show that an optimal working point for the HCA could be

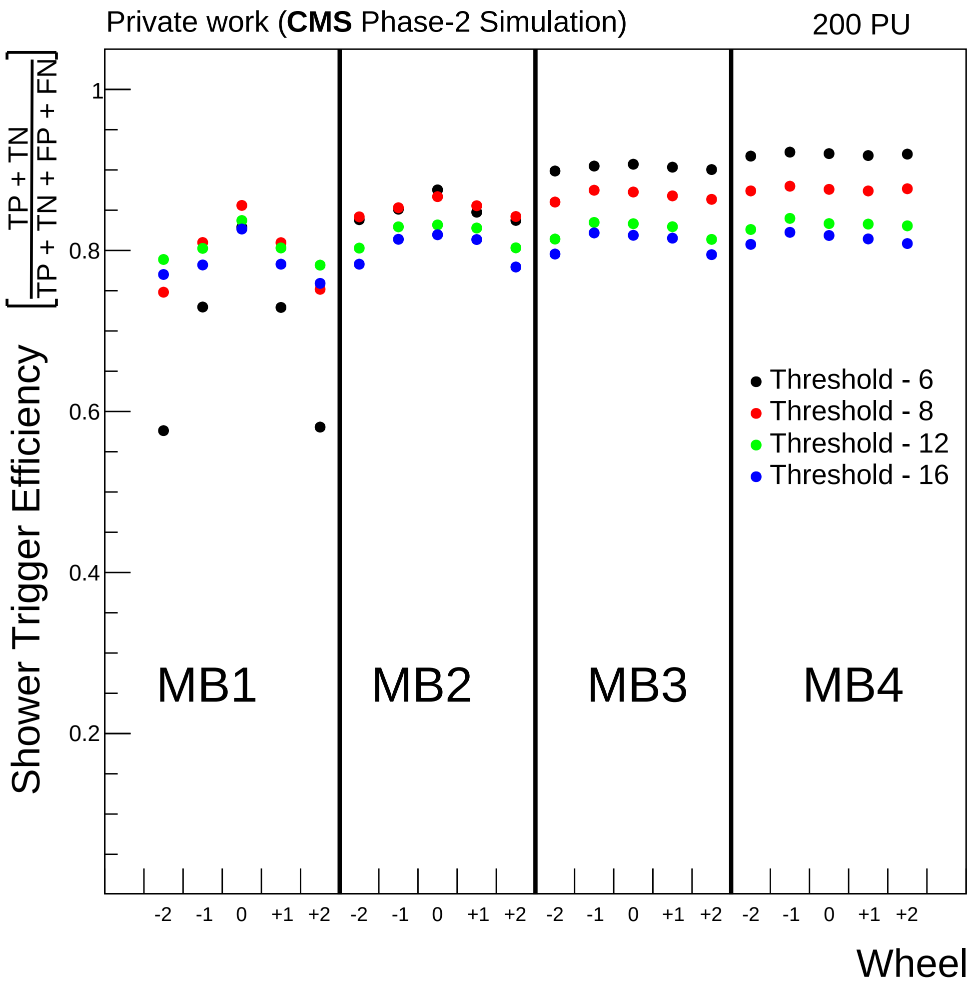

FIGURE. 8.10: Shower trigger efficiency for different MB chambers, splitted by wheel, and integrated over the different sectors of CMS. Several curves are shown for different thresholds used to define the shower regime, ranging from 6 to 16 hits.

achieved by setting a threshold at 6 or 8 hits. A slight decrease of efficiency for the 6 hits threshold is observed in the MB1 chambers in the outermost wheels, likely related to an statistical limitation of events in that region. The complete optimization of the threshold must be balanced against rate studies, as using a very low threshold could lead to a significant increase in the number of triggers sent to the next stage. This, in turn, could negatively impact the overall data taking performance due to the high trigger rate.

In addition to the efficiency studies of the HCA itself, it was also tested how much efficiency could be recovered by a joint action of both the HCA and the AM algorithms, as both are supposed to be the two algorithms that will be implemented in the BMTL1 boards for the Phase-2. The results for these studies are presented in Figure 8.11. Assuming that the ouput of the AM when a muon showers is not optimal, the observed drop of efficiency is about 20-30% depending on the wheel and station. The event triggering efficiency can be recovered by the HCA, particularly in the central region of the detector, considering the OR of the two algorithms.

These results are obtained under a conservative assumption in which the output of the AM is discarded in the presence of a shower. Further studies exploring less pessimistic scenarios are currently being conducted. Nevertheless, the results clearly highlight the need for a trigger strategy that explicitly accounts for showering events.

8.5 Summary and Prospects

Phase-2 represents a major milestone in the field of particle physics. At present, the CMS experiment is operating during Run 3, with data taking expected to continue until june 2026. The Phase-2 upgrade will be implemented during the long shutdown that follows Run 3. As such, it is essential that all components of the upgrade are fully prepared ahead of time. The dataset achieved after the Phase-2 is expected to be 3000 fb^{-1}, and it will be the last dataset obtained with the LHC.

In this chapter, several aspects related to DT studies and trigger developments have been presented, with a particular focus on their relevance to the upcoming HL-LHC upgrade.

During Phase-2, the CMS experiment will retain the legacy instrumentation for the DT chambers. This means that by the end of the HL-LHC, the DT system is expected to have accumulated a radiation dose of approximately 2500 mGy. Continuous exposure to irradiation may impact detector performance, primarily through ageing effects on the wires that interface with the front-end electronics. These effects can influence signal thresholds and overall response accuracy. However, extensive studies carried out at the GIF++ facility have demonstrated that, even if local hit efficiency in the DTs degrades due to ageing, the overall muon reconstruction performance remains robust. These studies have been particularly focused on the MB1 and MB2 chambers, which are most susceptible to radiation damage due to their proximity to the beam pipe. As a result, good muon

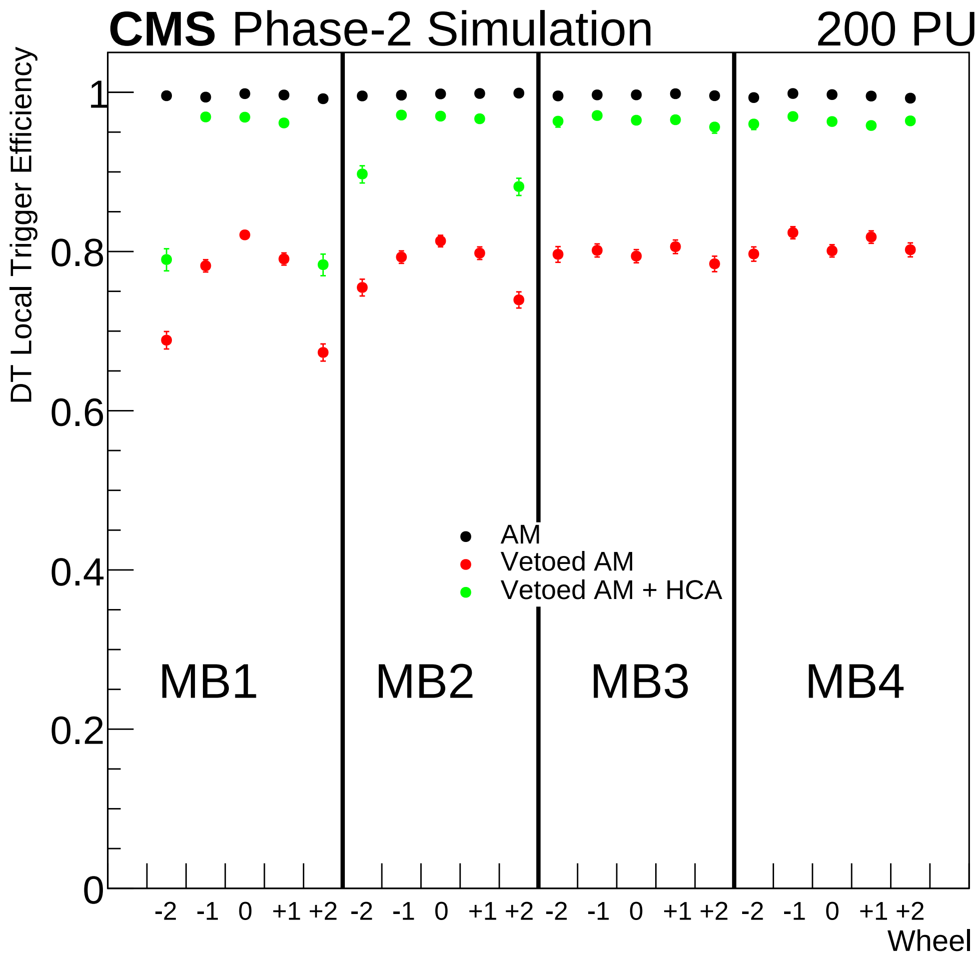

FIGURE. 8.11: Efficiency of both the AM and the shower trigger. Results are shown for each type of MB chamber, integrated over all CMS sectors and further split by wheel. The reference AM efficiency measured in the Z′ sample is shown as black points under the assumption that showers do not affect its performance, and as a red points in a pessimistic scenario where the AM output is discarded in the presence of showering events. The joint performance of the HCA trigger and the AM is shown as green points in the figure.

reconstruction performance in the central region of CMS is expected to be maintained throughout Phase-2.

As part of my contributions to the trigger upgrade, I have developed the first version of the HCA. This algorithm is designed to identify shower-like events in the barrel region by exploiting the characteristic high-multiplicity hit patterns produced by electromagnetic showers in the DTs. While the algorithm was initially developed to target high-p_T muon signatures, it also holds potential for identifying BSM phenomena —such as displaced hadrons that punch through the initial layers of the DT system and leave behind dense clusters of hits.

The HCA is currently being integrated into the CMS software framework, making it an official algorithm of the L1 trigger menu for the Phase-2. Further studies aiming to measure rates, and configuration of the shower thresholds will be the next steps towards having a full working version of the algorithm. In addition, the algorithm has also been demonstrated in firmware, using vivado simulation. The current version is able to fit within the FPGA inside the BMTL1 board, alongside the AM method algorithm. There are currently plans to include it in the CMS slice test [135] for validation using real collision data.

9 Summary and conclusions

In this document, several crucial measurements, analyses, and developments within the context of high energy physics have been covered. My work has contributed significantly to the ongoing research program at the CMS experiment, particularly in the areas of $\mathrm{t\bar{t}W}$ and WZ cross section measurements, as well as the ongoing preparations for the high luminosity era of the LHC.

In the first part of this thesis, measurements related to the $\mathrm{t\bar{t}W}$ production process, focusing on both inclusive and differential cross-sections, were presented. Both the inclusive and differential results presented are of great importance in future iterations of $\mathrm{t\bar{t}W}$ results, both for the CMS and ATLAS collaborations. The inclusive cross-section measurements reaffirmed the mild tensions previously observed in dedicated $\mathrm{t\bar{t}H}$ measurements, achieving a higher level of precision from building a dedicated measurement of the $\mathrm{t\bar{t}W}$ process. The final measured cross sections was found to be:

$$\sigma_{\text{total}}(\mathrm{pp} \rightarrow \mathrm{t\bar{t}W}) = 868.0 \pm 40\,(\text{stat}) \pm 51\,(\text{syst})\ \text{fb}.$$

which stands as the most precise determination of the $\mathrm{t\bar{t}W}$ cross section up to date. A notable challenge in the inclusive cross-section measurement was the contribution from very low cross-section backgrounds, which unexpectedly influenced the final uncertainty despite contributing only a few events. This issue was especially relevant in the signal-dominated bins, where the NN approach struggled to separate the $\mathrm{t\bar{t}W}$ signal from these small background processes. Addressing this challenge calls for improved MC modeling and dedicated measurement of these low contributing cross section backgrounds.

Additionally, differential measurements were conducted by unfolding the distributions for processes relevant to the $\mathrm{t\bar{t}W}$ process. These measurements were compared at the generator level with the latest MC simulations. The validation studies performed with stable resonances were conclusive regarding that the new modeling for the weak jets had a non-negligible contribution in the FXFX merging and matching performance for the $\mathrm{t\bar{t}W}$ process. These effects were, however, not confirmed when studying $\mathrm{t\bar{t}W}$ at the differential level. Although the differential measurements are still largely dominated by statistical uncertainties, and a larger dataset could shed more light on the observed differences, a closer look into new modelings is needed. One of the possible improvements that can help close the gap between data and prediction is the inclusion of matrix element corrections [136]. Further validation studies of the $\mathrm{t\bar{t}W}$ modeling at the decay level are now coordinated by me within CMS.

The second major contribution of this work is the measurement of the WZ production cross section at a centre-of-mass energy of 13.6 TeV. A particularly significant aspect of this analysis is the implementation of an updated lepton MVA-based selection strategy. This development not only played a key role in improving the performance of the current measurement but also has broader implications, as the updated MVA is now adopted as the standard approach for most Run 3 analyses. Future measurements will benefit from its enhanced lepton identification capabilities, contributing to increased precision and robustness across a wide range of physics studies.

For the first time at 13.6 TeV, the measurement of the WZ production cross section is given in a fiducial phase space, which closely matches the detector acceptance and minimizes theoretical extrapolation, and in an extrapolated total phase space to allow for comparison with broader theoretical predictions. The measured values for the WZ production cross section were, respectively:

$$\sigma_{\text{fiducial}}(\text{pp} \to \text{WZ}) = 297.6 \pm 6.4\,(\text{stat}) \pm 6.4\,(\text{syst}) \pm 4.2\,(\text{lumi}) \pm 1.5\,(\text{theo})\ \text{fb},$$
$$\sigma_{\text{total}}(\text{pp} \to \text{WZ}) = 55.2 \pm 1.2\,(\text{stat}) \pm 1.2\,(\text{syst}) \pm 0.8\,(\text{lumi}) \pm 0.3\,(\text{theo})\ \text{pb}.$$

These results represent the most precise measurements of the WZ production cross section to date, with a total uncertainty of 3.4%. They additionally complete the picture of WZ cross section measurements after 15 years of LHC operation, as it can be seen in Figure 9.1, where the WZ cross section as a function of centre-of-mass energy are reported.

They are in excellent agreement with SM predictions at NNLO QCD $\times$ NLO EW accuracy. Looking ahead, the continued development of more advanced MC simulations, including the transition to NNLO generators, will be crucial for reducing theoretical uncertainties and improving the precision of WZ measurements in future analyses. Part of this work has already been started, motivated from the measurements that have been presented.

The final part of this thesis discusses preparations for the Phase-2 upgrade of the CMS experiment, particularly focusing on the upgrades to the DT system and trigger developments for the HL-LHC. During Phase-2, the CMS experiment will continue to use the DT chambers, which are expected to accumulate a radiation dose of approximately 2500 mGy by the end of the HL-LHC. This sustained exposure will introduce challenges, particularly with ageing effects on the wires that interface with the front-end electronics, potentially affecting signal thresholds and response accuracy. However, studies at the GIF++ facility have shown that, despite local hit efficiency degradation, the overall muon reconstruction performance will remain robust.

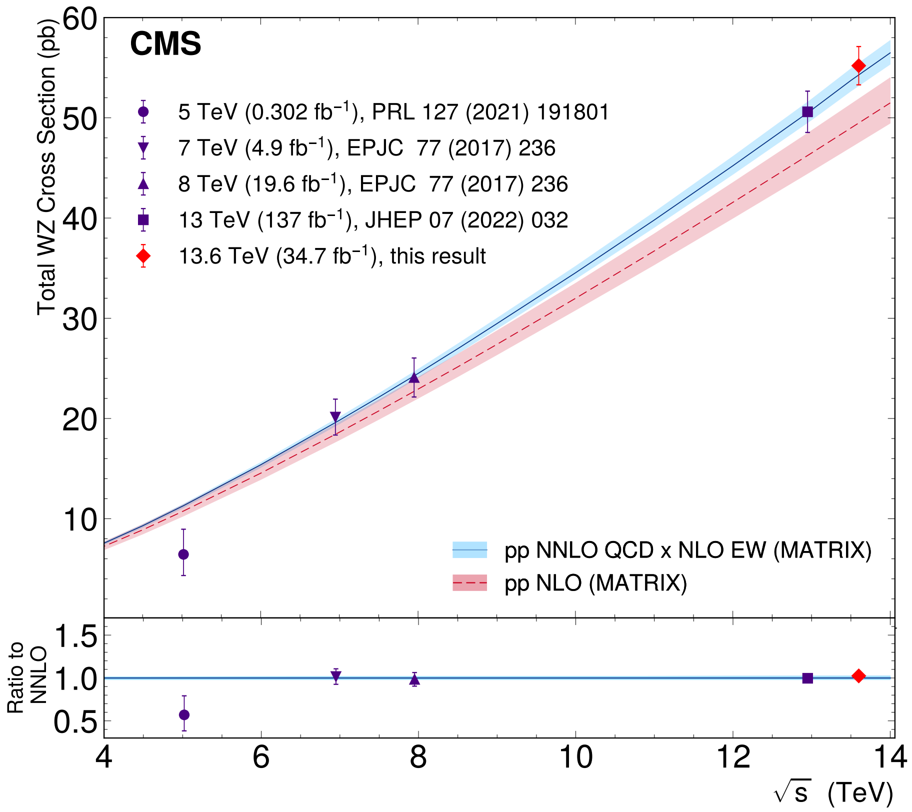

FIGURE. 9.1: Measurement obtained in the measurement I published in Ref. [17] ("this result", in the legend, shown as a red filled marker), compared with previous CMS measurements of the WZ production cross section at various centre-of-mass energies [78, 122, 123]. Predictions at NNLO QCD $\times$ NLO EW and NLO QCD, computed with MATRIX, are also shown.

Alongside these studies, the trigger system will undergo significant upgrades, including the incorporation of tracking information at the L1 trigger, allowing for extending the CMS acceptance with new event topologies and enhanced sensitivity to BSM physics already at the earliest stages of identification. A key contribution to this upgrade is the development of the HCA, which is designed to identify shower-like events in the barrel region. This algorithm was initially developed to target high-p_T muon signatures, but it also holds promise for identifying BSM phenomena, such as displaced hadrons. The algorithm is being integrated into the CMS software framework, and it is expected to be tested using real collision data during the Phase-2 slice test, with further improvements to be made based on the test results.

The work presented in this thesis contributes significantly to both ongoing and future measurements at the LHC. From the precision measurements of the $t\bar{t}W$ and WZ cross sections to the preparation for the Phase-2 upgrades, this research not only enhances our understanding of fundamental processes in particle physics but also paves the way for future breakthroughs. The developments in both MC modeling and trigger algorithms will have a lasting impact on the CMS experiment.

10 Resumen y conclusiones

En este documento se han presentado varias medidas, análisis y desarrollos fundamentales dentro del área de la física experimental de altas energías. Mi trabajo ha contribuido de manera significativa al actual programa de investigación del experimento CMS, particularmente en el ámbito de medidas de sección eficaz de los procesos $\mathrm{t\bar{t}W}$ y WZ, así como en los preparativos para las mejoras del detector CMS de cara a la era de alta luminosidad del LHC.

En la primera parte de esta tesis, se presentaron medidas relacionadas con el proceso $\mathrm{t\bar{t}W}$, centrándose tanto en su sección eficaz inclusiva como diferencial. Los resultados inclusivos y diferenciales aquí presentados son de gran relevancia para futuras iteraciones de medidas realizadas en torno a las propiedades del proceso $\mathrm{t\bar{t}W}$, tanto para la colaboración CMS como ATLAS. Las medidas de la sección eficaz inclusiva reafirman ligeras tensiones observadas anteriormente en medidas dedicadas al proceso $\mathrm{t\bar{t}H}$, alcanzando un mayor nivel de precisión gracias al desarrollo de una estrategia específica para el proceso $\mathrm{t\bar{t}W}$. La sección eficaz final medida fue:

$$\sigma_{\text{total}}(\mathrm{pp} \to \mathrm{t\bar{t}W}) = 868.0 \pm 40\,(\text{stat}) \pm 51\,(\text{syst})\ \text{fb}.$$

que constituye la determinación más precisa hasta la fecha de la sección eficaz de $\mathrm{t\bar{t}W}$ a nivel inclusivo. Un desafío notable en esta medida fue la estimación de la contribución de fondos con secciones eficaces muy bajas, que influyeron de forma inesperada en la incertidumbre final a pesar de aportar solo unos pocos eventos en la selección final. Este problema fue especialmente relevante en las regiones dominadas por la presencia de señal, donde el enfoque basado en redes neuronales dio lugar a dificultades para separar la señal $\mathrm{t\bar{t}W}$ de estos fondos. Abordar este desafío requiere una mejor modelización del MC, asi como medidas específicas de las propiedades de estos fondos.

Además, se han presentado medidas diferenciales de algunas de las distribuciones más relevantes al proceso $\mathrm{t\bar{t}W}$. Estas medidas fueron comparadas a nivel de generador con las simulaciones de MC más recientes. Los estudios de validación realizados manteniendo todas las resonancias estables confirmaron que la nueva modelización de los *weak jets* tiene una contribución no despreciable en el entendemiento del proceso de *matching* y *merging* que se codifica en el algoritmo FXFX para el proceso $\mathrm{t\bar{t}W}$. Sin embargo, estos mismos efectos no fueron observados al estudiar $\mathrm{t\bar{t}W}$ a nivel diferencial, considerando el caso en el que las resonancias se desintegran en estados finales leptónicos. Aunque las medidas diferenciales están todavía dominadas por incertidumbres estadísticas, y un conjunto de datos mayor podría arrojar más luz sobre las diferencias observadas, se necesita un análisis más profundo de nuevos métodos para modelar las contribuciones de $t\bar{t}W$. Una de las posibles mejoras para cerrar la brecha entre datos y predicción es la inclusión de correcciones a los elementos de matriz [136]. Actualmente soy coordinador de estudios adicionales de validación de la modelización de $t\bar{t}W$ dentro del experimento CMS, en colaboración con el experimento ATLAS.

La segunda contribución principal de este trabajo es la medida de la sección eficaz de producción de WZ a una energía en centro de masas de 13.6 TeV. Un aspecto particularmente significativo de este análisis es la implementación de una estrategia de selección basada en un MVA para identificación de leptones especificamente actualizada para su uso en Run 3. Este desarrollo no solo fue clave en la medida actual, sino que también tiene implicaciones más amplias dentro de la colaboración, ya que el nuevo MVA ha sido adoptado como una estrategia estándar para la mayoría de los análisis del Run 3. Las futuras medidas se beneficiarán de estas mejoras, lo que contribuirá a una mayor precisión y robustez en una amplia gama de estudios sobre física de partículas.

Por primera vez a 13.6 TeV, la medida de la sección eficaz de producción de WZ se presenta tanto en un espacio de fases fiducial, que se ajusta estrechamente a la aceptancia del detector y minimiza la extrapolación teórica, como en un espacio de fases total que permite una comparación con predicciones teóricas más generales. Los valores medidos para la sección eficaz de producción de WZ fueron:

$$\sigma_{\text{fiducial}}(\text{pp} \to \text{WZ}) = 297.6 \pm 6.4\,(\text{stat}) \pm 6.4\,(\text{syst}) \pm 4.2\,(\text{lumi}) \pm 1.5\,(\text{theo})\ \text{fb},$$
$$\sigma_{\text{total}}(\text{pp} \to \text{WZ}) = 55.2 \pm 1.2\,(\text{stat}) \pm 1.2\,(\text{syst}) \pm 0.8\,(\text{lumi}) \pm 0.3\,(\text{theo})\ \text{pb}.$$

Estos resultados representan las medidas más precisas hasta la fecha de la sección eficaz de producción de WZ, con una incertidumbre total del 3.4%. Además, completan el panorama de las medidas de la sección eficaz de WZ tras 15 años de operación del LHC, como se muestra en la Figura 10.1, donde se presentan los valores medidos de la sección eficaz de WZ en función de la energía en centro de masas.

Los resultados están en excelente acuerdo con las predicciones del Modelo Estándar (ME) a precisión NNLO QCD $\times$ NLO EW. De cara al futuro, el desarrollo continuo de simulaciones MC más avanzadas, incluyendo la transición a generadores NNLO, será crucial para reducir las incertidumbres teóricas y mejorar la precisión de las medidas de WZ en análisis futuros. Parte de este trabajo ya ha comenzado, motivado por las medidas aquí presentadas.

La parte final de esta tesis aborda los preparativos para la actualización de la Fase 2 del experimento CMS, centrándose particularmente en las mejoras del sistema de tubos

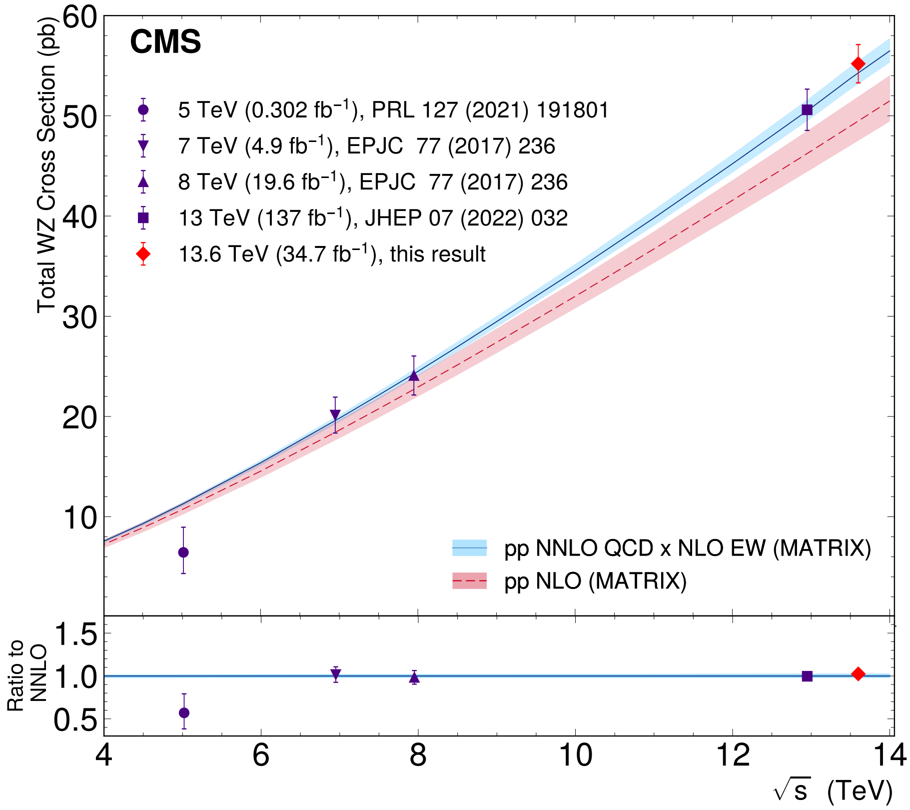

FIGURE. 10.1: Medida obtenida en el trabajo publicado en Ref. [17] ("this result", en la leyenda, marcado con un punto rojo), comparada con medidas previas de CMS de la sección eficaz de producción de WZ a distintas energías en centro de masas [78, 122, 123]. También se muestran predicciones a NNLO QCD $\times$ NLO EW y QCD a orden NLO, calculadas con MATRIX.

de deriva (DT) y los desarrollos del sistema de *trigger* para el HL-LHC. Durante la Fase 2, el experimento CMS continuará utilizando las cámaras DT, que se espera acumulen una dosis de radiación de aproximadamente 2500 mGy al final del HL-LHC. Esta exposición sostenida presenta desafíos, especialmente debido a los efectos de envejecimiento en los cables que conectan con la electrónica, lo cual podría afectar a la precisión en la respuesta del detector al paso de partículas cargadas. Sin embargo, estudios desarrollados en GIF++ han demostrado que, a pesar de la degradación en la eficiencia local de identificación, la eficiencia de reconstrucción de muones se mantendrá a unos niveles similares a los actuales.

El sistema de *trigger* será objeto de mejoras significativas, incluyendo la incorporación de información de *tracking* en el L1-*trigger*, permitiendo una extensión de la aceptancia del experimento CMS con nuevas topologías y una sensibilidad aumentada a física más allá del Modelo Estándar (BSM) incluso en los primeros pasos en el proceso de detección. Una contribución clave a esta mejora es el desarrollo del *Hit Counting Algorithm* (HCA), diseñado para identificar eventos en los que se han producido cascadas electromagnéticas en la región del barril de CMS. Este algoritmo fue desarrollado inicialmente para identificar señales características de muones con alto momento transverso, aunque también tiene potencial para identificar fenómenos BSM, como hadrones desplazados. El algoritmo está siendo integrado como parte de la simulación central de CMS, y se espera que sea probado con datos reales de colisiones como parte del *slice test* de Fase 2.

El trabajo presentado en esta tesis contribuye de manera significativa tanto a las medidas actuales como futuras en el LHC. Desde las medidas de precisión de las secciones eficaces de $t\bar{t}W$ y WZ hasta la preparación para las actualizaciones de Fase 2, esta investigación no solo mejora nuestra comprensión de los procesos fundamentales en física de partículas, sino que también prepara el camino para futuros avances. Los desarrollos en modelización de MC y algoritmos de *trigger* tendrán un impacto duradero en el experimento CMS.

Bibliography

[1] Steven Weinberg. A Model of Leptons. *Phys. Rev. Lett.*, 19:1264–1266, 1967.

[2] Abdus Salam. Weak and Electromagnetic Interactions. *Conf. Proc. C*, 680519:367–377, 1968.

[3] A. Rousset. The discovery of weak neutral currents. *Nucl. Phys. B Proc. Suppl.*, 36:339–361, 1994.

[4] S. L. Glashow. Partial Symmetries of Weak Interactions. *Nucl. Phys.*, 22:579–588, 1961.

[5] G. Arnison et al. Experimental Observation of Isolated Large Transverse Energy Electrons with Associated Missing Energy at $\sqrt{s} = 540$ GeV. *Phys. Lett. B*, 122:103–116, 1983.

[6] G. Arnison et al. Experimental Observation of Lepton Pairs of Invariant Mass Around 95-GeV/c**2 at the CERN SPS Collider. *Phys. Lett. B*, 126:398–410, 1983.

[7] M. Banner et al. Observation of Single Isolated Electrons of High Transverse Momentum in Events with Missing Transverse Energy at the CERN anti-p p Collider. *Phys. Lett. B*, 122:476–485, 1983.

[8] P. Bagnaia et al. Evidence for $Z^0 \to e^+e^-$ at the CERN $\bar{p}p$ Collider. *Phys. Lett. B*, 129:130–140, 1983.

[9] F. Abe et al. Observation of top quark production in $\bar{p}p$ collisions. *Phys. Rev. Lett.*, 74:2626–2631, 1995.

[10] S. Abachi et al. Observation of the top quark. *Phys. Rev. Lett.*, 74:2632–2637, 1995.

[11] Serguei Chatrchyan et al. Observation of a New Boson at a Mass of 125 GeV with the CMS Experiment at the LHC. *Phys. Lett. B*, 716:30–61, 2012.

[12] Georges Aad et al. Observation of a new particle in the search for the Standard Model Higgs boson with the ATLAS detector at the LHC. *Phys. Lett. B*, 716:1–29, 2012.

[13] S. Navas et al. Review of particle physics. *Phys. Rev. D*, 110(3):030001, 2024.

[14] Armen Tumasyan et al. Measurement of the cross section of top quark-antiquark pair production in association with a W boson in proton-proton collisions at $\sqrt{s}$ = 13 TeV. *JHEP*, 07:219, 2023.

[15] Measurement of the $\mathrm{t\bar{t}W}$ differential cross section and charge asymmetry at $\sqrt{s} =$ 13 TeV. Technical report, CERN, Geneva, 2025.

[16] Celine Degrande, Nicolas Greiner, Wolfgang Kilian, Olivier Mattelaer, Harrison Mebane, Tim Stelzer, Scott Willenbrock, and Cen Zhang. Effective Field Theory: A Modern Approach to Anomalous Couplings. *Annals Phys.*, 335:21–32, 2013.

[17] Aram Hayrapetyan et al. Measurement of the inclusive WZ production cross section in pp collisions at $\sqrt{s}$ = 13.6 TeV. *Submitted to JHEP*, 12 2024.

[18] Richard Phillips Feynman. *The principle of least action in quantum mechanics*. PhD thesis, Princeton U., 1942.

[19] Wesley E. Brittin and Asim Orhan Barut, editors. *Lorentz Group. Proceedings, 7th Summer Institute for Theoretical Physics: Boulder, CO, USA, 1964*, volume 7A of *Lectures in Theoretical Physics*, Boulder, 1965. Colorado Univ. Press.

[20] Emmy Noether. Invariant Variation Problems. *Gott. Nachr.*, 1918:235–257, 1918.

[21] Richard Brauer and Hermann Weyl. Spinors in n dimensions. *American Journal of Mathematics*, 57(2):425–449, 1935.

[22] Peter W. Higgs. Spontaneous Symmetry Breakdown without Massless Bosons. *Phys. Rev.*, 145:1156–1163, 1966.

[23] F. Englert and R. Brout. Broken Symmetry and the Mass of Gauge Vector Mesons. *Phys. Rev. Lett.*, 13:321–323, 1964.

[24] Fred Jegerlehner. The hierarchy problem of the electroweak Standard Model revisited. 5 2013.

[25] Armen Tumasyan et al. A portrait of the Higgs boson by the CMS experiment ten years after the discovery. *Nature*, 607(7917):60–68, 2022. [Erratum: Nature 623, (2023)].

[26] Vladimir Chekhovsky et al. High-precision measurement of the W boson mass with the CMS experiment at the LHC. 12 2024.

[27] G. L. Bayatian et al. CMS Physics: Technical Design Report Volume 1: Detector Performance and Software. 2006.

[28] S. Chatrchyan et al. The CMS Experiment at the CERN LHC. *JINST*, 3:S08004, 2008.

[29] J Quijada. Recent upgrades and results from the cms experiment. *Journal of Physics: Conference Series*, 912:012005, 10 2017.

[30] V. Karimäki. The CMS tracker system project: Technical Design Report. 1997.

[31] H. Bichsel, D. E. Groom, and S. R. Klein. Passage of particles through matter. 2008.

[32] Vardan Khachatryan et al. The CMS trigger system. *JINST*, 12(01):P01020, 2017.

[33] A. Hayrapetyan et al. Performance of the CMS high-level trigger during LHC Run 2. *JINST*, 19(11):P11021, 2024.

[34] A. M. Sirunyan et al. Particle-flow reconstruction and global event description with the CMS detector. *JINST*, 12(10):P10003, 2017.

[35] R. Fruhwirth. Application of Kalman filtering to track and vertex fitting. *Nucl. Instrum. Meth. A*, 262:444–450, 1987.

[36] Serguei Chatrchyan et al. Description and performance of track and primary-vertex reconstruction with the CMS tracker. *JINST*, 9(10):P10009, 2014.

[37] W. Adam, R. Frühwirth, A. Strandlie, and T. Todorov. Reconstruction of Electron Tracks With the Gaussian-Sum Filter. 3 2003.

[38] Matteo Cacciari, Gavin P. Salam, and Gregory Soyez. The anti-k_t jet clustering algorithm. *JHEP*, 04:063, 2008.

[39] Matteo Cacciari, Gavin P. Salam, and Gregory Soyez. FastJet User Manual. *Eur. Phys. J. C*, 72:1896, 2012.

[40] Albert M Sirunyan et al. Pileup mitigation at CMS in 13 TeV data. *JINST*, 15(09):P09018, 2020.

[41] Daniele Bertolini, Philip Harris, Matthew Low, and Nhan Tran. Pileup Per Particle Identification. *JHEP*, 10:059, 2014.

[42] Murray Gell-Mann. A Schematic Model of Baryons and Mesons. *Phys. Lett.*, 8:214–215, 1964.

[43] Yuri L. Dokshitzer. Calculation of the Structure Functions for Deep Inelastic Scattering and e+ e- Annihilation by Perturbation Theory in Quantum Chromodynamics. *Sov. Phys. JETP*, 46:641–653, 1977.

[44] V. N. Gribov and L. N. Lipatov. Deep inelastic e p scattering in perturbation theory. *Sov. J. Nucl. Phys.*, 15:438–450, 1972.

[45] Guido Altarelli and G. Parisi. Asymptotic Freedom in Parton Language. *Nucl. Phys. B*, 126:298–318, 1977.

[46] Richard D. Ball et al. Parton distributions for the LHC Run II. *JHEP*, 04:040, 2015.

[47] R. D. Ball, V. Bertone, S. Carrazza, L. Del Debbio, S. Forte, P. Groth-Merrild, A. Guffanti, N. P. Hartland, Z. Kassabov, J. I. Latorre, E. R. Nocera, J. Rojo, L. Rottoli, E. Slade, and M. Ubiali. Parton distributions from high-precision collider data. *Eur. Phys. J. C*, 77:663, 2017.

[48] H. Lehmann, K. Symanzik, and W. Zimmermann. On the formulation of quantized field theories. *Nuovo Cim.*, 1:205–225, 1955.

[49] R. P. Feynman. Space - time approach to quantum electrodynamics. *Phys. Rev.*, 76:769–789, 1949.

[50] P. Nason. A new method for combining NLO QCD with shower Monte Carlo algorithms. *JHEP*, 11:040, 2004.

[51] S. Frixione, P. Nason, and C. Oleari. Matching NLO QCD computations with parton shower simulations: the POWHEG method. *JHEP*, 11:070, 2007.

[52] S. Alioli, P. Nason, C. Oleari, and E. Re. A general framework for implementing NLO calculations in shower Monte Carlo programs: the POWHEG BOX. *JHEP*, 06:043, 2010.

[53] Stefano Frixione, Paolo Nason, and Giovanni Ridolfi. A Positive-weight next-to-leading-order Monte Carlo for heavy flavour hadroproduction. *JHEP*, 09:126, 2007.

[54] J. Alwall, R. Frederix, S. Frixione, V. Hirschi, F. Maltoni, O. Mattelaer, H.-S. Shao, T. Stelzer, P. Torrielli, and M. Zaro. The automated computation of tree-level and next-to-leading order differential cross sections, and their matching to parton shower simulations. *JHEP*, 07:079, 2014.

[55] R. Frederix, S. Frixione, V. Hirschi, D. Pagani, H. S. Shao, and M. Zaro. The automation of next-to-leading order electroweak calculations. *JHEP*, 07:185, 2018. [Erratum: JHEP 11, 085 (2021)].

[56] Christian Bierlich et al. A comprehensive guide to the physics and usage of PYTHIA 8.3. *SciPost Phys. Codeb.*, 2022:8, 2022.

[57] Vardan Khachatryan et al. Event generator tunes obtained from underlying event and multiparton scattering measurements. *Eur. Phys. J. C*, 76(3):155, 2016.

[58] Armen Tumasyan et al. CMS pythia 8 colour reconnection tunes based on underlying-event data. *Eur. Phys. J. C*, 83(7):587, 2023.

[59] Rikkert Frederix and Stefano Frixione. Merging meets matching in MC@NLO. *JHEP*, 12:061, 2012.

[60] Michelangelo L. Mangano, Mauro Moretti, Fulvio Piccinini, and Michele Treccani. Matching matrix elements and shower evolution for top-quark production in hadronic collisions. *JHEP*, 01:013, 2007.

[61] Rikkert Frederix, Davide Pagani, and Marco Zaro. Large NLO corrections in $t\bar{t}W^{\pm}$ and $t\bar{t}t\bar{t}$ hadroproduction from supposedly subleading EW contributions. *JHEP*, 02:031, 2018.

[62] S. Frixione, V. Hirschi, D. Pagani, H. S. Shao, and M. Zaro. Electroweak and QCD corrections to top-pair hadroproduction in association with heavy bosons. *JHEP*, 06:184, 2015.

[63] Luca Buonocore, Simone Devoto, Massimiliano Grazzini, Stefan Kallweit, Javier Mazzitelli, Luca Rottoli, and Chiara Savoini. Precise Predictions for the Associated Production of a W Boson with a Top-Antitop Quark Pair at the LHC. *Phys. Rev. Lett.*, 131(23):231901, 2023.

[64] Pierre Artoisenet, Rikkert Frederix, Olivier Mattelaer, and Robbert Rietkerk. Automatic spin-entangled decays of heavy resonances in Monte Carlo simulations. *JHEP*, 03:015, 2013.

[65] Anna Kulesza, Leszek Motyka, Daniel Schwartländer, Tomasz Stebel, and Vincent Theeuwes. Associated top quark pair production with a heavy boson: differential cross sections at NLO+NNLL accuracy. *Eur. Phys. J. C*, 80(5):428, 2020.

[66] Rikkert Frederix and Ioannis Tsinikos. On improving NLO merging for $t\bar{t}W$ production. *JHEP*, 11:029, 2021.

[67] M. Grazzini, S. Kallweit, J. M. Lindert, S. Pozzorini, and M. Wiesemann. NNLO QCD + NLO EW with MATRIX+OPENLOOPS: precise predictions for vector-boson pair production. *JHEP*, 02:087, 2020.

[68] Tom Melia, Paolo Nason, Raoul Rontsch, and Giulia Zanderighi. W+W-, WZ and ZZ production in the POWHEG BOX. *JHEP*, 11:078, 2011.

[69] P. Nason and G. Zanderighi. W^+W^-, WZ and ZZ production in the POWHEG -BOX-V2. *Eur. Phys. J. C*, 74:2702, 2014.

[70] Pier Francesco Monni, Paolo Nason, Emanuele Re, Marius Wiesemann, and Giulia Zanderighi. MiNNLO$_{PS}$: a new method to match NNLO QCD to parton showers. *JHEP*, 05:143, 2020. [Erratum: JHEP 02, 031 (2022)].

[71] Jonas M. Lindert, Daniele Lombardi, Marius Wiesemann, Giulia Zanderighi, and Silvia Zanoli. WZ production at NNLO QCD and NLO EW matched to parton showers with MiNNLO$_{PS}$. *JHEP*, 11:036, 2022.

[72] A. M. Sirunyan et al. Identification of heavy-flavour jets with the CMS detector in pp collisions at 13 TeV. *JINST*, 13(05):P05011, 2018.

[73] Performance of the DeepJet b tagging algorithm using 41.9/fb of data from proton-proton collisions at 13TeV with Phase 1 CMS detector. 2018.

[74] Huilin Qu, Congqiao Li, and Sitian Qian. Particle Transformer for Jet Tagging. 2 2022.

[75] Huilin Qu and Loukas Gouskos. ParticleNet: Jet Tagging via Particle Clouds. *Phys. Rev. D*, 101(5):056019, 2020.

[76] Uttiya Sarkar. Run 3 performance and advances in heavy-flavor jet tagging in CMS. *PoS*, ICHEP2024:992, 2025.

[77] Albert M Sirunyan et al. Measurement of the Higgs boson production rate in association with top quarks in final states with electrons, muons, and hadronically decaying tau leptons at $\sqrt{s} = 13$ TeV. *Eur. Phys. J. C*, 81(4):378, 2021.

[78] Armen Tumasyan et al. Measurement of the inclusive and differential WZ production cross sections, polarization angles, and triple gauge couplings in pp collisions at $\sqrt{s}$ = 13 TeV. *JHEP*, 07:032, 2022.

[79] Aram Hayrapetyan et al. Muon identification using multivariate techniques in the CMS experiment in proton-proton collisions at sqrt(s) = 13 TeV. *JINST*, 19(02):P02031, 2024.

[80] Search for CP violation in events with top quarks and Z bosons. Technical report, CERN, Geneva, 2025.

[81] Vardan Khachatryan et al. Jet energy scale and resolution in the CMS experiment in pp collisions at 8 TeV. *JINST*, 12(02):P02014, 2017.

[82] Vardan Khachatryan et al. Measurements of Inclusive W and Z Cross Sections in *pp* Collisions at $\sqrt{s} = 7$ TeV. *JHEP*, 01:080, 2011.

[83] Aram Hayrapetyan et al. The CMS Statistical Analysis and Combination Tool: Combine. *Comput. Softw. Big Sci.*, 8(1):19, 2024.

[84] CMS Luminosity Measurements for the 2016 Data Taking Period. 2017.

[85] CMS luminosity measurement for the 2017 data-taking period at $\sqrt{s} = 13$ TeV. 2018.

[86] CMS luminosity measurement for the 2018 data-taking period at $\sqrt{s} = 13$ TeV. 2019.

[87] CMS Collaboration. Luminosity measurement in proton-proton collisions at 13.6TeV in 2022 at CMS. CMS Physics Analysis Summary CMS-PAS-LUM-22-001, 2024.

[88] J. Butterworth et al. PDF4LHC recommendations for LHC Run II. *J. Phys. G*, 43:023001, 2016.

[89] Jon Butterworth, Stefano Carrazza, Amanda Cooper-Sarkar, Albert De Roeck, Joël Feltesse, Stefano Forte, Jun Gao, Sasha Glazov, Joey Huston, Zahari Kassabov, Ronan McNulty, Andreas Morsch, Pavel Nadolsky, Voica Radescu, Juan Rojo, and Robert Thorne. PDF4LHC recommendations for LHC Run II. *Journal of Physics G: Nuclear and Particle Physics*, 43(2):023001, jan 2016.

[90] S. Schael et al. Precision electroweak measurements on the Z resonance. *Phys. Rept.*, 427:257–454, 2006.

[91] Vardan Khachatryan et al. Performance of Electron Reconstruction and Selection with the CMS Detector in Proton-Proton Collisions at $\sqrt{s}$ = 8 TeV. *JINST*, 10(06):P06005, 2015.

[92] Heribertus B. Hartanto, Barbara Jager, Laura Reina, and Doreen Wackeroth. Higgs boson production in association with top quarks in the POWHEG BOX. *Phys. Rev. D*, 91(9):094003, 2015.

[93] Carlos. F. Erice Cid. *Study of beyond the standard model processes in leptonic final states with the CMS detector at the Run 2 of the LHC*. PhD thesis, University of Oviedo, Oviedo, Spain, September 2021.

[94] Albert M Sirunyan et al. Evidence for associated production of a Higgs boson with a top quark pair in final states with electrons, muons, and hadronically decaying τ leptons at $\sqrt{s} = 13$ TeV. *JHEP*, 08:066, 2018.

[95] Armen Tumasyan et al. Measurement of the inclusive and differential $t\bar{t}\gamma$ cross sections in the single-lepton channel and EFT interpretation at $\sqrt{s}$ = 13 TeV. *JHEP*, 12:180, 2021.

[96] A. M. Sirunyan et al. Search for electroweak production of charginos and neutralinos in multilepton final states in proton-proton collisions at $\sqrt{s} = 13$ TeV. *JHEP*, 03:166, 2018.

[97] Armen Tumasyan et al. Inclusive and differential cross section measurements of single top quark production in association with a Z boson in proton-proton collisions at $\sqrt{s}$ = 13 TeV. *JHEP*, 02:107, 2022.

[98] Albert M Sirunyan et al. Search for standard model production of four top quarks with same-sign and multilepton final states in proton–proton collisions at $\sqrt{s}$ = 13 TeV. *Eur. Phys. J. C*, 78(2):140, 2018.

[99] Albert M Sirunyan et al. Observation of the Production of Three Massive Gauge Bosons at $\sqrt{s}$ =13 TeV. *Phys. Rev. Lett.*, 125(15):151802, 2020.

[100] Georges Aad et al. Measurement of the total and differential cross-sections of $t\bar{t}W$ production in pp collisions at $\sqrt{s}$ = 13 TeV with the ATLAS detector. *JHEP*, 05:131, 2024.

[101] V. M. Abazov et al. Measurement of the WZ $\to \ell\nu\ell\ell$ cross section and limits on anomalous triple gauge couplings in $p\bar{p}$ collisions at $\sqrt{s} = 1.96$ TeV. *Phys. Lett. B*, 695:67, 2011.

[102] A. Abulencia et al. Observation of W Z production. *Phys. Rev. Lett*, 98:161801, 2007.

[103] Georges Aad et al. Measurement of the $W^{\pm}Z$ production cross section and limits on anomalous triple gauge couplings in proton-proton collisions at $\sqrt{s} = 7$ TeV with the ATLAS detector. *Phys. Lett. B*, 709:341, 2012.

[104] Georges Aad et al. Measurement of WZ production in proton-proton collisions at $\sqrt{s} = 7$ TeV with the ATLAS detector. *Eur. Phys. J. C*, 72:2173, 2012.

[105] Georges Aad et al. Measurement of the WW + WZ cross section and limits on anomalous triple gauge couplings using final states with one lepton, missing transverse momentum, and two jets with the ATLAS detector at $\sqrt{\mathrm{s}} = 7$ TeV. *JHEP*, 01:049, 2015.

[106] Georges Aad et al. Measurements of $\mathrm{W}^{\pm}\mathrm{Z}$ production cross sections in pp collisions at $\sqrt{s} = 8$ TeV with the ATLAS detector and limits on anomalous gauge boson self-couplings. *Phys. Rev. D*, 93:092004, 2016.

[107] Morad Aaboud et al. Measurement of the $\mathrm{W}^{\pm}\mathrm{Z}$ boson pair-production cross section in pp collisions at $\sqrt{s} = 13$ TeV with the ATLAS Detector. *Phys. Lett. B*, 762:1, 2016.

[108] Morad Aaboud et al. Search for anomalous electroweak production of WW/WZ in association with a high-mass dijet system in pp collisions at $\sqrt{s} = 8$ TeV with the ATLAS detector. *Phys. Rev. D*, 95:032001, 2017.

[109] Morad Aaboud et al. Measurement of WW/WZ $\rightarrow \ell\nu qq^{'}$ production with the hadronically decaying boson reconstructed as one or two jets in pp collisions at $\sqrt{s} = 8$ TeV with ATLAS, and constraints on anomalous gauge couplings. *Eur. Phys. J. C*, 77:563, 2017.

[110] Georges Aad et al. Search for the electroweak diboson production in association with a high-mass dijet system in semileptonic final states in pp collisions at $\sqrt{s} = 13$ TeV with the ATLAS detector. *Phys. Rev.*, D100(3):032007, 2019.

[111] Morad Aaboud et al. Measurement of $W^{\pm}Z$ production cross sections and gauge boson polarisation in pp collisions at $\sqrt{s} = 13$ TeV with the ATLAS detector. *Eur. Phys. J.*, C79(6):535, 2019.

[112] Serguei Chatrchyan et al. Study of the dijet mass spectrum in $\mathrm{pp} \rightarrow \mathrm{W}+$ jets events at $\sqrt{s} = 7$ TeV. *Phys. Rev. Lett.*, 109:251801, 2012.

[113] Serguei Chatrchyan et al. Measurement of the sum of WW and WZ production with W+dijet events in pp collisions at $\sqrt{s} = 7$ TeV. *Eur. Phys. J. C*, 73:2283, 2013.

[114] Serguei Chatrchyan et al. Measurement of WZ and ZZ production in pp collisions at $\sqrt{s} = 8$ TeV in final states with b-tagged jets. *Eur. Phys. J. C*, 74:2973, 2014.

[115] Vardan Khachatryan et al. Measurement of the WZ production cross section in pp collisions at $\sqrt{s} = 13$ TeV. *Phys. Lett. B*, 766:268, 2017.

[116] V. Khachatryan et al. Measurement of the WZ production cross section in pp collisions at $\sqrt{s} = 7$ and 8 TeV and search for anomalous triple gauge couplings at $\sqrt{s} = 8$ TeV. *Eur. Phys. J. C*, 77:236, 2017.

[117] A. M. Sirunyan et al. Search for anomalous couplings in boosted WW/WZ $\rightarrow \ell\nu \mathrm{q}\bar{\mathrm{q}}$ production in proton-proton collisions at $\sqrt{s} = 8$ TeV. *Phys. Lett. B*, 772:21, 2017.

[118] Albert M Sirunyan et al. Search for anomalous electroweak production of vector boson pairs in association with two jets in proton-proton collisions at 13 TeV. 2019.

[119] Albert M Sirunyan et al. Search for anomalous triple gauge couplings in WW and WZ production in lepton + jet events in proton-proton collisions at $\sqrt{s} = 13$ TeV. 2019.

[120] Albert M Sirunyan et al. Measurement of electroweak WZ boson production and search for new physics in WZ + two jets events in pp collisions at $\sqrt{s} = 13$TeV. *Phys. Lett.*, B795:281–307, 2019.

[121] Albert M Sirunyan et al. Measurements of the pp $\to$ WZ inclusive and differential production cross section and constraints on charged anomalous triple gauge couplings at $\sqrt{s} = 13$ TeV. *JHEP*, 04:122, 2019.

[122] A. Tumasyan et al. Measurements of the electroweak diboson production cross sections in proton-proton collisions at $\sqrt{s} = 5.02\mathrm{TeV}$ using leptonic decays. *Phys. Rev. Lett.*, 127:191801, 2021.

[123] V. Khachatryan et al. Measurement of the WZ production cross section in pp collisions at $\sqrt{s} = 7$ and $8\mathrm{TeV}$ and search for anomalous triple gauge couplings at $\sqrt{s} = 8\mathrm{TeV}$. *Eur. Phys. J. C*, 77:236, 2017.

[124] HEPData record for this analysis, 2024.

[125] The Phase-2 Upgrade of the CMS Level-1 Trigger. Technical report, CERN, Geneva, 2020. Final version.

[126] Archie Sharma. The Phase-2 upgrade of the CMS Drift Tube detectors for High Luminosity LHC. Technical report, CERN, Geneva, 2023.

[127] The Phase-2 Upgrade of the CMS Muon Detectors. Technical report, CERN, Geneva, 2017. This is the final version, approved by the LHCC.

[128] Isidro Gonzalez Caballero. Longevity studies for the CMS Drift Tubes towards HL-LHC. Technical report, CERN, Geneva, 2024.

[129] Carlos Vico Villalba. Background Measurements in the CMS Drift Tubes during LHC Run2 and Long Term Irradiation Studies. In *2020 IEEE Nuclear Science Symposium (NSS) and Medical Imaging Conference (MIC)*, 10 2020.

[130] Javier Sastre Alvaro. The OBDT board: A prototype for the Phase 2 Drift Tubes on-detector electronics. Technical report, CERN, Geneva, 2020.

[131] G. Abbiendi et al. The Analytical Method algorithm for trigger primitives generation at the LHC Drift Tubes detector. *Nucl. Instrum. Meth. A*, 1049:168103, 2023.

[132] J. Prado, C. Vico, and S. Folgueras. Triggering on muon showers. *JINST*, 20(03):C03024, 2025.

[133] Albert M Sirunyan et al. Performance of the reconstruction and identification of high-momentum muons in proton-proton collisions at $\sqrt{s} = 13$ TeV. *JINST*, 15(02):P02027, 2020.

[134] High Multiplicity Trigger for Long-Lived Particles in CMS Detector in 2022 and 2023. 2024.

[135] C. Battilana. A slice-test demonstrator for the upgrade of the CMS drift tubes at High-Luminosity LHC. *JINST*, 17(10):C10007, 2022.

[136] Rikkert Frederix, Leif Gellersen, and Jasmina Nasufi. Matrix element corrections in top quark decays for the $t\bar{t}W^{\pm}$ process. *Eur. Phys. J. C*, 84(4):410, 2024.

[137] Michael E. Peskin and Daniel V. Schroeder. *An Introduction to quantum field theory*. Addison-Wesley, Reading, USA, 1995.